Adhesion of Novel High Performance Polymers to Carbon Fibers: Fiber Surface Treatment, Characterization, and Microbond Single Fiber Pull-Out Test

by

Cheryl L. Heisey

Dissertation Submitted to the Faculty of the
Virginia Polytechnic Institute and State University in
partial fulfillment of the requirements for the degree of

Doctor of Philosophy
in
Chemistry

Approved:

J. P. Wightman, Chairman

D. A. Dillard

H. Marand

J. S. Riffle

T. C. Ward

November, 1993
Blacksburg, VA

Adhesion of Novel High Performance Polymers to Carbon Fibers: Fiber Surface Treatment, Characterization, and Microbond Single Fiber Pull-Out Test

by

Cheryl L. Heisey

Committee Chairman: J. P. Wightman

Chemistry

(Abstract)

The adhesion of carbon fibers to several high performance polymers, including a phosphorus-containing bismaleimide, a cyanate ester resin, and a pyridine-containing thermoplastic, was evaluated using the microbond single fiber pull-out test. The objective was to determine the chemical and mechanical properties of the fiber and the polymer which affect the fiber/polymer adhesion in a given composite system. Fiber/matrix adhesion is of interest since the degree of adhesion and the nature of the fiber/matrix interphase has a major influence on the mechanical properties of a composite.

The surface chemical composition, topography, tensile strength, and surface energy of untreated AU-4 and commercially surface treated AS-4 carbon fibers were evaluated using x-ray photoelectron spectroscopy (XPS), scanning electron microscopy (SEM), single fiber tensile tests, and dynamic contact angle analysis. The commercial surface treatment which converted the AU-4 to the AS-4 fiber oxidized the carbon fiber surface. The surface of the AS-4 carbon fiber was further modified using air, oxygen, ammonia, and ethylene plasmas. The AS-4 fiber tow was also characterized following exposure to the aqueous poly(amic acid) solution used to disperse the matrix powder during aqueous suspension prepregging of thermoplastic matrix composites.

The air and oxygen plasma treatments significantly oxidized and roughened the surface of the AS-4 carbon fibers. In addition, the air and oxygen plasma increased the the polar component of the AS-4 fiber surface energy. The ammonia plasma increased the concentration of nitrogen on the fiber surface, without significantly altering the fiber topography (at a magnification of 50,000X). The atomic oxygen present in the air and oxygen plasma treatments is capable of reacting with both the edge and basal planes in the carbon fiber structure. As a result, the oxygen-containing plasmas progressively ablated the organic material in the carbon fiber surface. Energetic species in the ammonia plasma cleaned the fiber surface and reacted with the carbon fiber surface, increasing the concentration of amine groups in the fiber surface. The ethylene plasma deposited a layer of plasma polymerized polymer on the carbon fiber surface. The AS-4 carbon fibers were coated with poly(amic acid) when the tow was wet with the aqueous suspension prepregging solution.

The carbon fiber adhesion of bis(3-maleimido phenoxy) triphenylphosphine oxide was compared to that of Ciba-Geigy's Matrimid 5292 A/B bismaleimide system. With both bismaleimides, the carbon fiber adhesion increased significantly when the fiber received an oxidative commercial surface treatment or was exposed to an air or ammonia plasma prior to bonding. In contrast, the poly(pyridine-bis A) microbond pull-out test results showed that the carbon fiber adhesion of poly(pyridine-bis A) was not affected by the fiber surface chemical composition, fiber surface energy, or topography.

To Martin
& my family

Your love has given me great joy and encouragement.
-Philemon 7

ACKNOWLEDGEMENTS

I would like to thank the following individuals and organizations for their contributions to this research:

Dr. J. P. Wightman, my committee chairman, for his support and guidance during the last four years and for the opportunity to present my research at professional meetings.

Dr. D. A. Dillard, Dr. H. Marand, Dr. J. S. Riffle, and Dr. T. C. Ward for serving on my committee. I particularly thank Dr. Riffle for her help with the pyridine-containing polymers synthesized in her laboratory.

National Science Foundation Science & Technology Center for High Performance Polymeric Adhesives and Composites and the Adhesive & Sealant Council, Inc. for funding.

Ciba-Geigy, Inc. for providing the Matrimid 5292 bismaleimide resin.

Dr. Paul Wood and Dr. J. E. McGrath for their helpful suggestions and for providing the phosphine oxide containing bismaleimide.

Dr. R. M. Davis, Mr. Tae-Hwa Yu, and Mr. Alvaro Gonzalez for collaborative work with the polyimide-coated carbon fibers.

Mr. Andy Brink for his helpful suggestions and for providing the poly(pyridine-bis A) and thermal analysis data on this material.

My group colleagues, Ms. Mojee Babai-Cline, Ms. Joannie Chin, Dr. Pascal Commerçon, Ms. Holly Grammer, Dr. Tim Lin, Dr. Marc Mantel, Ms. Beena Menon, Mr. Nick Shephard, Dr. Francis Webster, and Ms. Hong Zhuang for their friendship and many helpful conversations. I especially thank Pascal, who initiated use of the microbond test in Dr. Wightman's group and was kind enough to share his equipment and expertise, and Joannie who performed the FT-IR analysis of the ethylene plasma polymer.

Mr. Satya Srinivasin, for collaborative work with the cyanate esters.

Dr. Joyce Kaltenecker-Commerçon, for thermal analysis assistance and for writing the computer program for statistical analysis of the contact angle measurements.

Mr. Steve McCartney, for taking the high resolution scanning electron photomicrographs.

Mr. Frank Cromer, for his surface analysis advise, technical expertise, and patience.

Ms. Katy Hatfield, Ms. Kim Linkous, and Ms. Virginia Keller for all their help in the Center for Adhesive & Sealant Science office.

Ms. Esther Brann, Ms. Joyce Moser, Ms. Millie Ryan, and Ms. Laurie Good for their assistance in the NSF Science and Technology Center office.

Ms. Pamela Percha for inviting me into her home during my last weeks in Blacksburg. Pamela, your kindness meant a lot to me.

and, finally, Dr. Martin Rogers, for making these four years in graduate school, the first four years of our marriage, very happy times. My love to you, Martin, for all your encouraging words, your thoughtfulness, and most of all, your sense of humor.

TABLE OF CONTENTS

LIST OF FIGURES

LIST OF TABLES

CHAPTER 1
INTRODUCTION

1.1 CARBON FIBER-REINFORCED COMPOSITES

Combining and orienting materials to achieve superior properties is a well-proven concept. Evidence of man-made composites, such as straw-reinforced bricks and boats constructed of reeds and pitch, are found throughout recorded history [1, 2]. In addition, many biological materials are complex composite systems based on fibrous polymeric structures. Examples of such biocomposites include wood and tendons [3]. Today, the demand for high performance, lightweight materials has led to considerable research and development in the field of fiber-reinforced resin matrix composites. Advanced composites are formed by aligning extremely strong and stiff continuous fibers in a polymer matrix [1]. Composites can be fabricated from a wide variety of reinforcement fibers and matrix resins and, therefore, their properties may vary over a considerable range.

The majority of advanced composites are manufactured for use in aerospace applications [1, 4]. Although metals can withstand higher temperatures and are generally less expensive, composites are attractive for weight savings, which average from 20 to 30% [4]. Weight reduction translates into several advantages specific to the aerospace industry including fuel economy, increased range or speed, and shorter takeoff and landing distances [4]. Advanced composites are also used in industrial machinery, automobiles, sports equipment, and in marine products [5-8]. In general, carbon fiber-reinforced composites possess a number of advantages relative to conventional materials including high strength and stiffness, excellent compressive properties, light weight, improved fatigue resistance and vibration damping, good friction and wear qualities, low

thermal expansion, and thermal and electrical conductivity [9, 10]. Properties of carbon fiber composites are compared to those of steel and aluminum in Figure 1.1 [11].

The matrix material in an advanced resin matrix composite may be either a thermoset or a thermoplastic polymer. The matrix must adhere well to the reinforcing fibers, be strong, offer environmental protection, damage resistance, and good thermal properties [12]. In 1989, thermosets accounted for about 99% of the advanced composite market [4]. This is largely due to the low viscosity of thermosetting resins, which facilitates fiber impregnation during composite fabrication. However, because thermosetting resins must be cured, thermosetting matrix composites are time consuming to process and difficult to repair [13].

Epoxies account for about 80 to 90% of the thermosetting resins used in advanced composites, followed by bismaleimides and polyimides [4]. Epoxy resins are the composite matrix resin of choice because they are easy to process, adhere well to reinforcing fibers, offer low shrinkage upon cure, chemical resistance, and good electrical insulation [1, 10, 14, 15]. However, the upper use temperature of epoxy for structural performance is approximately 350°F (177°C) in dry and only 300°F (149°C) in moist environments [4, 14]. Therefore, the application of epoxy composites is limited to non-thermally critical structural parts. Recently, interest has developed in making parts for thermally critical areas such as engines and in the use of high performance composites in military aircraft, where skin temperatures can be higher than epoxy resin capabilities [14]. Higher temperature performance resins such as bismaleimides and polyimides are needed for composites when epoxies cannot be used [14].

In contrast to thermosets, thermoplastics are not crosslinked and promise high volume processing, an associated low cost per part, and superior impact resistance [13].

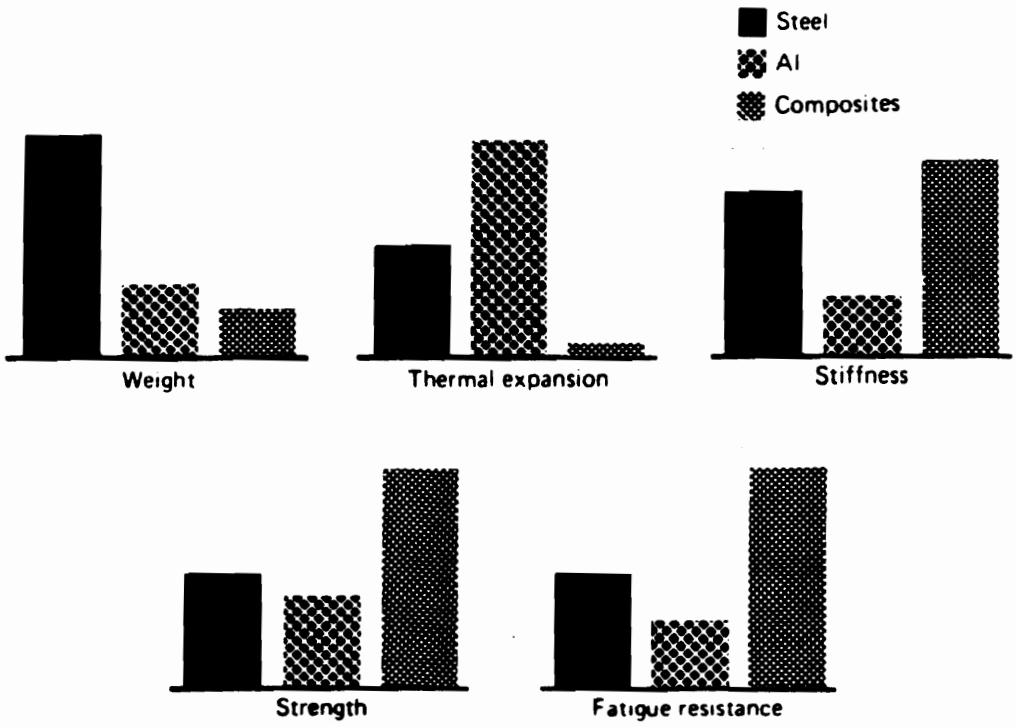

Figure 1.1. Properties of carbon fiber composites compared with those of steel and aluminum [11].

The advantages and disadvantages of continuous-fiber reinforced thermoplastic versus continuous-fiber reinforced thermoset composites are listed in Table 1.1 [5]. A large number of high temperature thermoplastic polymers have been investigated for use in advanced composites, including polyetheretherketone, polyphenylene sulfide, polyetherimide, polyamideimide, and thermoplastic polyimide [13]. These materials are of interest due to their high use temperatures, low flammability and smoke generation, and resistance to a variety of chemicals and solvents [4].

In one cubic meter of continuous fiber composite, there are from 9 to 18 square meters of fiber/matrix interfacial area [16]. It is generally accepted that this extensive region must play a key role in the basic mechanical properties of the composite and in its environmental stability. Indeed, "good" fiber/matrix adhesion is essential to achieve high interfacial and off-axis strength, efficient load transfer from the matrix to the fiber, and long term property retention [17]. The fiber/matrix bond may have both a chemical component and a physical component [18]. On a clean carbon fiber surface, chemical interactions may occur between the fiber and the matrix at active sites located on the edges of the layer planes in the carbon fiber structure as well as at imperfections in the structure. In addition, fiber/matrix adhesion may either increase or decrease with surface roughness, depending on the magnitude and geometry of the roughness and, the ability of the matrix material to wet the rough fiber surface [18].

Carbon fibers are normally treated to improve fiber/matrix adhesion. The objectives of these treatments are to etch the surface, remove any weakly bonded carbon debris and impurities, leave polar hydrophilic oxygen-containing groups on the surface, and increase the fiber wettability and bondability to the resin matrix [10]. Various techniques have been studied to improve the fiber/matrix adhesion by chemically modifying the fiber surface [10, 11, 19]. Interest in carbon fiber plasma treatments has been promoted by the

Table 1.1. Advantages and disadvantages of continuous-fiber-reinforced thermoplastic composites as compared to continuous-fiber reinforced thermoset composites [5].

ADVANTAGES: 1. Infinite storage capability (shelf life). 2. Variety of thermoplastic materials available to meet such specific requirements as abrasion resistance, UV resistance, good electrical properties, and weathering resistance. 3. Shorter fabrication time. 4. Post-formable 5. Ease of handling - no "tack" problems. 6. Ease of repair - welding, solvent bonding, adhesive bonding. 7. Reprocessing capability. 8. Lower cost.
DISADVANTAGES: 1. Creep 2. Limited temperature capability 3. Limited processing technology available. 4. Limited chemical resistance of materials used to date.

development of continuous plasma treatment equipment and because plasma treatment is environmentally responsible with no harmful by-products.

The shear strength of the fiber/matrix bond can be estimated using tests on real composites and on model single fiber composites [20]. When evaluating a number of surface treatments or when working with novel matrix materials, the preparation and testing of real composite samples may be expensive and time consuming. Single fiber tests are an economical alternative [21]. Single fiber tests have been used extensively in the study of fiber/epoxy adhesion [22, 23]. However, few researchers have used single fiber tests to investigate the effect of carbon fiber surface treatments on the adhesion of high performance polymers.

1.2 RESEARCH OBJECTIVES

The objective of this research is to study the adhesion of high performance polymers to "as received" and plasma treated carbon fibers using the microbond single fiber pull-out test. The effects of air, oxygen, ammonia, and ethylene plasma treatments on the carbon fiber tensile strength, surface free energy, surface atomic composition, and topography were explored. The carbon fiber properties were related to the fiber/matrix adhesion of commercially available and novel high performance thermoplastic and thermoset polymers.

1.3 REFERENCES

1. F. P. Gerstle, Jr. in High Performance Polymers and Composites, J. I. Kroschwitz (ed.), Encyclopedia Reprint Series, Wiley-Interscience, New York (1991) .
2. R. P. Sheldon, Composite Polymeric Materials, Applied Science, New York (1982).
3. R. J. Morgan, E. Baer, and A. Hiltner, *SAMPE J.* **29** (2) (1993) 9.
4. A. M. Thayer, *C &E News*, (July 23, 1990) 37.

5. D. M. Riggs, R. J. Shuford, and R. W. Lewis in Handbook of Composites, G. Lubin (ed.), Van Nostrand Reinhold, New York (1982) 196.

6. M. Martin and J. F. Dockum, Jr. in Handbook of Composites, G. Lubin (ed.), Van Nostrand Reinhold, New York (1982) 679.

7. W. R. Graner, in Handbook of Composites, G. Lubin (ed.), Van Nostrand Reinhold, New York (1982) 699.

8. G. Lubin and S. J. Dastin in Handbook of Composites, G. Lubin (ed.), Van Nostrand Reinhold, New York (1982) 722.

9. R. M. Gill, Carbon Fibres in Composite Materials, The Plastics Institute, London, (1972).

10. J. P. Riggs in Encyclopedia of Polymer Science & Engineering-Vol. 2, 2nd ed., H. F. Mark, N. M. Bikales, C. G. Overberger, and G. Menges (eds.), Wiley-Interscience, New York (1985) 640.

11. J. Delmonte, Technology of Carbon and Graphite Fiber Composites, Van Nostrand Reinhold, New York (1981).

12. B. Harris, Engineering Composite Materials, The Institute of Metals, North American Publications Center, Brookfield, VT (1986).

13. D. M. Bigg in International Encyclopedia of Composites-Vol. 6, S. M. Lee (ed.), VCH Publishers, New York (1990) 10.

14. D. Landman in Developments in Reinforced Plastics-Vol. 5, G. Pritchard (ed.), Elsevier Applied Science, New York, (1986).

15. L. S. Penn and T. T. Chiao in Handbook of Composites, G. Lubin (ed.), Van Nostrand Reinhold, New York (1982) 57.

16. W. D. Bascom in International Encyclopedia of Composites-Vol. 3, S. M. Lee (ed.), VCH Publishers, New York (1990) 411.

17. V. Rao, P. Herrera-Franco, A. D. Ozzello, and L. T. Drzal, *J. Adhesion*, **34** (1991) 65.

18. W. P. Hoffman, W. C. Hurley, P. M. Liu, and T. W. Owens, *J. Mater. Res.* **6** (8) (1991) 1685.

19. J. B. Donnet and R. C. Bansal, Carbon Fibers, 2nd ed., Marcel Dekker, New York (1990).

20. M. R. Piggot, *Compos. Sci. Technol.* **42** (1991) 57.

21. J. C. Figueroa, T. E. Carney, L. S. Schadler, and L. C. Laird, *Compos. Sci. Technol.* **42** (1991) 77.

22. J. D. H. Hughes, *Compos. Sci. Technol.* **41** (1991) 13.

23. P. J. Herrara-Franco and L. T. Drzal, *Composites* **23** (1) (1992) 2.

CHAPTER 2
CARBON FIBER ADHESION PRINCIPLES, SURFACE TREATMENT, AND CHARACTERIZATION

2.1 LITERATURE REVIEW

2.1.1 Adhesion Principles

Adhesion may be defined either thermodynamically or in terms of adhesive performance [1-3].

2.1.1.1 Thermodynamic Adhesion

Thermodynamic adhesion is the atomic or molecular attractive force across an interface [1-3]. Because attractive interfacial forces cannot be directly measured, the thermodynamic definition of adhesion is a qualitative description explaining why bonded materials resist separation [1].

The equilibrium condition for a surface in terms of the Gibbs' free energy (G) is,

$$dG = \sum \mu_i dn_i + VdP - SdT + \gamma dA = 0 \qquad (2.1)$$

where μ_i is the chemical potential of species i, n_i is the number of moles of species i, P is the pressure, V is the volume, T is the absolute temperature, S is the entropy, γ is the surface tension, and A is the surface area [4, 5]. Therefore, surface tension is the change in free energy with change in surface area as shown in equation 2.2 [4, 5].

$$\gamma = (\partial G/\partial A)_{T, P, n} \qquad (2.2)$$

Generally, the terms 'surface tension,' 'surface energy,' and 'surface free energy' are used interchangeably [5, 6].

The work of adhesion is the reversible work per unit area required to separate two phases in intimate contact to give two clean surfaces. The Dupré equation states that the

work of adhesion (W_a) must equal the free energy change of the system as described in equation 2.3,

$$W_a = \gamma_1 + \gamma_2 - \gamma_{12} \tag{2.3}$$

where γ_1 and γ_2 are the respective surface tensions of the two phases and γ_{12} is the interfacial surface tension between them [6-9].

The work of adhesion between liquids and solids is determined from equilibrium or quasi-equilibrium measurements of contact angles [1]. Figure 2.1 shows the balance of surface tensions in the contact angle experiment [5]. When $\theta = 0°$, the liquid spreads over the surface and is said to completely wet it. Complete wetting occurs when the molecular attraction between the liquid and solid molecules is greater than that between similar liquid molecules [8]. When $\theta > 90°$, the liquid is said to not wet the solid.

The equilibrium contact angle is such that the total surface free energy of the system (i.e., $\gamma_S A_S + \gamma_{SL} A_{SL} + \gamma_L A_L$) is at a minimum. If the liquid making an equilibrium contact angle (θ) spreads an infinitesimal amount further to cover an extra area (dA) of the solid surface, the increase in the liquid-vapor interfacial area is $dA\cos\theta$ and the change in the free energy of the system (dG) is given by equation 2.4,

$$dG = \gamma_{SL} dA + \gamma_L dA \cos\theta - \gamma_S dA \tag{2.4}$$

where γ_S is the surface tension of the solid surface in equilibrium with the vapor of the wetting liquid, γ_L is the surface tension of the liquid, and γ_{SL} in the interfacial surface tension between the solid and the liquid [9]. If the system is at equilibrium, $dG = 0$, and the balance of surface free energies is expressed by equation 2.5, known as the Young equation [4, 6].

$$\gamma_{SV} = \gamma_{SL} + \gamma_{LV} \cos\theta \tag{2.5}$$

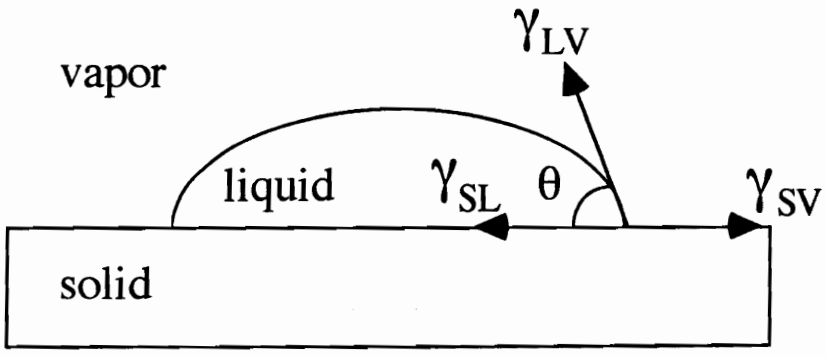

Figure 2.1. Balance of surface tensions in the contact angle experiment.

When equations 2.3 and 2.5 are combined to give equation 2.6, the work of adhesion is expressed by the Young-Dupré equation [6, 10].

$$W_a = \gamma_{LV}(1 + \cos\theta) \tag{2.6}$$

2.1.1.2 Adhesive Performance

Adhesive performance is a measure of the mechanical resistance to separate a system of joined materials and is influenced by the testing geometry, the interface topography, the chemical nature of the materials, the mechanical responses of the solid and the viscoelastic phases, strain rates, the testing environment, and such unknowns as the thermodynamic state of the system [1, 3]. Adhesive performance is the quantitative measure of the energy required to break an adhesive bond [1].

2.1.2 Adhesion Theories

The theories proposed to explain adhesion have been classified into five categories: (1) adsorption, (2) mechanical interlocking, (3) interdiffusion, (4) electrostatic attraction, and (5) rheological [1, 7, 8, 11]. At present, there is no single theory which accounts for all adhesion-related phenomena. This is probably due to the wide range of materials which are bonded and to the interdisciplinary nature of adhesion. Adhesion science involves chemistry, mechanics, and an understanding of the adhesive/adherend interface or interphase.

2.1.2.1 Adsorption

The adsorption theory assumes that adhesion is caused by physical and chemical adsorption interactions between the atoms in the two materials being bonded [1, 7]. The interactions which may occur across an interface include dispersion forces, hydrogen bonds, dipole/dipole forces, dipole/induced dipole forces, acid/base interactions, and covalent bonds [7]. These forces are effective over distances in the range of a few tens of

angstroms [7]. Therefore, for these forces to occur across an interface between two materials, the materials must be in very close molecular contact.

2.1.2.2 Mechanical Interlocking

The mechanical interlocking theory proposes that adhesion is due to irregularities on the adherend surface into which the polymeric adhesive may flow or to projections around which the adhesive solidifies [8]. Mechanical interlocking is enhanced by increasing the adherend surface roughness or by promoting penetration of the adhesive into surface pores. To separate the adhesive and adherend, energy must be expended and work done to deform and draw the material of lower compliance, provided that the surface features of the more rigid material are strong enough to withstand the force and do not fracture [7].

Mechanical interlocking probably plays a role in the adhesion of certain systems, such as the adhesion of rubber to textiles [12] and adhesion to anodised metals [13-15]. It must be noted, however, that when a surface is roughened in preparation for bonding there may be explanations other than mechanical interlocking for an increase in adhesive performance. For example, when a surface is roughened, the surface area over which adsorption interactions may occur between the adhesive and adherend is increased. In addition, the change in the adherend microgeometry may affect the local microdeformation, failure, and adhesive performance of the joint [1].

2.1.2.3 Interdiffusion

The interdiffusion or diffusion theory, introduced by Voyutskii, attributes adhesion to intermolecular entanglements across the interface [16]. This theory proposes that a liquid adhesive may dissolve and diffuse into the substrate material or that polymer chains may become entangled across a polymer/polymer interface when an adhesive joint is heated above the glass transition temperature of the polymers. The extent of diffusion

depends upon the affinity of the different types of molecules for one another and the mobility of the polymer chains.

2.1.2.4 Electrostatic Attraction

Deryaguin proposed that electrostatic forces develop at an interface between an adhesive and a substrate with different electronic band structures [17]. Electrons are transferred across the interface, creating positive and negative charges that attract one another.

2.1.2.5 Rheological

Bikerman states that the performance of an adhesive joint is due to the mechanical properties of the materials comprising the joint and to the local stresses in the joint [18]. The adhesive performance is not determined by interfacial forces because clean adhesive failure is highly uncommon.

2.1.3 Concept of an Interphase

Very often, only the properties of the adherend(s) and the adhesive are considered in an adhesive joint. In reality, although the chemical and mechanical properties of these materials may be well understood in the bulk, their surfaces may be compositionally, structurally, and morphologically complex and vary with both processing and handling [1, 11, 19, 20]. The nature of these surface layers and their effects on adhesive joint behavior have been discussed by Bikerman in the context of "weak boundary layers" [18].

When adhesive performance data is evaluated, it is necessary to consider the three-dimensional interfacial region or interphase which may have properties different from either the bulk adherend or the bulk adhesive. The interphase includes the two-dimensional area of contact and incorporates a region of some finite thickness extending

on both sides of the interface [21]. Sharpe defined this boundary layer or interphase as a region intermediate to two phases in contact, the composition and/or structure and/or properties of which may be variable across the region and which also may differ from the composition and/or structure and/or properties of either of the two contacting phases [1, 11].

Herrera-Franco and Drzal illustrated the complexity of the fiber/matrix interphase in a composite using the schematic illustration in Figure 2.2 [21]. The fiber/matrix interphase is characterized by the fiber morphology, fiber topography, fiber surface chemistry, any adsorbed material or coatings on the fiber, and by the properties of the matrix in close proximity to the fiber surface.

2.1.4 Fiber/Matrix Adhesion

There is general agreement that the degree of adhesion between the fiber and the matrix and the nature of the fiber/matrix interphase has a major influence on the mechanical properties of a composite in both the off-axis and fiber directions [21, 22]. "Good" fiber/matrix adhesion is required for effective transfer of stress from the matrix to the reinforcing fibers.

2.1.4.1 Mechanical Tests Used to Measure Fiber/Matrix Adhesion

A number of mechanical tests have been developed to determine the capacity of the interface to transfer stress from the matrix to the fiber in a composite. Tests which measure fiber/matrix interface strength include tests on real composites (usually unidirectional composites) with a high fiber-volume fraction (typically 60% by volume) and tests on model single-fiber composites [23]. The most commonly used tests on real composites are the

- short beam shear test,
- Iosipescu shear test,

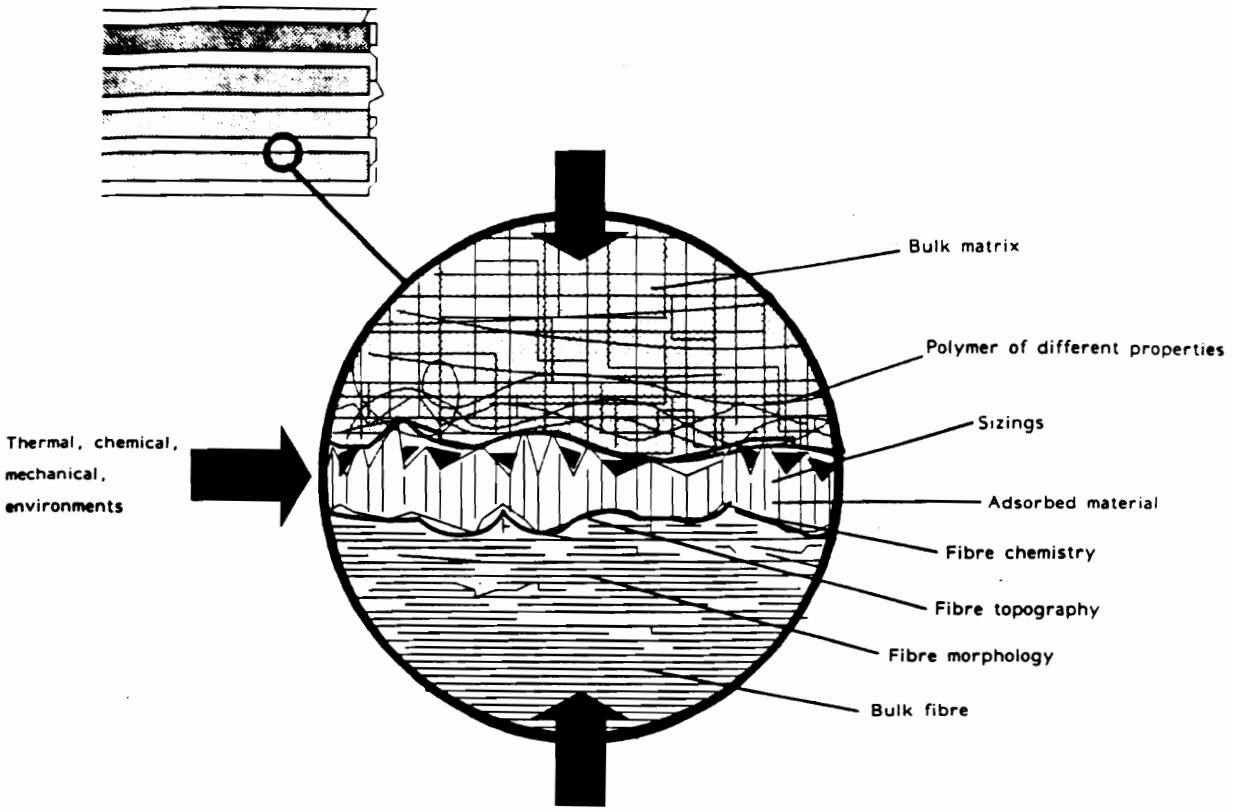

Figure 2.2. Characteristics of the fiber/matrix interphase in a composite material [21].

- transverse and off-axis tensile tests, and
- indentation tests.

The most commonly used tests on model single fiber composites are the

- pull-out and microbond tests and
- fragmentation test.

The geometries of these tests are described in Figures 2.3, 2.4, and 2.5 [21, 23, 27, 30].

The short beam shear test is used to estimate the interlaminar shear strength [24]. A unidirectional composite specimen with a small span-to-depth ratio is loaded in such a way that failure occurs in a shear mode parallel to the fibers. The fibers are oriented in the direction perpendicular to the axes of the support. In the Iosipescu shear test, a state of uniform pure shear is achieved when the test section of the specimen in loaded as shown in Figure 2.3(b) [25]. The fibers can be aligned either in the direction or perpendicular to the direction of the applied force. In transverse ($\theta = 90°$) and off-axis tensile tests, unidirectional composites are subjected to an off-axis tensile stress by varying the angle (θ) between the direction of the applied load and the fibers. In the transverse tensile test, the fiber/matrix interface is directly submitted to tensile load. Experiments in which the composite is under a state of combined stress rather than pure shear are also carried out at small values of θ (10° to 15°) or at $\pm$ 45° [26].

Indentation tests may be performed using either a micro- or a meso-indentation technique. A composite specimen is sectioned perpendicular to the fiber axis and polished until the surface is flat. In the micro-indentation experiment, the end of a single fiber is compression-loaded with a very fine diamond tip, and the fiber is pushed out of the composite [27]. Micro-indentation experiments have been performed on real composites [21, 28] and on model single fiber composites [29]. In meso-indentation, a portion of the polished composite surface which encompasses the ends of many fibers is

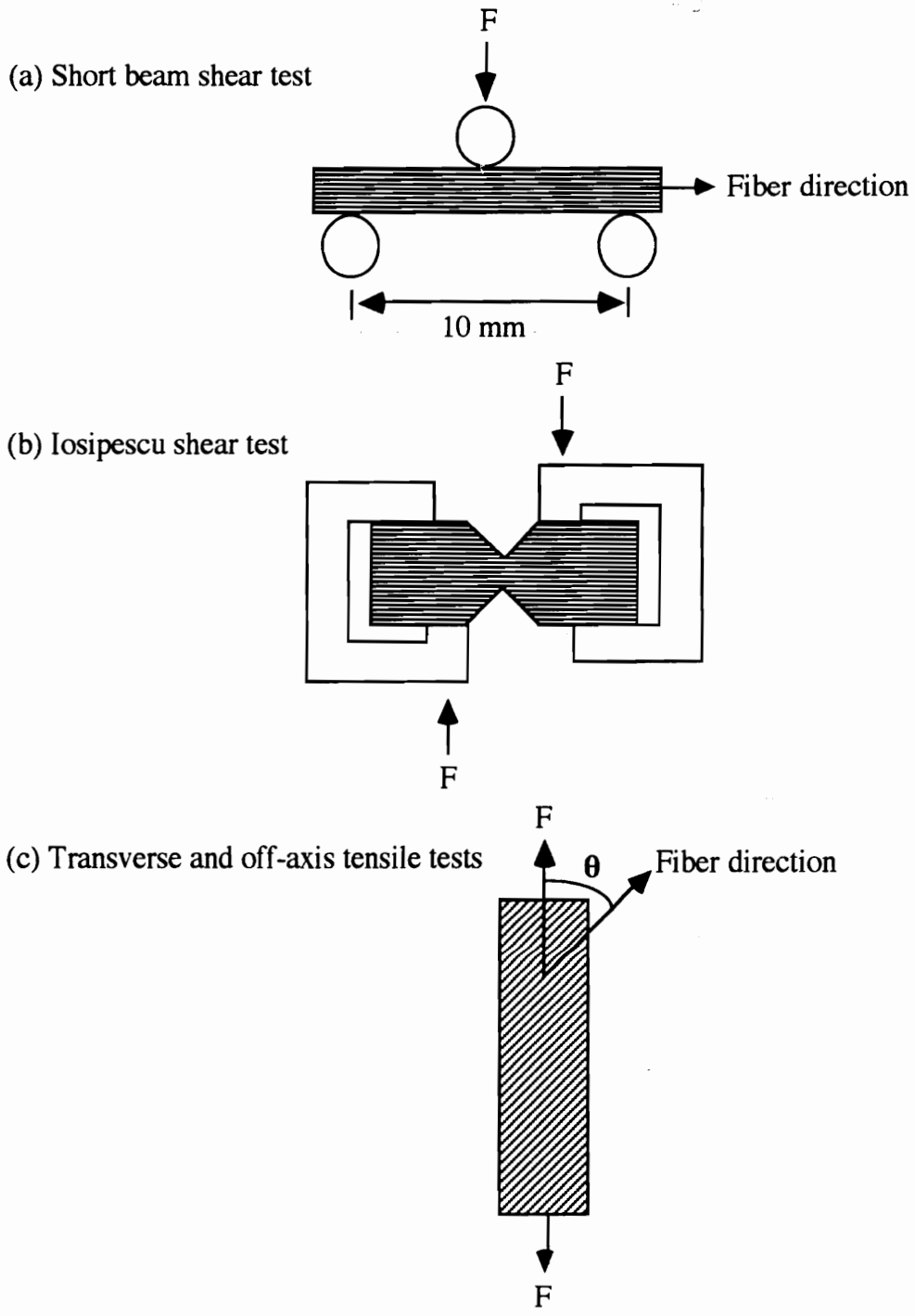

Figure 2.3. Commonly used mechanical tests to assess the fiber/matrix interface strength in real composites include (a) short beam shear, (b) Iosipescu shear, and (c) transverse and off-axis tensile tests [adapted from refs. 21 and 23].

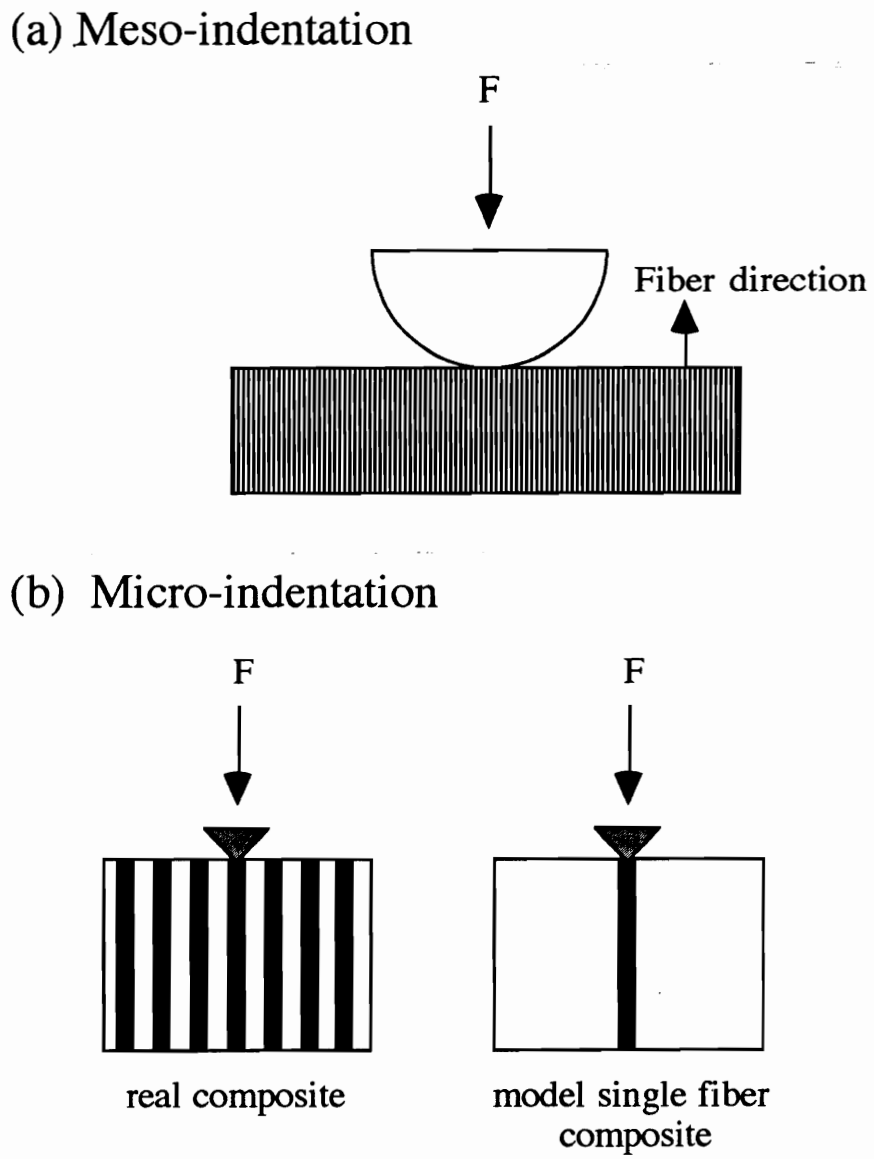

Figure 2.4. (a) Meso-indentation and (b) micro-indentation tests used to assess the fiber/matrix interface strength in real and model composites [adapted from refs. 21, 27, and 30].

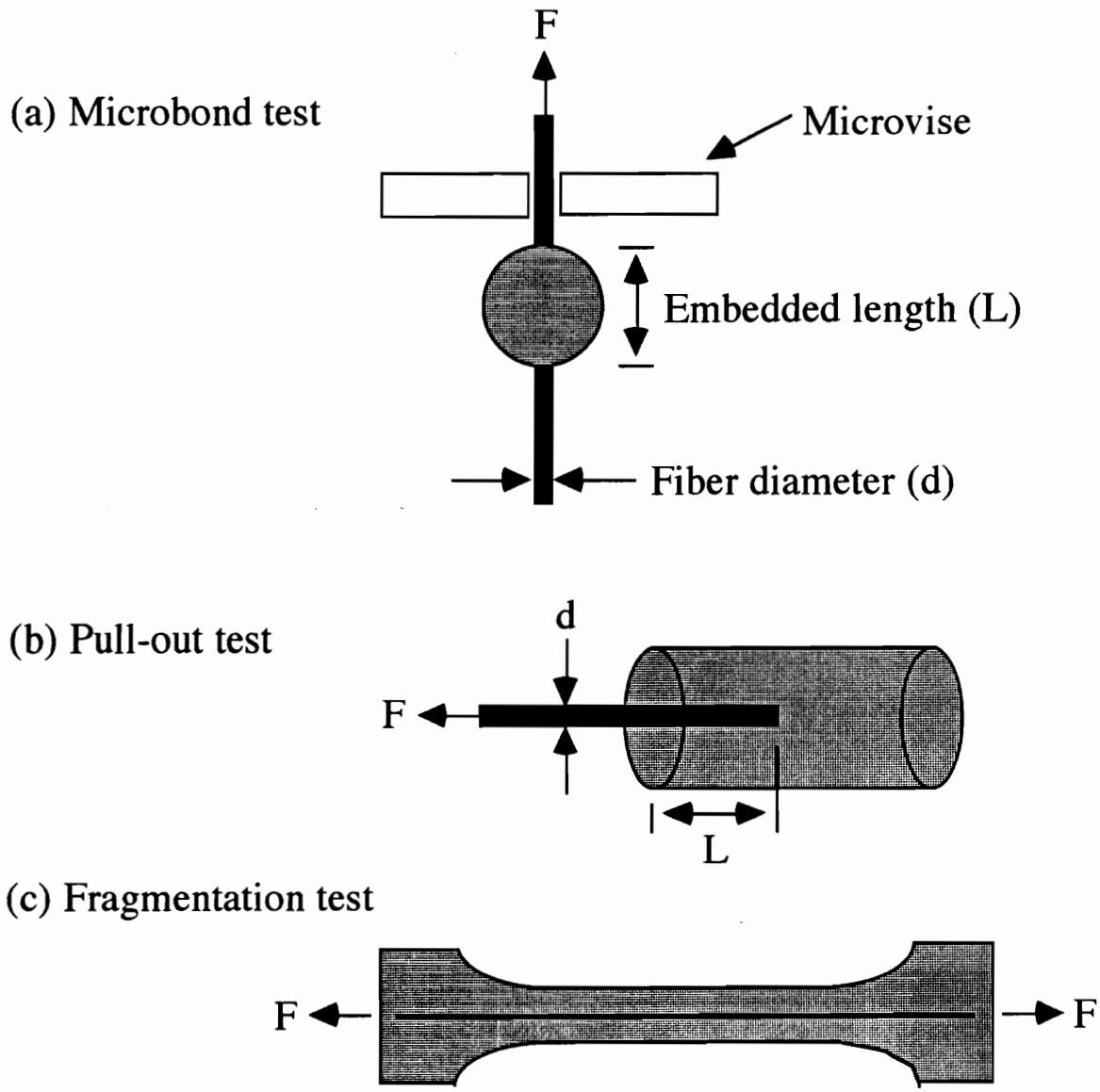

Figure 2.5. Commonly used mechanical tests to assess the fiber/matrix interface strength in model single fiber composites include the (a) microbond, (b) pull-out, and (c) fragmentation tests [adapted from ref. 21 and 23].

indented using a continuous ball indenter [30].

In the single-fiber fragmentation test, a single fiber is encapsulated in a dogbond tensile coupon, the coupon is strained in the fiber axial direction to near its point of rupture, and then the fiber fragment lengths inside the specimen are measured. The fiber/matrix shear strength is calculated by applying Weibull statistics to the distribution of fragment lengths [21, 23]. In a fiber pull-out test, the end of a single fiber is embedded in a resin plug with the fiber axis perpendicular to the surface of the matrix. When the resin plug is an axisymmetric resin drop, the pull-out test is called the microbond test. An increasing force is applied to the free fiber end and the fiber is pulled out of the matrix [21, 23].

Each of these methods has inherent problems that limit its applicability as a universal test method for characterization of interfacial shear strength [31]. Herraro-Franco and Drzal performed the single fiber fragmentation, microbond, micro-indentation, ± 45° tensile, short beam shear, and Iosipescu shear tests using an epoxy matrix (Epon 828/m-PDA) and AU-4 and AS-4 carbon fibers [21]. Table 2.1 lists the range of values they obtained for the fiber/matrix interfacial shear strength using these test methods. The interfacial shear strength reported by Lesko using the meso-indentation technique with AU-4 carbon fibers and an epoxy matrix (Epon 828/m-PDA) is also given in Table 2.1 [30]. While the interfacial shear strength values obtained vary over a considerable range, the AS-4 carbon fiber showed the greatest shear strength in each case.

There is an extensive amount of literature available on fiber/matrix adhesion measurement including work that involves single fiber fragmentation [32-54], indentation [21, 27-30, 55-58], microbond [21, 31, 54, 59-72], fiber pull-out from a resin block [73-90], fiber pull-out from a microcomposite [91], the use of laser Raman spectroscopy to determine fiber strain in composites [92], a three fiber pull-out technique [93], and the

Table 2.1. Summary of interfacial shear strength values [21, 30].

Test	AU-4/828, mPDA (MPa)	AS-4/828, mPDA (MPa)	Ratio AS-4/AU-4
Single-fiber fragmentation[21]	37.20	68.30	1.8
Microbond test[21]	23.44	50.30	2.1
Micro-indentation technique[21]	55.54	71.53	1.3
Meso- indentation technique[30]	71.7	---	---
$(\pm 45)_{3s}$ tensile test[21]	37.16	72.19	1.9
Iosipescu shear test[21]	54.98	95.28	1.7
Short-beam shear test[21]	47.52	84.04	1.8

use of mechanical tests [21, 94-106]. The microbond fiber pull-out test was used in this work and will be the only technique discussed in detail in this review.

2.1.4.2 Fiber Pull-Out Tests

In the pull-out experiment, a single fiber is partially embedded in a plug of matrix material of known geometry. An increasing force is applied to the free end of the fiber to pull it out of the matrix. Assuming that the shear stress is uniformly distributed along the embedded length (L) the mean value of the shear strength (τ) of the fiber/matrix interface is given by equation 2.7,

$$\tau = \frac{F_d}{\pi \; d \; L} \tag{2.7}$$

where d is the fiber diameter and F_d is the force required for fiber debonding [23].

Pulling thin fibers out of various matrices has been used since the 1960's to investigate the basic characteristics of the fiber/matrix interface and to assess the effects of new surface treatments or sizings on the fiber/matrix interface strength [107-110]. As demonstrated with glass/cement systems [111] and tungsten/copper systems [112], it is relatively easy to carry out pull-out tests with rods or thick fibers. However, when a high level of adhesion is established at the fiber/matrix interface and the fiber diameter is small (< 10 μm for carbon fibers) the length of fiber embedded in the matrix must be less than a critical length in order to pull the fiber out the matrix instead of breaking the fiber.

Depending upon the strength of the fiber, the fiber embedded length must usually be kept between 50 and 150 μm [68]. Pull-out test specimens with such small fiber embedded depths may be quite difficult to prepare [107]. In order to more easily prepare pull-out samples with very small fiber embedded lengths, Miller and coworkers developed the microdrop or microbond test in which the fiber is pulled out of a small axisymmetrical drop of resin [59].

The advantages and limitations of the microbond technique as summarized by Herrera-Franco and Drzal are listed below [21].

Advantages of the Microbond Technique:

- The value of the force at the moment of debonding can be measured.
- The technique can be used for almost any fiber/matrix combination.

Limitations of the Microbond Technique:

- The debonding force is a function of the embedded length. When using fibers with a diameter ranging from 5 to 50 μm, embedded lengths longer than 50 to 100 μm may cause fiber fracture.
- The meniscus that is formed on the fiber by the resin makes measurement of the embedded length somewhat inaccurate.
- The small microdrop size makes the failure process difficult to observe.
- The state of stress in the droplet can vary with both droplet size and with variations in the distance between the blades used to debond the microdrop.
- The presence of a meniscus has a large effect on the interfacial stresses which oscillate along the embedded fiber and makes calculation of an average shear strength value questionable.
- Premature failure of the meniscus region due to tensile stresses could lead to premature debonding of the microdrop.
- The mechanical properties of the microdrop may vary with size due to variation of curing agent concentration.
- For a given fiber/matrix combination, a relatively large scatter in the test data is obtained from the microbond test. This data scatter has been attributed to testing parameters such as position of the microdrop in the loading fixture, droplet gripping, faulty measurement of fiber diameters, and variation in the chemical, physical or morphogical nature of the fiber along its length [59, 68, 113-115].

2.1.4.2.1 Theoretical Analyses of the Fiber Pull-Out Test

Désarmot and Favre state that in spite of the unrealistic character of the single fiber pull-out test when compared to the complexity of a composite material, much information can be derived that has to do with the most fundamental aspects of the fiber/matrix mechanical interaction [107]. However, the interpretation of pull-out test data is still open to discussion [107]. The shear stress in the pull-out test has been analysed using a shear lag approach and a fracture energy approach. The analyses presented are applied to pull-out from either a resin plug or a microdrop.

2.1.4.2.1.1 Shear Lag Approach

The shear lag analysis proposed by Greszczuk shows that the elastic interfacial shear strength (τ_x) varies as a function of the depth (x) as described in Figure 2.6 [23, 107, 116]. Assuming that debonding occurs instantaneously in a catastrophic way, the shear stress at any point x is given by equation 2.8,

$$\tau_x = \tau\alpha L\left[\coth(\alpha L)\cosh(\alpha x) - \sinh(\alpha x)\right] \tag{2.8}$$

where τ is the mean shear strength given by equation 2.7, L is the fiber embedded length, and α is an elastic coefficient,

$$\alpha^2 = \frac{2G_i}{b_i r_f E_f} = \frac{2G_m}{r_f^2 E_f \ln(R/2r_f)} \tag{2.9}$$

where b_i is the thickness of the interfacial layer, G_i is the shear modulus of the interfacial layer, G_m is the shear modulus of the matrix, E_f is the Young's modulus of the fiber, and R is the radius of the matrix involved by the shear stress.

At x = 0, the shear strength reaches its maximum value (τ_{max}),

$$\tau_{max} = \tau\alpha L\coth(\alpha L) = \frac{\alpha F_d}{\pi d}\coth(\alpha L) \tag{2.10}$$

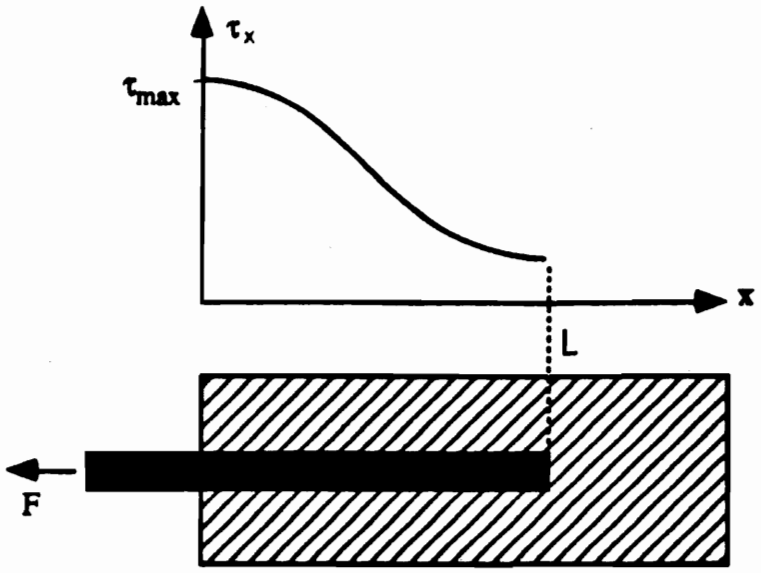

Figure 2.6. Variation of interfacial shear strength (τ_x) along the fiber embedded length [adapted from ref. 23].

Equation 2.10 may then be rearranged to give equation 2.11, an expression for the debonding force (F_d).

$$F_d = 2\pi r_f \frac{\tau_d}{\alpha} \tanh(\alpha L) \tag{2.11}$$

Extensions of Greszczuk's theory have been presented by Lawrence [117], Takaku and Arridge [118], Gray [119], Laws [120], and Banbaji [121,122]. In addition, Chua and Piggott expressed equation 2.11 in terms of fiber and matrix parameters as described in equation 2.12,

$$F_d = 2\pi r_f^2 \frac{\tau_d}{n} \tanh(nL/r_f) \tag{2.12}$$

where,

$$n^2 = \frac{E_m}{E_f(1+\upsilon_m)\ln(R/r_f)}, \tag{2.13}$$

and E_m and υ_m are the Young's modulus and Poisson's ratio of the matrix, respectively [123]. Reviews of the analyses based on Greszczuk's shear lag model have been written by Herrera-Franco and Drzal [21] and Désarmot and Favre [107].

2.1.4.2.1.2 Fracture Energy Approach

Based on experimental results which suggest that the mode of failure in the pull-out experiment is sudden and catastrophic, an energy approach was developed in which the interfacial fracture energy (U_t) is equal to the sum of the energy stored in the fiber (U_f) and in the matrix (U_m) as described by equation 2.14,

$$U_t = U_m + U_f = 2\pi r_f L G_a \tag{2.14}$$

where G_a is the interfacial fracture energy per unit surface area [74, 76, 124-126]. Equation 2.15 was obtained for the debonding force (F_d),

$$F_d^2 = 4\pi^2 r_f^2 \beta r_f L E_f G_a \tanh(\beta L) \tag{2.15}$$

where,

$$\beta^2 = \frac{2G_m}{\left[r_f^2 E_f \ln(R/r_f)\right]} \tag{2.16}$$

At a long embedded length ($\tanh \beta L \approx 1$), the debonding force is proportional to the square root of the fiber embedded length.

$$F_d = 2\pi r_f \sqrt{\beta r_f L E_f G_a} \equiv \sqrt{L} \tag{2.17}$$

While, at a short embedded length ($\tanh \beta L \approx \beta L$), the debonding force is directly proportional to the fiber embedded length.

$$F_d = 2\pi r_f \beta L \sqrt{r_f E_f G_a} \equiv L \tag{2.18}$$

Penn and Lee extended the fracture energy analysis by introducing the concept of an initial crack length [113]. Jiang and Penn proposed an improved model in which the pull-out test geometry is divided into three regions as shown in Figure 2.7 and a matrix compression contribution and the work of friction between the debonded fiber and the matrix are taken into account [127]. An energy balance was applied to the interfacial crack propagation process. Some of the strain energy (U) stored in the system upon loading and released during debonding propagates a crack through the bonded interface and some is dissipated by friction. That is,

$$G_c + \frac{1}{2\pi r_f}\frac{\partial W_f}{\partial a} \le \frac{1}{2\pi r_f}\frac{\partial U}{\partial a} \tag{2.19}$$

where U is the total elastic strain energy stored in the sysytem, W_f is the work of friction, G_c is the interfacial fracture energy per unit area, and a is the initial crack length. The

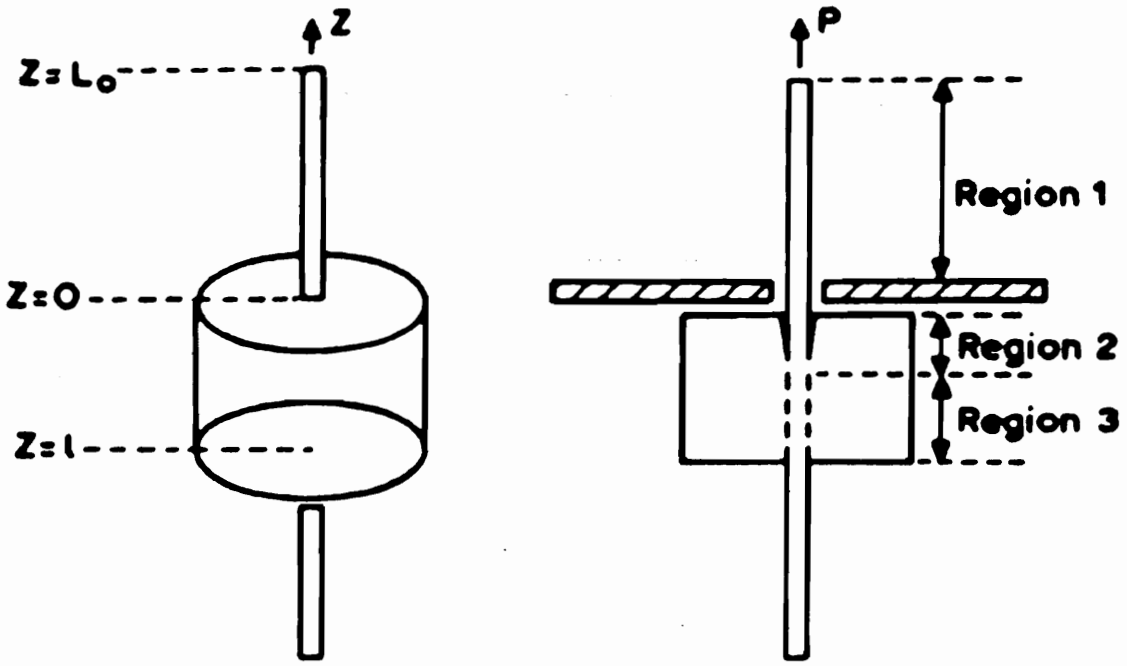

Figure 2.7. Schematic illustration of single fiber pull-out test specimen with three regions. Region 1 is fiber alone, Region 2 is fiber and matrix debonded at the interface, and Region 3 is fiber and matrix bonded at the interface [127].

total strain energy stored in the system (U) is the sum of the strain energy stored in region 1 (U_1), region 2 (U_2), and region 3 (U_3) as described by equation 2.20.

$$U = U_1 + U_2 + U_3 \tag{2.20}$$

The free fiber (region 1) is treated as a thin elastic rod loaded in tension. The strain energy stored in region 1 (U_1) is given by equation 2.21,

$$U_1 = \frac{A_f L_o \sigma_f^2}{2E_f} \tag{2.21}$$

where A_f is the fiber cross-section area, E_f is the Young's modulus of the fiber, σ_f is the fiber tensile stress, and L_o is the length of the fiber between the load cell and the polymer plug.

The strain energy stored in region 2 (U_2) is the sum of the strain energy contributed by tension in the fiber (U_{2f}), compression in the matrix ($U_{2m,comp.}$), and shear in the matrix ($U_{2m,shear}$) as described by equation 2.22,

$$U_2 = U_{2f} + U_{2m,comp.} + U_{2m,shear} \tag{2.22}$$

where,

$$U_{2f} = \frac{A_f^2}{6E_f f}\left\{\sigma_f^3 - \left[\sigma_f - (fa/A_f)\right]^3\right\} \tag{2.23}$$

$$U_{2m,comp} = \frac{A_f^3}{A_m E_m 6f}\left\{\sigma_f^3 - \left[\sigma_f - (fa/A_f)\right]^3\right\} \tag{2.24}$$

$$U_{2m,shear} = \frac{f^2 a(1+\upsilon_m)}{2\pi E_m}\ln(R/r_f) \tag{2.25}$$

E_m is the Young's modulus of the matrix, f is the friction force per unit length, A_m is the matrix cross section area, and υ_m is the Poisson's ratio of the matrix.

The strain energy stored in region 3 (U_3) also originates from tension in the fiber (U_{3f}), compression in the matrix ($U_{3m,comp.}$), and shear in the matrix ($U_{3m,shear}$) as given by equation 2.26,

$$U_3 = U_{3f} + U_{3m,comp.} + U_{3m,shear} \tag{2.26}$$

where,

$$U_{3f} = \frac{A_f\left[\sigma_f - (fa/A_f)\right]^2}{2nE_f}\left\{\coth(ns) - \frac{ns}{\left[\sinh(ns)\right]^2}\right\} \tag{2.27}$$

$$U_{3m,comp.} = \frac{r_f A_f^2\left[\sigma_f - (fa/A_f)\right]^2}{4nA_m E_m}\left\{\coth(ns) - \frac{ns}{\left[\sinh(ns)\right]^2}\right\} \tag{2.28}$$

$$U_{3m,shear} = \frac{A_f\left[\sigma_f - (fa/A_f)\right]^2}{4nE_f}\left\{\coth(ns) - \frac{ns}{\left[\sinh(ns)\right]^2}\right\} \tag{2.29}$$

where n is defined by equation 2.13 and s equals (L/r_f).

Penn and Jiang rewrote the energy balance in equation 2.19 in the form of equation 2.30,

$$\frac{dU}{da} = \frac{\partial U_1}{\partial a} + \frac{\partial U_2}{\partial a} + \frac{\partial U_3}{\partial a} = 2\pi r_f G_c + \frac{\partial W_f}{\partial a} \tag{2.30}$$

recognizing that the strain energy release rate is the derivative of the strain energy with respect to the interfacial crack area. They obtained the following expression for the work of friction in region 2,

$$W_f = \left[1 - \frac{A_f E_f}{A_m E_m}\right]\frac{fa^2\left[\sigma_f - (fa/3A_f)\right]}{2E_f} \tag{2.31}$$

and solved the equation for the critical load for crack propagation P_c,

$$P_c = \sigma_f A_f = A_f \left[\frac{\sqrt{B^2 - 4AC}}{2A} - \frac{B}{2A} \right] + fa \tag{2.32}$$

where,

$$A = \frac{(1+\alpha)A_f}{2E_f} + \frac{(2+\alpha)A_f \operatorname{csch}^2(ns)}{4E_f} \tag{2.33}$$

$$B = -\frac{(1-\alpha)fa}{E_f} - \frac{(2+\alpha)r_f f \coth(ns)}{2nE_f} \tag{2.34}$$

$$C = -\frac{f^2(1+\upsilon_m)\ln(R/r_f)}{2\pi nE_f} - \frac{(1-\alpha)f^2a^2}{2E_fA_f} - 2\pi r_f G_c \tag{2.35}$$

and,

$$\alpha = \frac{E_f A_f}{E_m A_m} \tag{2.36}$$

Jiang and Penn used equation 2.32 as a mathematical model to generate the debonding load versus embedded length curves shown in Figure 2.8 [127]. Figure 2.8(a) shows that increasing the interfacial fracture energy (G_c) while leaving all other parameters in equation 2.32 unchanged, increases the slope of the rising portion of the curve and elevates the plateau. Figure 2.8(b) shows that an increase in the matrix modulus (E_m) raises the curve at low embedded length, but has no effect at high embedded length. This moves the knee in the curve to the left.

The present mathematical models does not accurately predict all experimentally obtained pull-out test data. For example, when the theoretical curves calculated using equation 2.32, were compared to experimental data for Spectra fiber/epoxy [127], aramid

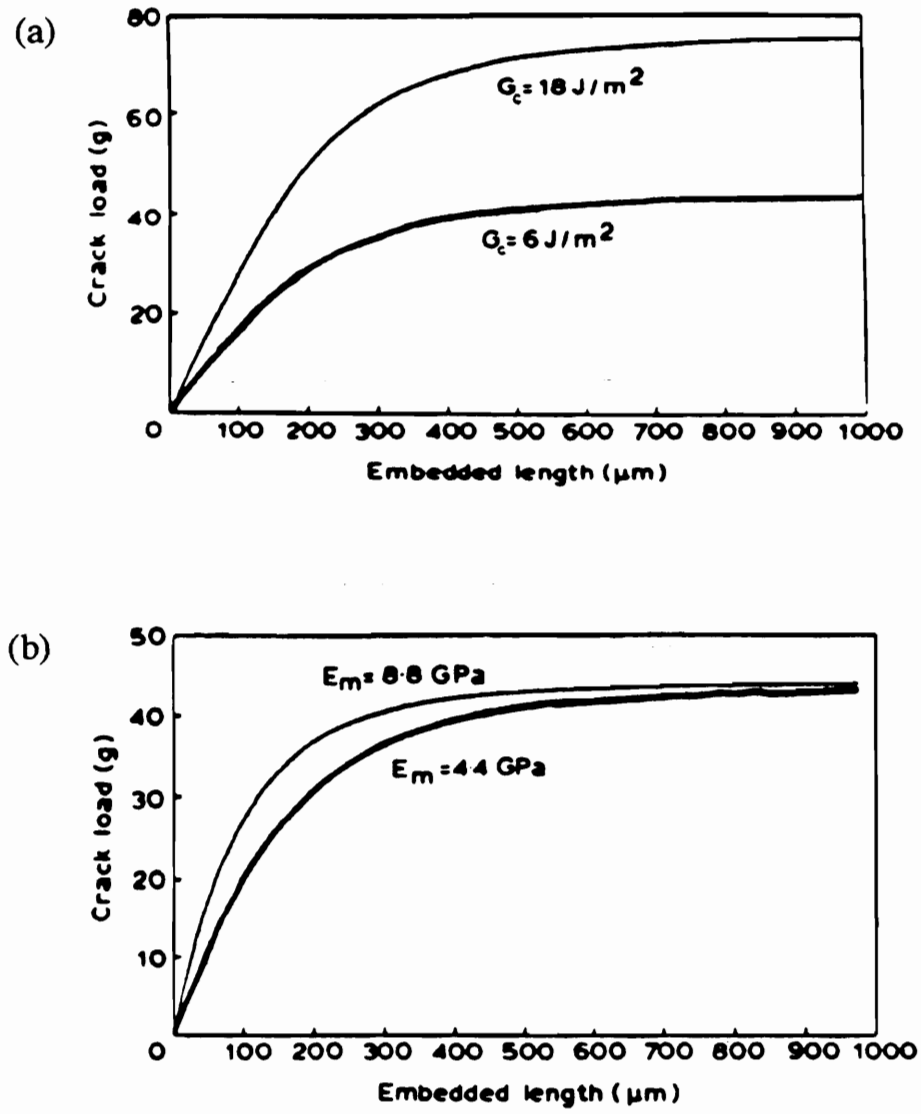

Figure 2.8. Theoretical curves of debonding load versus embedded length computed from equation 2.32 when (a) the interfacial fracture energy (G_c) and (b) the matrix modulus (E_m) are increased [127].

fiber/epoxy [114], and aramid fiber/thermoplastic systems [128], the data exhibited an initial rising region followed by a plateau, but there was considerable discrepancy between the curves at low embedded lengths.

2.1.4.2.2 Evaluation of Experimental Parameters in the Microbond Test

Equation 2.7 implies that during a pull-out experiment, the applied force is distributed uniformly and equally along the fiber/matrix interface. During the microbond pull-out test, however, the force is applied to a small portion of the drop and is not evenly distributed along the fiber/matrix interface. The force decreases with the distance from the point of application. When a certain amount of force produces pull-out, most of it has been applied to the top of the interface to produce the initial bond rupture which then propagates down the interface [31].

Wu and Claypool investigated the effects of the droplet geometry, loading points, and the interphase modulus on the fiber-matrix interfacial shear stress using a finite element model [129, 130]. The shear stress distribution along the fiber/matrix interface was found to be non-uniform with the maximum stress occurring at the top of the droplet. In addition, they found that the state of stress along the interface was identical whether the drop was in the form of a sphere or an ellipsoid.

Herrera-Franco and Drzal used photoelastic and finite element analysis to study the effects of the drop meniscus and the distance between the shearing plates on the failure mode and the state of stress along the interface [21]. They found that the maximum shear stress increases and the point of occurrence of the maximum shear stress varies as the shearing plates are moved closer to the fiber. The loading conditions also affect the radial stress distribution both in magnitude and point of occurrence. The radial stress is tensile at the point where the fiber emerges from the drop and decreases rapidly toward zero and then becomes compressive, going through a low point toward the center of the drop.

When drops are formed around a fiber a meniscus, as shown in Figure 2.9, will always exist at the contact point of the fiber and matrix [131, 132]. Herraro-Franco and Drzal found that this meniscus affects the shear stress distribution along the fiber/matrix interface. When the resins drops debond, a small cone of polymer is often left behind on the fiber where the drop was originally located. Herraro-Franco and Drzal attributed this to the tensile stresses in the meniscus area [21].

Gaur and Miller noted that when force traces from individual microbond tests are inspected, the loading rate (slope of the force trace before debonding) is not always the same. The variation in the loading rate is caused by differences in the distance between the droplet and the point where the fiber is attached to the force cell. They found no significant effect of loading rate on shear strength over the normal loading rate range (1-3 grams/second) obtained for four systems [31].

2.1.5 Carbon Fiber Properties

2.1.5.1 Fiber Preparation and Structure

Carbon fibers exhibit a unique combination of performance advantages which make them ideal reinforcing materials for use in advanced composites [133]. Carbon fiber properties are anisotropic. That is, they are strong and stiff in the longitudinal (fiber axis, 0°) direction and weak transverse (or 90°) to the fiber axis. This is due to orientation of the carbon fiber graphite crystals parallel to the fiber axis [134].

As shown in Figure 2.10, the graphite single crystal is composed of many sheet-like layers of carbon atoms [134-136]. In the plane of the sheet (the basal plane), the carbon atoms are linked together by strong covalent bonds. In the direction normal to the basal plane, the sheet-like layers of carbon atoms are held together by relatively weak van der Waals forces. The majority of the crystallites in a carbon fiber are not perfect single

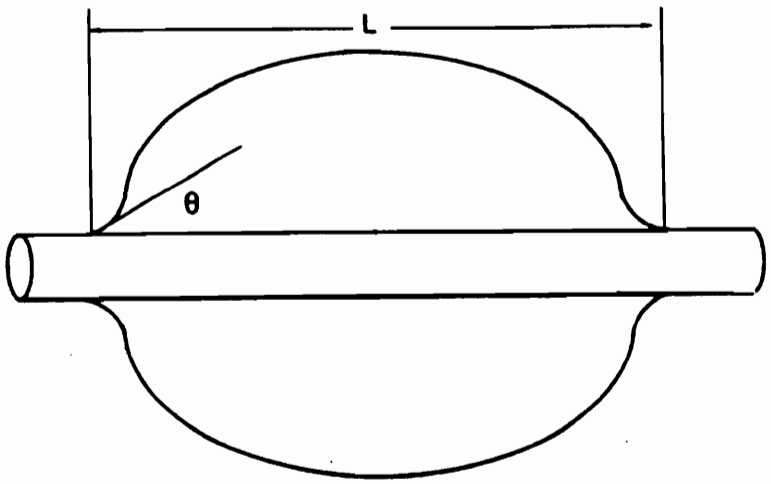

Figure 2.9. Shape of a liquid drop on a cylindrical fiber [132].

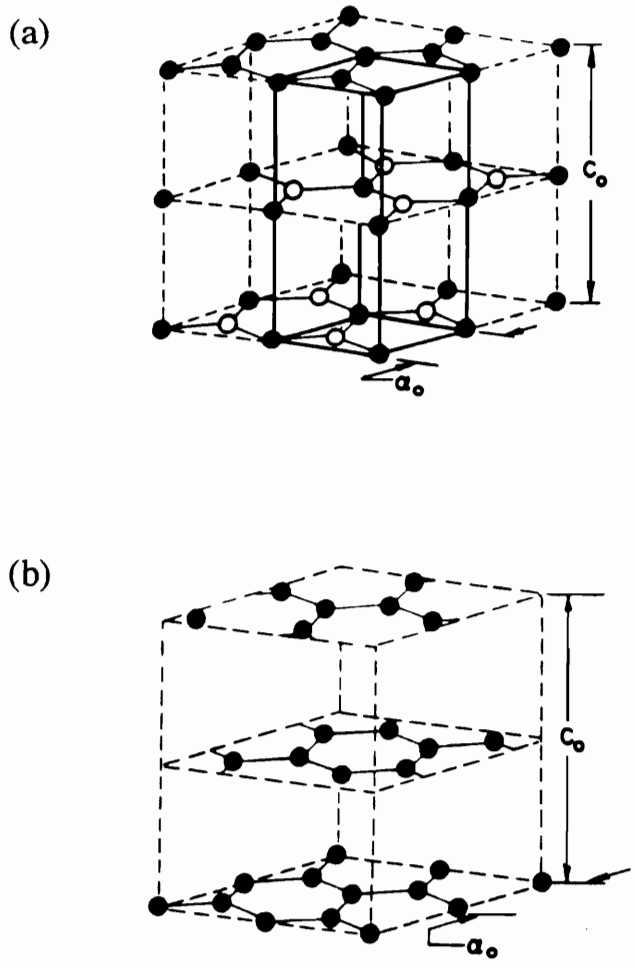

Figure 2.10. Crystallographic structure of (a) the graphite single crystal and (b) turbostratic graphite [134].

crystals. Instead, the stacking of the carbon sheets is slightly displaced and the crystallites are in the form of "turbostratic" graphite [134, 136]. The spacing between the basal planes in turbostratic graphite is approximately 3.40 to 3.45 Å as compared to the 3.35 Å separation for perfect graphite [134, 135, 137].

Carbon fibers are produced by pyrolyzing organic precursor fibers. Rayon, polyacrylonitrile (PAN), and petroleum or coal tar pitch are the most commonly used carbon fiber precursors [138]. PAN is widely used due to a high carbon yield and the ability to tailor the structure of the final product [138]. The material used to form PAN-based carbon fibers is not a homopolymer of acrylonitrile. Instead, it is a copolymer or terpolymer containing in excess of 85 weight% acrylonitrile. Typical comonomers include methyl acrylate, itaconic acid, methacrylic acid, hydroxyethylacrylonitrile, and sodium alkyl sulfonate [133, 138]. These comonomers are used to facilitate fiber spinning and to assist in the stabilization process [133].

The production of carbon fibers involves the following steps:

1) extrusion of a fine polymer fiber,
2) stretching of the fiber to orient the molecules parallel to the fiber axis,
3) stabilization by preoxidation at relatively low temperature (200 - 450°C) in air,
4) carbonization in an inert atmosphere at 1000-2000°C,
5) graphitization in an inert atmosphere at temperatures greater than 2500°C, and
6) surface treatment.

The preparation of carbon fibers has been reviewed by Gupta et al., Goodhew et al., Peebles, Henrici-Olivé and Olivé, Watt, Riggs, Thorne, Fitzer et al., Damodaran et al., Rajalingam and Radhakrishnan, Bashir, Diefendorf et al., Gerhartz, and Donnet and Bansal [138-154].

The basic carbon fiber structural unit consists of a stack of turbostratic layers as shown in Figure 2.11 where A-A' is the fiber direction, a is a defect in the basic structural

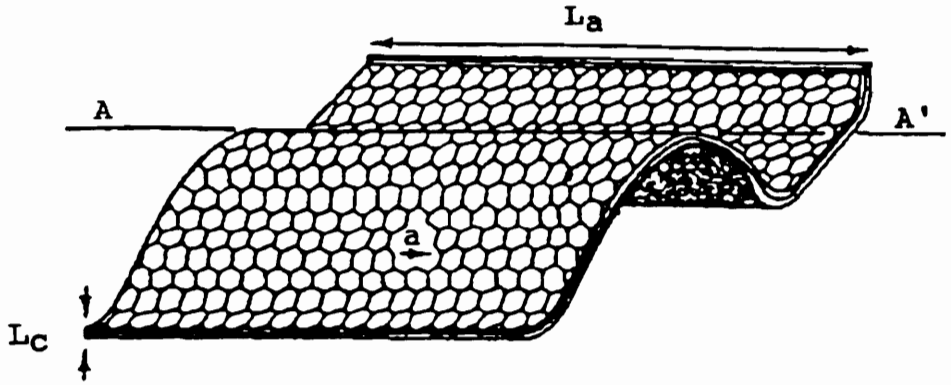

Figure 2.11. The basic structural unit of carbon fibers [155].

unit, L_a is a measure of the mean length of "straight" basal planes, and L_c is the stack height [155]. This basic structural unit can split, twist, fold, and join other basic structural units which can also split, twist, fold, and join within a carbon fiber [156]. The growth of the turbostratic graphite sheets results in the formation of long, undulating ribbons or microfibrils oriented in the general direction of the fiber axis [134, 157].

The schematic illustrations in Figure 2.12 depict the ribbon-like structures which make up carbon fibers. These models were prepared based on x-ray diffraction and electron microscopy data [150, 158-160]. Since the contours of these ribbons do not match, the space cannot be completely filled and needle-shaped voids are created within the fiber [134]. The mean length of the "straight" basal planes and the stack height of the ribbons increase and the microporosity decreases as the heat treatment temperature and the orientation of the ribbons in the fiber axis direction are increased [134].

Therefore, the fine structure of carbon fibers is a rather chaotic collection of basic structural units formed into microfibrils and interspersed with pores [153]. Bennett and Johnson proposed the three-dimensional model of the carbon fiber shown in Figure 2.13 [161] and Diefendorf and Tokarsky constructed the three-dimensional model of the PAN-based carbon fiber shown in Figure 2.14 [150]. Both of these models show a difference in ordering and density of the carbon ribbons at the surface compared to that of the core. Perret and Ruland [158], Guigon et al. [155], and Barnet and Norr have also proposed three-dimensional models of the PAN-based carbon fiber [162].

2.1.5.2 Carbon Fiber Surface Treatment

Carbon fibers are treated to improve fiber/matrix adhesion. Proctor and Sherwood state that fiber/matrix adhesion may be affected by three main factors:

(1) physical and chemical adsorption of resin molecules onto the surface functional groups at edge sites,

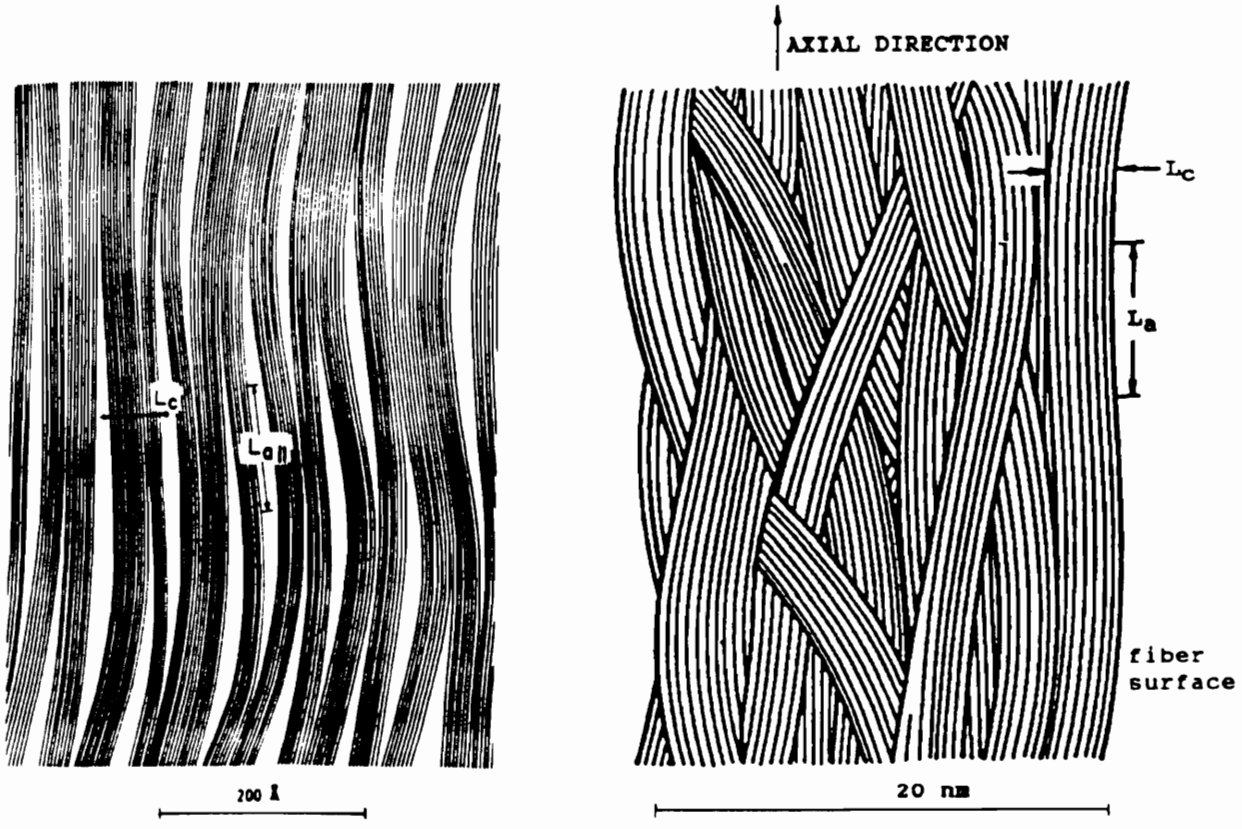

Figure 2.12. Model of carbon fiber ribbon structure proposed by (a) Perret and Ruland [158] and (b) Diefendorf and Tokarsky [150].

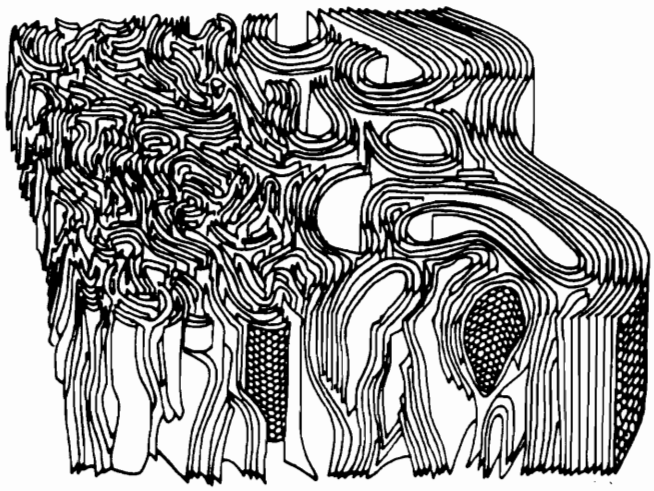

Figure 2.13. Three-dimensional model of the carbon fiber proposed by Bennett and Johnson [161].

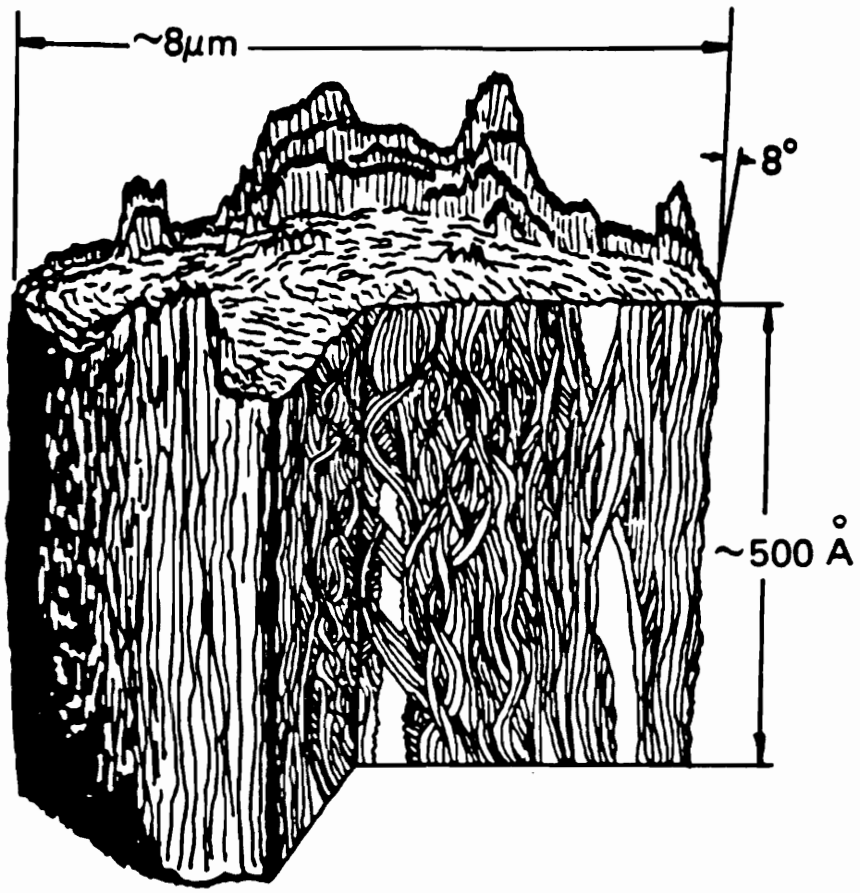

Figure 2.14. Three-dimensional model of the PAN-based carbon fiber proposed by Diefendorf and Tokarsky [150].

(2) physical adsorption of resin molecules onto basal surfaces, and

(3) fiber roughness and surface area [163].

The modification of carbon fibers to improve composite properties has been reviewed by Delmonte [164], Ehrberger and Donnet [165], Riggs [143], Donnet and Bansal [154], and Wright [166, 167]. Treatments are commonly used to clean the fiber surface and/or to incorporate functional groups into the fiber surface which faciliate resin/fiber wetting and interaction. The fiber surface has been modified using anodic oxidation [168-173], plasma treatment [46, 63, 67, 98, 106, 174-195], electrodeposition [196-198], wet and dry oxidation [163, 195, 199], and the application of fiber coatings [39, 70, 200-202].

The effects of these surface treatments on carbon fibers have been studied using a wide variety of techniques including titration, reaction of surface functional groups with more easily identifiable tags, x-ray photoelectron spectroscopy, Auger spectroscopy, secondary ion mass spectroscopy, infrared spectroscopy, Raman spectroscopy, surface energy by wetting analysis, inverse gas chromatography, gas or liquid adsorption, scanning tunneling microscopy, and scanning electron microscopy. Figure 2.15 compares the sampling depths of several surface analysis techniques [153]. There are several reviews of carbon fiber surface analysis in the literature [153, 154, 203-208].

Donnet and Guilpain state that commercially surface treated carbon fibers are oxidized electrochemically using a continuous anodization process [209]. Anodic oxidations have been performed in aqueous acidic or basic solutions of sodium hydroxide, potassium hydroxide, sulfuric acid, nitric acid and amine salts. Following commercial surface treatment, carbon fibers are often sized with a matrix compatible coating to protect the fiber surface from damage during handling, to protect the surface chemistry created by the surface treatment, enhance fiber/matrix wetting and adhesion, and improve the mechanical properties of the interphase [202].

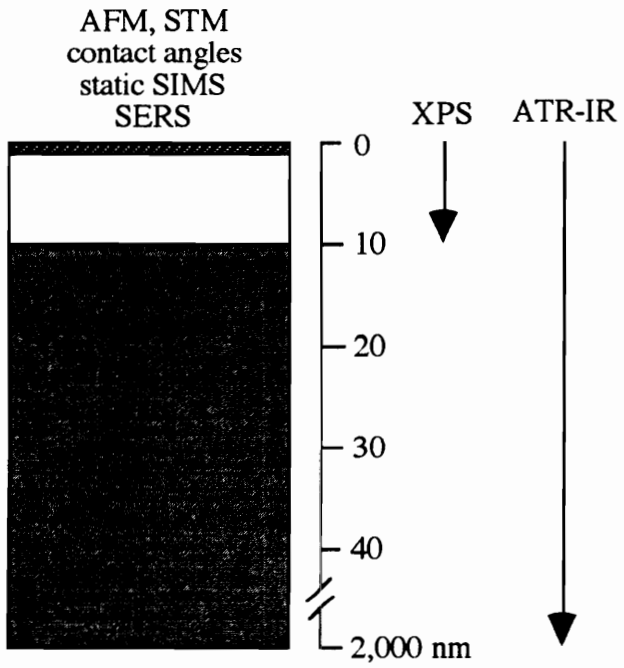

Figure 2.15. A comparison of sampling depths for several surface analysis techniques [adapted from ref. 153].

Figure 2.16 shows some oxygen-containing functional groups thought to be present on oxidized carbon surfaces [210]. XPS studies support the presence of carboxyl, carbonyl, hydroxyl, ester, and quinone functional groups [207]. DeVilbiss used fluorine-containing reagents to confirm the presence of amine and hydroxyl groups on the surface Hercules AS-4 carbon fibers by XPS [51]. Drzal also detected amine groups by studying the thermal desorption of compounds from the surface of AS-4 carbon fibers using mass spectrometry [211]. Sellitti, Koenig, and Ishida used functionalization reactions and attenuated total reflection Fourier transform infrared spectroscopy (ATR-IR) to characterize the surface of carbon fibers oxidized by refluxing in 70% nitric acid [212]. ATR-IR detected the functional groups shown in Figure 2.17 [212].

The effect of fiber surface treatments on the carbon fiber adhesion of thermoset and thermoplastic polymers will be reviewed in Chapters 3 and 4.

2.1.5.2.1 Plasma Treatment

A plasma is a partially ionized gas with an essentially equal density of positively and negatively charged species [213]. The charged species arrange themselves within a distance of a Debye length (λ_D) to achieve local charge neutrality over regions greater than the Debye length. The Debye length (λ_D) is defined by equation 2.37,

$$\lambda_D = \sqrt{\frac{\varepsilon_o k T_e}{ne^2}} = 6.9\sqrt{\frac{T_e}{n}} \qquad (2.37)$$

where, ε_o is the permittivity of free space, k is the Boltzmann constant, e is the charge on the electron, T_e is the electron temperature, and n is the electron density [214, 215]. For a confined plasma, equation 2.37 is satisfied if the physical dimensions of the system are large compared with the Debye length and if there are a sufficient number of electrons within a sphere of radius (λ_d) to produce shielding. For a cylindrical geometry of radius (R_o), the plasma criteria are met if [214]:

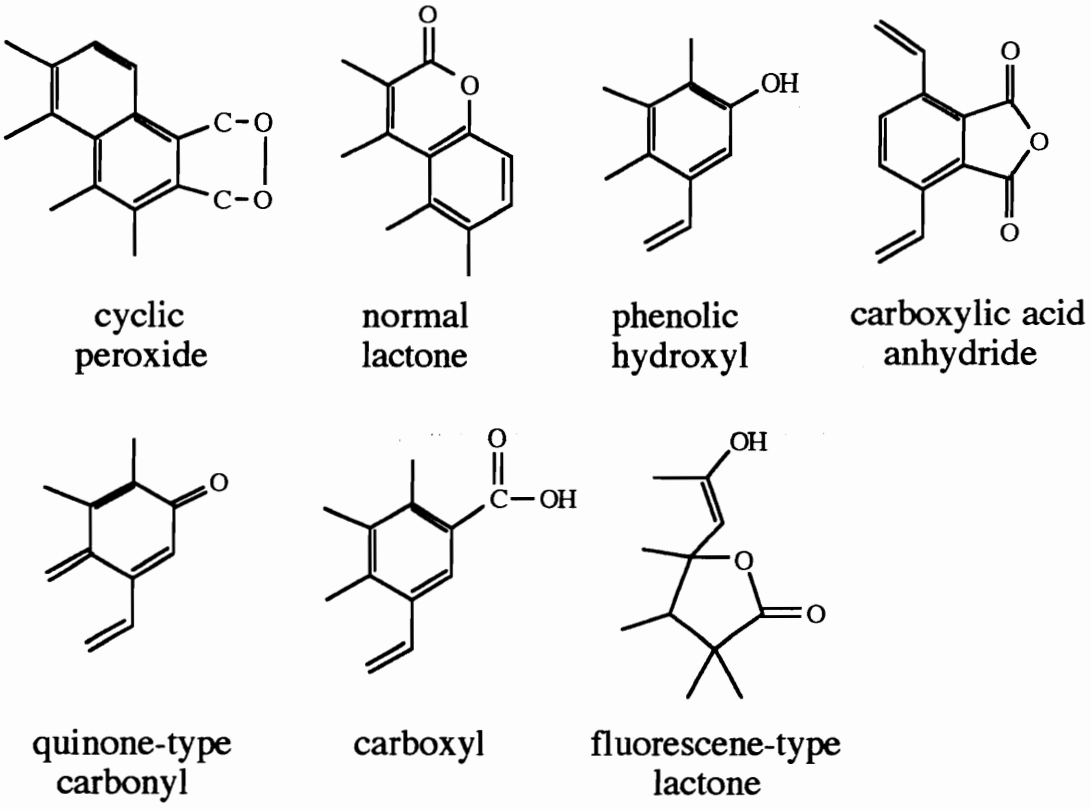

Figure 2.16. Proposed oxygen-containing functional groups present on oxidized carbon fiber surfaces [210].

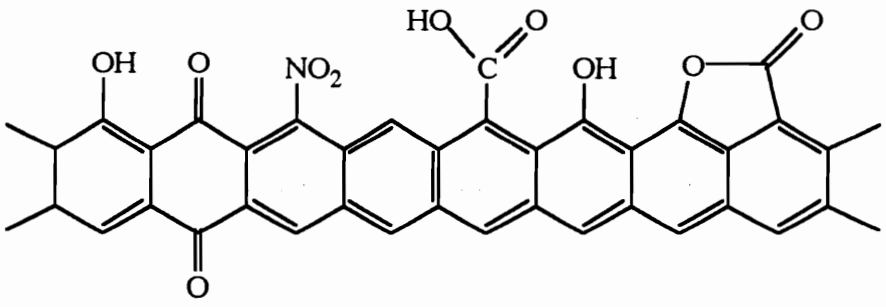

Figure 2.17. Functional groups detected by ATR-IR on the surface of carbon fibers oxidized using nitric acid [212].

$$\lambda_D < R_o \tag{2.38}$$

$$n << \left(1.9 \times 10^6\right) T_e^3 \tag{2.39}$$

Figure 2.18 illustrates the variety and wide range of ionized systems that are categorized as plasmas [215].

Radio frequency-generated glow-discharge plasmas are widely used in laboratory experiments due to convenience of handling, low energy requirements, and because bench top rf-discarge plasma reactors are commercially available [214]. In a radio-frequency glow-discharge, a rf field is used to accelerate the free electrons in a gas held at low pressure. These excited free electrons collide with the gas molecules and transfer energy from the electric field to the gas. Elastic electron-molecule collisions increase the kinetic energy of the gas molecules, while inelastic collisions generally result in excitation, fragmentation, and ionization of the gas molecules. As a result, the glow discharge plasma is made up of positive ions, negative ions, electrons, metastables, atoms, free radicals, and photons of ultraviolet, vacuum ultraviolet, and visible radiation [214, 215]. Glow discharges are also referred to as cold plasmas or nonequilibrium plasmas [216].

The extremely energetic chemical environment of the plasma is used to alter the wettability, molecular weight, and chemical composition of the surface of a material without changing the appearance or bulk properties of the material [213, 217]. The energies of the reactive species in a glow discharge and some typical bond energies are given in Tables 2.2 and 2.3, repectively [214, 218]. When the reactive species in a glow discharge plasma impinge on an organic surface, they have sufficient energy to break bonds in that surface and abstract atoms or molecular fragments from the surface. These organic fragments can react further in the plasma to form volatile species that are

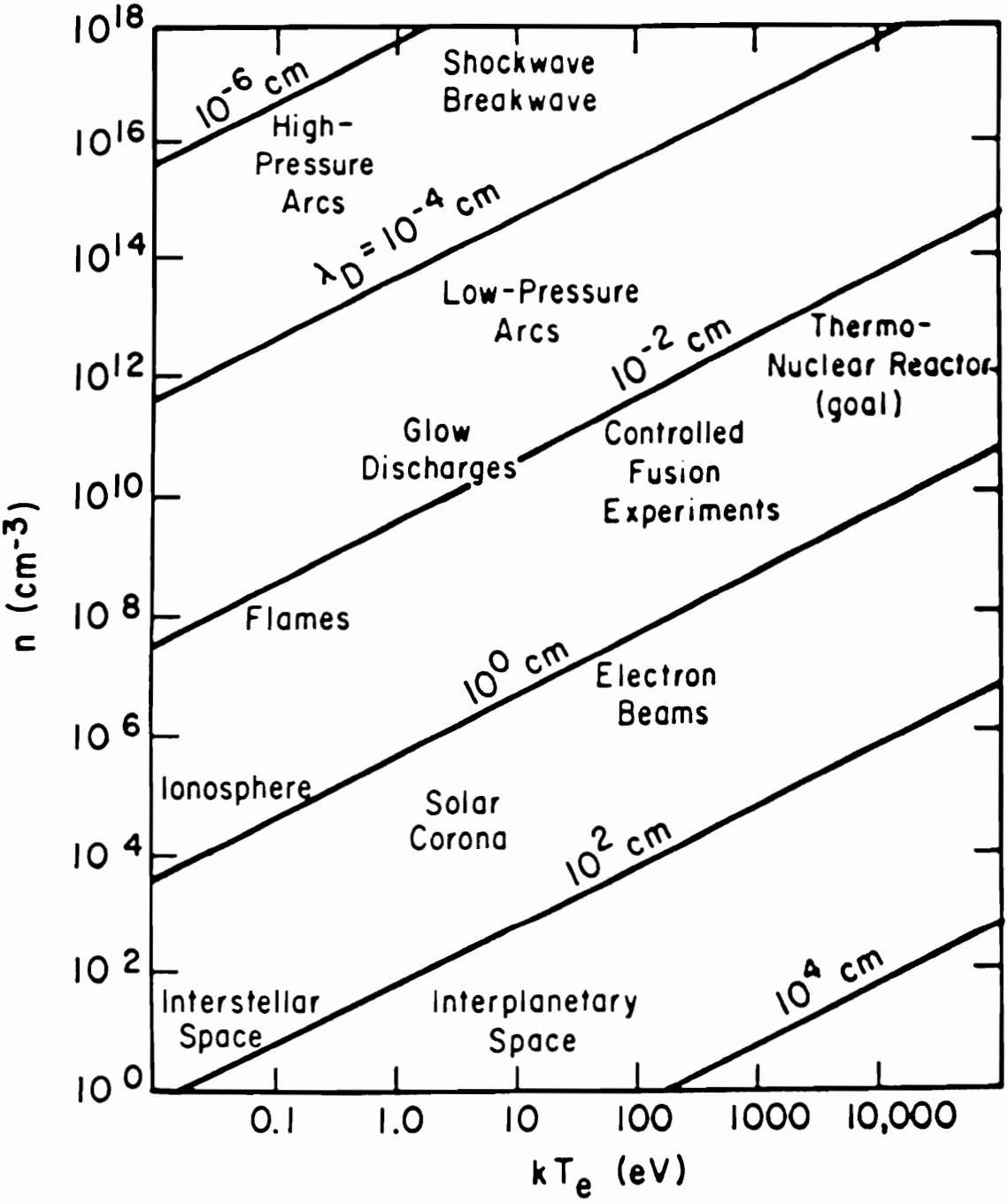

Figure 2.18. Typical plasmas classified by their electron energy and density [215].

Table 2.2. Energies of the species present in a glow discharge plasma [214].

Species	Energy (eV)
electron	0-20
ions	0-2
metastables	0-20
UV/visible	3-40

Table 2.3. Typical bond energies [218].

Bond	Bond energy (eV)
C-H	4.3
C-C	3.6
C=O	7.8
C-O	3.7
C=C	6.4 (2.7 for π bond)
C-N	3.2
C=N	9.3
N-H	4.0
O-O	1.5
O-H	4.8

removed by the vacuum system. The breaking of bonds in the surface causes a progressive ablation of the organic surface and creates free radicals in the surface. These surface free radicals may either react with themselves to produce surface cross-linking or react with the plasma gas to create new chemical species in the surface. If the plasma is an inert gas, the surface will contain a large number of stable radicals that will persist until they are exposed to some reactive gas [213].

Clark and Dilks reported that the free radicals formed in the outermost surface (tens of angstroms) of a material are predominantly created by direct reaction with the ions and free radicals in the plasma and the free radicals formed deeper within the sample (hundreds of angstroms) are the result of vacuum ultraviolet radiation [219]. It is estimated that the concentration of free radicals in a glow discharge plasma is five to six orders of magnitude greater than that of ions and that all significant reactions are based on free radical chemistry [214]. The actual physical and chemical properties of a glow discharge plasma depend upon the type of gas or combination of gases used, the geometry of the reactor and electrodes, and the operating power, gas flow rate, pressure, and temperature [214, 215].

Carbon fibers have been plasma treated using ammonia, nitrogen, air, oxygen, argon, fluorine, carbon dioxide, hydrogen, acetylene, propylene, ethylene, methylene, styrene, acrylonitrile, tetrafluoromethane, and Freon gases [46, 63, 98, 178-182, 186, 190-195, 220-223]. Carbon fibers are plasma treated to clean the fiber surface, remove weak surface layers, control the surface functional group composition and concentration, alter the fiber surface energy, functionalize the surface basal planes, and to directly polymerize layers of polymer on the fiber surface.

In general, oxidizing plasmas such as air and oxygen are more reactive to the carbon fiber surface than either nitrogen, ammonia, or argon plasmas. Jones and Sammann attributed this the reactivity of the species present in the oxygen plasma. The reactive

species in air and oxygen plasmas can react with both the edge and basal planes of carbon fibers, but the species present in the nitrogen and ammonia plasmas can only attack the fiber edge planes [177]. One of the components of air and oxygen plasmas is atomic oxygen. Pattabiraman and coworkers have shown that exposure to atomic oxygen physically and chemically alters the carbon fiber surface [224]. Hoffman examined carbon fibers exposed to argon and oxygen plasmas and found that the oxygen plasma roughened the fiber surface and incorporated oxygen-containing functional groups into the fiber surface, increasing both the total and the active surface area [225]. The argon plasma treatment enhanced the active surface area but not the total surface area [225].

Plasma polymerization is used to deposit polymer films on carbon fibers to tailor the fiber surface chemistry and the properties of the fiber/matrix interphase [98, 222, 226]. Virtually any vaporizable organic species can be polymerized under plasma conditions. Bell discussed the elementary steps involved in an ethylene plasma [227]. The acetylene monomer and a first generation of active species are formed in the reactions depicted in Table 2.4. The free radicals and ions produced during the initiation step subsequently react with either ethylene or acetylene to produce additional free radicals and ionic species. These radicals and ions react further with either ethylene or acetylene to increase the molecular weight of the polymer.

2.2 EXPERIMENTAL TECHNIQUES

2.2.1 Materials

The PAN-based high strength, low modulus carbon fibers used in this study and their properties are summarized in Table 2.5 [228]. The "S" designation indicates that the fiber underwent a proprietary surface treatment as part of manufacture. The "U" designation indicates that the fiber was not surface treated. All of the fibers were received without sizing in a tow containing 12,000 continuous filaments. The fibers were

Table 2.4. Proposed reactions involved in ethylene plasma polymerization [227].

Reaction	Heat of reaction (ΔH) (eV)
$e^- + C_2H_4 \rightarrow C_2H_2 + H_2 + e^-$	1.8
$e^- + C_2H_4 \rightarrow C_2H_2 + 2H\bullet + e^-$	6.3
$e^- + C_2H_4 \rightarrow 2CH_2 + e^-$	7.3
$e^- + C_2H_4 \rightarrow C_2H_4^+ + 2e^-$	10.5
$e^- + C_2H_4 \rightarrow C_2H_2^+ + H_2 + 2e^-$	13.1
$e^- + C_2H_4 \rightarrow C_2H_3^+ + H\bullet + 2e^-$	13.3

Table 2.5. Carbon fibers properties [228].

Producer	Fiber	Tensile Modulus (GPa)	Tensile Strength (GPa)	Elongation at Break (%)
Hercules	AU-4	221	3.93	1.60
Hercules	AS-4	221	3.93	1.60

used as received. Fiber samples were taken randomly along the length of the tow.

The LaRC-TPI™ polyamic acid was obtained from the Mitsui Toatsu Chemical Company. An aqueous solution containing 3 weight% of the ammonium salt of LaRC-TPI polyamic acid and a 12 mole% excess of NH_4OH was prepared and used the same day to minimize hydrolysis of the polyamic acid as depicted in Figure 2.19.

2.2.2 Exposure to Poly(amic acid) Solution

AS-4 carbon fiber tows were passed through an aqueous LaRC-TPI polyamic acid solution (3 wt.% of the ammonium salt of LaRC-polyamic acid and 12 mole% excess NH_4OH). The fiber tows were first dried under ambient conditions and then placed in a preheated convection oven and either dried at 110°C for 1 hour or imidized by heating to 100°C for 1 hour and 250°C for 1 hour. The imidization reaction of LaRC-polyamic acid is depicted in Figure 2.20. A film was prepared under vacuum from the LaRC-polyamic acid solution in a clean glass evaporating dish. A portion of this LaRC-polyamic acid film was imidized to LaRC-TPI by heating to 100°C for 1 hour and 250°C for 1 hour.

2.2.3 Plasma Treatment

A March solid state Plasmod® was used to produce a radiofrequency (13.56 MHz)-generated 50 watt glow discharge plasma. A March GCM-200 Gas Control Module regulated the chamber pressure to 1 torr. Figure 2.21 is a schematic illustration of the plasma system [229]. The barrel-shaped sample reactor was made of quartz. Air, oxygen, and ammonia plasmas were used to incorporate oxygen and nitrogen containing functional groups on the carbon fiber surface. An ethylene plasma was used to deposit a layer of plasma polymer on the carbon fiber surface. The ethylene gas was obtained from Scott Specialty Gases (99.5% purity), the ammonia gas was obtained from Matheson Gas Products (99.999%), and the oxygen gas was obtained from Airco, Inc. (99.95%). Room air was used for the air plasma treatment.

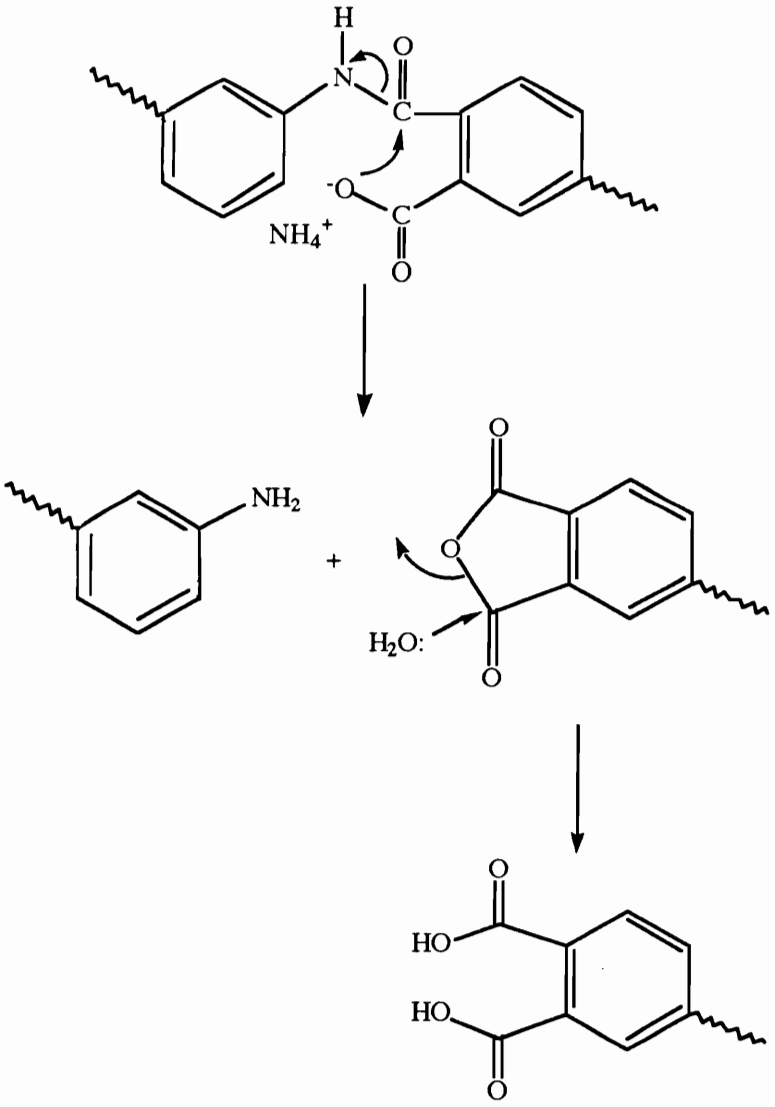

Figure 2.19. Proposed mechanism for the hydrolysis of poly(amic acid) in an aqueous ammonium hydroxide solution.

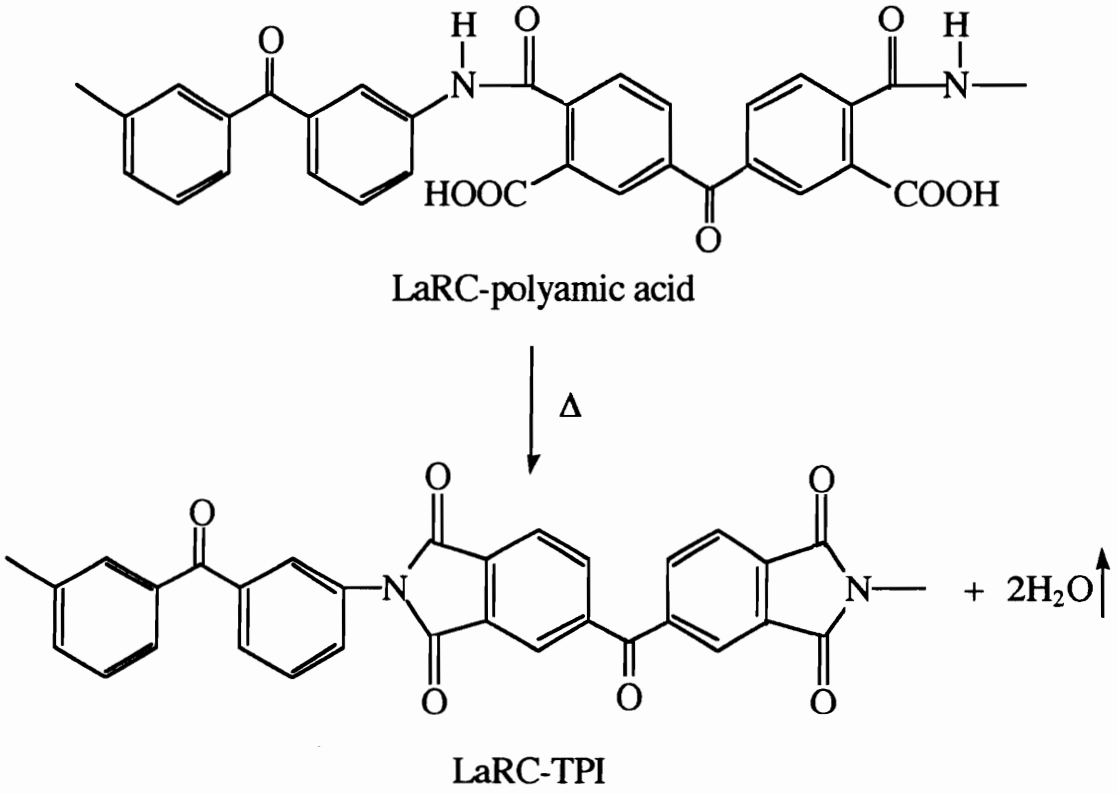

Figure 2.20. LaRC-polyamic acid imidization reaction.

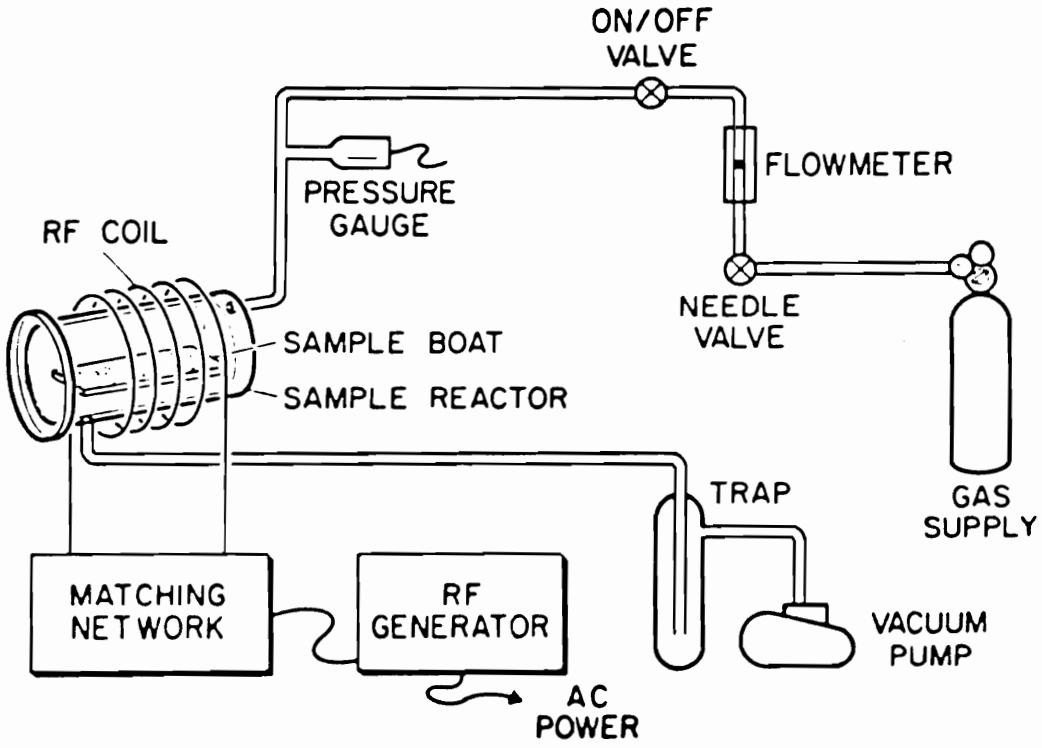

Figure 2.21. Schematic illustration of the plasma system [229].

2.2.4 X-ray Photoelectron Spectroscopy (XPS)

XPS was used to determine the elemental surface composition of "as received" AU-4 and AS-4 carbon fibers and to characterize the changes in the fiber surface chemistry following either plasma treatment or exposure to the LaRC-TPI polyamic acid solution. XPS was also used to analyze LaRC-TPI polyamic acid and imidized LaRC-TPI polymer films. In x-ray photoelectron spectroscopy, the sample is irradiated with an achromatic beam of x-rays. The x-rays penetrate deep into the sample and cause photoelectrons to be emitted from the atoms in the sample. The sampling depth (d) of the XPS experiment is governed by the inelastic mean free path (λ) of the photoelectrons in the solid sample. Approximately 95% of the XPS signal arises from the first 3λ of the sample. The first 3λ of the sample is approximately 6 nm when the kinetic energy of the photoelectrons is between 500 and 1000 eV [191].

Conservation of energy requires that the binding energy (BE) of the photoelectron be defined by equation 2.40,

$$BE = h\upsilon - KE + \vartheta_s \tag{2.40}$$

where $h\upsilon$ is the energy of the x-ray photon, KE is the kinetic energy of the photoelectron, and ϑ_s is the spectrometer work function [230]. The kinetic energies of the photoelectrons which emerge from the sample are measured and the binding energies of the photoelectrons are calculated. The binding energies are characteristic of the elements from which the photoelectrons originate and provide a qualitative identification of the elements present in the sample surface. Quantitative information is obtained based upon the area intensities of the photopeaks, the mean free path of the photoelectron of interest, and the efficiency of the x-ray absorption by the subshell of interest.

The carbon fiber tows and the polymer films were analyzed using a Perkin-Elmer PHI 5400 x-ray photoelectron spectrometer with a Mg K_α x-ray source (1253.6 eV),

operating at 15 kV and 400 watts with an emission current of 30 mA. The spectrometer was calibrated to the gold $4f_{7/2}$, copper $2p_{3/2}$, and silver $3d_{5/2}$ photopeaks according to the Perkin-Elmer standard procedure. Pressure inside the spectrometer sample chamber was held below 5×10^{-7} torr during analysis. The area of the sample which was analyzed was approximately 1 mm x 3 mm in size.

The polymer films were mounted to an aluminum XPS sample mount using double sided adhesive tape. The carbon fiber tows were introduced into the spectrometer using an aluminum mount machined for use with fibers. A single fiber tow was placed on the mount and an aluminum ring was placed on top of the tow, covering the fiber ends. The aluminum ring was then secured on the aluminum mount with two screws.

Survey scans were taken in the range of 0-1100 eV and narrow scans were obtained on any significant peaks observed in the survey spectra. The binding energy of each photopeak was referenced to the carbon 1s photopeak at 285.0 eV for polymer samples and 284.6 eV for carbon fiber samples. The binding energies of the carbon 1s photopeaks were determined by sputtering the samples with gold and referencing the carbon 1s photopeak to the the gold $4f_{7/2}$ photopeak at 83.8 eV. The PHI software (version 4.0) was used to obtain peak areas, calculate atomic concentrations, and to fit the photopeaks with Gaussian-Lorentzian curves. The carbon 1s, oxygen 1s, and nitrogen 1s photopeaks were fit with 80 ± 10% Gaussian curves, varying the peak intensity and binding energy while holding the full width at half maximum (FWHM) at 1.4 ± 0.1, 2.0 ± 0.1, and 1.7 ± 0.1 eV, respectively.

The XPS sampling depth was varied using a technique known as Angle Dependent XPS. The sample was tilted by an angle (θ) with respect to the analyser and spectra representative of different sample depths were collected. The decrease in the XPS sampling depth (d) with a decrease in the take-off angle (θ) is defined by equation 2.41,

$$d = 3\lambda \sin\theta \qquad (2.41)$$

where λ is the electron inelastic mean free path. When carbon fibers are arranged on the XPS mount so that the long fiber axis is parallel to that of the analyser, the analyser is effectively "seeing" a flat surface [191]. Figure 2.22 is a schematic illustration of the enhancement of XPS surface sensitivity by decreasing the "take-off angle" [191]. In this work, spectra were obtained at take-off angles of 15°, 45°, and 90° as noted.

2.2.5 Scanning Electron Microscopy (SEM)

An ISI-SX-40 scanning electron microscope (SEM) and a Philips EM-420T scanning transmission electron microscope (STEM) were used to take photomicrographs of the "as received" carbon fibers, the plasma treated carbon fibers, and the carbon fibers exposed to a LaRC-polyamic acid solution. The ISI-SX-40 SEM was operated at an acceleration voltage of 10 kV and used to take photomicrographs at magnifications less than 10,000X. The samples were secured on aluminum mounts using silver paint and sputter coated with gold using an Edwards Sputter Coater S150B. The Philips EM-420T STEM was operated with an acceleration voltage of 60 kV and used to take photomicrographs at magnifications of 12,500X and 50,000X. The samples were secured on copper mounts using silver paint and coated with gold using a Polaron high resolution sputter coater.

2.2.6 Wetting Analysis

2.2.6.1 Dynamic Contact Angle Analysis

Several researchers have directly measured the contact angle of drops of liquid on single fibers under a microscope [231]. A simpler, less tedious method for contact angle determination is to measure the wetting force of the fiber when it comes into contact with

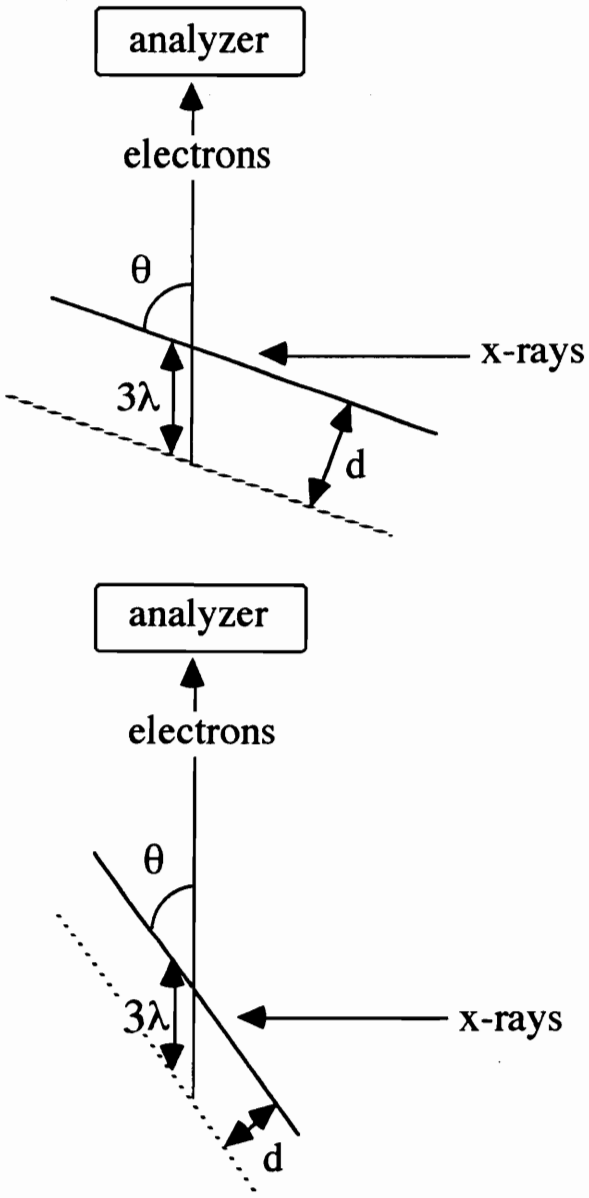

Figure 2.22. Enhancement of XPS surface sensitivity by decreasing the take-off angle [adapted from ref. 191].

a liquid using dynamic contact angle analysis [232-235]. Individual carbon fibers were separated from the carbon fiber tow with the aid of forceps and a piece of adhesive tape. A single fiber was mounted to the end of a 100 μm diameter copper wire hook with cyanoacrylate adhesive. The fibers were carefully cut and handled to avoid damage or contamination. A fiber specimen was suspended by the wire hook from the arm of a CAHN dynamic contact angle system microbalance. A 10 ml glass beaker containing the liquid to be used for the contact angle measurement was raised to the fiber tip at a speed of 20 μm per second.

Upon contact of the carbon fiber with the liquid, the microbalance registered a wetting force (F) given by equation 2.42,

$$F = \pi d \gamma_{LV} \cos\theta - B \tag{2.42}$$

where γ_{LV} is the surface free energy of the wetting liquid, θ is the contact angle, πd is the perimeter of the fiber at the liquid/solid interface, and B is the effect of buoyancy. When using small diameter carbon fibers, buoyancy is negligle and the contact angle is given by equation 2.43.

$$\theta = \cos^{-1}\left[\frac{F}{\pi d \gamma_{LV}}\right] \tag{2.43}$$

The advancing contact angle was calculated using the average force measured as the fiber was immersed in the wetting liquid and the receding contact angle was calculated using the average force measured as the fiber was removed from the liquid. Each fiber was contacted one time with only one liquid to avoid cross contamination or changes in the fiber surface chemistry.

The diameters of the carbon fibers used in this study were determined using both scanning electron microscopy and dynamic contact angle analysis. The fiber diameter

was measured from scanning electron photomicrographs (10,000X magnification) using a ruler. The fibers were also wet with *n*-hexane which formed a 0° contact angle with the fiber surface. When $\theta = 0°$, $\cos\theta = 1$ and equation 2.43 may be rearranged to define the fiber diameter as,

$$d = \frac{F}{\pi\gamma_{LV}\cos\theta} = \frac{F}{\pi\gamma_{LV}} \tag{2.44}$$

where γ_{LV} of *n*-hexane at 25°C is 18.6 mJ/m^2. The diameters of the fibers used in this study, determined using both scanning electron microscopy and wetting analysis, are listed in Table 2.6. The diameters determined by microscopy and by wetting analysis correspond relatively well. This correspondence validates the assumption that *n*-hexane forms a 0° contact angle with the carbon fiber surface. The diameters of the AU-4 and AS-4 carbon fibers were less than that reported in the literature, due to normal variation in fiber diameters among different fiber lots. The average fiber diameters determined by wetting with *n*-hexane were used in equation 2.43 to calculate the contact angles.

The source, purity, and surface energies of the liquids used in this study are listed in Table 2.7. The total surface energy of each liquid was determined using the Wilhelmy slide method [6]. Fisherfinest™ premium glass cover slips, 24 x 30 x 0.15 mm in size, were obtained from Fisher Scientific and were wet with the liquid of interest using a CAHN dynamic contact analyzer. The liquid surface tension was determined using equation 2.45,

$$\gamma_L = \frac{F}{p\cos\theta} = \frac{F}{48.30\text{mm}} \tag{2.45}$$

where, the perimeter of the glass slip (p) was 48.30 mm and, the contact angle (θ) between the clean glass cover slips and all of the liquids used in this study was zero. The glass cover slips were cleaned by passing them through the flame of a Bunsen burner,

Table 2.6. Diameter of the "as received" and plasma treated carbon fibers determined using scanning electron microscopy and wetting analysis.

FIBER	<DIAMETER> ± σ_{n-1} (μm)		
	scanning electron microscope (n = 10)	wetting with *n*-hexane (n = 15)	reference
"as received" AU-4	6.5 ± 0.2	7.0 ± 0.4	8.0 ± 0.5 [222]
"as received" AS-4	6.8 ± 0.6	6.9 ± 0.5	8 [236], 8.0 ± 0.4 [222]
15 sec. air plasma AS-4	6.7 ± 0.3	6.9 ± 0.5	---
1 min. NH_3 plasma AS-4	7.2 ± 0.4	6.8 ± 0.3	---
3.5 min. ethylene plasma AS-4	6.6 ± 0.5	6.8 ± 0.6	---

Table 2.7. Surface energies, source, and purity of liquids used in wetting analysis.

Liquid	Source	Purity	γ_L (mJ/m^2)	γ_L^p (mJ/m^2)	γ_L^d (mJ/m^2)
deionized water	lab distilled H_2O tap passed through deionizer cartridges	na*	72.7	49.2	23.5
formamide	Aldrich Chemical	99+%, spectrometric grade	58.3	25.3	33.0
diiodomethane	Aldrich Chemical	99%	50.8	2.4	48.4
bromonaphthalene	Fisher Scientific	reagent grade	44.6	0	44.6
n-hexane	Fisher Scientific	optima	18.6	0	18.6
n-octane	Aldrich Chemical	99+%, gold label	21.5	0	21.5
n-decane	Fisher Scientific	certified	23.8	0	23.8
n-hexadecane	Fisher Scientific	99.8%, certified	27.8	0	27.8
decahydronaphthalene	Fisher Scientific	certified	31.8	0	31.8

*not available

being careful not to melt the edges and alter the slip perimeter. If the glass slip was not cleaned properly, a non-zero angle formed with the glass slip and the advancing contact angle was greater than the receding angle. The wetting traces obtained with deionized water on an unflamed glass slip and on a flamed glass slip are shown in Figure 2.23.

The polar and dispersive components to the liquid surface energies were determined using the relationship proposed by Fowkes for the interfacial surface energy between a liquid and a solid interacting only with dispersion forces [4].

$$\gamma_{SL} = \gamma_S + \gamma_L - 2\sqrt{\gamma_S^d \gamma_L^d} \tag{2.46}$$

Equation 2.5 and equation 2.46 can be combined to give equation 2.47.

$$\cos\theta = -1 + 2\sqrt{\gamma_S^d}\frac{\sqrt{\gamma_L^d}}{\gamma_L} \tag{2.47}$$

Reference plots of $\cos\theta$ versus $\left[\sqrt{\gamma_L^d}/\gamma_L\right]$ were established using the contact angle of bromonaphthalene, a non-polar liquid, on three nonpolar solid surfaces: poly(ethylene), paraffin wax, and poly(tetrafluoroethylene). The three solid samples were wiped with methyl ethyl ketone using a Kimwipe tissue. The average contact angle between bromonaphthalene and each nonpolar solid was measured using a Rame-Hart goniometer as described in section 2.2.6.2. A reference plot was prepared for each of the three solids by plotting the average bromonaphthalene contact angle versus $\left[\sqrt{\gamma_L^d}/\gamma_L\right]$ and drawing a a straight line, with a y-axis intercept of -1, through the data point. The average contact angle of deionized water, formamide, and diiodomethane was then measured on each of the nonpolar solids and the cosine of the average contact angle was placed on the appropriate reference lines.

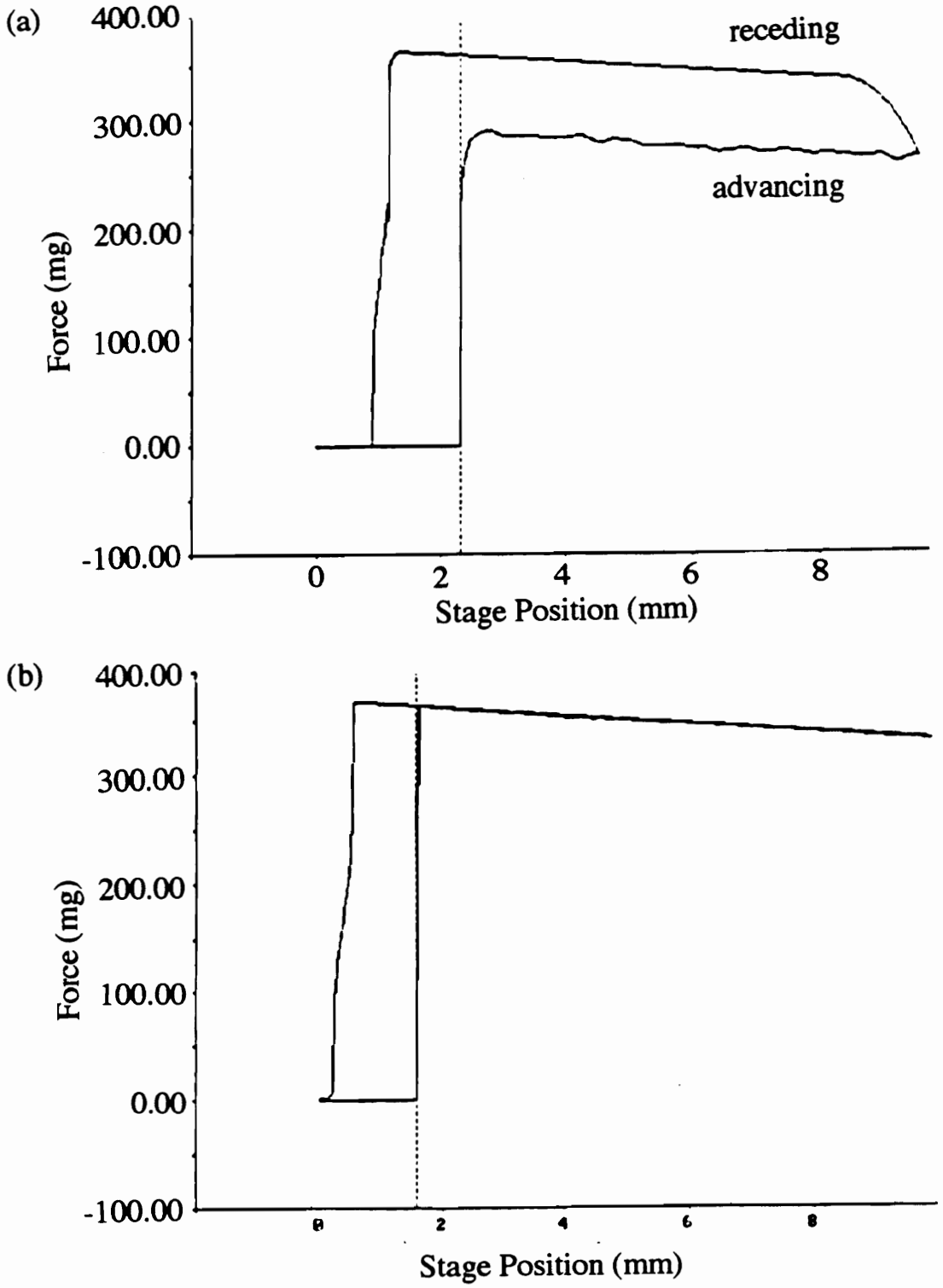

Figure 2.23. Wetting traces obtained with deionized water and a glass cover slip (a) "as received" and (b) flamed in a Bunsen burner.

The reference plots and the contact angle results for deionized water, formamide, and diiodomethane are shown in Figure 2.24. By extrapolating down to the x-axis, an average value of γ_L^d was obtained for each liquid. The assumption was made that the total surface free energy (γ) is equal to the sum of the polar (γ^p) and the dispersion (γ^d) components as given in equation 2.48.

$$\gamma_L = \gamma_L^p + \gamma_L^d \tag{2.48}$$

The polar component γ_L^p was then obtained by substracting γ_L^d from γ_L.

2.2.6.1.1 One-Liquid Technique

The polar and dispersive surface free energies of the carbon fibers were determined using the approach of Owens and Wendt [237] and Dynes and Kaelble [238, 239] in which the contact angle of the carbon fiber was measured with a variety of liquids having known polar and dispersive components of their total surface free energy. Figure 2.25 is a schematic diagram of the one-liquid contact angle experiment.

The surface energy of the liquid and the solid is split into polar and dispersive components as described by equations 2.48 and 2.49,

$$\gamma_S = \gamma_S^p + \gamma_S^d \tag{2.49}$$

where the subscript S denotes a solid surface and the subscript L denotes a liquid surface. The total work of adhesion is also the sum of polar and dispersive contributions as given by equation 2.50

$$W_a = W_a^d + I_{SL}^p \tag{2.50}$$

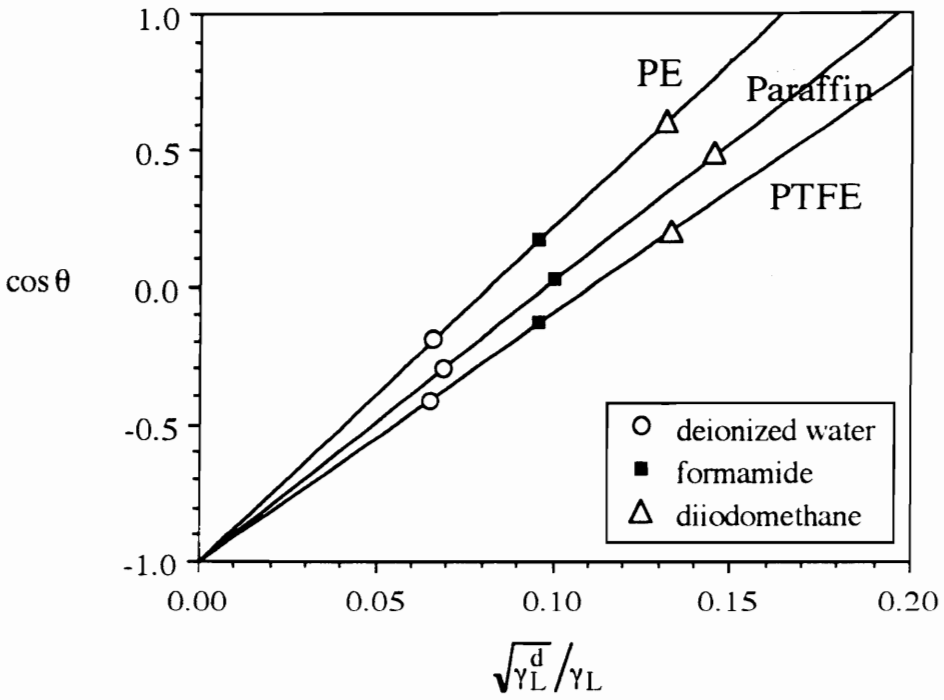

Figure 2.24. Relation of contact angle to liquid surface tension.

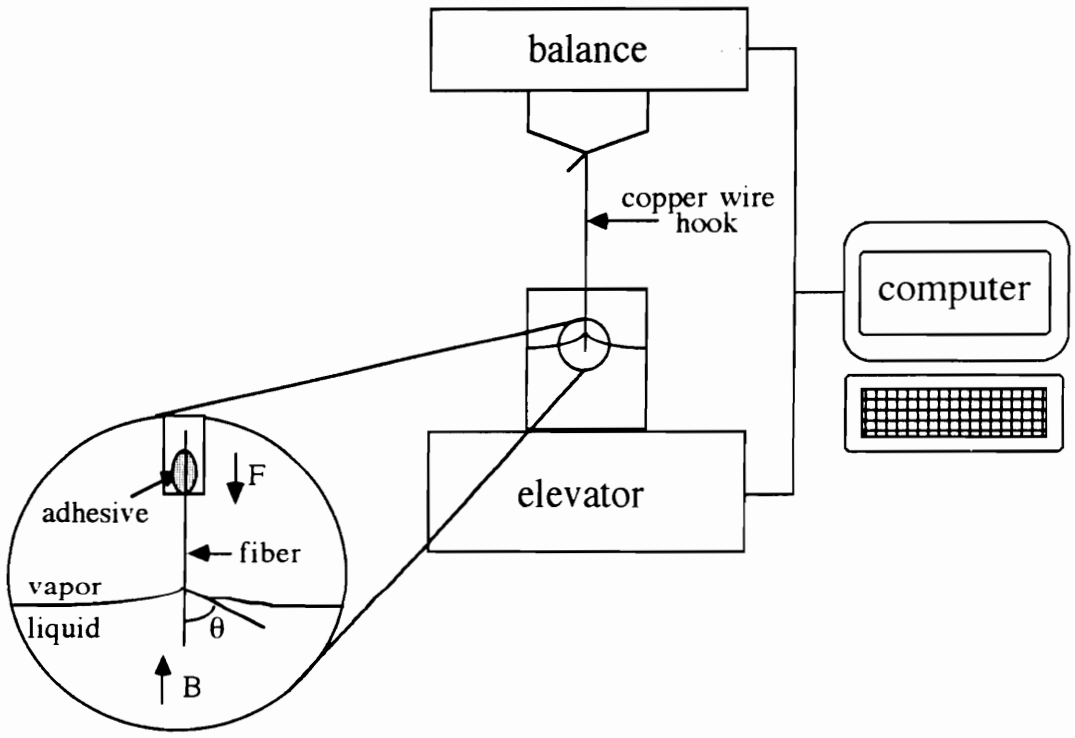

Figure 2.25. Schematic illustration of one-liquid contact angle measurement using the Wilhelmy technique.

where, I_{SL}^{p} is the polar interaction term between the solid and the liquid and the dispersive term is twice the geometric mean of the dispersive components as indicated in equation 2.51.

$$W_a^d = 2\sqrt{\gamma_S^d \gamma_L^d} \tag{2.51}$$

For nonpolar liquids, I_{SL}^{p} is zero. For polar liquids, I_{SL}^{p} was given by Kaelble and Uy as twice the geometric mean of the polar components as indicated in equation 2.52 [240].

$$I_{SL}^{p} \approx 2\sqrt{\gamma_S^p \gamma_L^p} \tag{2.52}$$

Fowkes stated that equation 2.52 is incorrect and sets the polar interaction term (I_{SL}^{p}) equal to an acid-base interaction (W_a^{AB}) [241].

Equations 2.6, 2.51, and 2.52 were combined by Owens and Wendt [237] and Dynes and Kaelble [238, 239] to give equation 2.53.

$$\gamma_L(1+\cos\theta) = 2\sqrt{\gamma_S^d \gamma_L^d} + 2\sqrt{\gamma_S^p \gamma_L^d} \tag{2.53}$$

Equation 2.53 was rearranged to,

$$\frac{\gamma_L(1+\cos\theta)}{2\sqrt{\gamma_L^d}} = \sqrt{\gamma_S^d} + \sqrt{\gamma_S^p}\sqrt{\gamma_L^p/\gamma_L^d} \tag{2.54}$$

so that, values of γ_S^d and γ_S^p can be obtained from the intercept and the slope of a linear plot of $\left[\gamma_L(1+\cos\theta)\right]/2\sqrt{\gamma_L^d}$ versus $\sqrt{\gamma_L^p/\gamma_L^d}$.

2.2.6.1.2 Two-Liquid Technique

In the two-liquid technique, the fiber was immersed in a 10 ml beaker containing two immiscible liquids: formamide and a hydrocarbon [154, 232]. The hydrocarbons

used were hexane, octane, decane, hexadecane, and decahydronaphthalene. A schematic diagram of the experimental setup is shown in Figure 2.26.

At the fiber/hydrocarbon/air interface, equations 2.3 and 2.50 may be equated and the work of adhesion may be expressed as,

$$W_{a,H} = \gamma_S + \gamma_H - \gamma_{S/H} = 2\sqrt{\gamma_S^d \gamma_H} \tag{2.55}$$

and,

$$\gamma_S = \gamma_{S/H} - \gamma_H + 2\sqrt{\gamma_S^d \gamma_H} \tag{2.56}$$

since there are no polar interactions. At the fiber/formamide/hydrocarbon interface, equation 2.5 may be expressed as,

$$\gamma_{S/H} = \gamma_{S/F} + \gamma_{F/H}\cos(\theta_{S/F/H}) \tag{2.57}$$

and the work of adhesion is given by,

$$W_{a,F} = \gamma_S + \gamma_F - \gamma_{S/F} = 2\sqrt{\gamma_S^d \gamma_F^d} + I_{S/F}^p \tag{2.58}$$

Rearranging and substituting equations 2.56 and 2.57 into equation 2.58 leads to equation 2.59,

$$\gamma_F - \gamma_H + \tau = 2\sqrt{\gamma_S^d}\left[\sqrt{\gamma_F^d} - \sqrt{\gamma_H}\right] + I_{S/F}^p \tag{2.59}$$

where, γ_F and γ_F^d are the total surface energy and the dispersive component of the surface energy of formamide, γ_H is the surface tension of the hydrocarbon, $I_{S/F}^p$ is the polar interaction parameter, and,

$$\tau = \gamma_{F/H}\cos\theta_{S/F/H} = \frac{F - F_H}{\pi d} \tag{2.60}$$

where $\theta_{S/F/H}$ is the contact angle at the triple phase line, $\gamma_{F/H}$ is the interfacial energy between formamide and the hydrocarbon, πd is the fiber perimeter, F_H is the force

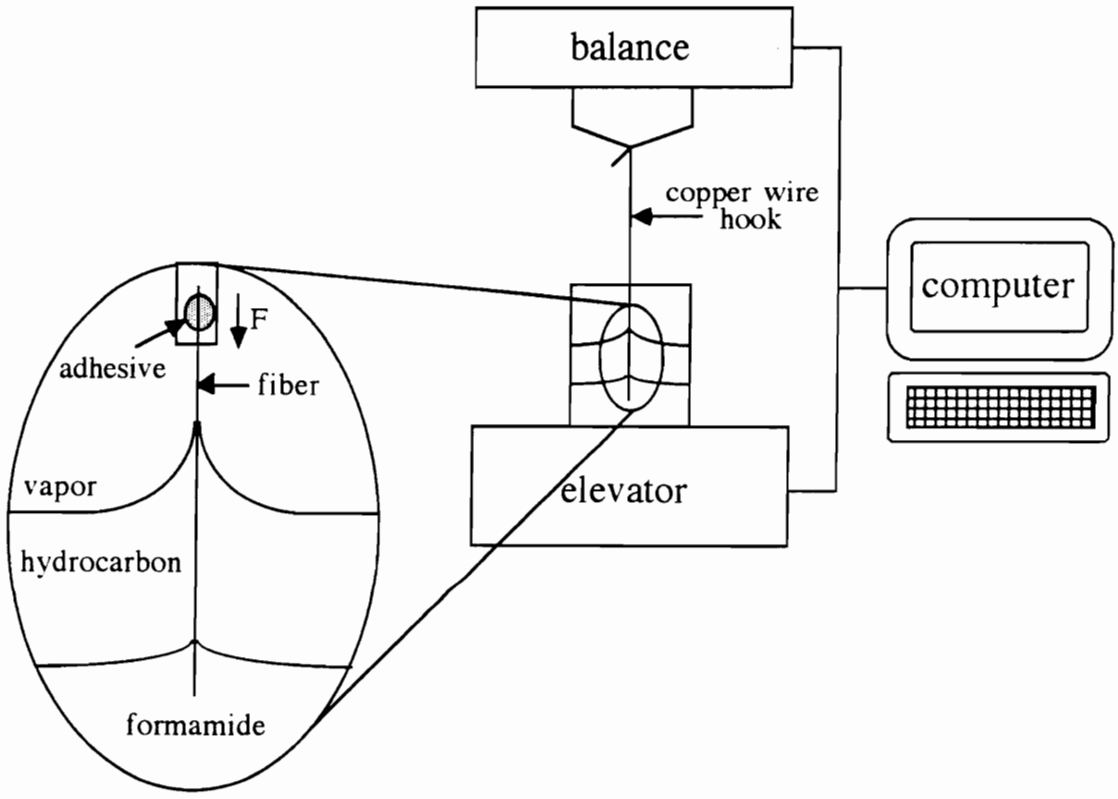

Figure 2.26. Schematic illustration of two-liquid contact angle measurement using the Wilhelmy technique.

recorded by the balance when the fiber is immersed in the hydrocarbon layer, and F is the total force recorded by the balance when the fiber has passed through the hydrocarbon layer and entered the formamide. The dispersion component (γ_S^d) is calculated from the slope of a straight line fit to a plot of $\gamma_F - \gamma_H + \tau$ versus $\sqrt{\gamma_F^d} - \sqrt{\gamma_H}$. The polar interaction term ($I_{S/F}^p$) is obtained from the intercept.

Equation 2.60 assumes that the formamide displaces the hydrocarbon during immersion of the fiber and that the hydrocarbon displaces the formamide during the emersion stage. The displacement criteria have been derived by Shanahan and coworkers and are given in equations 2.61 and 2.62 [242].

advancing: $$I_{S/F}^p > 2\left[\sqrt{\gamma_S^d} - \sqrt{\gamma_H}\right]\left[\sqrt{\gamma_H} - \sqrt{\gamma_F^d}\right] \tag{2.61}$$

receding: $$I_{S/F}^p < 2\left[\gamma_F^p - \left(\sqrt{\gamma_S^d} - \sqrt{\gamma_F^d}\right)\right]\left[\sqrt{\gamma_F^d} - \sqrt{\gamma_H}\right] \tag{2.62}$$

These criteria are based on the assumptions that the equilibrium spreading pressure of both liquids is negligible and that the surface is perfectly homogeneous and smooth.

2.2.6.2 Contact Angle Goniometer

The surface energy of the polymer coating created in the ethylene plasma was determined by exposing glass slips to the ethylene plasma for 3.5 minutes and then measuring liquid contact angles on the slip surface using the sessile drop technique. The contact angle of a drop placed on the solid surface was measured using a Rame-Hart 100-00 115 NRL contact angle goniometer as illustrated in Figure 2.27. Five microliter drops of liquid were carefully placed on the substrate using a Hamilton microliter syringe held in an upright position. The contact angles at the left and the right sides of five drops were measured and averaged.

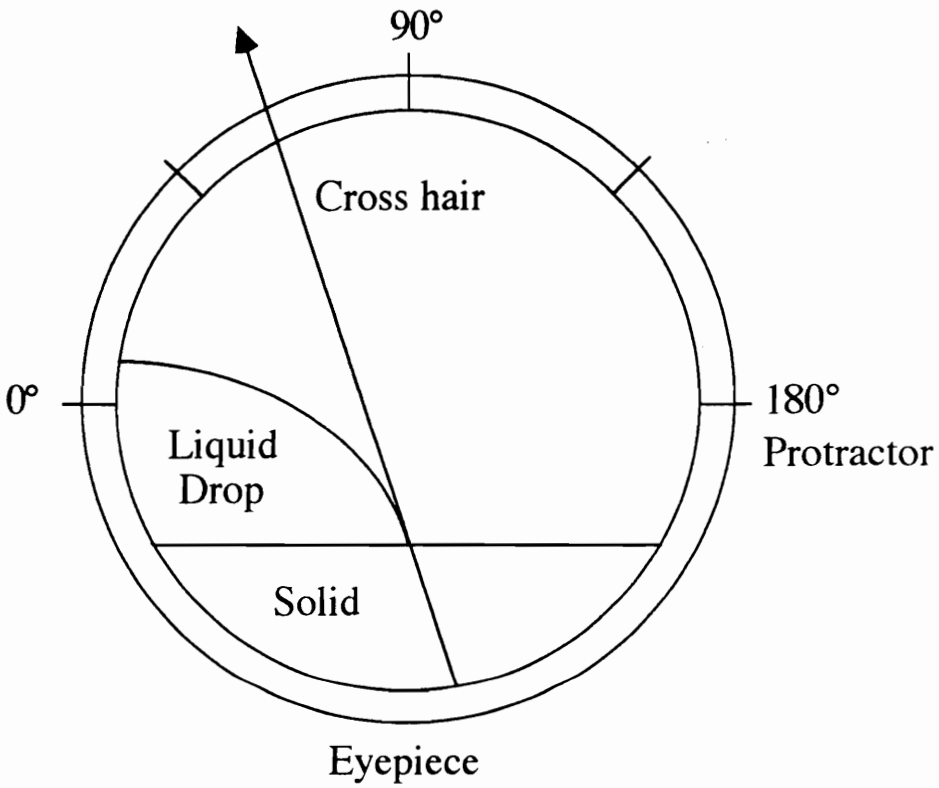

Figure 2.27. Sessile drop contact angle measurement using a goniometer [adapted from ref. 4].

2.2.7 Tensile Strength Measurement

The tensile strengths of the "as received" and plasma treated carbon fibers were measured as shown in Figure 2.28. A solid and a hole-punched aluminum tab were connected with thin strips of construction paper and an epoxy adhesive. A single fiber was separated from the tow and mounted between the two aluminum tabs. Care was taken to align the fiber long axis in the tensile direction. The fiber was affixed to the aluminum tabs using an epoxy adhesive and the epoxy was allowed to cure for 8 hours at room temperature.

A metal hook was hung from the bottom of a Mettler PM300 balance. The tensile strength specimen was suspended from the hook by the hole-punched aluminum tab. The lower tab was secured between the blades of a microvise mounted on an elevator. Once the tensile specimen was secured in the vise, portions of both paper strips were burned away using a soldering iron and only the single fiber was suspended between the aluminum tabs. The elevator was lowered at a rate of 5 μm per second and the load applied to the fiber was recorded as a function of time with a personal computer.

There is great variation in the tensile strengths of carbon fibers both along and between tows within a spool as well variation between spools and lot numbers [153]. The distribution of strengths is often described by the Weibull distribution given by,

$$F = 1 - \exp\left\{-L\left[(\sigma - \sigma_u)/\sigma_o\right]^m\right\} \tag{2.63}$$

where L is the fiber gauge length, m is the "Weibull" modulus, σ is the fiber tensile strength, σ_o is a scaling parameter, σ_u is an arbitrary parameter which is often set equal to zero, and F is the cumulative probabily of failure [243].

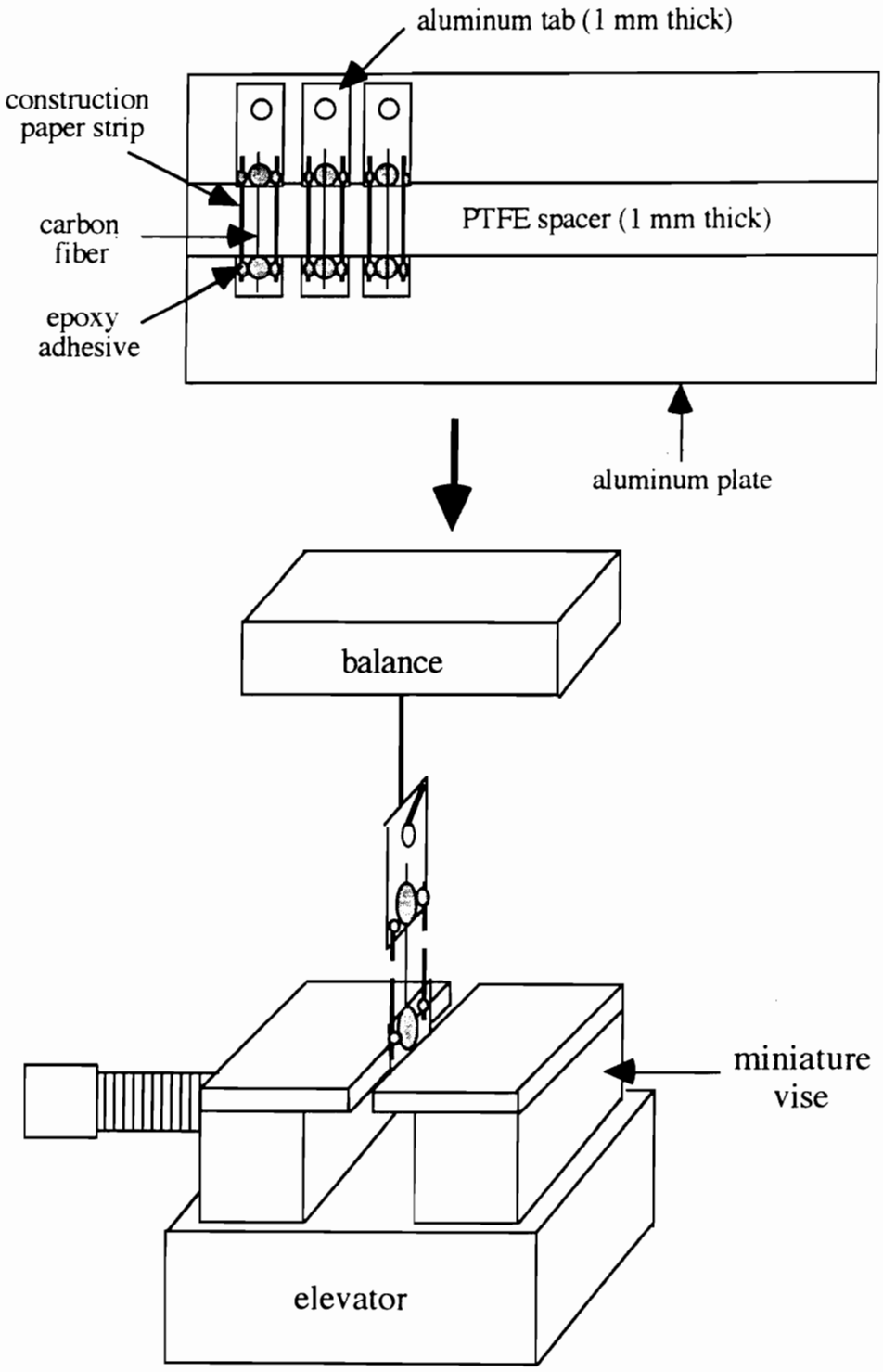

Figure 2.28 Measurement of carbon fiber tensile strength.

The value of F is determined from the experimental tensile strength measurements by first ranking the data in ascending order and then assigning a cumulative probability (F) to each a data point. The cumulative probability of a data point of rank (R) falls somewhere in the interval,

$$\frac{R-1}{N} \le F \le \frac{R}{N} \tag{2.64}$$

where N is the total number of data points. For a large number of data points, the precise definition of F becomes unimportant. Equation 2.65 is one way of assigning a value to F.

$$F = \frac{R}{N+1} \tag{2.65}$$

If equation 2.63 is rearranged to give,

$$\ln\left(-\ln(1-F)\right) = m\ln(\sigma - \sigma_u) - m\ln(\sigma_o) + \ln L \tag{2.66}$$

m and σ_o can be obtained from the slope and the intercept of a linear plot of ln(-ln(1-F)) versus ln σ. The average tensile strength of the fiber ($\bar{\sigma}$) is given by equation 2.67,

$$\bar{\sigma} = \sigma_u + \sigma_o L^{1/m}\Gamma\left(1+\frac{1}{m}\right) \tag{2.67}$$

where Γ is the complete gamma function.

2.2.8 Analysis of Ethylene Plasma Polymer

2.2.8.1 Thermogravimetric Analysis (TGA)

Dynamic thermogravimetric analysis was performed using a Perkin Elmer TGA7 to determine the relative thermal stabilities of the polymer formed in the ethylene gas plasma and conventional low density poly(ethylene) from Eastman Chemical Company. The samples were heated in crimped aluminum pans in an air atmosphere at a rate of

10°C per minute. The weight loss of the sample was measured as a function of temperature.

2.2.8.2 Differential Scanning Calorimetry (DSC)

Differential scanning calorimetry was conducted on a Perkin Elmer DSC7 to determine the relative melting temperatures of the low density poly(ethylene) and the polymer formed in the ethylene gas plasma. DSC scans were run under a nitrogen atmosphere at 10°C per minute.

2.2.8.3 Fourier Transform Infrared Spectroscopy (FT-IR)

The plasma polymer powder was analyzed was pressed with dry KBr to form a pellet. The sample pellet was analyzed using a Nicolet 510 Fourier tranform infrared spectrometer with a resolution of 4 cm^{-1}. The spectrometer bench was purged with dry nitrogen prior to analysis.

2.3 RESULTS AND DISCUSSION

2.3.1 Analysis of "As Received" AU-4 and AS-4 Carbon Fibers

2.3.1.1 Surface Chemical Composition

Carbon, oxygen, and nitrogen were detected on the AU-4 carbon fiber surface using XPS. Carbon, oxygen, and nitrogen, as well as a trace amount of sodium were detected on the AS-4 carbon fiber surface. The concentration of each element detected in the fiber surfaces is listed in Table 2.8. There was more oxygen on the surface of the AS-4 carbon fiber than on the AU-4 carbon fiber. This was the result of the oxidative surface treatment that the AS-4 carbon fiber received during production. The sodium present on the AS-4 carbon fiber was a residual impurity from the sodium alkyl sulfonate added to the PAN carbon fiber precursor material [138]. The XPS data reported in the literature

Table 2.8. Surface composition of "as received" AU-4 and AS-4 carbon fibers (XPS, 45° take-off angle).

FIBER	CONCENTRATION (<atomic %> ± σ_{n-1} for 3 samples)				ATOMIC RATIO		
	Carbon	Oxygen	Nitrogen	Sodium	O/C	N/C	Na/C
AU-4	91.9 ± 0.9	6.0 ± 0.8	2.1 ± 0.2	nsp*	0.065	0.022	nsp
AS-4	87.8 ± 1.2	9.3 ± 1.0	2.7 ± 0.1	0.2 ± 0.1	0.11	0.031	0.003

*no significant peak

for the AU-4 and AS-4 carbon fibers, compiled in Table 2.9, varies over a considerable range. This may be due to variation among fiber lots and contamination of the fibers during handling and storage.

Desimoni and coworkers stressed the importance of cleaning carbon fibers prior to XPS analysis [207]. When they placed carbon fibers in a 50°C ultrasonic bath of carbon tetrachloride for thirty minutes, stored the fibers in a vacuum dessicator for twelve hours, and then heated them in an air oven for thirty minutes, the XPS O/C ratio of HMU carbon fibers decreased from 0.16 to 0.05. Evidence of adsorbed oxygen containing species on carbon fiber surfaces has also been presented by Drzal and coworkers, Lavielle and Schultz, Vukov and Gray, and Wilkinson [32, 244-247]. Drzal and coworkers [244] concluded that physisorbed water, carbon monoxide, and carbon dioxide are volatilized from both high strength and high modulus carbon fibers at temperatures up to 200°C. It has also been found, using inverse gas chromatography, that heat treatment of carbon fibers at low temperatures increases the dispersive component of surface energy [245-247]. This increase has been attributed to the desorption of species such as water and carbon dioxide from the carbon fiber surface.

In this work, attempts to clean the carbon fibers using ultrasonic solvent baths and heat treatments did not decrease the concentration of oxygen on the fiber surface. Exposure of the fibers to ambient conditions prior to XPS analysis and more importantly, heating the fibers in contaminated air ovens affected the carbon fiber cleaning results. For example, in one cleaning attempt a significant amount of silicon was detected on the carbon fiber surface. This silicon was deposited on the fiber surface when the fiber tow was heated in an air oven in which materials coated with a silicon containing release agent had recently been heated.

The carbon 1s photopeak of carbon fibers generally exhibits a pronounced asymmetric tailing toward higher binding energy values. This tail arises partly from the

Table 2.9. Surface composition of "as received" AU-4 and AS-4 carbon fiber reported in the literature (XPS, 45° take-off angle).

FIBER	CONCENTRATION (atomic %)				Reference
	Carbon	Oxygen	Nitrogen	Sodium	
AU-4	96	1.8	2.0	---*	[51]
AU-4	90	10	0.0	---	[98]
AU-4	86	9	2	3	[233]
AU-4	96	2.7	1.7	---	[222]
AS-4	86	12	2.5	---	[222]
AS-4	91	5.3	3.7	---	[194]
AS-4	85	10	4.0	1.0	[39]
AS-4	70	20	7	4	[233]
AS-4	84	9.9	5.0	0.8	[51]
AS-4	87	9.1	3.5	---	[244]

*not reported

intrinsic asymmetry of the graphitic carbon peak and partly from peaks arising from oxygen and nitrogen-containing functional groups [207, 248]. In this study, the carbon 1s photopeak of the "as received" fibers was fit with six peaks as shown in Figure 2.29. The carbon 1s peak assignments were made based on the binding energies listed in Table 2.10 [207, 248] and on the work of Beamson and Briggs with nitrogen-containing polymers [249]. Desimini et al. [207, 248] compiled the carbon 1s assignments listed in Table 2.10 from papers of Sherwood and coworkers [172, 250-253].

The first peak was fit at 284.6 eV and assigned to both the graphitic and aliphatic carbon to carbon bonding. The second peak was fit at 285.9 eV and was assigned to carbon singly bonded to oxygen and to carbon singly, doubly, or triply bonded to nitrogen. The third peak was fit at 287.3 eV and was assigned to carbonyl and N-C=O groups. The fourth peak was fit at 288.7 eV and was assigned to carboxylic groups. The fifth peak was fit at about 290.0 eV and was attributed to carbonate groups and to adsorbed CO_2. A plasmon loss peak was fit at 291.4 eV as described by Proctor and Sherwood [250]. The contributions of each carbon 1s curve-fit peak for the "as received" AU-4 and AS-4 carbon fibers, expressed in percent of the total composition, are summarized in Table 2.11.

The peak at 284.6 eV was not fit with the characteristic high binding energy asymmetric tail exhibited by graphitic materials. Small changes in the symmetry of this peak can cause a considerable difference in the amount of oxidized carbon features that can be fitted to the carbon 1s region [207]. Nakayama and coworkers showed the effect of using either an asymmetric graphitic peak shape or a symmetric aliphatic peak shape for the carbon 1s photopeak on the calculated concentration of oxygen groups [254]. Therefore, the percentage of the carbon 1s photopeak attributed to oxygen and nitrogen functionality in Table 2.11 is probably skewed to a high value.

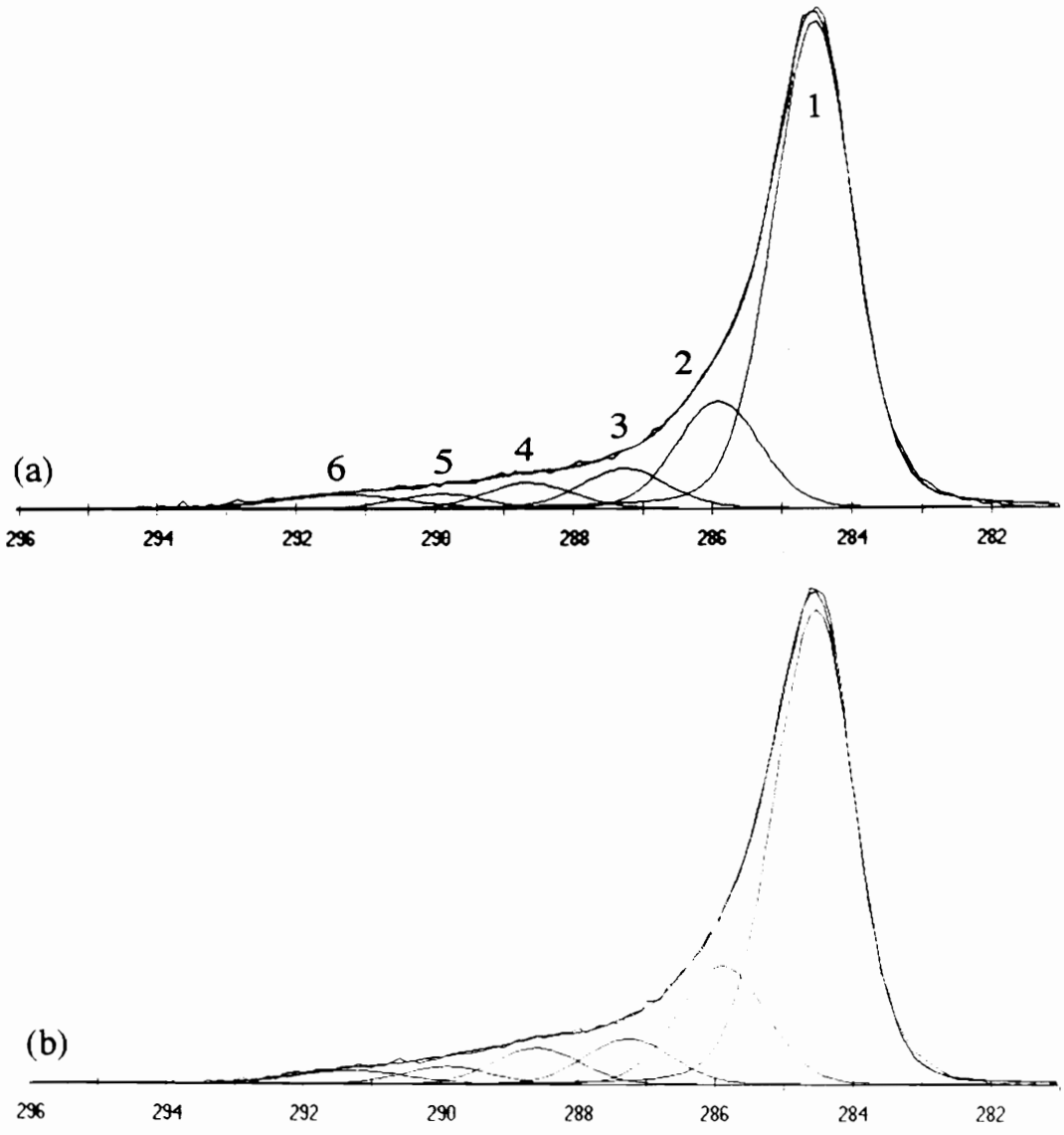

Figure 2.29. Curve-fit carbon 1s photopeaks of "as received" (a) AU-4 and (b) AS-4 carbon fibers.

Table 2.10. Binding energies of carbon 1s XPS signals [207, 248].

Carbon Atom Type	Binding Energy* (eV)
Graphite, aromatics	284.6
Aliphatics, β-carbons	285.1-285.3
Alcohols, phenols	286.1
Keto-groups	287.6
Carboxylic groups	289.1
Carbonate, CO_2	290.6
Plasmon loss	291.3

*Uncertainty on the carbon 1s contributions is ± 0.3 eV.

Table 2.11. Carbon 1s curve-fitting results for "as received" AU-4 and AS-4 carbon fibers.

FIBER	<% of Total Carbon 1s Peak Area> ± σ_{n-1} for 3 samples					
	Binding Energy* (eV)					
	284.6	285.9	287.3	288.7	290.0	291.4
AU-4	68.8 ± 0.1	14.1 ± 1.9	6.3 ± 0.3	4.1 ± 0.1	2.9 ± 0.8	3.8 ± 0.6
AS-4	65.5 ± 0.2	16.7 ± 0.8	6.8 ± 0.2	5.5 ± 0.3	2.7 ± 0.1	2.8 ± 0.3
ORIGIN	C-Hx	C-OH C-O-C C-N C=N C ≡ N	C=O N-C=O	O=C-OH O=C-OR	O-CO-O O=C-O O=C=O	plasmon loss
PEAK NO.	1	2	3	4	5	6

*Uncertainty on carbon 1s contributions is ± 0.1 eV.

The assignment of the oxygen 1s region is even more complex owing to uncertainty in the binding energy values of the various oxygen species. Previous studies reported the oxygen binding energies and assignments listed in Table 2.12 [248]. The alcoholic group falls in the range 532.2-533.3 eV and the carbonyl group falls in the range of 531.1-531.8 eV. Water falls at 535.5-536.1 eV. The oxygen 1s photopeak of the "as received" carbon fibers was fit with three peaks as shown in Figure 2.30.

The first peak was fit at about 532.0 eV and was assigned to oxygen doubly bonded to carbon and to oxygen singly bonded to two carbon atoms. The second peak was fit at 533.5 eV and was assigned to oxygen singly bonded to carbon. The third peak was fit at 536.2 eV and was assigned to adsorbed water and/or molecular oxygen. The oxygen 1s curve-fit results for the "as received" AU-4 and AS-4 carbon fibers are summarized in Table 2.13.

Curve-fitting of the carbon fiber nitrogen 1s photopeak is not often reported in the XPS literature due to the low concentration of nitrogen in the carbon fiber surface and to the poorly resolved nitrogen peak. In this work, the shape of the nitrogen 1s photopeak changed significantly when the carbon fibers were exposed to an ammonia plasma, so an attempt was made to curve-fit the nitrogen 1s photopeaks. The nitrogen 1s photopeaks of the "as received" AU-4 and AS-4 carbon fibers were fit with five peaks as shown in Figure 2.31. Peak assignments were made based on the work of Sherwood and coworkers [253] with carbon fibers and the work of Beamson and Briggs with nitrogen containing polymers [249].

The first three peaks around 397.8, 399.1, and 400.8 eV were attributed to cyano, aromatic amine and -C=NH, and aliphatic amine groups, respectively. The fourth and fifth peaks at 401.9 and 403.8 eV were attributed to NH_3^+ groups and shake-up. The nitrogen 1s curve-fitting results for the "as received" AU-4 and AS-4 carbon fibers are listed in Table 2.14.

Table 2.12. Binding energies of oxygen 1s XPS signals [248].

Oxygen Atom Type	Binding Energy* (eV)
Alcohol, C-OH in carboxylic acids	532.3-533.3
Ketone, C=O in carboxylic acids or carbonates	531.1-531.8
Adsorbed water	535.5-536.1

*Uncertainty on oxygen 1s contributions is ± 0.3 eV.

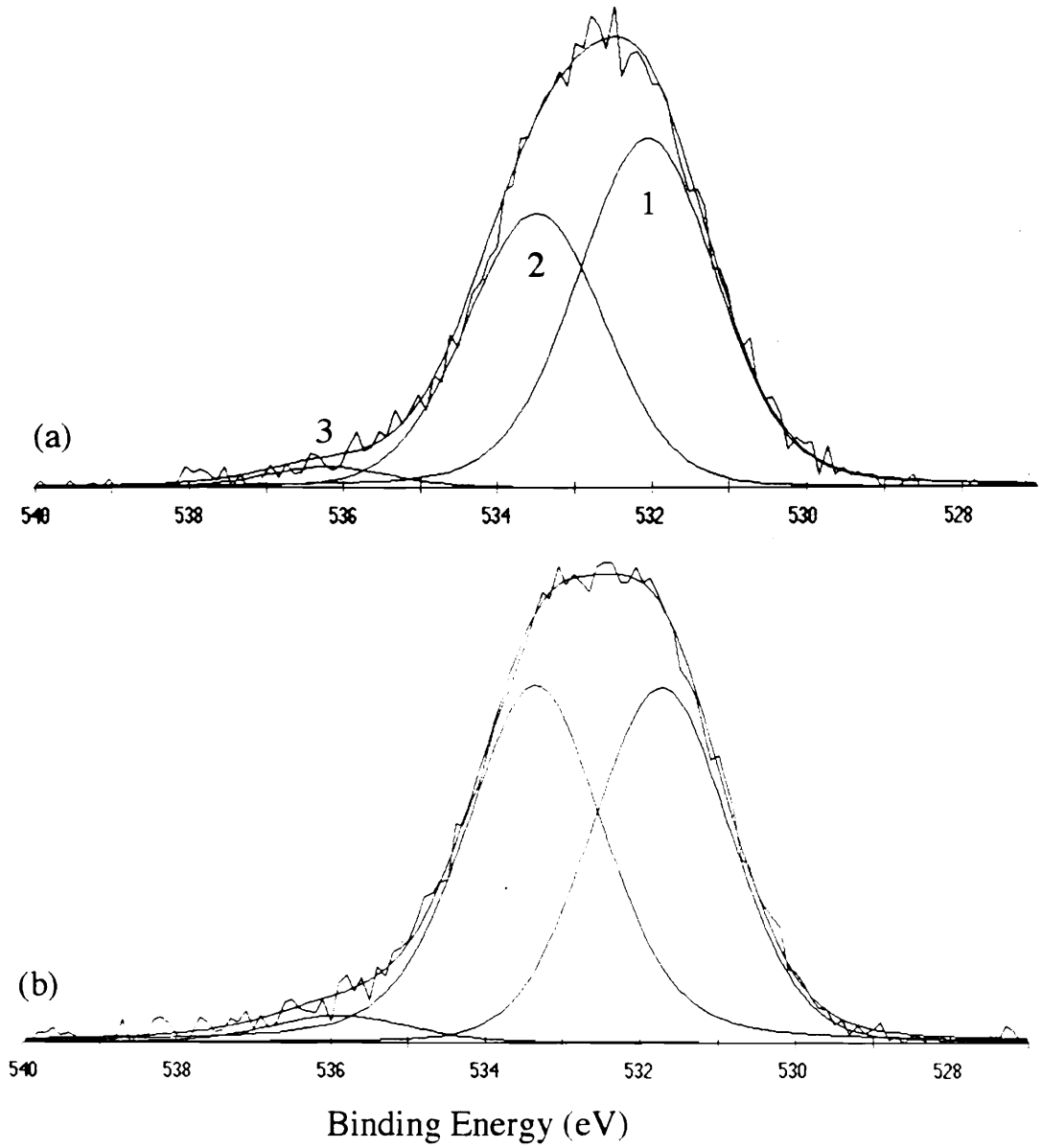

Figure 2.30. Curve-fit oxygen 1s photopeaks of "as received" (a) AU-4 and (b) AS-4 carbon fibers.

Table 2.13. Oxygen 1s curve-fitting results for "as received" AU-4 and AS-4 carbon fibers.

FIBER	<% Total Oxygen 1s Peak Area> ± σ_{n-1} for 3 samples		
	Binding Energy* (eV)		
	532.0	533.5	536.2
AU-4	58.0 ± 3.1	40.6 ± 1.2	1.4 ± 1.9
AS-4	44.9 ± 1.5	51.9 ± 2.1	3.2 ± 0.7
ORIGIN	C=O C-O-C	C-OH	adsorbed H_2O and/or O_2
PEAK NO.	1	2	3

*Uncertainty on oxygen 1s contributions is ± 0.2 eV

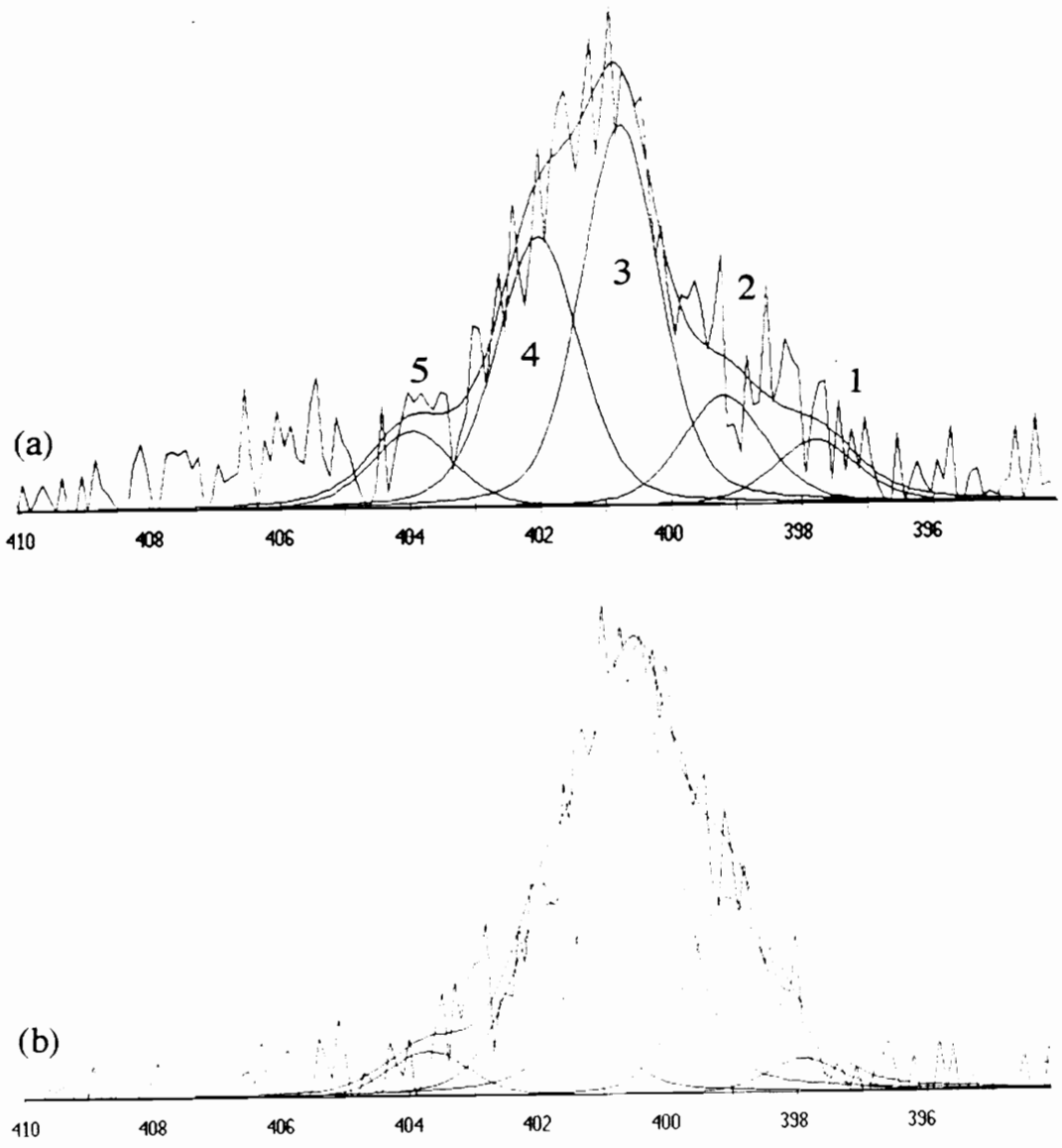

Figure 2.31. Curve-fit nitrogen 1s photopeaks of "as received" (a) AU-4 and (b) AS-4 carbon fibers.

Table 2.14. Nitrogen 1s curve-fitting results for "as received" AU-4 and AS-4 carbon fibers.

FIBER	<% of Total Nitrogen 1s Peak Area> ± σ_{n-1} for 3 samples				
	Binding Energy* (eV)				
	397.8	399.1	400.8	401.9	403.8
AU-4	6.0 ± 2.6	11.5 ± 1.2	43.7 ± 3.8	30.3 ± 0.9	8.6 ± 0.2
AS-4	4.3 ± 1.4	21.6 ± 0.1	46.6 ± 1.9	21.0 ± 2.0	6.5 ± 2.6
ORIGIN	-CN	Ph-NH_2 -C=NH	aliphatic amine	NH_3^+ shake-up	shake-up
PEAK NO.	1	2	3	4	5

*Uncertainty on nitrogen 1s contributions is ± 0.2 eV.

The surfaces of the "as received" AU-4 and AS-4 carbon fibers were also studied using angle dependent XPS. The fibers were analyzed at take-off angles of 15° and 90° to determine if the fiber atomic composition varied with the XPS sampling depth. The concentration of carbon, oxygen, nitrogen, and sodium detected in the AU-4 and AS-4 carbon fiber surfaces at take-off angles of 15°, 45°, and 90°is listed in Table 2.15. Bar charts which compare the O/C and N/C ratios obtained at take-off angles of 15° and 90° are shown in Figure 2.32.

The O/C ratios of the "as received" AU-4 and AS-4 carbon fibers increased as the XPS take-off angle and sampling depth was decreased. It was therefore concluded that there was more oxygen on the outermost surface of the carbon fibers than in the bulk. The N/C ratio of the AS-4 carbon fiber did not vary significantly between 15° and 90°. However, the N/C ratio of the AU-4 carbon fiber was slightly higher at 90° than at 15°. The carbon 1s photopeaks obtained at take-off angles of 15° and 90° with the "as received" AU-4 and AS-4 carbon fibers are shown in Figure 2.33. There was no significant difference in the shape of the carbon 1s, oxygen 1s, and nitrogen 1s photopeaks obtained at take-off angles of 15° and 90°.

2.3.1.2 Topography

SEM photomicrographs of the "as received" AU-4 and AS-4 carbon fibers magnified 12,500X and 50,000X are shown in Figures 2.34 and 2.35, respectively. At a magnification of 12,500X, longitudinal ridges are clearly evident on both the AU-4 and AS-4 carbon fibers. These axial striations are created during extrusion of the PAN precursor fiber [225]. At 50,000X, the surface appears textured, but the surface structure is poorly resolved.

Table 2.15. Surface composition of "as received" AU-4 and AS-4 carbon fibers obtained at take-off angles of 15°, 45°, and 90° (XPS).

FIBER	TAKE-OFF ANGLE	CONCENTRATION (<atomic %> ± σ_{n-1} for 3 samples)			
		Carbon	Oxygen	Nitrogen	Sodium
AU-4	15°	89.6	8.8	1.6	nsp*
	45°	91.9 ± 0.9	6.0 ± 0.8	2.1 ± 0.2	nsp
	90°	92.7	5.2	2.1	nsp
AS-4	15°	82.9	13.9	2.9	0.3
	45°	87.8 ± 1.2	9.3 ± 1.0	2.7 ± 0.1	0.2 ± 0.1
	90°	88.0	8.8	2.9	0.3

*no significant peak

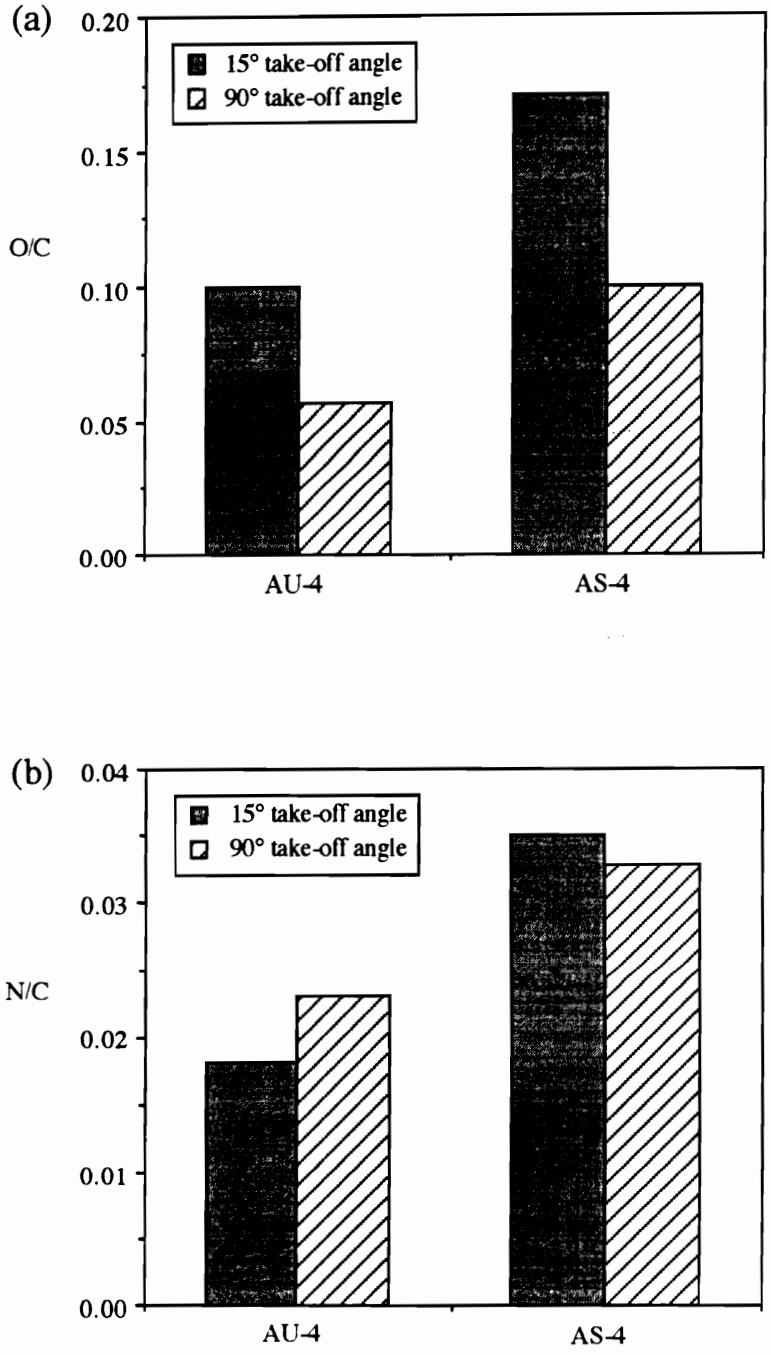

Figure 2.32. (a) O/C and (b) N/C ratios obtained at take-off angles of 15° and 90° with "as received" AU-4 and AS-4 carbon fibers.

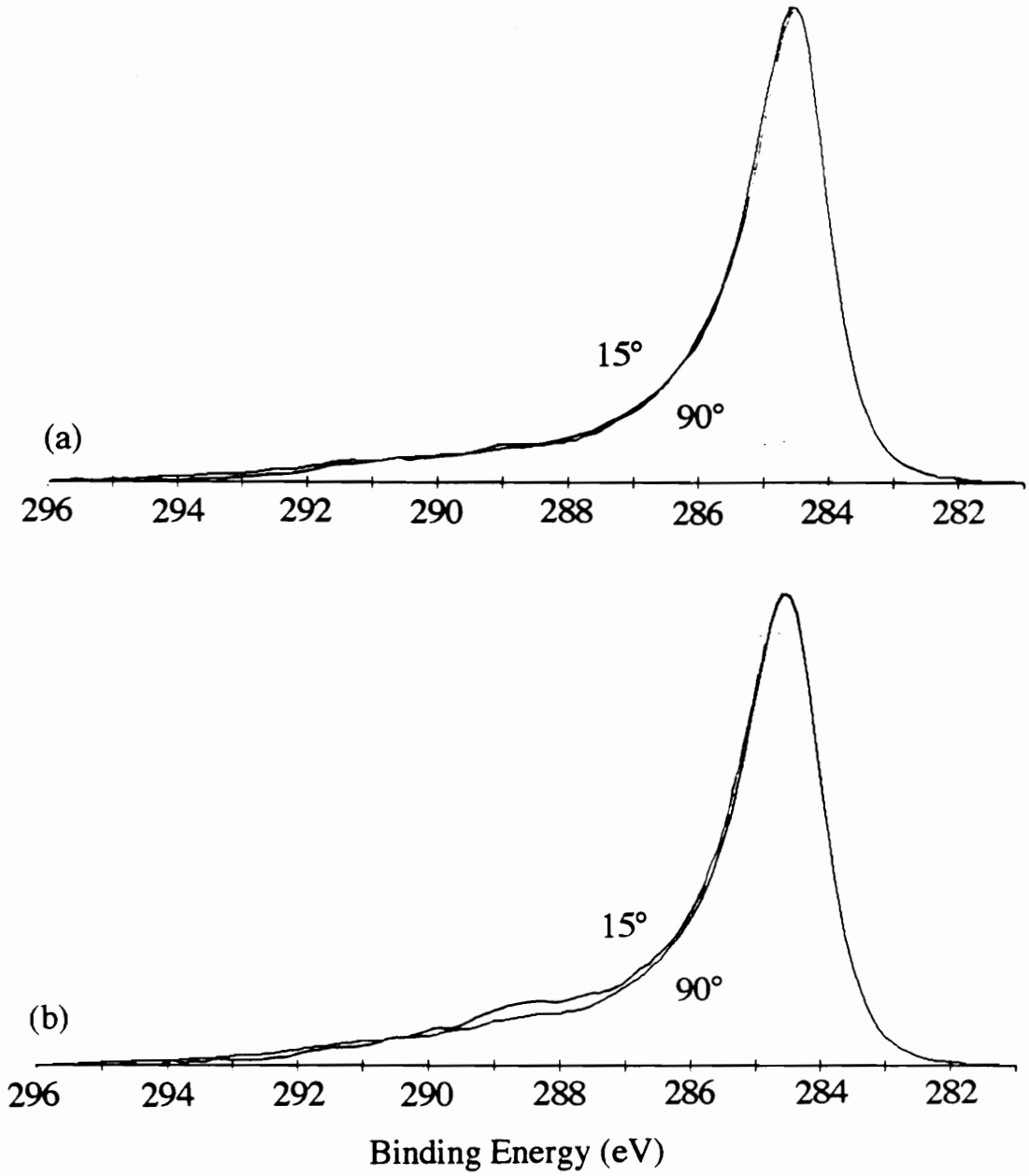

Figure 2.33. Carbon 1s photopeaks obtained at take-off angles of 15° and 90° for "as received" (a) AU-4 and (b) AS-4 carbon fibers.

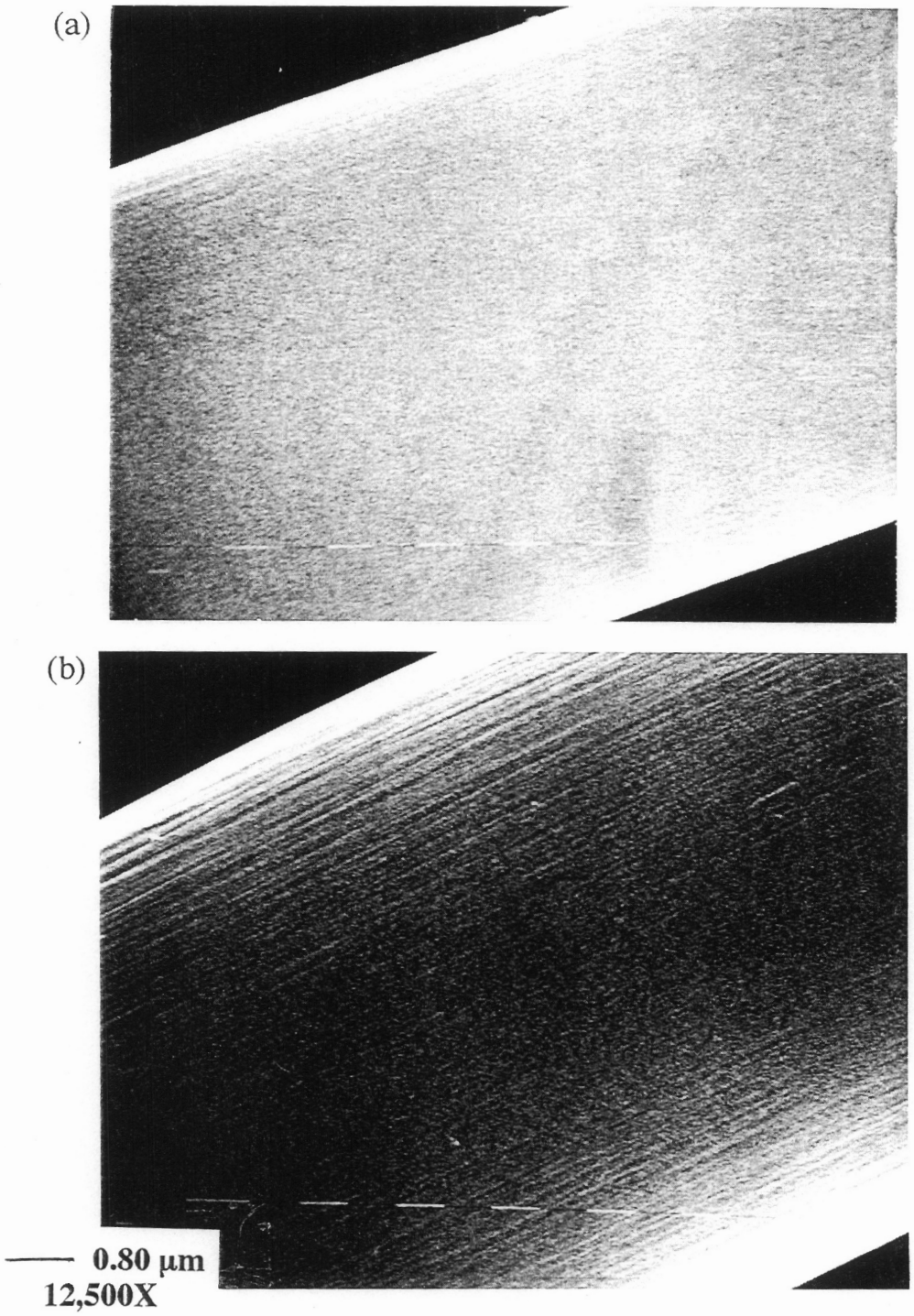

Figure 2.34. SEM photomicrographs of "as received" (a) AU-4 and (b) AS-4 carbon fibers at a magnification of 12,500X.

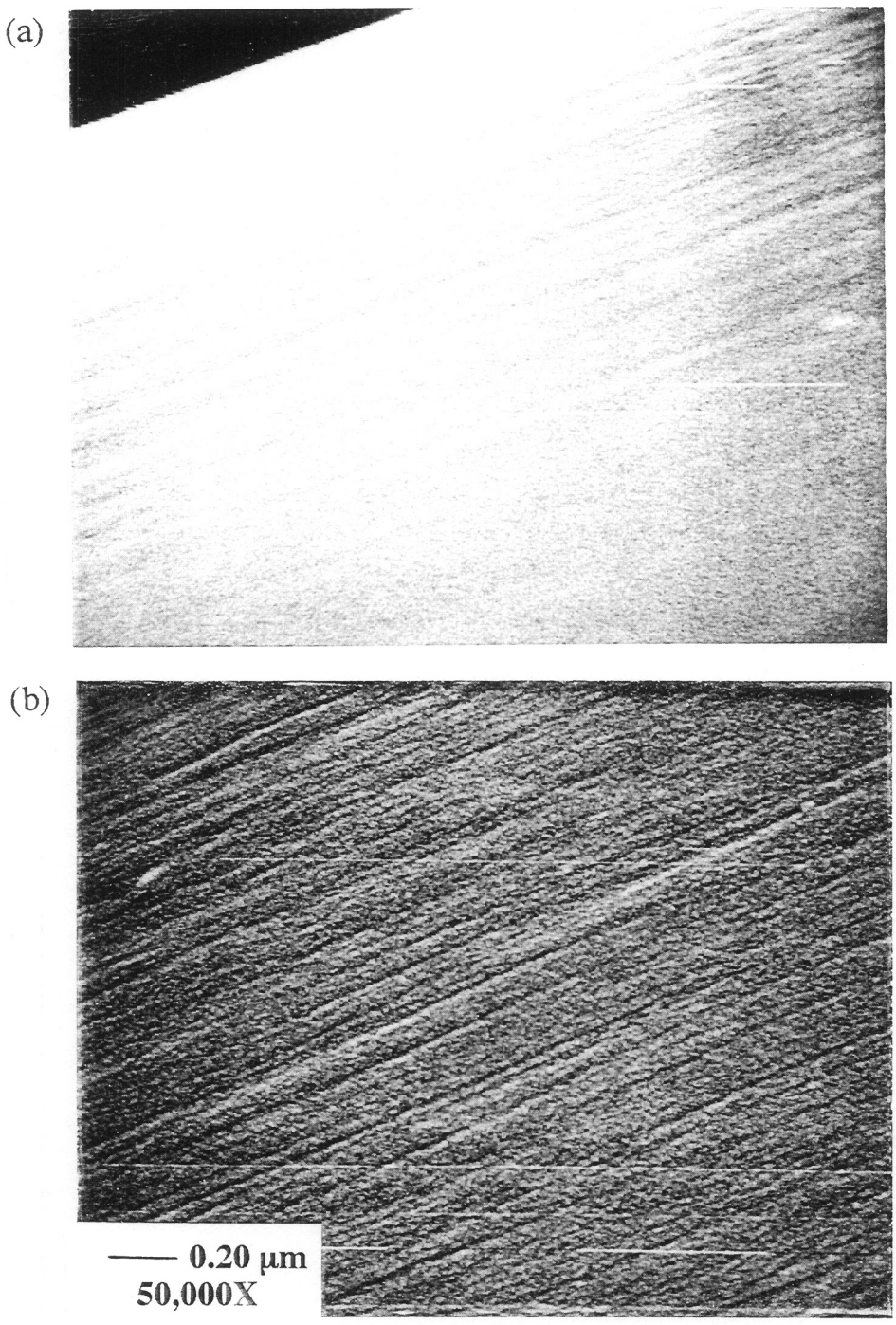

Figure 2.35. SEM photomicrographs of "as received" (a) AU-4 and (b) AS-4 carbon fibers at a magnification of 50,000X.

2.3.1.3 Surface Energy Analysis

The surface energies of the "as received" AU-4 and AS-4 carbon fibers were determined using two different techniques.

2.3.1.3.1 One-Liquid Technique

Examples of traces obtained during dynamic contact angle experiments in five different liquids with "as received" AU-4 and AS-4 carbon fibers are shown in Figures 2.36 and 2.37, respectively. The force, initially equal to zero, rose to a plateau when the fiber end penetrated the liquid.

The polar and the dispersive components to the total fiber surface energy were calculated by plotting the contact angle results in the form of equation 2.54. These linear regression plots are shown in Figure 2.38. The surface energy results obtained from these plots are listed in Table 2.16. While the total surface energies corresponded relatively well to the literature surface energy data for AU-4 and AS-4 carbon fibers listed in Table 2.17, the polar component was significantly less than that reported in the literature. This may be due to the use of different wetting liquids, variation between fiber lots, or contamination of the fiber surfaces.

In addition, to show which liquids formed a zero contact angle with the carbon fiber surface, the advancing wetting force was plotted versus the surface free energy of the wetting liquid. Based on equation 2.43, a linear curve with an intercept of zero may be fit through the data points when $\theta = 0°$. Liquids which display a finite contact angle ($\theta \geq 0°$), provide data points below the linear curve. In general, liquids will spread and form a zero degree contact angle on a solid which has a surface tension less than that of the liquid. Therefore, the plots in Figure 2.39 suggest that the total surface energy of both the AU-4 and the AS-4 carbon fibers is between 44.6 and 50.8 mJ/m^2. In fact the total surface energies determined for the AU-4 and AS-4 carbon fibers, listed in Table 2.16, do

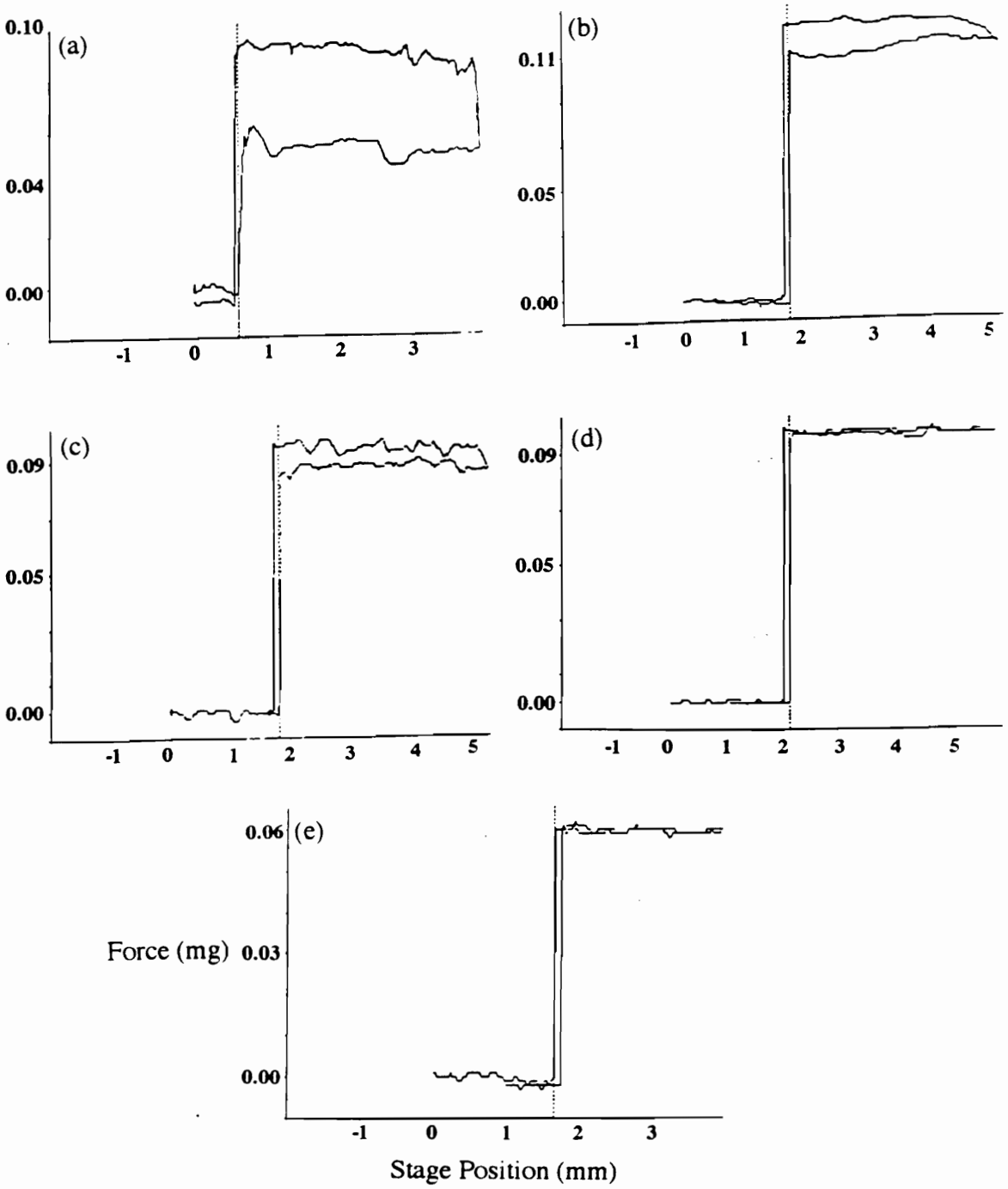

Figure 2.36. Wetting traces obtained with AU-4 carbon fibers and (a) deionized water, (b) formamide, (c) diiodomethane, (d) bromonaphthalene, and (e) hexadecane.

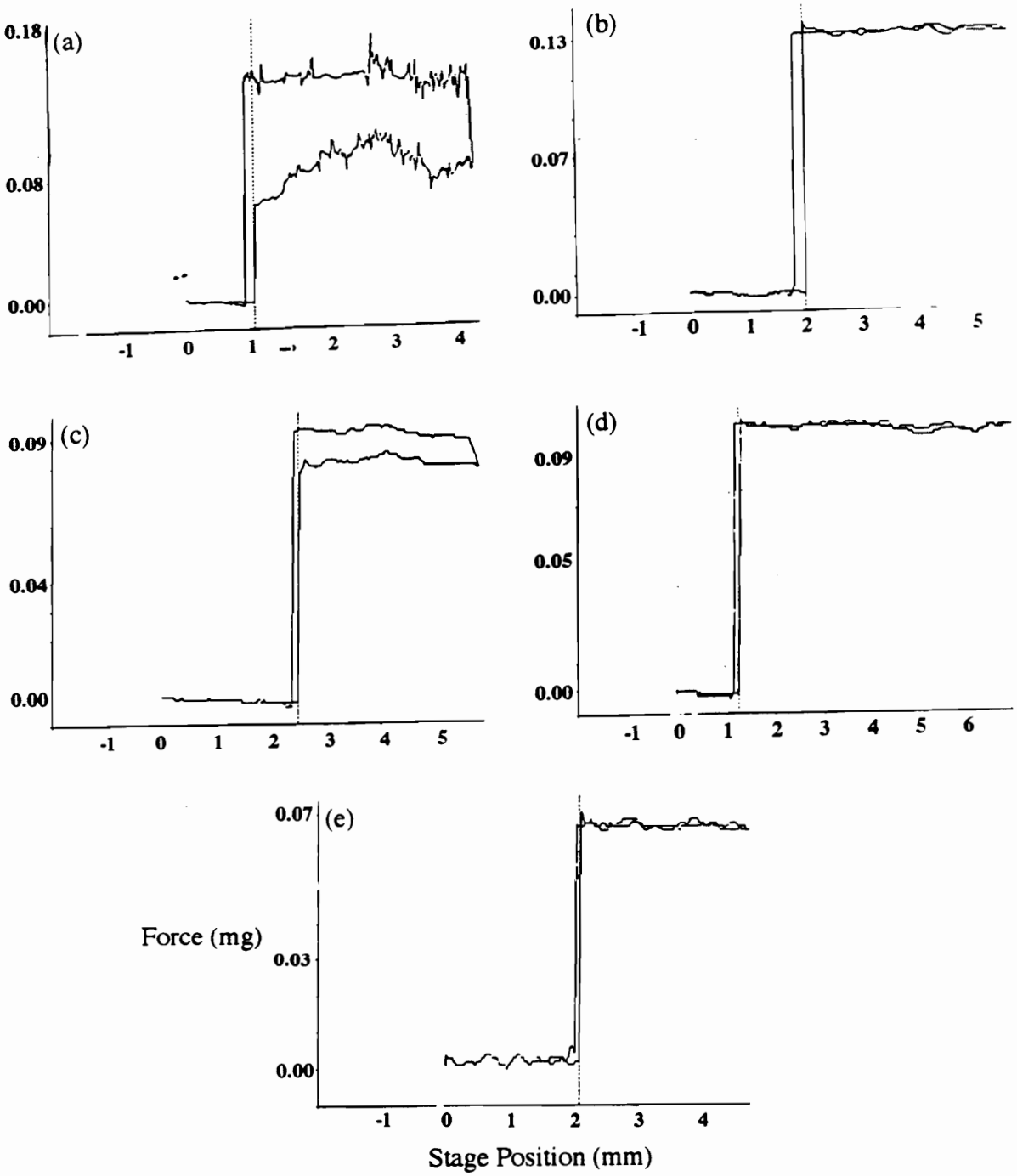

Figure 2.37. Wetting traces obtained with AS-4 carbon fibers and (a) deionized water, (b) formamide, (c) diiodomethane, (d) bromonaphthalene, and (e) hexadecane.

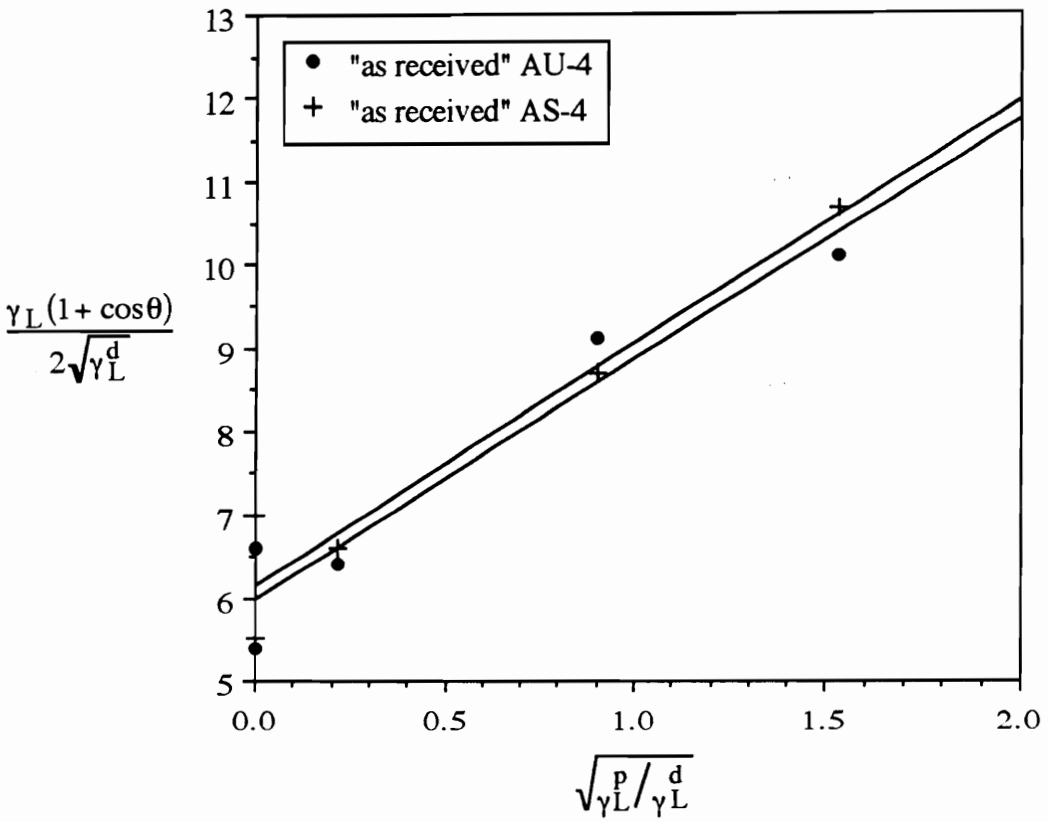

Figure 2.38. One-liquid wetting analysis plots for "as received" AU-4 and AS-4 carbon fibers.

Table 2.16. Surface energy results for "as received" AU-4 and AS-4 carbon fibers.

FIBER	CARBON FIBER SURFACE ENERGY (mJ/m^2)						
	one-liquid technique			two-liquid technique			
	γ_S	γ_S^d	γ_S^p	γ_S	γ_S^d	γ_S^p	I_{SF}^p
AU-4	44 ± 3	36 ± 1	8 ± 2	38 ± 3	27 ± 3	11 ± 2	38 ± 2
AS-4	47 ± 2	38 ± 1	9 ± 2	51 ± 7	36 ± 6	15 ± 3	44 ± 3

Table 2.17. Literature surface energy values for AU-4 and AS-4 carbon fibers, determined using the one-liquid technique.

FIBER	CARBON FIBER SURFACE ENERGY (mJ/m^2)			Reference
	γ_S	γ_S^d	γ_S^p	
AU-4	46	28	18	[51]
AU-4	54.3 ± 2.5	27.9 ± 2.9	26.4 ± 4.7	[234]
AU-4	51.0 ± 2.6	27.4 ± 0.3	23.6 ± 2.6	[233]
AS-4	51	29	22	[51]
AS-4	56.6 ± 3.5	26.7 ± 3.0	29.9 ± 5.8	[234]
AS-4	56.4 ± 1.7	26.4 ± 0.1	30.0 ± 1.7	[233]

fall within this range. The total surface energies obtained for the AU-4 and AS-4 carbon fibers were 44 ± 3 and 47 ± 2 mJ/m^2, respectively.

When the liquid did not completely wet the fiber surface ($\theta > 0°$), the advancing wetting force value fell below the linear curve in Figure 2.39 and the measured advancing contact angle was greater than the receding angle. This phenomenon, known as contact angle hysteresis, was seen with water, formamide, and diiodomethane with both the AU-4 and AS-4 carbon fibers (see Figures 2.36 (a, b, c) and 2.37 (a, b, c)). In general, contact angle hysteresis is attributed to the presence of chemical or physical heterogeneities on the solid surface. These heterogeneities "anchor" the wetting liquid at the solid/liquid/vapor triple line when the liquid recedes from the solid surface causing the receding angle to be lower than the advancing contact angle [255].

2.3.1.3.2 Two-Liquid Technique

Examples of the wetting traces obtained when the AU-4 and AS-4 carbon fibers were immersed in a beaker containing two immiscible liquids (formamide and a hydrocarbon) are shown in Figure 2.40 and 2.41. The force, initially equal to zero, rose to a plateau as the fiber end penetrated the hydrocarbon. The force increased a second time when the fiber end passed through the hydrocarbon-formamide interface. Hysteresis was seen in all the wetting traces in Figures 2.40 and 2.41 in the formamide layer, showing that the total surface energies of the AU-4 and AS-4 carbon fibers were less than that of formamide, 58.3 mJ/m^2.

The surface energies of the AU-4 and AS-4 carbon fibers were obtained by plotting the wetting analysis results in the form of equation 2.59. These linear regression plots are shown in Figure 2.42. The slope of the line is equal to $2\sqrt{\gamma_S^d}$ and the intercept is equal to the non-dispersion term I_{SF}^p. The polar component to the total surface energy was calculated from I_{SF}^p using equation 2.52. The total surface energies, listed in Table 2.16,

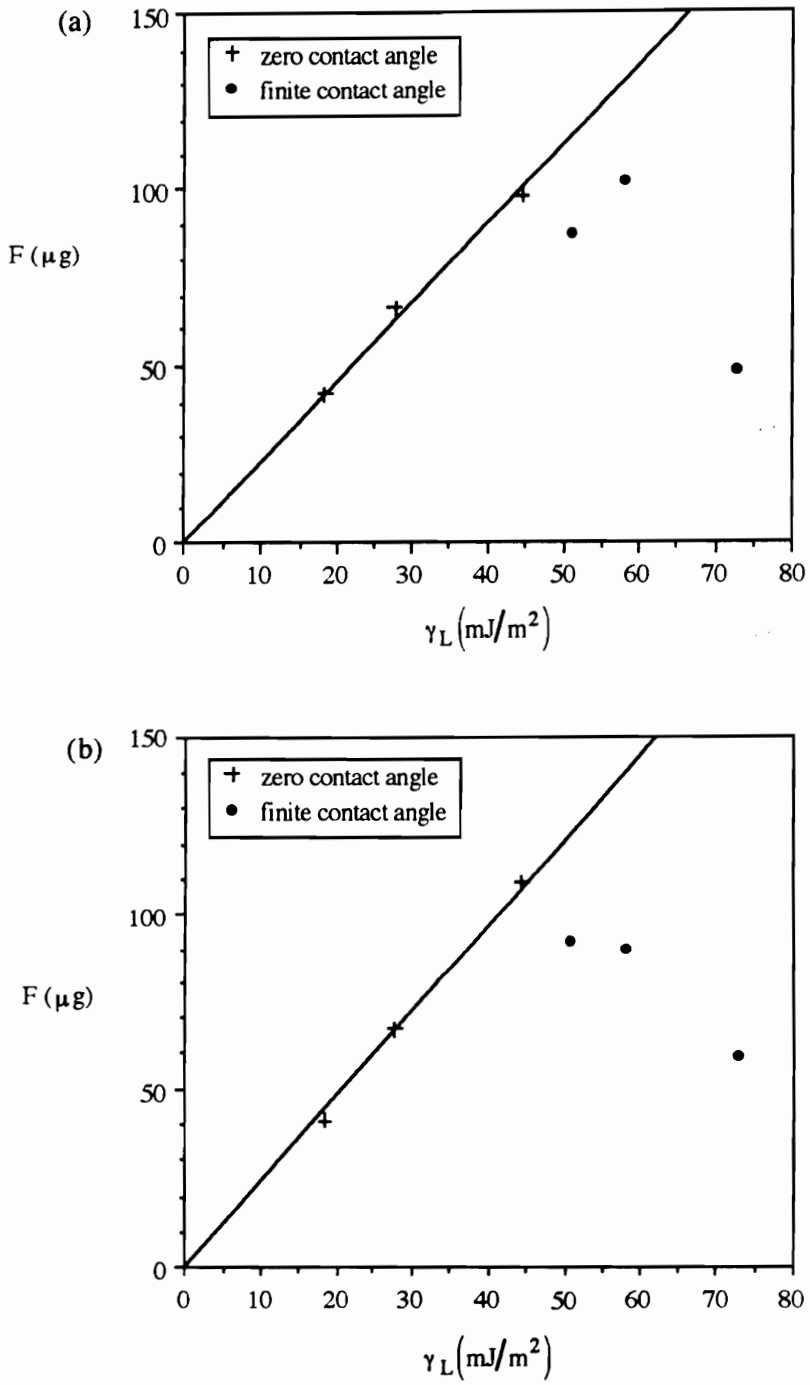

Figure 2.39. Plot of Wilhelmy wetting force versus the surface energy of the wetting liquid for (a) AU-4 and (b) AS-4 carbon fibers.

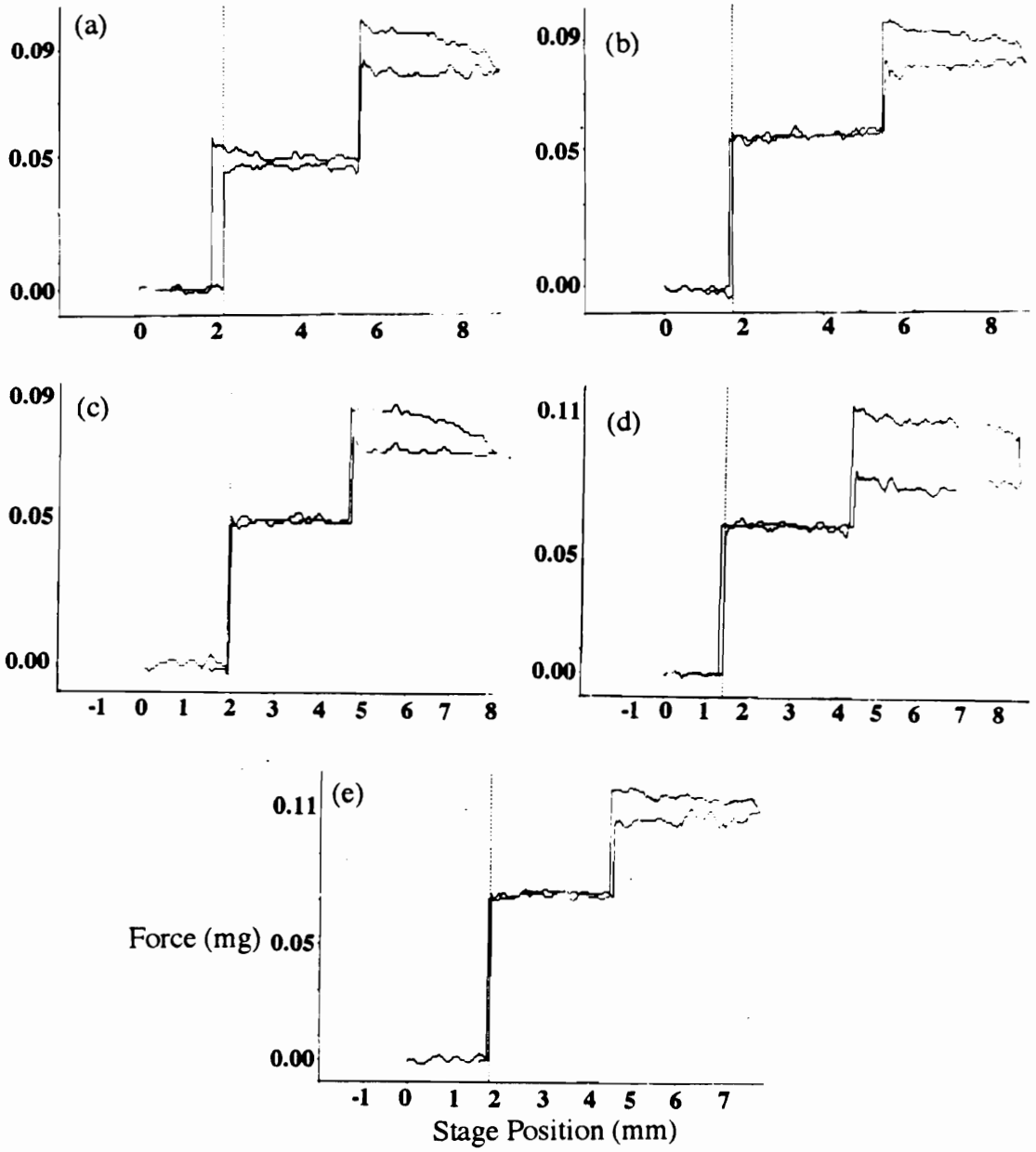

Figure 2.40. Wetting traces obtained with AU-4 carbon fibers using formamide and (a) hexane, (b) decane, (c) octane, (d) hexadecane, and (e) decahydronaphthalene.

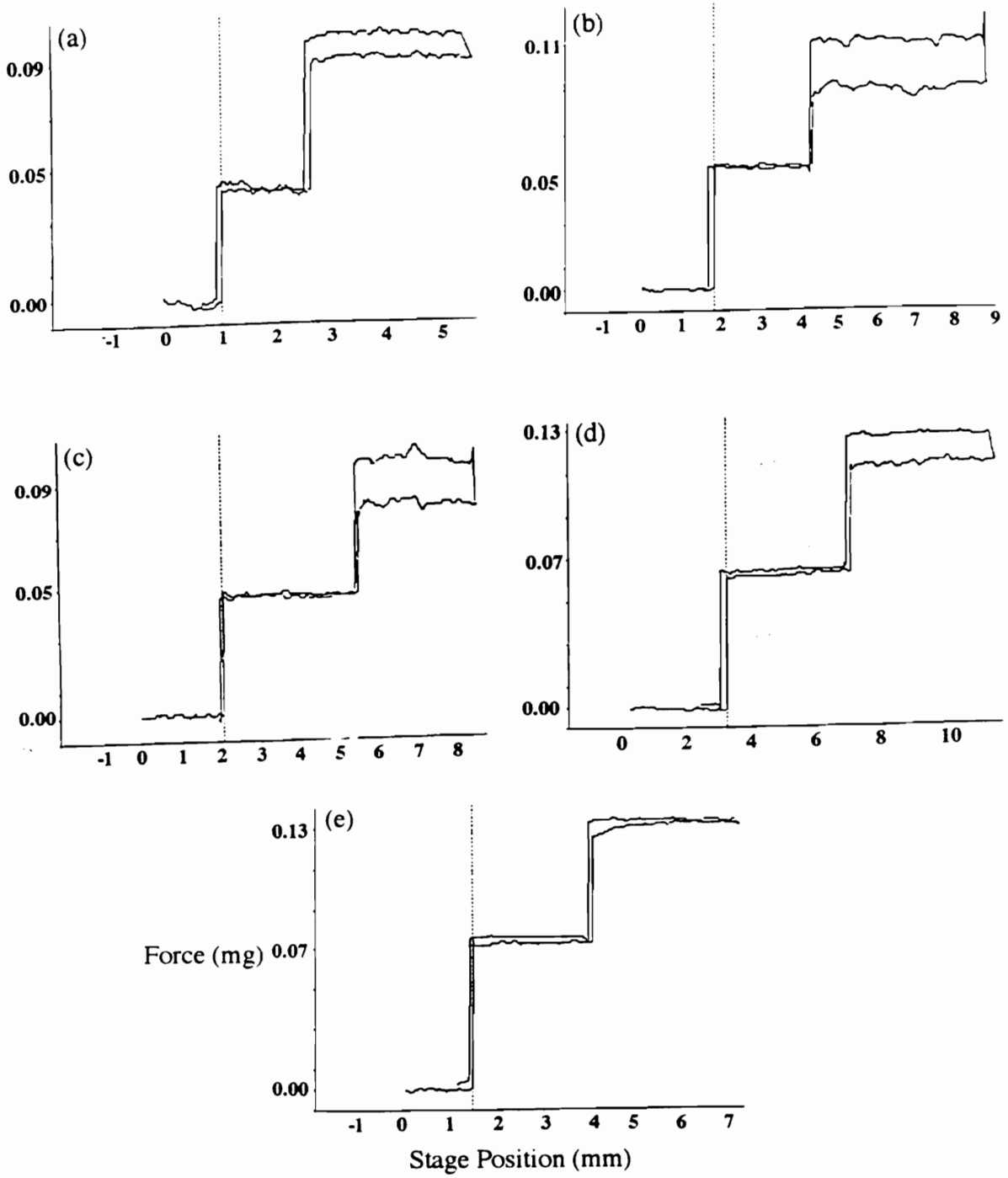

Figure 2.41. Wetting traces obtained with AS-4 carbon fibers using formamide and (a) hexane, (b) decane, (c) octane, (d) hexadecane, and (e) decahydronaphthalene.

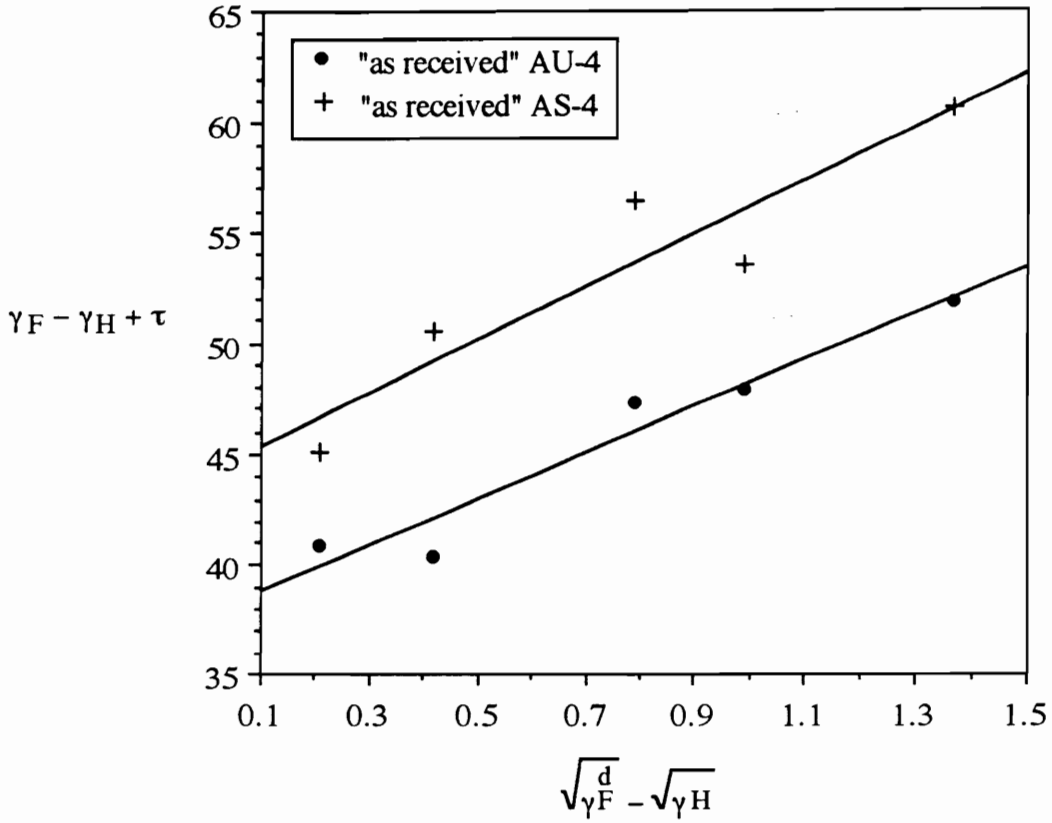

Figure 2.42. Two-liquid wetting analysis plots for AU-4 and AS-4 carbon fibers.

were calculated by summing the polar and dispersive components. The total surface energies of the AU-4 and AS-4 carbon fibers obtained using the one-liquid and the two-liquid techniques, were within experimental error. However, the dispersive and polar surface energies determined using the two different techniques did not correlate as well.

2.3.1.4 Tensile Strength

The tensile strengths of 10 mm long AU-4 and AS-4 carbon fibers are plotted in Figure 2.43. The error bars represent one standard deviation calculated using the Weibull distribution. There was no significant difference between the tensile strength of the "as received" AS-4 and AU-4 fibers. The tensile strength values are within experimental error of the manufacturer's specification, listed in Table 2.5.

2.3.2 Effect of Air, Oxygen, Ammonia, and Ethylene Plasma Treatments on AS-4 Carbon Fibers

2.3.2.1 Surface Chemical Composition

Carbon, oxygen, nitrogen, and sodium were detected by XPS on the AS-4 carbon fibers exposed to either an air, oxygen, or ammonia plasma. When the AS-4 carbon fiber was exposed to an ethylene plasma, only carbon, oxygen, and nitrogen were detected on the fiber surface. Changes in the O/C, N/C, and Na/C ratios of the AS-4 carbon fiber surface as a function of air, ammonia, and ethylene plasma exposure time are shown in Figures 2.44, 2.45, and 2.46 respectively. All three plasmas significantly changed the concentration of functional groups on the AS-4 carbon fiber surface.

Air plasma exposure increased the O/C ratio of the fiber surface from 0.11 to 0.27 in only 15 seconds while, the ammonia plasma treatment decreased the O/C ratio from 0.11 to 0.086 in approximately 1 minute. Additional treatment, for up to 5 minutes, in either the air, ammonia, or ethylene plasma did not bring about any further change in the O/C ratio. The N/C ratio of the AS-4 carbon fiber increased from 0.031 to 0.050

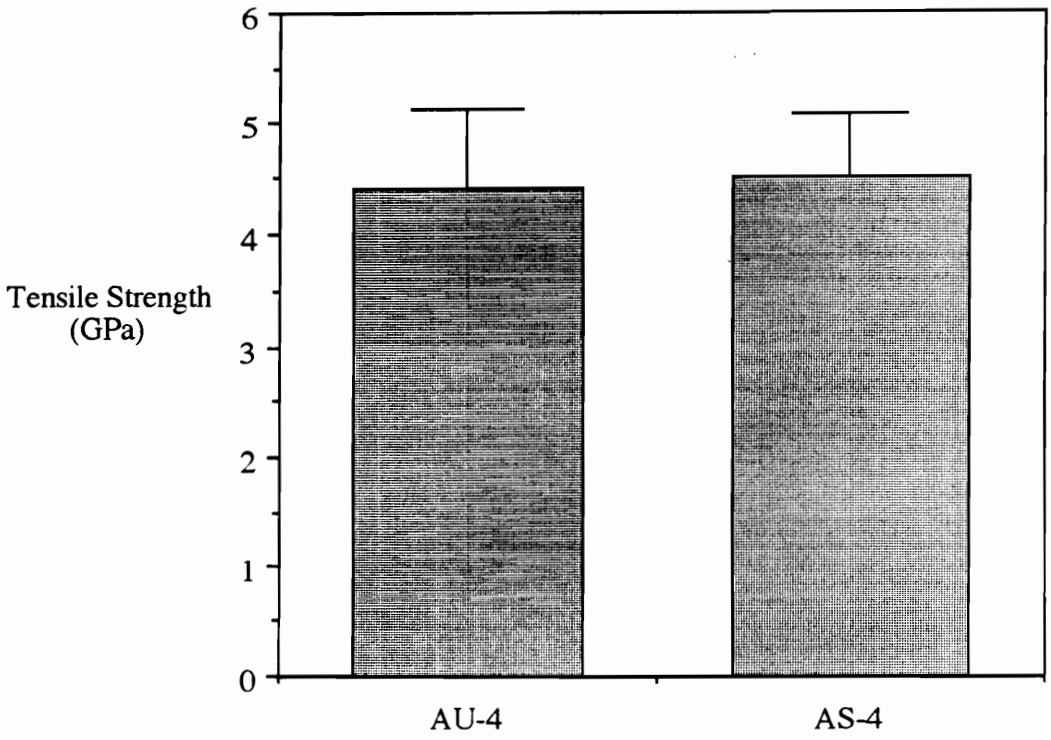

Figure 2.43. Tensile strength of AU-4 and AS-4 carbon fibers.

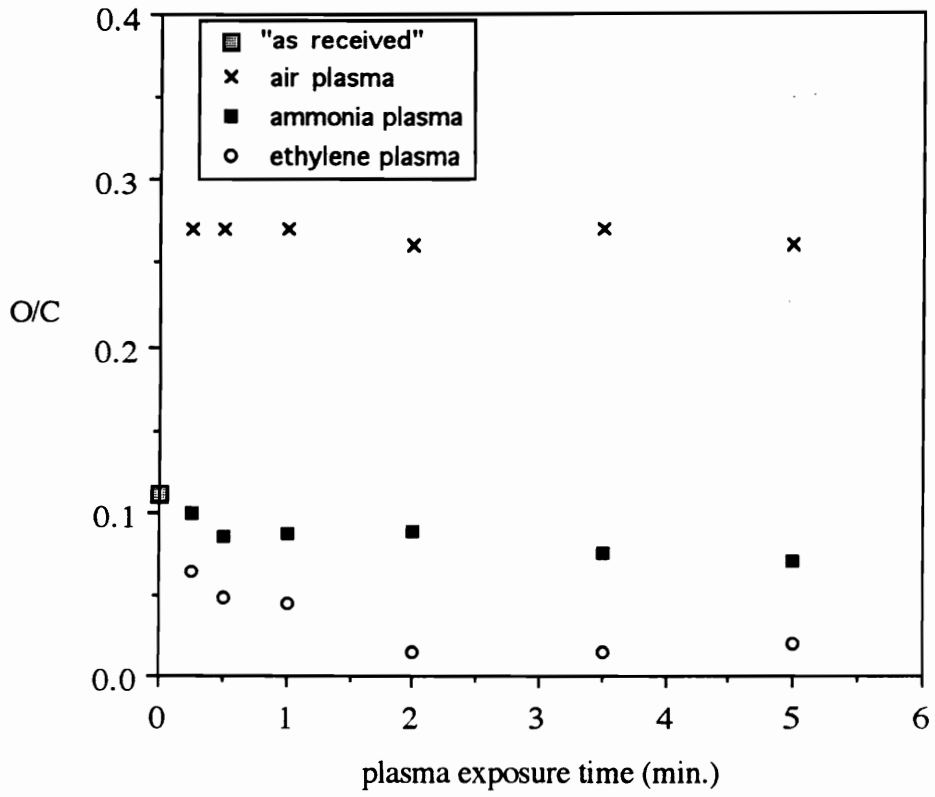

Figure 2.44. AS-4 carbon fiber O/C ratio as a function of plasma exposure time.

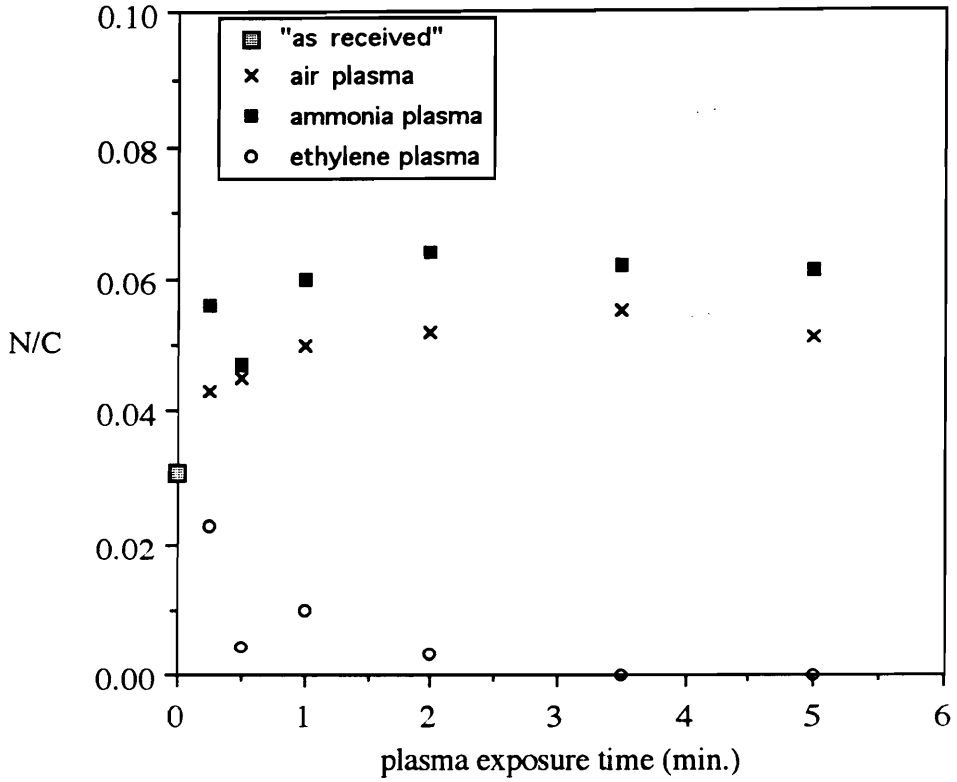

Figure 2.45. AS-4 carbon fiber N/C ratio as a function of plasma exposure time.

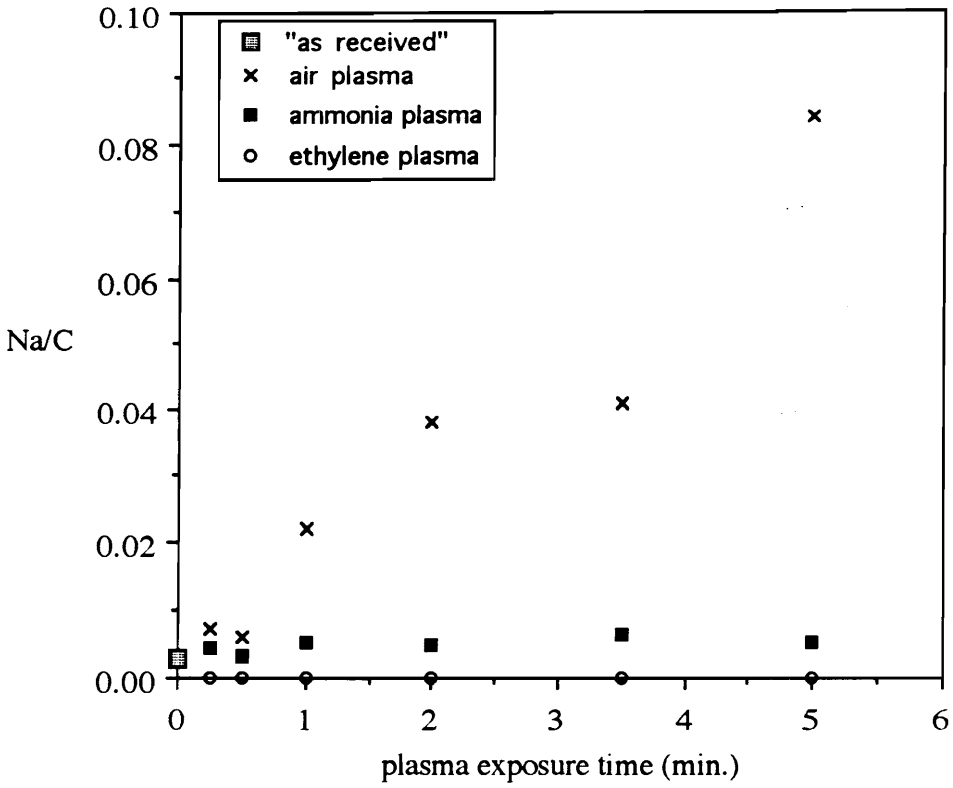

Figure 2.46. AS-4 carbon fiber Na/C ratio as a function of plasma exposure time.

following a 1 minute air plasma treatment and, from 0.031 to 0.060 with a 1 minute ammonia plasma treatment. As with the O/C ratio, additional air or ammonia plasma exposure did not bring about any further change in the N/C ratio.

The N/C and the O/C ratios of the air and ammonia plasma treated carbon fiber surfaces became independent of plasma treatment time once the active sites on the fiber surface were saturated or a steady state condition was established in which the rate of incorporation of functional groups was equivalent to the rate of removal of the functional groups by further oxidation. Jones and Sammann also reported that prolonged exposure of carbon fibers to an air plasma (from 30 seconds to 30 minutes) did not change the fiber surface oxygen concentration [177].

In the ethylene plasma, the O/C ratio decreased from 0.11 to 0.014 in about two minutes and the N/C ratio decreased from 0.031 to 0.000 in approximately 3.5 minutes. The nitrogen signal from the carbon fiber surface was no longer detected when a continuous layer of plasma polymer thicker than the XPS sampling depth was deposited on the carbon fiber surface. To confirm that the nitrogen detected in the ethylene plasma treated carbon fiber surface originated from the fiber surface, glass slips were exposed to the ethylene plasma. When the ethylene plasma treated glass slips were analyzed using XPS, no nitrogen was detected. In addition, after a 2 minute ethylene plasma treatment, no silicon was detected, showing that a continuous layer of plasma polymer was formed.

The air plasma treatment increased the Na/C ratio from 0.0026 to 0.0074 in 15 seconds and continued to increase with exposure time. The Na/C ratio reached 0.084 following a 5 minute air plasma treatment. Sodium is a residual impurity from the sodium alkyl sulfonate used in the PAN precursor spinning process. The air plasma ablated the carbon fiber surface as the organic portion of the carbon fiber surface was oxidized into volatile species. However, the sodium in the carbon fiber surface was not

removed as a volatile species. Therefore, as the organic portion of the fiber surface was etched away, the surface became enriched with sodium. This phenomenon has been observed when silicon- and phosphorus-containing polymers are treated in oxygen-containing plasmas [256-259], but has not been reported with the sodium present in carbon fibers.

The ammonia plasma increased the Na/C ratio of the AS-4 carbon fibers from 0.0026 to 0.0053 in 1 minute, after which the Na/C ratio remained relatively constant. The fact that the carbon fiber Na/C ratio did not increase as significantly in the ammonia plasma as in the air plasma treatment, demonstrated that the ammonia plasma was not nearly as ablative as the air plasma treatment. There was no sodium detected on the ethylene plasma treated AS-4 carbon fiber. The concentration of sodium on the "as received" AS-4 carbon fiber surface was so low, that even when a layer of ethylene plasma polymer thinner than the XPS sampling depth was deposited on the fiber surface the atomic% of sodium was below XPS detectable limits .

The goal of the plasma exposure time experiments was to choose appropriate plasma treatment times for the carbon fibers used in the fiber/matrix adhesion tests. Plasma treatment can ablate and roughen the carbon fiber surface. In order to determine if changes in the fiber/matrix adhesion are the result of changes in the fiber surface chemistry rather than the fiber topography, plasma treatment time must be minimized. Therefore, a 15 sec. air plasma, a 1 min. ammonia plasma, and a 3.5 min. ethylene plasma treatment were chosen. These were the shortest plasma treatment times at which the maximum changes in the fiber surface chemistry occurred. A 15 sec. oxygen plasma treatment was also attempted. While the changes in the fiber surface chemistry following the 15 sec. oxygen plasma were similar to that of the 15 sec. air plasma, the oxygen plasma treated surface was much rougher than the air plasma treated surface. Therefore, an air plasma was used instead of an oxygen plasma.

The atomic composition of the "as received", 15 sec. air plasma, 15 sec. oxygen plasma, 1 minute ammonia plasma, and 3.5 min. ethylene plasma treated AS-4 carbon fibers is listed in Table 2.18. The carbon 1s, oxygen 1s, and nitrogen 1s photopeaks of the plasma treated carbon fibers were curve-fit as described in section 2.3.1.1. The curve-fit carbon 1s, oxygen 1s, and nitrogen 1s photopeaks are shown in Figures 2.47, 2.48, and 2.49, respectively. The curve-fitting results are summarized in Tables 2.19, 2.20, and 2.21.

Based on the shape of the carbon 1s photopeak, it was evident that the air plasma increased the concentration of oxygen containing functional groups on the carbon fiber surface. The ammonia plasma increased the portion of the carbon 1s photopeak which originates from carbon to nitrogen bonding and decreased the portion of the peak attributed to oxygen-containing functional groups. The plasma polymer deposited on the carbon fiber in the ethylene plasma contained some oxygen-containing functional groups.

The air and ammonia plasmas did not significantly change the shape of the oxygen 1s photopeak. However, the absence of peak 3 in the oxygen 1s photopeak of the ammonia plasma treated fiber, suggests that there was less adsorbed H_2O and CO_2 present on the ammonia plasma treated fiber than on the "as received" and air plasma treated carbon fibers. The ethylene plasma decreased the amount of oxygen doubly bonded to carbon in the carbon fiber surface (peak 1). This decrease in oxygen doubly bonded to carbon following ethylene plasma treatment corresponds with the change in the shape of the carbon 1s photopeak.

The air plasma did not affect the shape of the nitogen 1s photopeak. However, the ammonia plasma increased the relative intensity of peak 2 fit to the nitrogen 1s photopeak. Peak 2 was fit at 399.1 eV and attributed to aromatic amine and imine (-C=NH) groups in the fiber surface. Nitrogen-containing functional groups are most likely created on the carbon fiber surface in free radical reactions with the $\bullet NH_2$ and $\bullet NH$

Table 2.18. Surface composition of "as received" and plasma treated AS-4 carbon fibers (XPS, 45° take-off angle).

FIBER	CONCENTRATION (<atomic %> ± σ_{n-1} for 3 samples)				ATOMIC RATIO		
	Carbon	Oxygen	Nitrogen	Sodium	O/C	N/C	Na/C
"as received" AS-4	87.8 ± 1.2	9.3 ± 1.0	2.7 ± 0.1	0.2 ± 0.1	0.11	0.031	0.003
15 sec. air plasma AS-4	76.3 ± 0.7	19.8 ± 0.8	3.3 ± 0.2	0.6 ± 0.3	0.28	0.043	0.007
15 sec. O_2 plasma AS-4	76.3 ± 0.3	20.4 ± 0.4	2.8 ± 0.1	0.5 ± 0.1	0.26	0.040	0.005
1 min. NH_3 plasma AS-4	86.8 ± 2.2	7.5 ± 1.4	5.2 ± 0.8	0.5 ± 0.1	0.086	.060	0.005
3.5 min. ethylene plasma AS-4	98.0 ± 0.7	2.0 ± 0.7	nsp*	nsp	0.020	nsp	nsp

*no significant peak

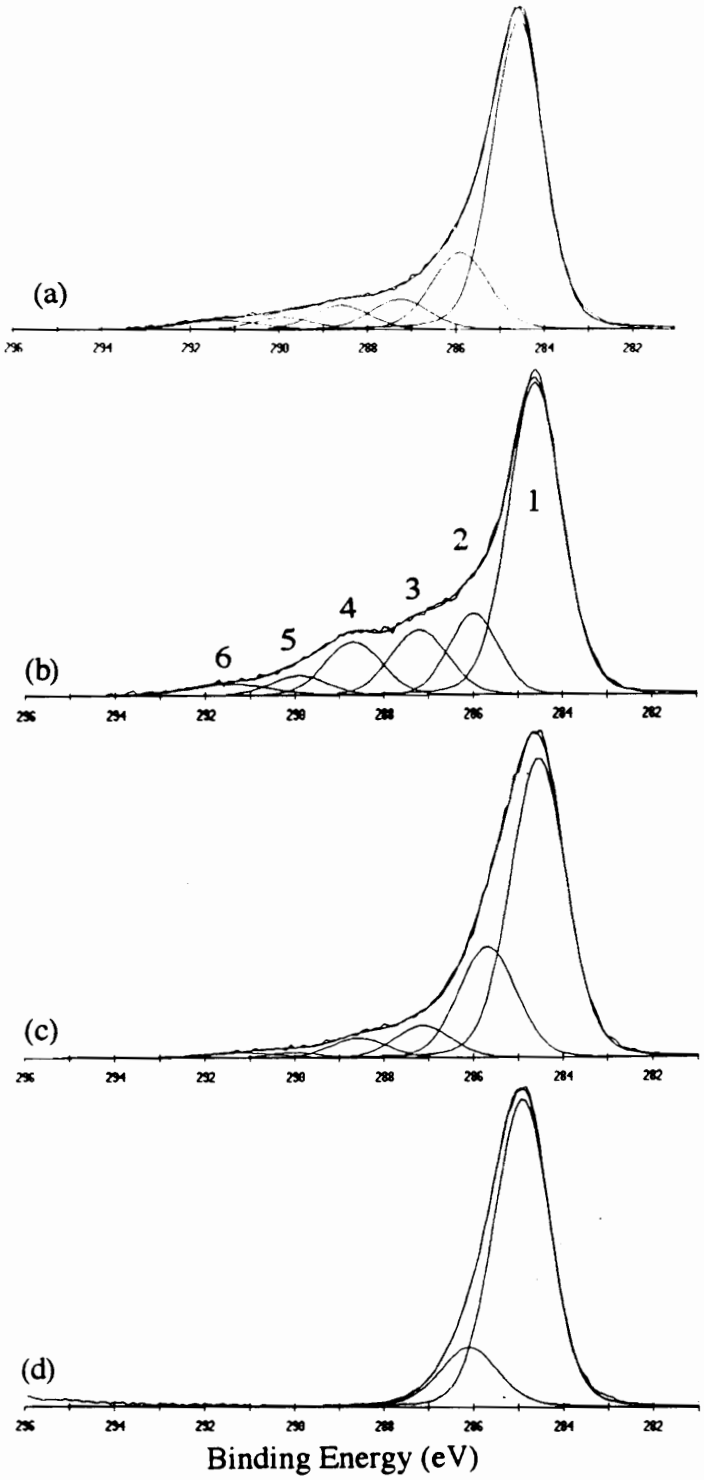

Figure 2.47. Curve-fit carbon 1s photopeak for (a) "as received," (b) 15 sec. air plasma, (c) 1 min. ammonia plasma, and (d) 3.5 min. ethylene plasma treated AS-4 carbon fibers.

Table 2.19. Carbon 1s curve-fitting results for "as received" and plasma treated AS-4 carbon fibers.

FIBER	<% of Total Carbon 1s Peak Area> ± σ_{n-1} for 3 samples					
	Binding Energy (eV)*					
	284.6	285.9	287.3	288.7	289.9	291.3
"as received" AS-4	65.5 ± 0.2	16.7 ± 0.8	6.8 ± 0.2	5.5 ± 0.3	2.7 ± 0.1	2.8 ± 0.3
15 sec. air plasma AS-4	55.4 ± 0.4	13.9 ± 1.5	11.9 ± 1.0	9.9 ± 1.0	5.1 ± 0.3	3.8 ± 0.2
1 min. NH3 plasma AS-4	61.4 ± 3.7	22.9 ± 2.0	7.3 ± 0.9	5.0 ± 0.9	1.6 ± 0.4	1.8 ± 0.3
3.5 min. ethylene plasma AS-4	(285.0 eV) 88.6 ± 4.3	(286.4 eV) 11.5 ± 4.3	nsp**	nsp	nsp	nsp
ORIGIN	C-H_X	C-OH C-O-C C-N C=N C ≡ N	C=O N-C=O	O=C-OH O=C-OR	O-CO-O O=C-O- O=C=O	plasmon loss
PEAK NO.	1	2	3	4	5	6

*Uncertainty in carbon 1s contributions is ± 0.2 eV.
**no significant peak

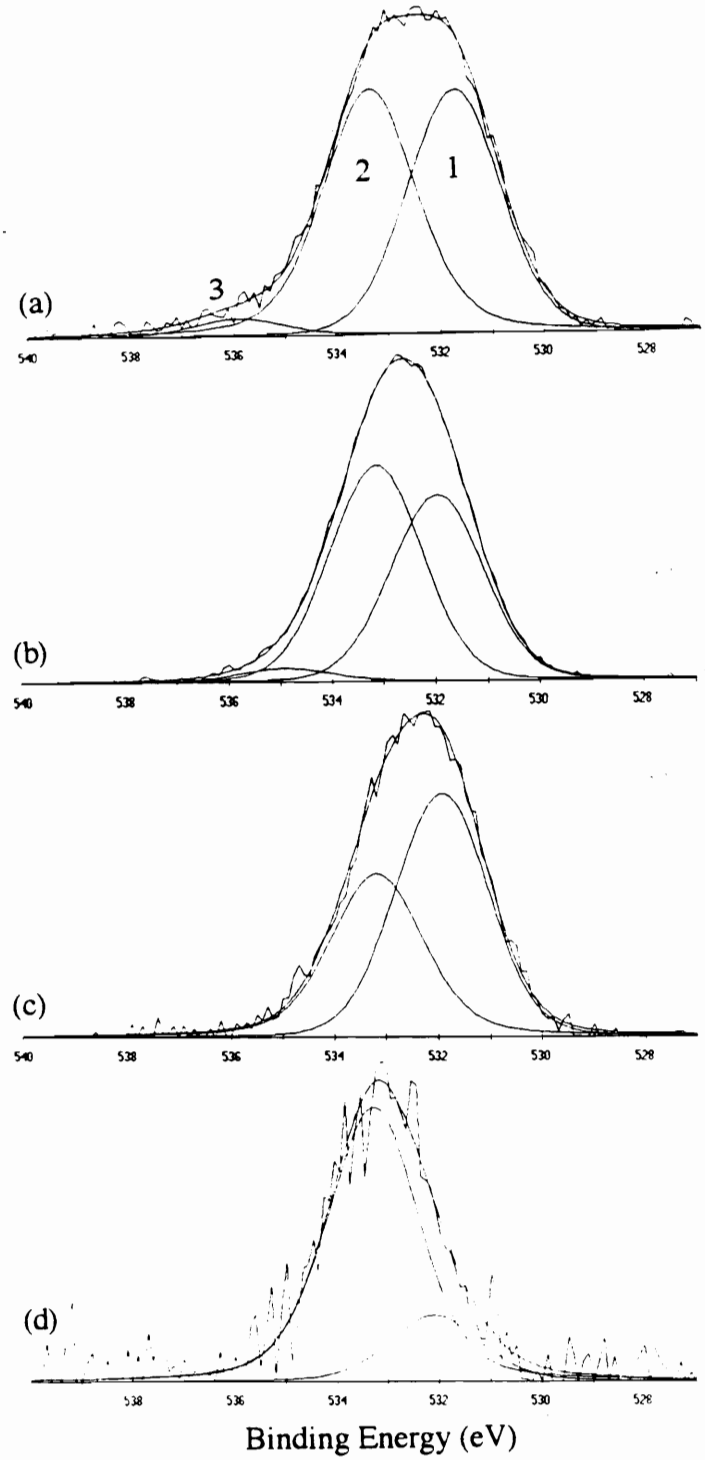

Figure 2.48. Curve-fit oxygen 1s photopeak for (a) "as received," (b) 15 sec. air plasma, (c) 1 min. ammonia plasma, and (d) 3.5 min. ethylene plasma treated AS-4 carbon fibers.

Table 2.20. Oxygen 1s curve-fitting results for "as received" and plasma treated AS-4 carbon fibers.

FIBER	<% of Total Oxygen 1s Peak Area> ± σ_{n-1} for 3 samples		
	Binding Energy (eV)*		
	532.0	533.5	536.2
"as received" AS-4	44.9 ± 1.5	51.9 ± 2.1	3.2 ± 0.7
15 sec. air plasma AS-4	38.6 ± 3.4	55.6 ± 1.7	4.8 ± 1.5
1 min. NH_3 plasma AS-4	56.2 ± 4.0	43.5 ± 4.3	0.3 ± 0.8
3.5 min. ethylene plasma AS-4	20.6 ± 3.7	79.4 ± 3.7	nsp**
ORIGIN	C=O C-O-C	C-OH	adsorbed H_2O and/or O_2
PEAK NO.	1	2	3

*Uncertainty in oxygen 1s contributions is ± 0.2 eV.
**no significant peak

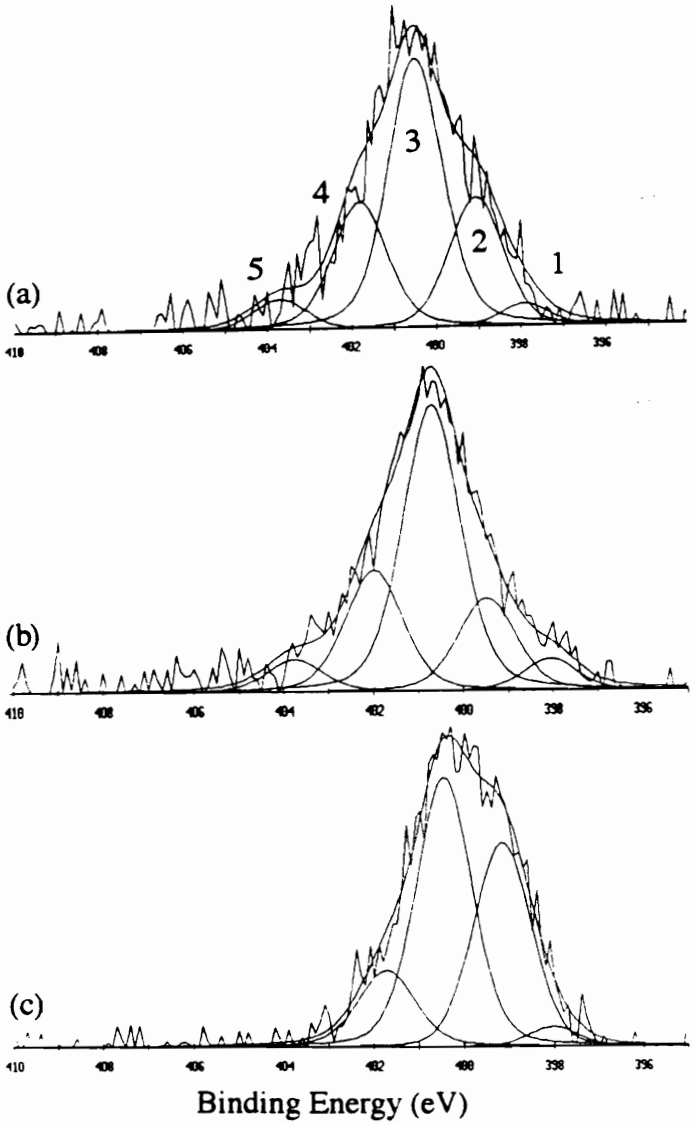

Figure 2.49. Curve-fit nitrogen 1s photopeaks for (a) "as received," (b) 15 sec. air plasma, and (c) 1 min. ammonia plasma treated AS-4 carbon fibers.

Table 2.21. Nitrogen 1s curve-fitting results for "as received" and plasma treated AS-4 carbon fibers.

FIBER	<% of Total Nitrogen 1s Peak Area> ± σ_{n-1} for 3 samples				
	Binding Energy (eV)*				
	397.8	399.1	400.8	401.9	403.8
"as received" AS-4	4.3 ± 1.4	21.6 ± 0.1	46.6 ± 1.9	21.0 ± 2.0	6.5 ± 2.6
15 sec. air plasma AS-4	4.3 ± 1.3	15.0 ± 1.9	53.4 ± 2.8	23.6 ± 3.0	3.8 ± 2.6
1 min. NH_3 plasma AS-4	2.6 ± 1.4	29.6 ± 3.7	51.8 ± 4.5	15.1 ± 2.1	1.0 ± 1.2
3.5 min. ethylene plasma AS-4	nsp**	nsp	nsp	nsp	nsp
ORIGIN	-C<u>N</u>	Ph-<u>N</u>H_2 -C=<u>N</u>H	aliphatic amine	<u>N</u>H_3^+ shake-up	shake-up
PEAK NO.	1	2	3	4	5

*Uncertainty on nitrogen 1s contributions is ± 0.2 eV.
**no significant peak

radicals produced in the ammonia plasma. Due to the reaction sequences and kinetics involved in the plasma decomposition of ammonia, the $\bullet NH_2$ radical is the most likely species available to react with the carbon fiber surface [98].

The plasma treated AS-4 carbon fibers were analyzed at take-off angles of 15° and 90° to determine the relative concentration of surface species on the outermost surface versus deeper within the bulk. The carbon 1s photopeaks of the air and ammonia plasma treated carbon fibers obtained at take-off angles of 15° and 90° are shown in Figure 2.50. Based on the shape of the carbon 1s photopeaks, it is evident that the oxygen functional groups created by the air plasma and the nitrogen functional groups introduced by the ammonia plasma are present in greater concentration on the very outermost surface (15°) of the carbon fibers than deeper within the bulk (90°). There was no significant difference in the shape of the 15° and 90° carbon 1s photopeaks for the "as received" (Figure 2.50(a)) and ethylene plasma treated AS-4 carbon fibers (not shown).

Bar charts showing the XPS O/C, N/C, and Na/C ratios of the plasma treated carbon fibers obtained at take-off angles of 15° and 90° are depicted in Figures 2.51, 2.52, and 2.53. The elemental compositions of the plasma treated fibers determined at take-off angles of 15°, 45°, and 90° are listed in Table 2.22. The O/C ratio was greater at 15° than 90° for the "as received," air plasma, and ammonia plasma treated AS-4 carbon fibers. There was no difference in the 15° and 90° O/C ratios for the ethylene plasma treated AS-4 carbon fibers. The N/C ratio was greater at 15° than at 90° for the ammonia plasma treated fiber, whereas, for the air plasma treated fiber the N/C ratio was slightly higher at 90°.

For the ammonia and air plasma treated fibers, the Na/C ratio was greater at 90° than at 15° showing that the sodium was greater in the bulk than on the outermost surface. Even though the fiber surface was enriched with sodium during the plasma treatments, the greatest concentration of sodium was not on the very outermost surface.

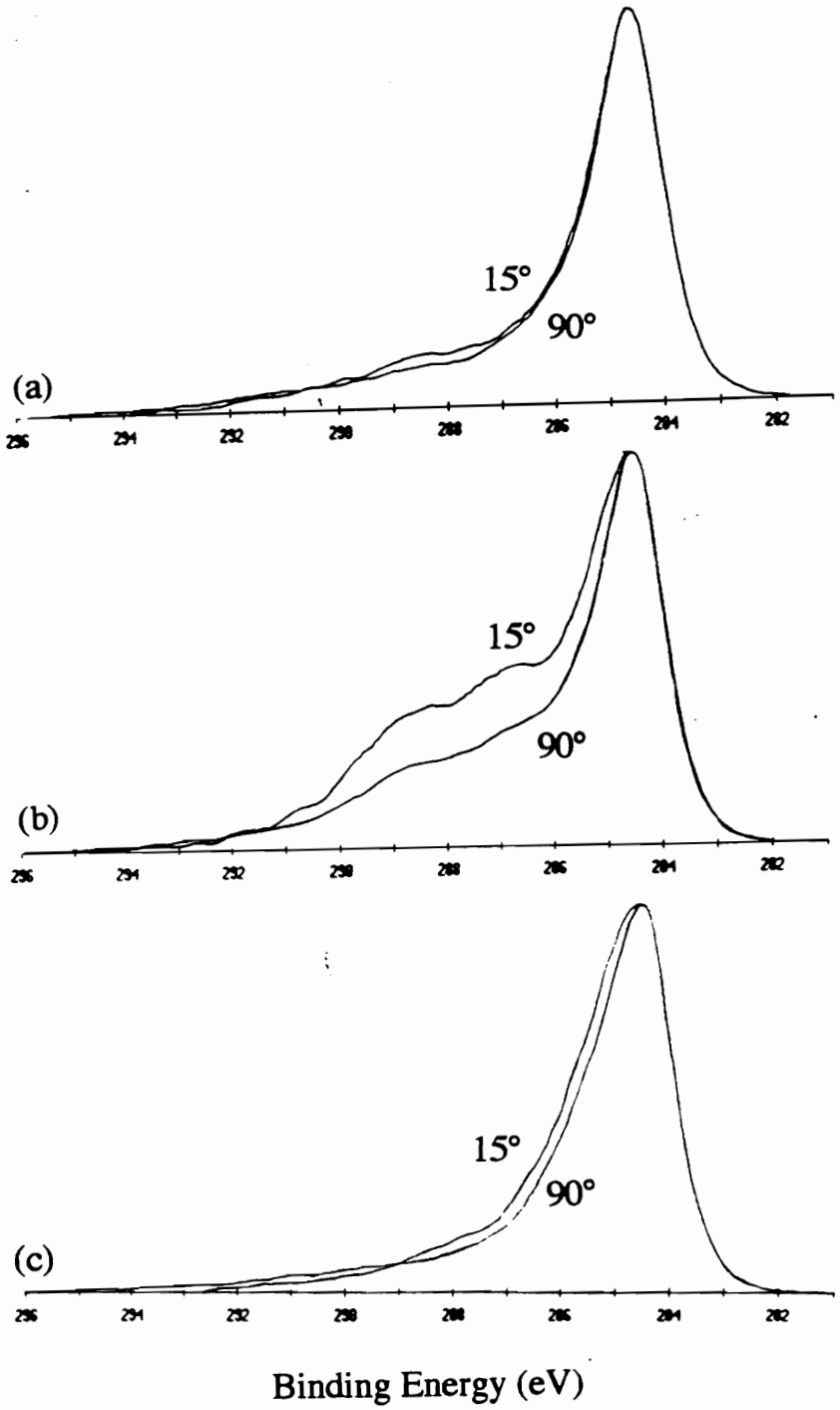

Figure 2.50. Carbon 1s photopeaks obtained at take-off angles of 15° and 90° for (a) "as received", (b) 15 sec. air plasma, and (c) 1 min. ammonia plasma treated AS-4 carbon fibers.

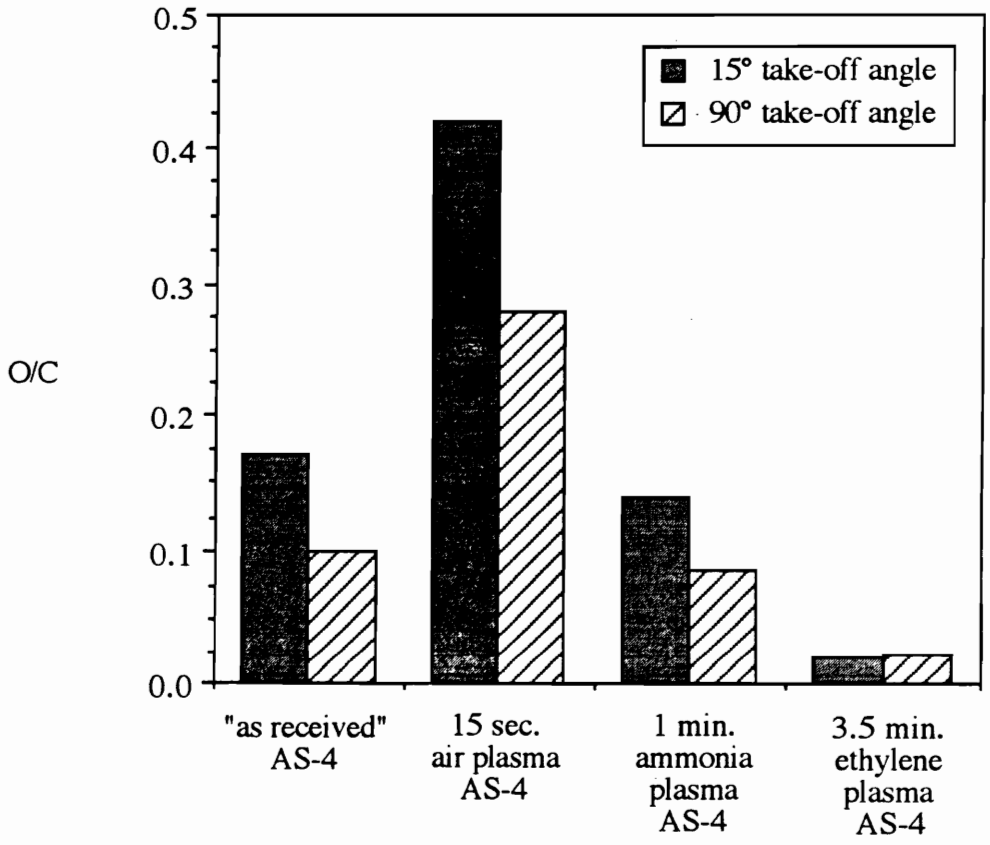

Figure 2.51. O/C ratio obtained at a take-off angle of 15° and 90° for "as received," 15 sec. air plasma, 1 min. ammonia plasma, and 3.5 min. ethylene plasma treated AS-4 carbon fibers.

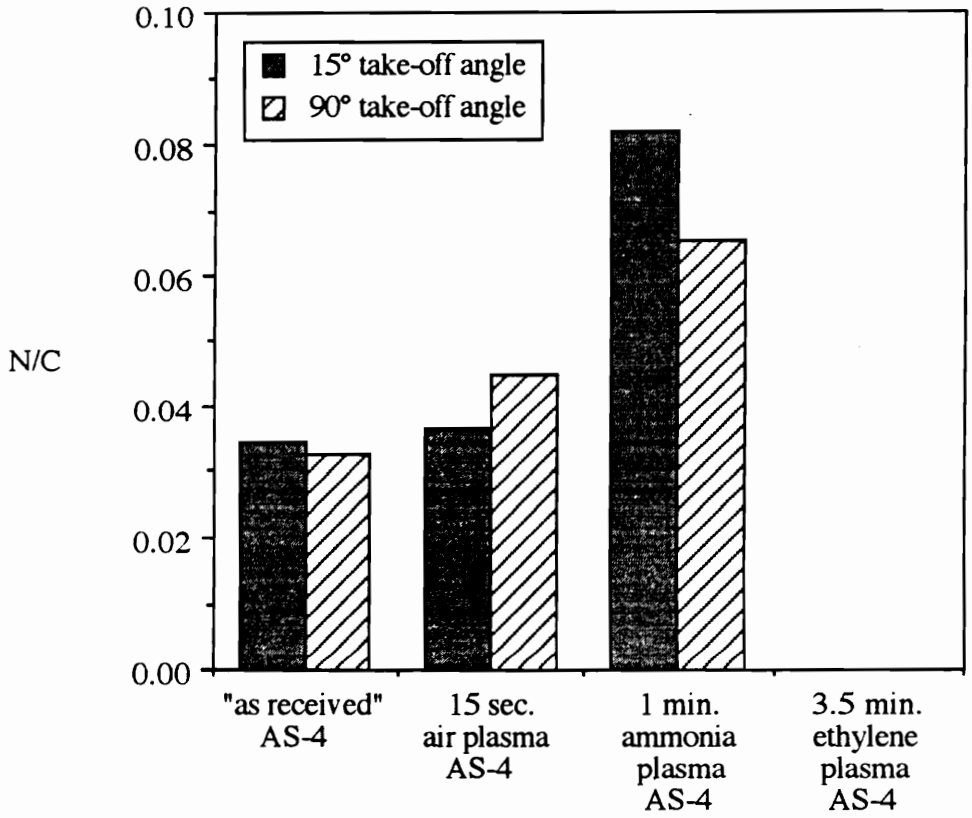

Figure 2.52. N/C ratio obtained at a take-off angle of 15° and 90° for "as received," 15 sec. air plasma, 1 min. ammonia plasma, and 3.5 min. ethylene plasma treated AS-4 carbon fibers.

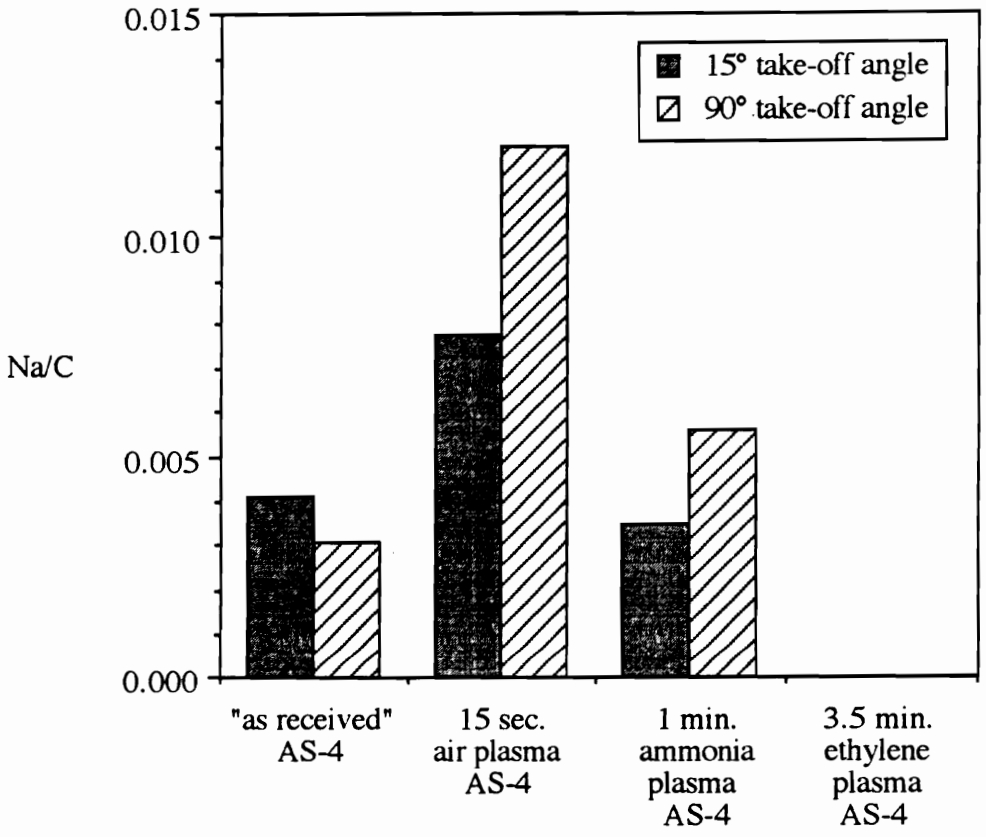

Figure 2.53. Na/C ratio obtained at a take-off angle of 15° and 90° for "as received," 15 sec. air plasma, 1 min. ammonia plasma, and 3.5 min. ethylene plasma treated AS-4 carbon fibers.

Table 2.22. Surface composition of "as received" AU-4 and AS-4 carbon fibers obtained at take-off angles of 15°, 45°, and 90° (XPS).

FIBER	TAKE-OFF ANGLE	CONCENTRATION (<atomic %> ± σ_{n-1} for 3 samples)			
		Carbon	Oxygen	Nitrogen	Sodium
"as received" AS-4	15°	82.9	13.9	2.9	0.3
	45°	87.8 ± 1.2	9.3 ± 1.0	2.7 ± 0.1	0.2 ± 0.1
	90°	88.0	8.8	2.9	0.3
15 sec. air plasma AS-4	15°	68.2	28.7	2.5	0.5
	45°	76.3 ± 0.7	19.8 ± 0.8	3.3 ± 0.2	0.6 ± 0.3
	90°	74.6	21.2	3.3	0.9
1 min. NH_3 plasma AS-4	15°	81.8	11.2	6.7	0.3
	45°	86.8 ± 2.2	7.5 ± 1.4	5.2 ± 0.8	0.5 ±0.1
	90°	86.5	7.4	5.6	0.5
3.5 min. ethylene plasma AS-4	15°	97.9	2.1	nsp*	nsp
	45°	98.0 ± 0.7	2.0 ± 0.7	nsp	nsp
	90°	97.7	2.3	nsp	nsp

*no significant peak

The concentration of sodium may be greater at 90° than at 15° due to post plasma reactions which occurred when the plasma treated sample was exposed to air. The oxygen incorporated in the surface as the result of post plasma reactions would be deposited on top of the plasma enriched sodium layer.

The 15 second air plasma treated AS-4 carbon fibers were stored in room air prior to XPS analysis from 1 hour to 24 days to test the stability of the plasma treated surface. The O/C, N/C, and Na/C ratios are plotted versus the room air exposure time in Figure 2.54. The O/C ratio varied insignificantly from 0.26 to 0.24 after a 24 day exposure to ambient conditions. In addition, there was no change in the shape of the XPS photopeaks. Therefore, there was no significant change in the surface composition of the air plasma treated carbon fibers following a 24 day exposure to ambient conditions.

2.3.2.2 Topography

Scanning electron photomicrographs of the "as received" , 15 sec. air plasma, 15 sec. oxygen plasma, and 1 min. ammonia plasma treated AS-4 carbon fibers at magnifications of 12,500X and 50,000X are shown in Figures 2.55 and 2.56, respectively. At 12,500X, the longitudinal ridges produced during extrusion of the PAN precursor fiber were clear on all four carbon fibers. At a magnification of 50,000X, it became evident that both the air and oxygen plasma treatments roughened the AS-4 carbon fiber surface. Even at the 50,000X magnification, there was no discernible difference between the topography of the "as received" AS-4 carbon fiber and ammonia plasma treated fiber. As shown in Figure 2.57, the roughness of the AS-4 carbon fiber surface increased with air plasma exposure time.

An increase in the carbon fiber surface roughness following oxygen plasma treatment was also observed using scanning electron microscopy by Yuan and coworkers [180] and Jang [98]. Yuan and coworkers saw a change in the carbon fiber topography

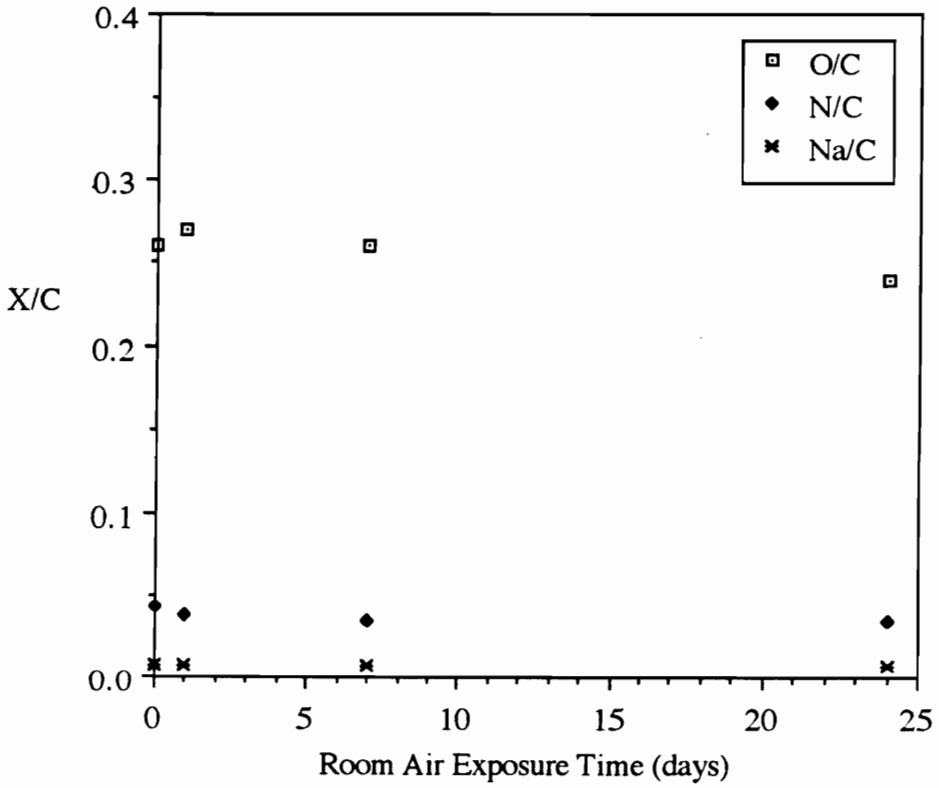

Figure 2.54. O/C, N/C, and Na/C ratios of 15 sec. air plasma treated AS-4 carbon fiber exposed to room air prior to XPS analysis.

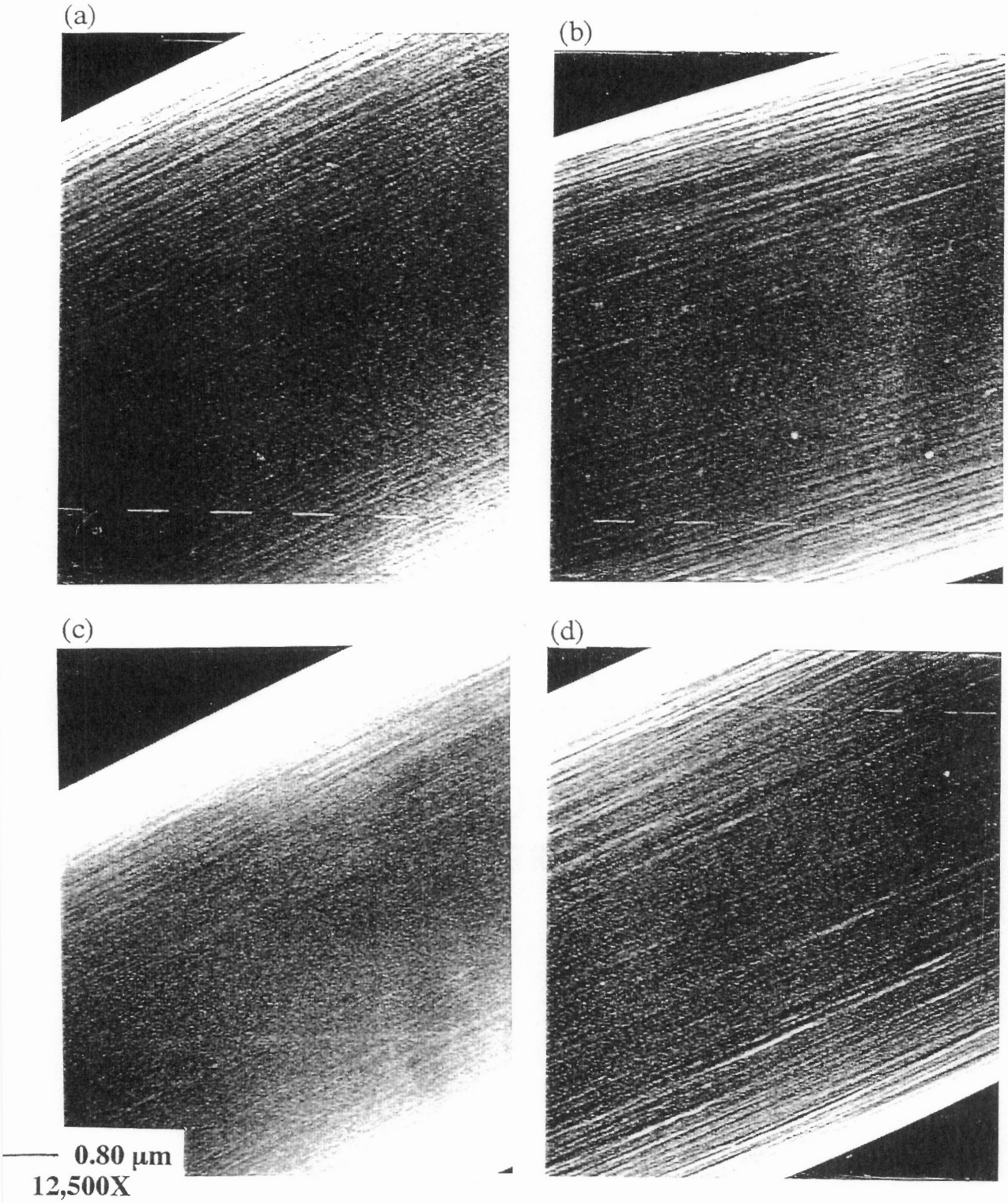

Figure 2.55. SEM photomicrographs of (a) "as received," (b) 15 sec. air plasma, (c) 15 sec. oxygen plasma, and (d) 1 min. ammonia plasma treated AS-4 carbon fibers at a magnification of 12,500X.

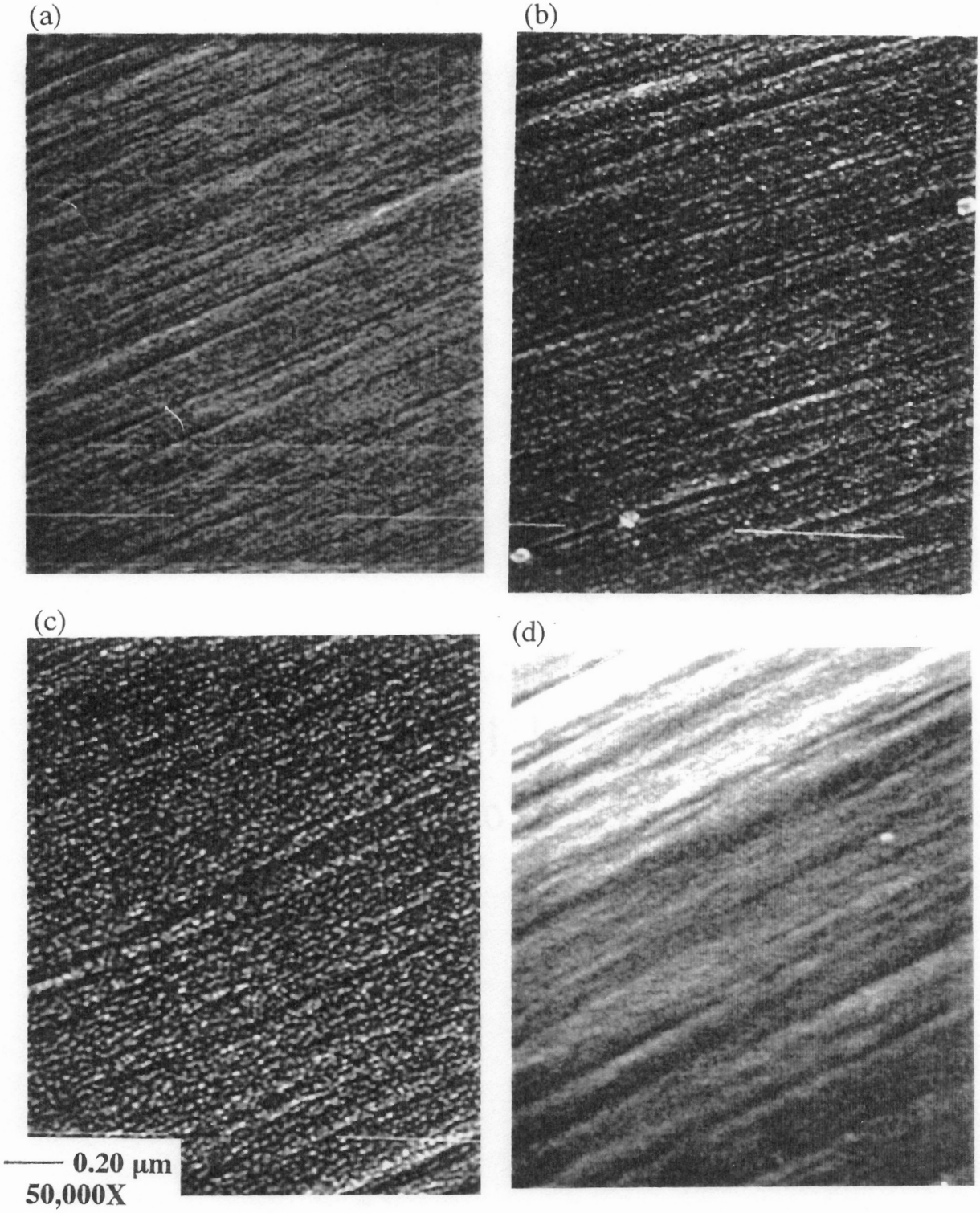

Figure 2.56. SEM photomicrographs of (a) "as received," (b) 15 sec. air plasma, (c) 15 sec. oxygen plasma, and (d) 1 min. ammonia plasma treated AS-4 carbon fibers at a magnification of 50,000X.

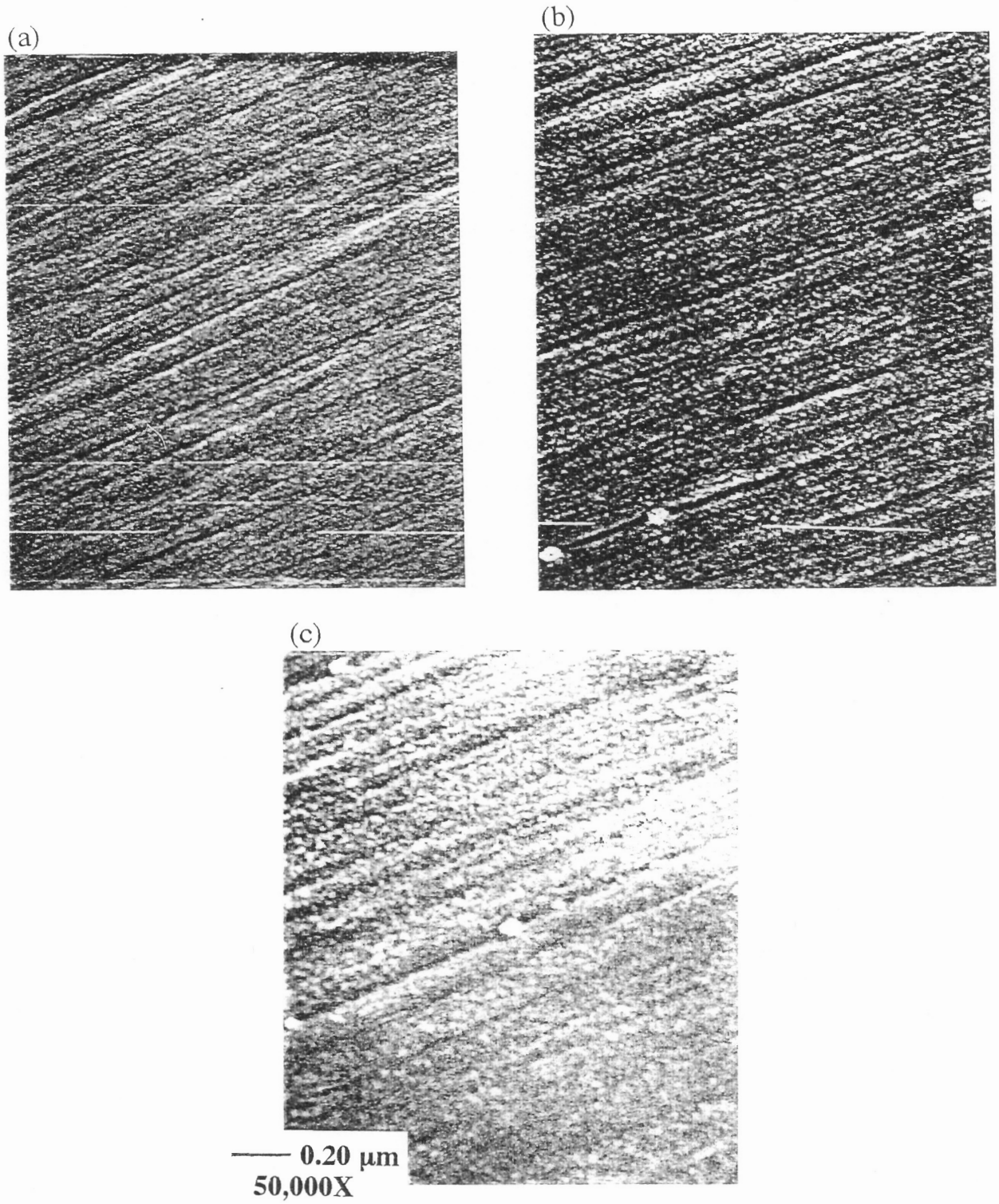

Figure 2.57. SEM photomicrographs of (a) "as received," (b) 15 sec. air plasma, and (c) 1 min. air plasma treated AS-4 carbon fibers at a magnification of 50,000X.

after a 1 minute oxygen plasma treatment at a 10,000X magnification [180]. Jang analyzed the carbon fibers at a 8,000X magnification and reported that the carbon fiber surface was roughened following a 3 minute oxygen plasma treatment. In this study, the increase in surface roughness was seen after only a 15 second plasma treatment at a 50,000X magnification. Pattabiraman and coworkers exposed PAN-based carbon fibers and carbon fiber-reinforced epoxy matrix composites to atomic oxygen, a component of oxygen and air plasmas. They concluded that atomic oxygen is very reactive to the delocalized π electrons in graphitic carbon [224].

Recently, the scanning tunneling microscope has been used to resolve the carbon fiber surface structures with atomic resolution [136, 260, 261]. Two views of the sharp, jagged, stepped surfaces of PAN-based carbon fibers obtained by Hoffman et al. are shown in Figure 2.58 [136]. As shown in Figure 2.59, Hoffman et al. also used the scanning tunneling microscope to observe the change in the surface of a pitch-based carbon fiber after an oxygen plasma treatment [262].

When the carbon fibers were exposed to an ammonia plasma, the surface was not roughened (at a magnification of 50,000X) and there was only a small, initial increase in the surface sodium concentration. This suggests that the carbon fiber surface was not significantly ablated by the ammonia plasma. The ammonia plasma cleaned the fiber surface and reacted with the fiber only at edge sites. This corresponds with the work of Jones and Sammann [177] who reported that the basal planes of graphite are inert to the components of an ammonia plasma, but can easily be oxidised by oxygen-containing plasmas [186]. Jones and Sammann [177] and Jang [98] also reported, as found in this work, that ammonia plasma treatment does not roughen the surface of PAN-based carbon fibers.

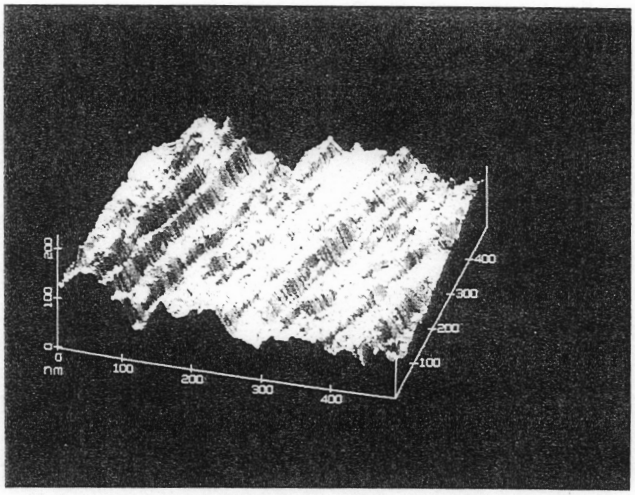

(a)

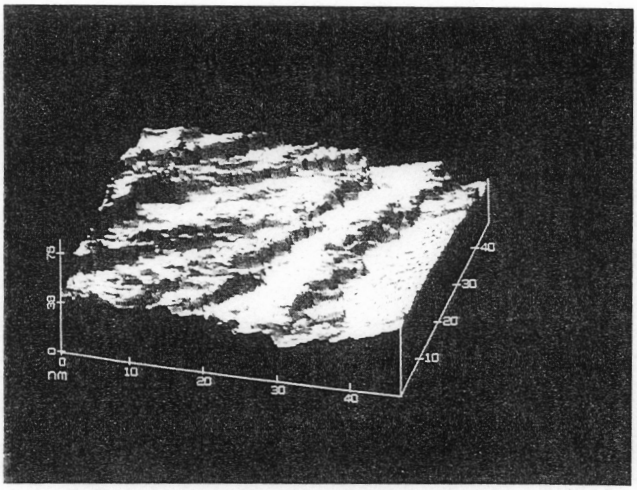

(b)

Figure 2.58. STM photomicrographs of the T-650/42 PAN-based carbon fiber at a scale of (a) 500 nm x 500 nm and (b) 50 nm x 50 nm [136].

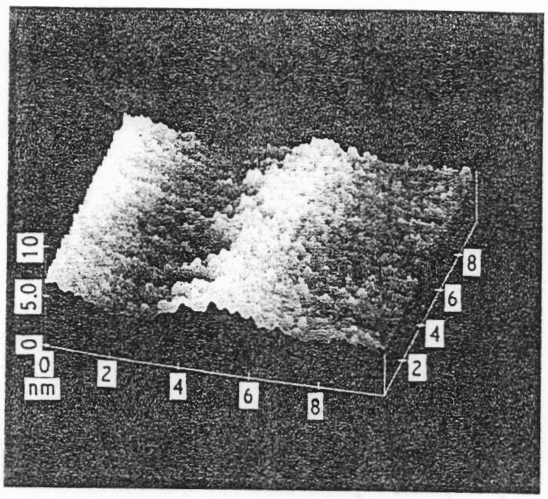

Figure 2.59. STM photomicrograph of the P-55 pitch-based carbon fiber surface treated in an oxygen plasma to a 0.66% weight loss exhibiting microroughness (9 nm x 9 nm) [262].

In the scanning electron photomicrographs of the 3.5 minute ethylene plasma treated AS-4 carbon fiber, shown in Figure 2.60, the plasma polymer film deposited on the fibers did not appear uniform or continuous. The nonuniform appearance of plasma polymer films was also reported by Havens and coworkers [263]. They showed that the films deposited in ethylene and styrene plasmas are composed of polymer spheres embedded in a polymer binder and, that the spheres have a higher density than the binder.

There was also evidence that, contrary to the SEM results, the polymer film deposited on the ethylene plasma treated carbon fibers was continuous. When carbon fibers or glass slips were exposed to the ethylene plasma for 3.5 minutes and analyzed using XPS, no nitrogen from the underlying carbon fiber surface or silicon from the glass surface were detected. In addition, when the ethylene plasma treated glass slips were placed in water, a coherent polymer film slid off the glass. Therefore, it was concluded that the carbon fiber surface was completely covered with an ethylene plasma polymer film but, that the film was possibly damaged when sputter-coated with gold.

In support of this conclusion, when an "as received" AS-4 carbon fiber was sputter-coated at the same time as the ethylene plasma treated fiber, some of the plasma polymer was removed from the ethylene plasma treated fiber and redeposited on the "as received" AS-4 carbon fiber. Figure 2.61 shows a scanning electron photomicrograph of an "as received" AS-4 carbon fiber sputter-coated alone and sputter-coated beside an ethylene plasma treated AS-4 carbon fiber. The surface of the "as received" AS-4 carbon fiber surface sputter-coated beside the ethylene plasma treated AS-4 carbon appears to be covered with particles of the ethylene plasma polymer.

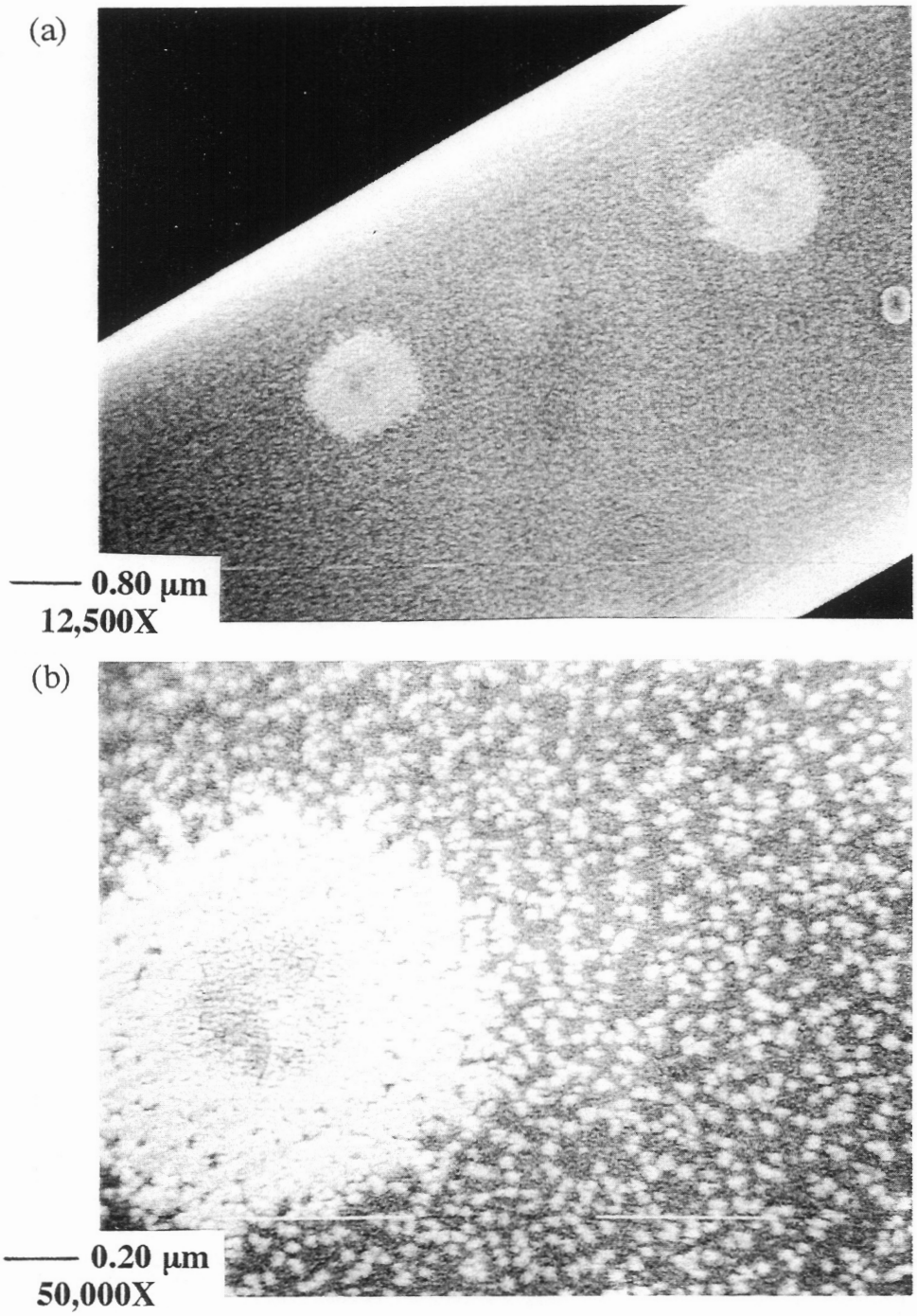

Figure 2.60. SEM photomicrographs of the 3.5 min. ethylene plasma treated AS-4 carbon fibers at a magnification of (a) 12,500X and (b) 50,000X.

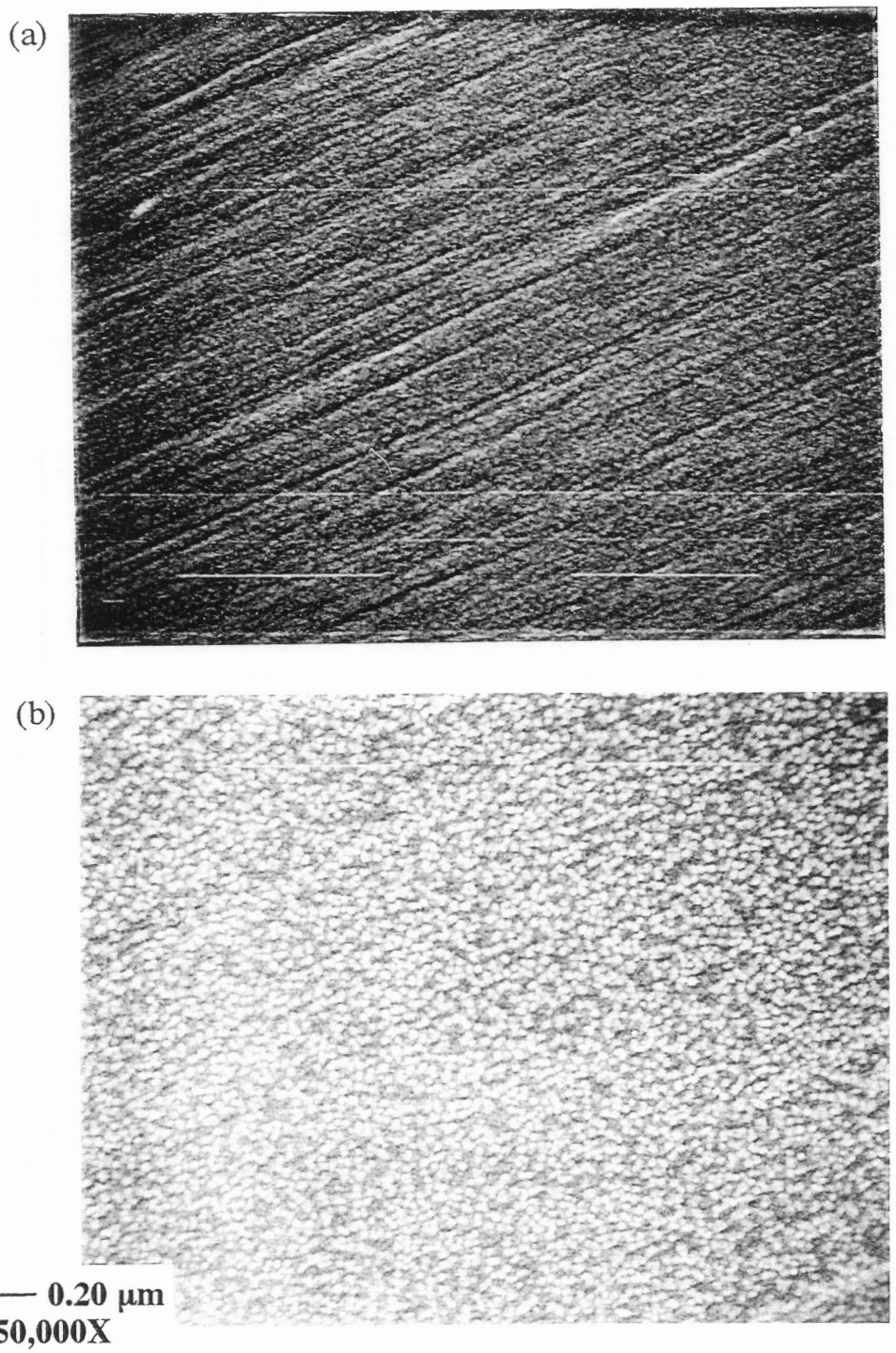

Figure 2.61. SEM photomicrographs of an "as received" AS-4 carbon fiber (50,000X) sputter-coated with gold (a) alone and (b) beside an ethylene plasma treated carbon fiber.

2.3.2.3 Surface Energy

The surface energies of the plasma treated AS-4 carbon fibers were determined using a one-liquid and a two-liquid technique.

2.3.2.3.1 One-Liquid Technique

Examples of wetting traces obtained during one-liquid dynamic contact angle experiments with the 15 sec. air plasma and 1 min. ammonia plasma treated AS-4 carbon fibers are shown in Figures 2.62 and 2.63, respectively. The force, initially equal to zero, rose to a plateau when the end of the fiber penetrated the liquid.

The advancing contact angle was calculated using equation 2.43 and the average wetting force measured as the fiber was immersed in the liquid. The polar and the dispersive components of the total fiber surface energy were determined by plotting the contact angle results in the form of equation 2.54. These linear regression plots are shown in Figure 2.64. The surface energy results obtained from these plots are listed in Table 2.23.

To show which liquids formed a zero contact angle with the carbon fiber surface, the average advancing wetting force was plotted versus the surface free energy of the wetting liquid. Based on equation 2.43, a linear curve with an intercept of zero may be fit through the data points when $\theta = 0°$. Liquids which display a finite contact angle ($\theta > 0°$) provide data points below the linear curve. In general, a liquid will spread and form a 0° contact angle on a solid which has a surface tension less than that of the liquid. Therefore, the plots shown in Figure 2.65 suggest that the total surface energy was greater than 72.6 mJ/m^2 for the 15 sec. air plasma treated fiber and was between 58.6 and 72.6 mJ/m^2 for the 1 min. ammonia plasma treated fiber.

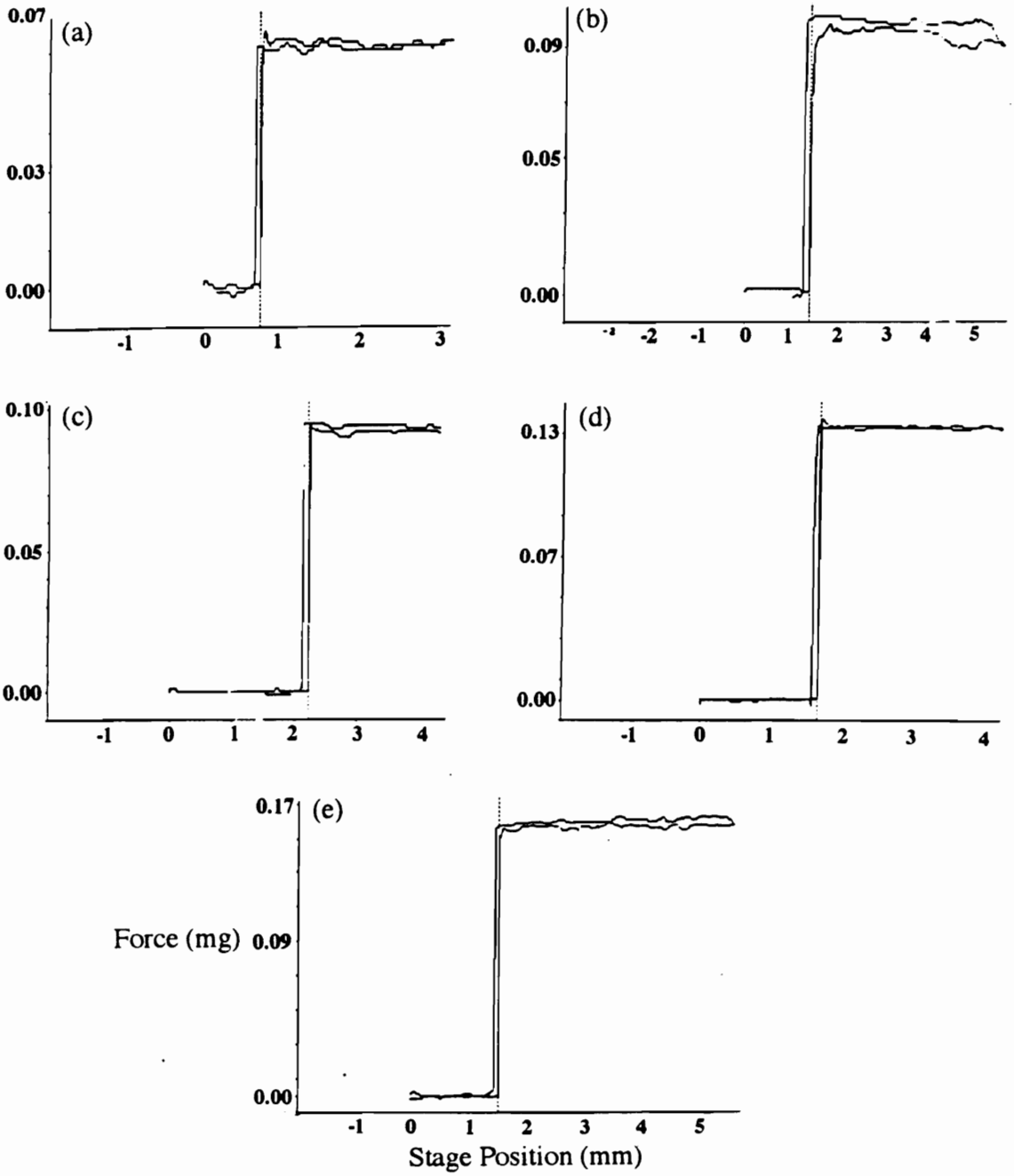

Figure 2.62. Wetting traces obtained with 15 sec. air plasma treated AS-4 carbon fibers and (a) deionized water, (b) formamide, (c) diiodomethane, (d) bromonaphthalene, and (e) hexadecane.

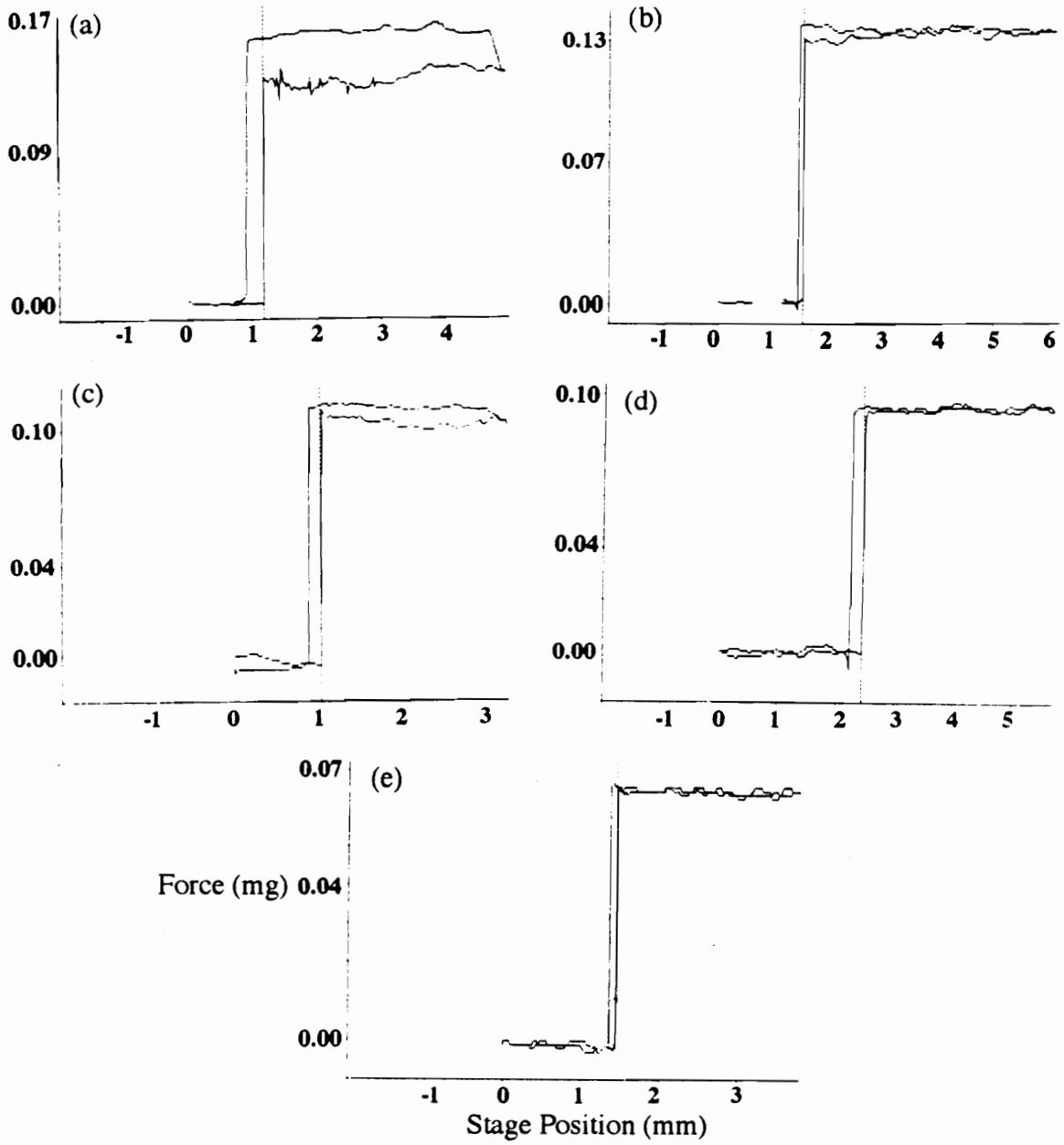

Figure 2.63. Wetting traces obtained with 1 min. ammonia plasma treated AS-4 carbon fibers and (a) deionized water, (b) formamide, (c) diiodomethane, (d) bromonaphthalene, and (e) hexadecane.

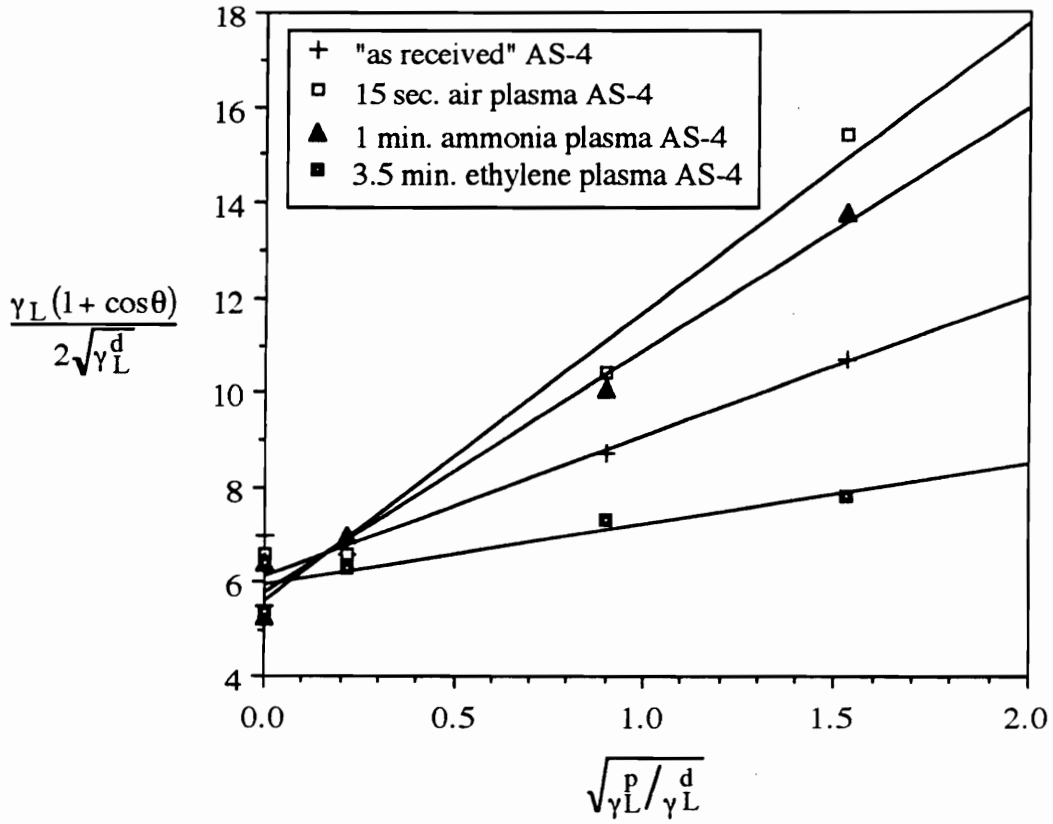

Figure 2.64. One-liquid wetting analysis plot for plasma treated AS-4 carbon fibers.

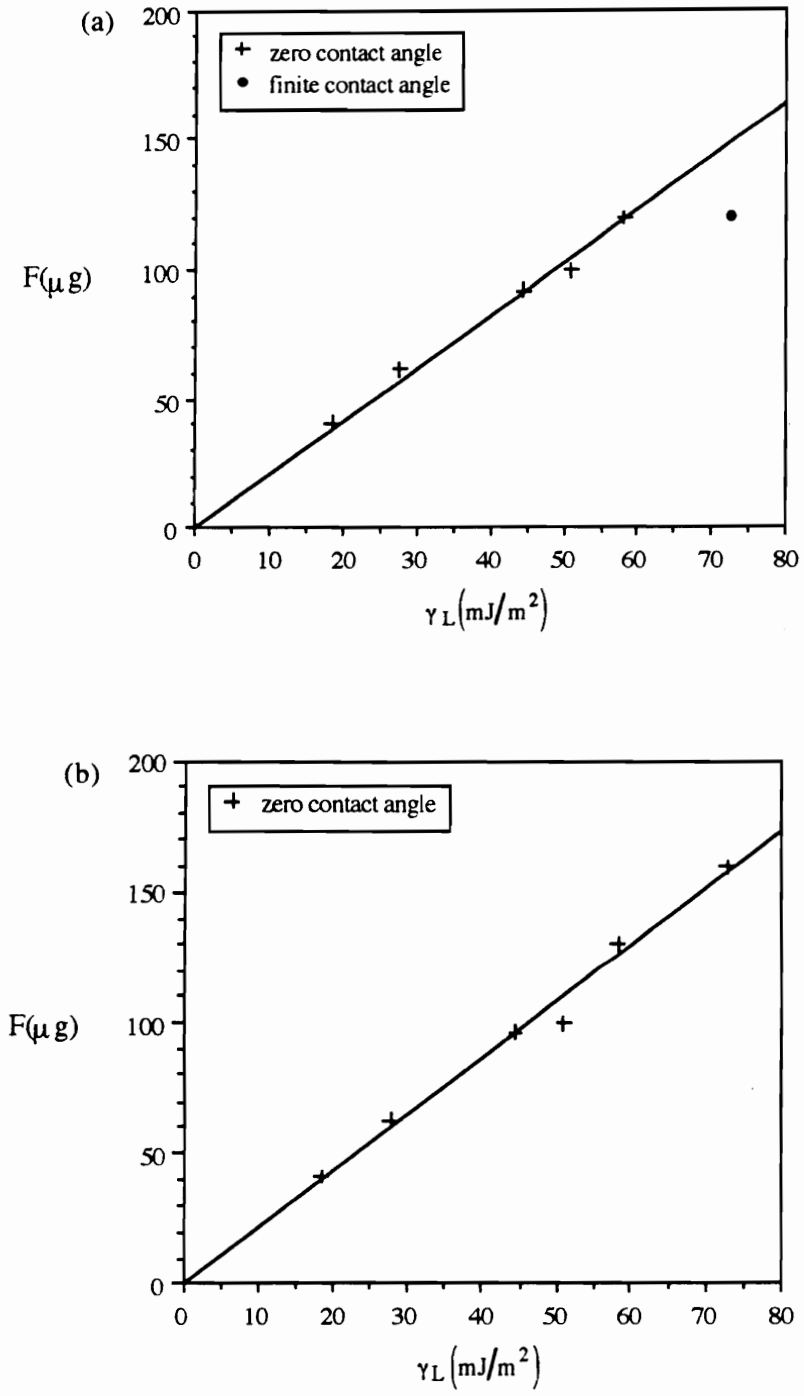

Figure 2.65. Average advancing wetting force versus the surface energy of the wetting liquid for (a) 1 min. ammonia plasma and (b) 15 sec. air plasma treated AS-4 carbon fibers.

Table 2.23. Surface energy results for plasma treated AS-4 carbon fibers.

FIBER	CARBON FIBER SURFACE ENERGY (mJ/m^2) ($<\gamma_S> \pm \sigma_{n-1}$, 7 samples/liquid)						
	one-liquid technique			two-liquid technique			
	γ_S	γ_S^d	γ_S^p	γ_S	γ_S^d	γ_S^p	I_{SF}^p
"as received" AS-4	47 ± 2	38 ± 1	9 ± 2	51 ± 7	36 ± 6	15 ± 3	44 ± 3
15 sec. air plasma AS-4	69 ± 2	32 ± 1	37 ± 2	44 ± 2	24 ± 2	20 ± 1	52 ± 1
1 min. NH_3 plasma AS-4	59 ± 3	34 ± 1	26 ± 2	63 ± 8	50 ± 8	13 ± 2	42 ± 3
ethylene plasma polymer	37 ± 1	36 ± 1	2 ± 1	nd*	nd	nd	nd

*not determined

Hysteresis was only consistently when the 1 min. ammonia plasma treated AS-4 carbon fiber was wet with water (Figure 2.63(a)). This is also the only fiber/liquid combination which shows a finite contact angle in Figure 2.65. In addition, both the local variations in the wetting force and the difference in the advancing and receding wetting force traces were greater when the "as received" AS-4 carbon fiber was wet with water (see Figure 2.37(a)) than when the ammonia plasma treated fiber was wet with water (see Figure 2.63(a)). Both the local variations in the wetting force and the contact angle hysteresis have been attributed to chemical and physical heterogeneities on the fiber surface [113, 255]. Therefore, the decrease in both the hysteresis and the local wetting force variation following ammonia plasma treatment suggests that the ammonia plasma cleaned the AS-4 carbon fiber and created a more homogeneous surface.

2.3.2.3.2 Two-Liquid Technique

Examples of the wetting traces obtained during dynamic contact angle experiments in a beaker containing two immiscible liquids (formamide and a hydrocarbon) with the 15 sec. air plasma and the 1 min. ammonia plasma treated AS-4 carbon fibers are shown in Figure 2.66 and 2.67, respectively. The surface energy was obtained by plotting the wetting analysis results in the form of equation 2.59. These linear regression plots are shown in Figure 2.68. The surface energy results are listed in Table 2.23. There was hysteresis between the advancing and receding wetting forces when the ammonia plasma treated fiber was in the formamide layer (see Figure 2.67), but not when the air plasma treated fiber was in the formamide layer (see Figure 2.66). This shows that the surface energy of the air plasma treated fiber was less than that of formamide and the surface energy of the ammonia plasma treated fiber was greater than that of formamide, 58.6 mJ/m^2. Indeed, the surface energies of the air and ammonia plasma treated fibers, calculated using the two-liquid technique and reported in Table 2.23, follow this trend.

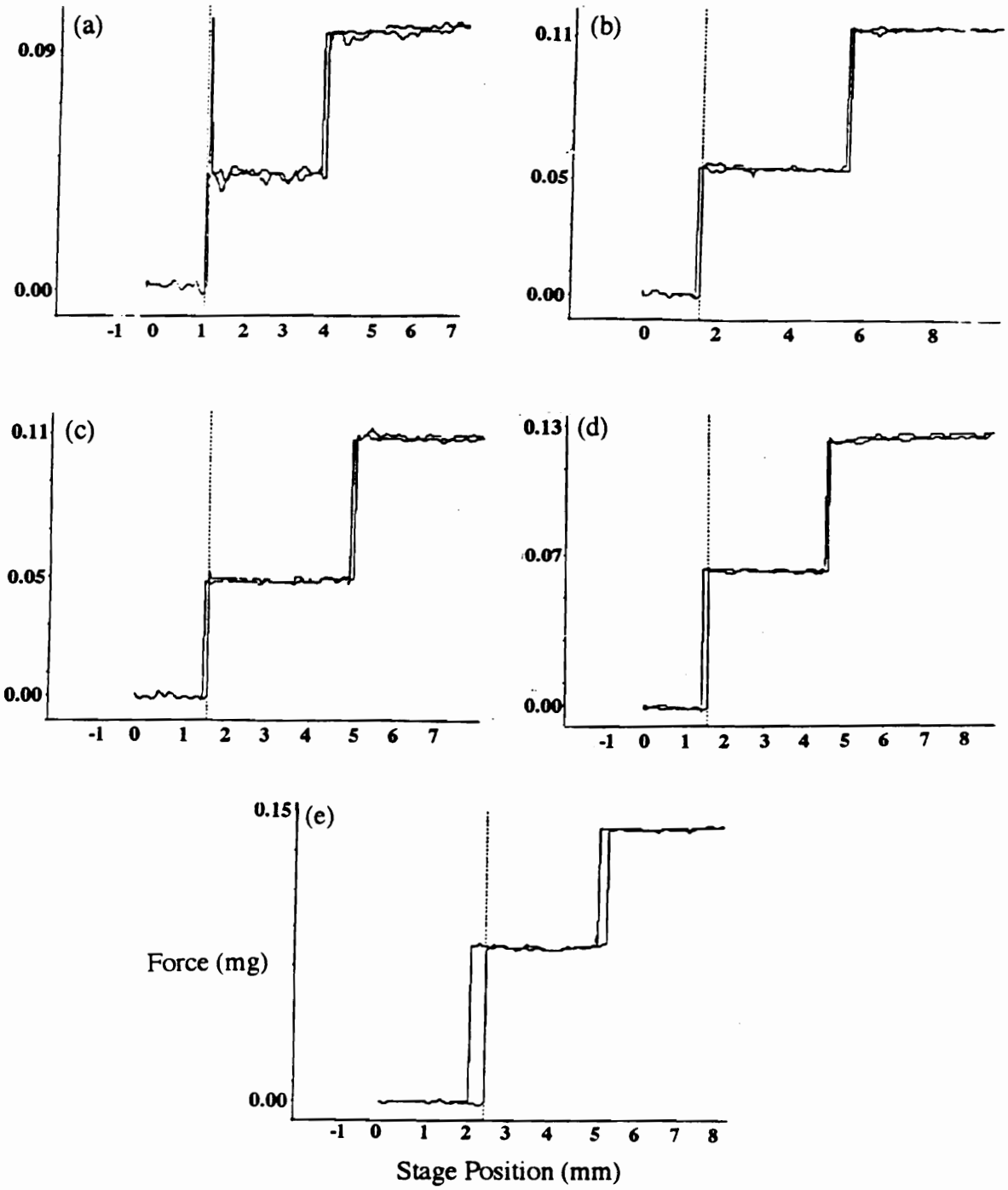

Figure 2.66. Wetting traces obtained with 15 sec. air plasma treated AS-4 carbon fibers using formamide and (a) hexane, (b) decane, (c) octane, (d) hexadecane, and (e) decahydronaphthalene.

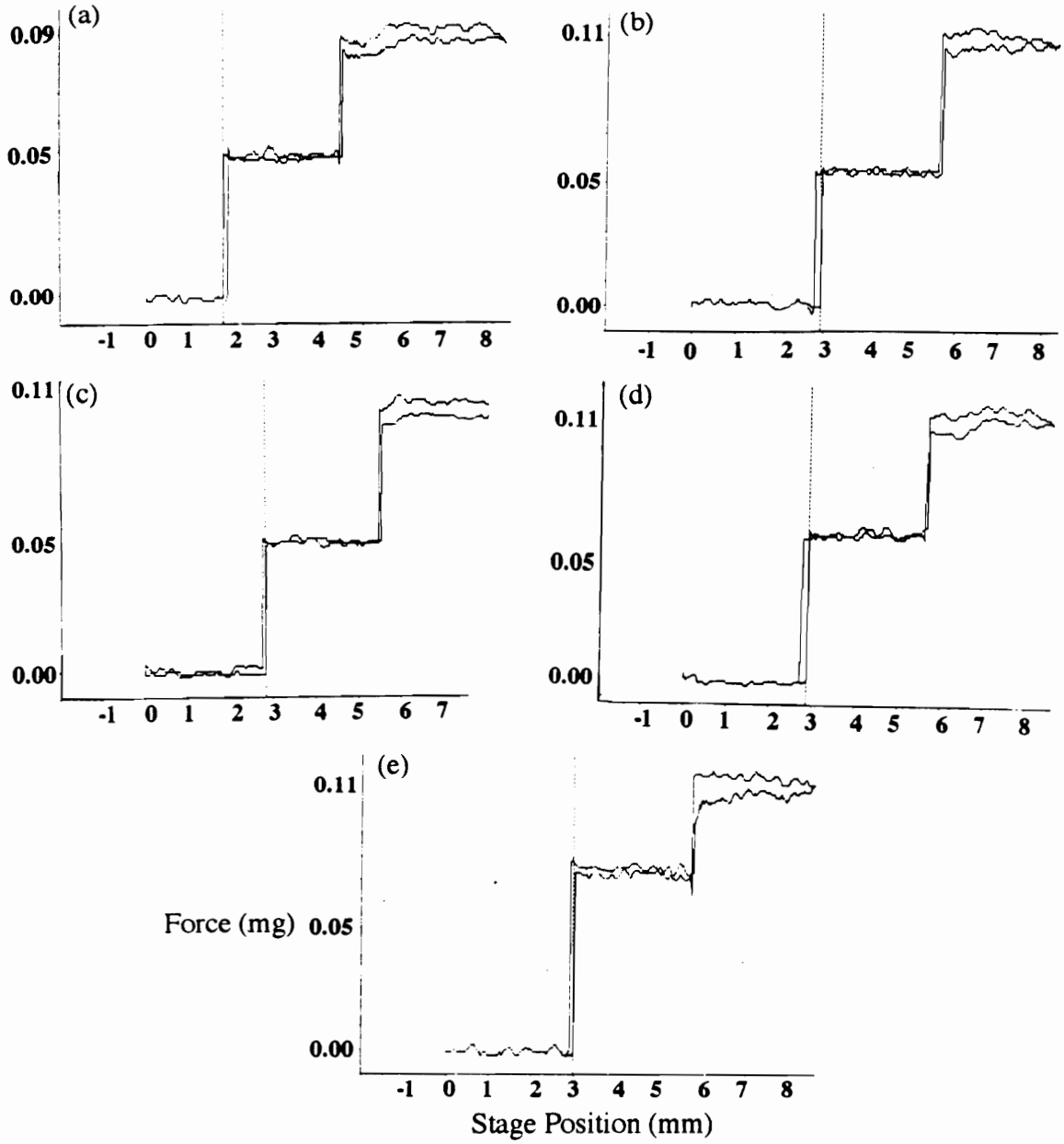

Figure 2.67. Wetting traces obtained with 1 min. ammonia plasma treated AS-4 carbon fibers using formamide and (a) hexane, (b) decane, (c) octane, (d) hexadecane, and (e) decahydronaphthalene.

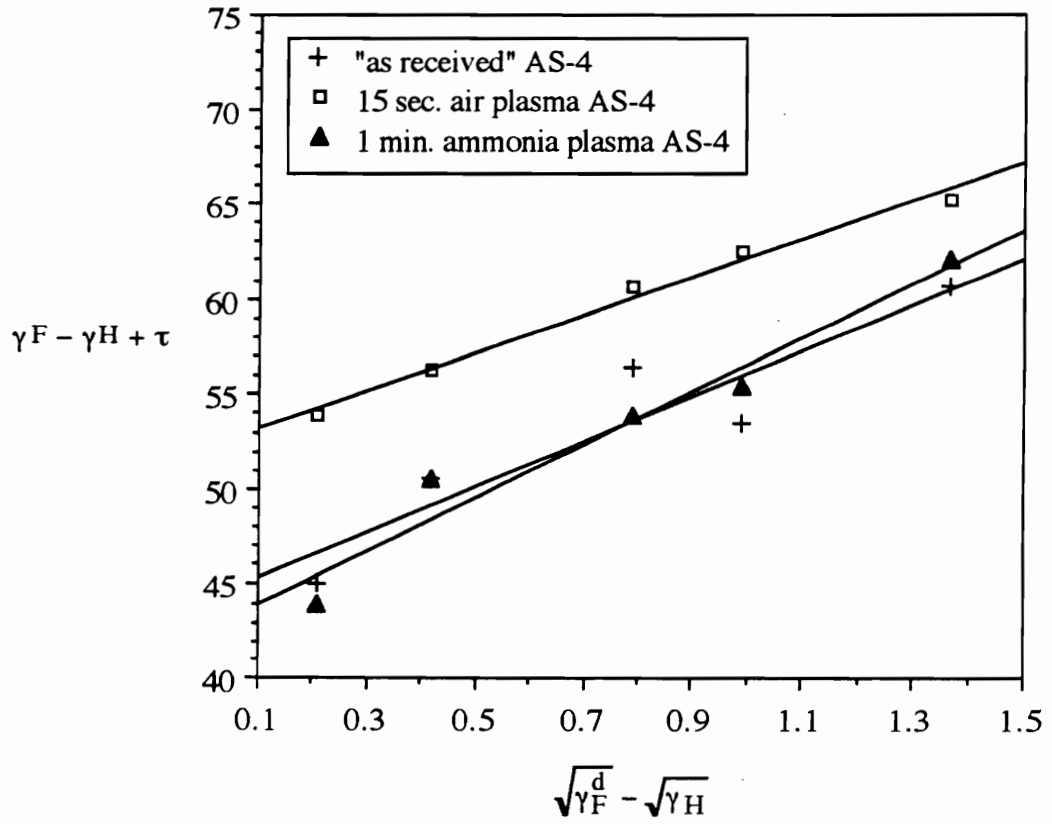

Figure 2.68. Two-liquid wetting plots for "as received," 15 sec. air plasma, and 1 min. ammonia plasma treated AS-4 carbon fibers.

The surface energy values obtained for the air and ammonia plasma treated carbon fibers with the one-liquid technique were significantly different from those obtained with the two-liquid technique. No direct comparison of the one-liquid and two-liquid wetting techniques is available in the literature. The difference in the surface energies obtained with the two different techniques in this work may be attributed to several things. First, in the two-liquid technique, the nonpolar liquid may not be completely displaced from the carbon fiber surface when the fiber passes into the formamide. It may be especially difficult for the formamide to displace the nonpolar liquid from crevices or "pores" on a rough carbon fiber surface. In addition, when the two-liquid technique is used, adsorbed material on the fiber surface may be displaced by the nonpolar liquid, before the fiber is wet with formamide.

In Figure 2.69, the polar surface energy and the polar interaction parameter, obtained using the one-liquid and the two-liquid techniques, are plotted versus the total concentration of oxygen and nitrogen detected on the carbon fiber surface using a 45° XPS take-off angle. With both techniques, the polar term increased as the concentration of oxygen and nitrogen on the fiber surface was increased. Figures 2.70 and 2.71 show that the dispersive surface energy remained relatively constant and the total surface energy increased with the concentration of oxygen and nitrogen on the carbon fiber surface when the one-liquid wetting technique was used. However, when the two-liquid technique was used, both the dispersive and the total surface energy varied with the concentration of oxygen and nitrogen on the carbon fiber surface. In addition, when the two-liquid technique was used, the error associated with the surface energies of the "as received" and ammonia plasma treated AS-4 fibers was much larger than with the one-liquid technique.

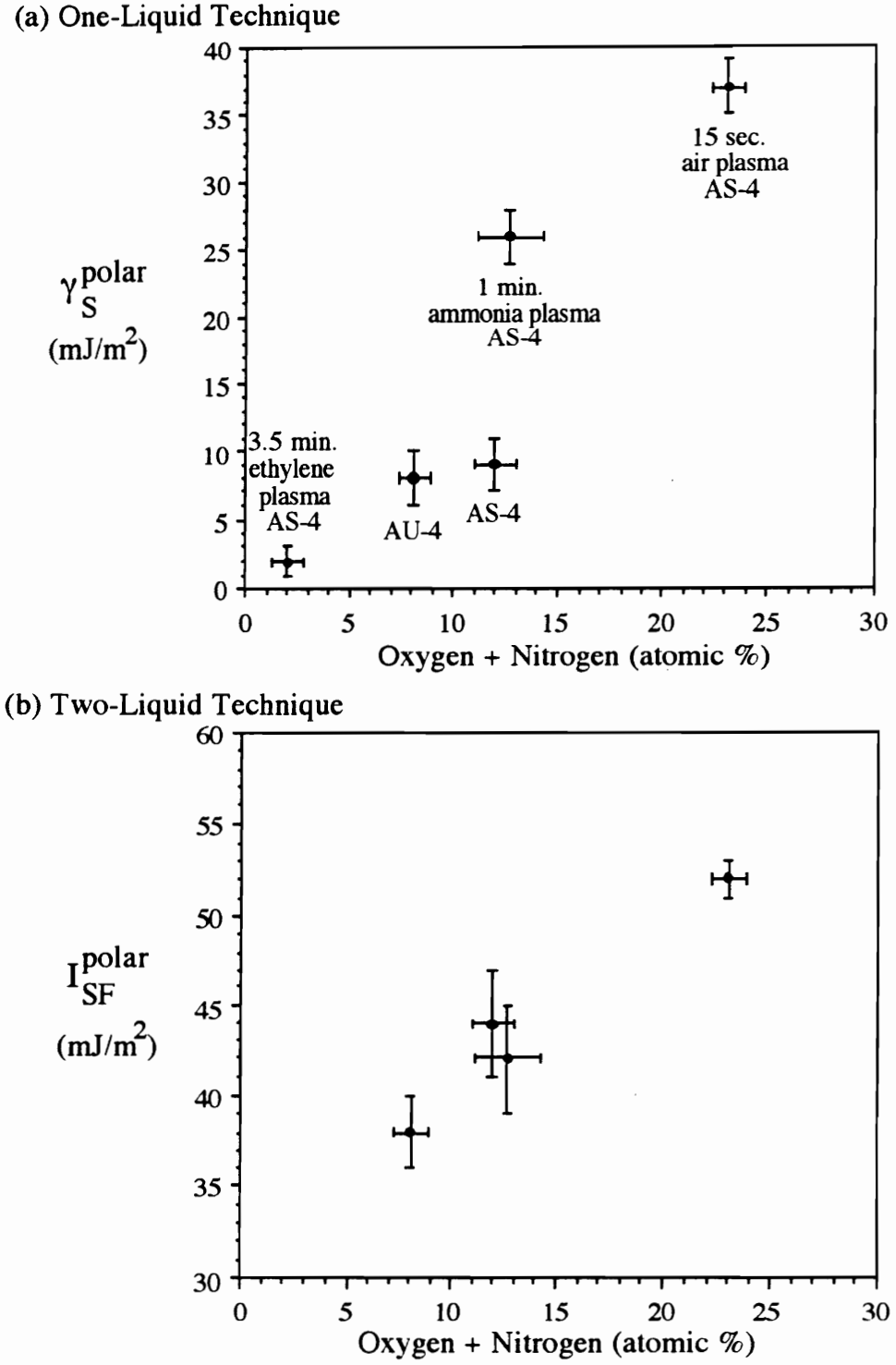

Figure 2.69. Surface energy polar components versus the concentration of oxygen and nitrogen on the carbon fiber surface.

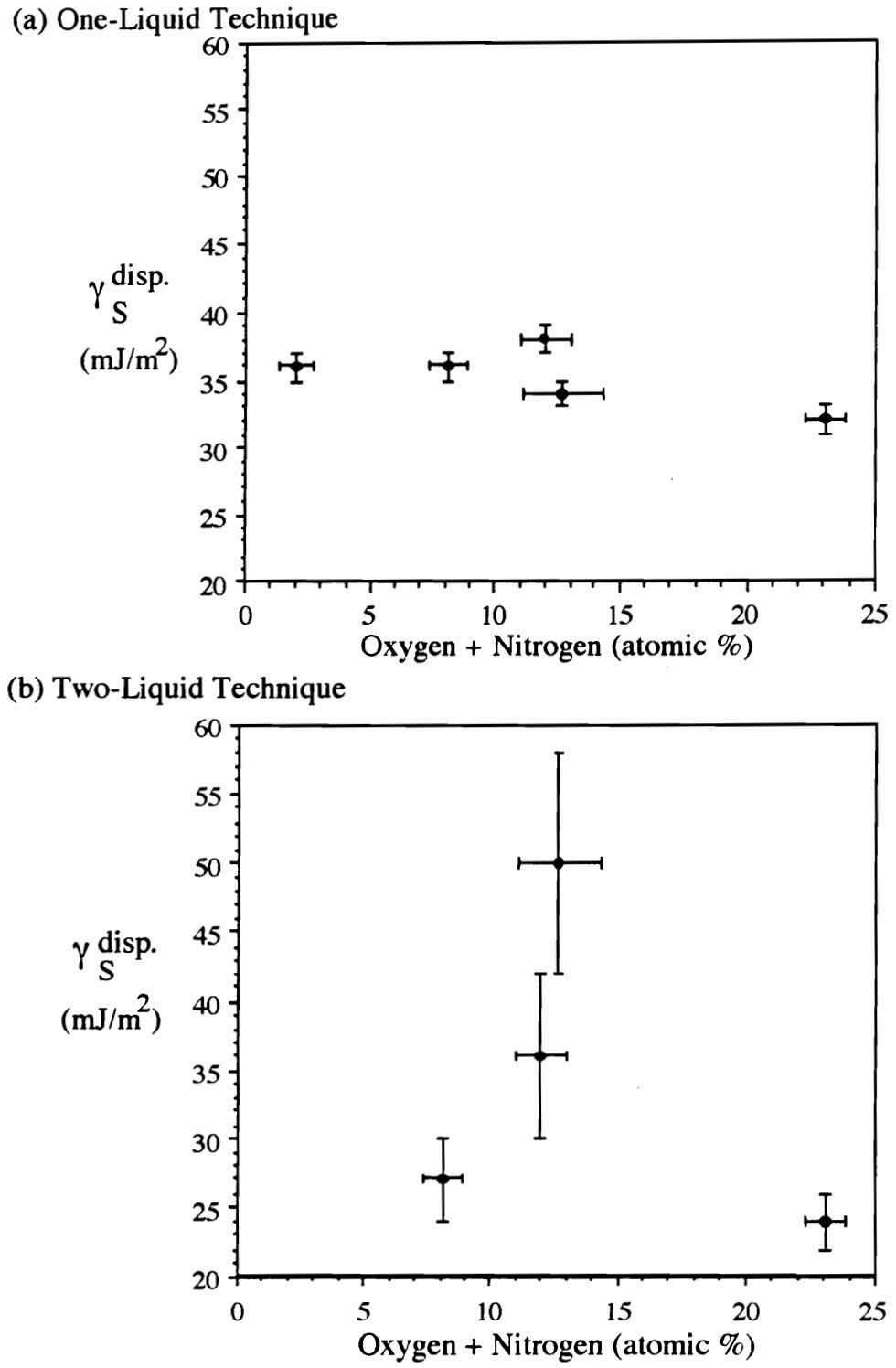

Figure 2.70. Dispersive surface energy versus the concentration of oxygen and nitrogen on the carbon fiber surface.

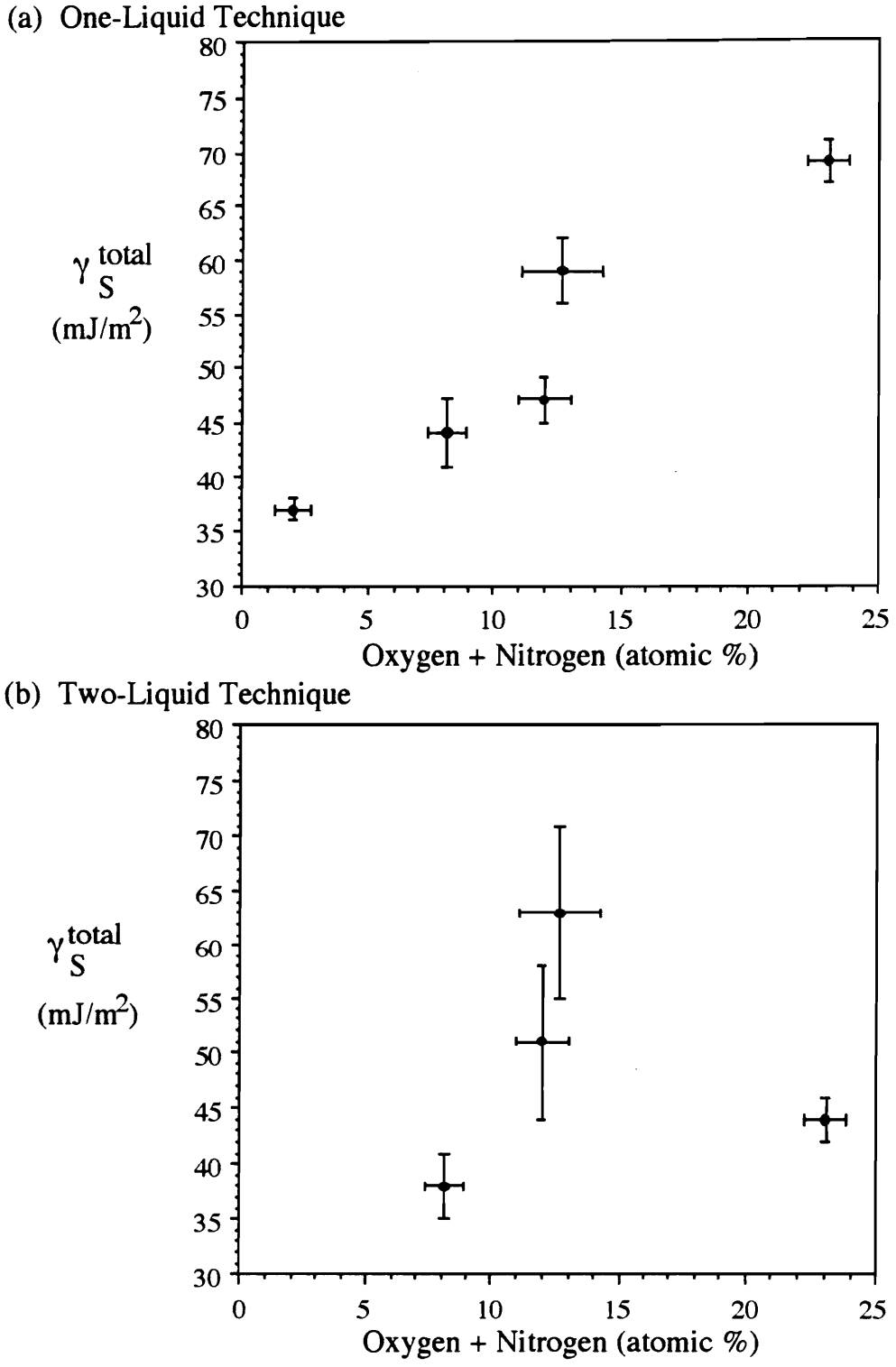

Figure 2.71. Total surface energy versus the concentration of oxygen and nitrogen on the carbon fiber surface .

The variation in the carbon fiber dispersive surface energy observed in this work with the two-liquid technique has been reported by other researchers. Donnet and coworkers observed a decrease in the dispersive surface energy component and an increase in the polar component of carbon fibers exposed to an air plasma [183]. Commerçon and Wightman reported a decrease in the dispersive surface component of carbon fibers following air plasma treatment [63]. The results of the two-liquid technique are difficult to explain based only on the oxygen and nitrogen concentration of the fiber surface. Detailed knowledge of the chemical bonding within the sample surface and the fiber rugosity would afford a better interpretation of the wetting results.

2.3.2.4 Tensile Strength

The average tensile strengths of one centimeter long "as received" and plasma treated AS-4 carbon fibers are given in Figure 2.72. The fiber tensile strength was not affected by plasma treatment, even following the ablative oxygen or air plasma treatments. Bian and coworkers also reported no significant change in the tensile strength of PAN-based carbon fibers exposed to oxygen or nitrogen plasmas [46].

Bennett & Johnson [156] showed that the flaws in carbon fibers which initiate failure contain misoriented crystals. Reynolds and Sharp proposed the mechanism of failure sketched in Figure 2.73 where a misoriented crystal links two crystals which are parallel to the fiber axis [264]. When a tensile stress is exerted parallel to the fiber axis, the layer planes rupture. Therefore, if carbon fiber failure initiates at misoriented crystals in the fiber structure and the tensile strength of the AS-4 carbon fibers was not affected by the plasma treatments, it follows that the plasma treatments must not eliminate the majority of misoriented crystals in the fiber. Indeed, while the plasma treatments may eliminate any flaws in the outermost surface of the fiber, the misoriented crystals present in the bulk of the fiber would not be affected.

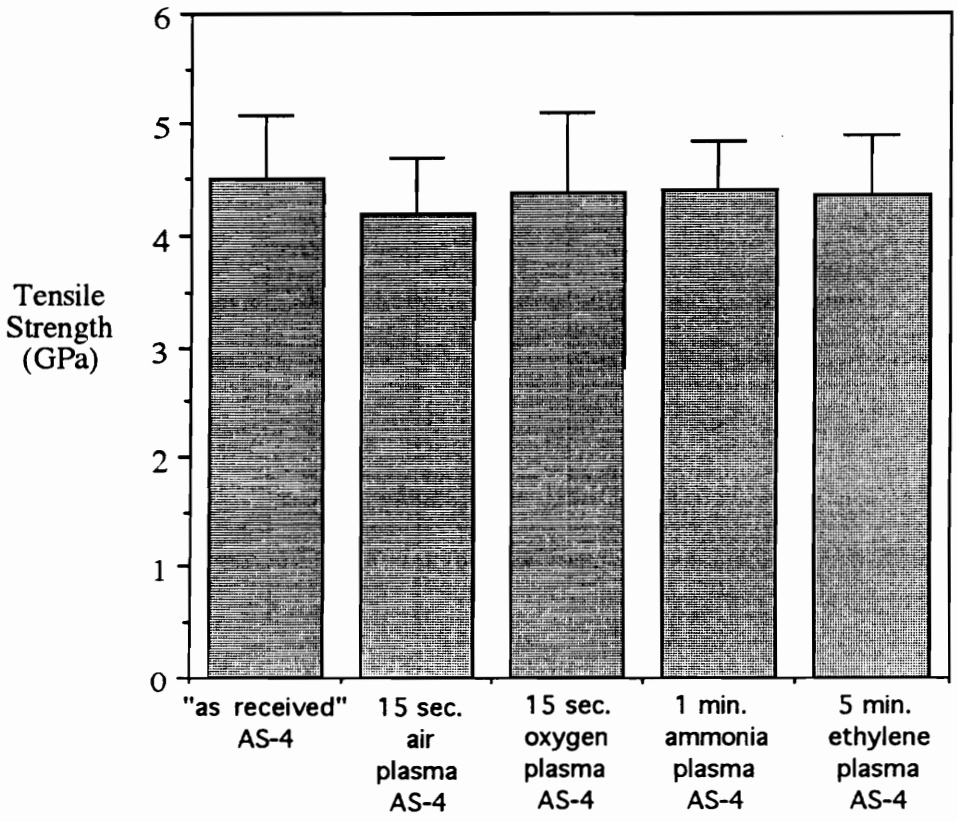

Figure 2.72. Tensile strength of "as received" and plasma treated AS-4 carbon fibers (<tensile strength> ± σ for 50 samples).

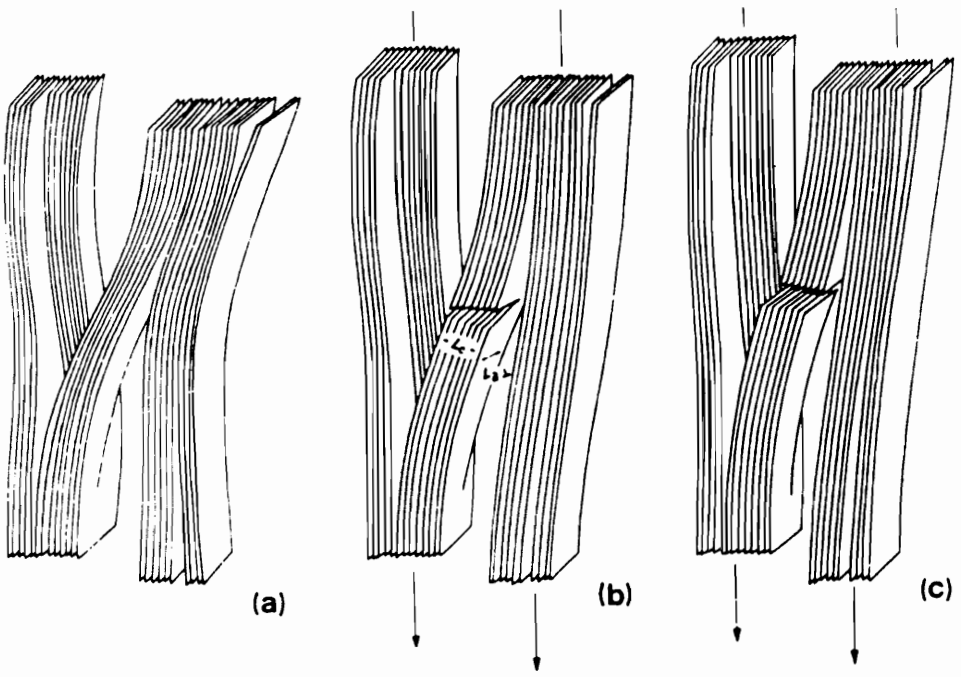

Figure 2.73. Sketch of tensile failure in a misoriented crystal in a carbon fiber [264].

The tensile strength of the "as received" AS-4 carbon fibers decreased as the gauge length of the fibers was increased from 0.5 to 2 cm as shown in Figure 2.74. The tensile strength decreased as the gauge length was increased due to the higher probability of finding a flaw to initiate failure for longer fibers [154]. In this study, gauge lengths from 0.5 to 2 cm were investigated as this was the approximate range of fiber gauge lengths in the microbond experiment.

2.3.2.5 Analysis of Ethylene Plasma Polymer

Polymer was created in the ethylene plasma in both film and powder form. The plasma polymer was light yellow in color and was not soluble in acetone or tetrahydrofuran, showing that it was not oily in nature. The general effect of pressure and ethylene flow rate on the plasma polymerization is illustrated in Figure 2.75 [214]. The ethylene glow discharge used in this work was generated with a power of 50 watts, a pressure of 1 torr, and an ethylene gas flow rate of 46 cm^3/min. Under these conditions, the plot in Figure 2.75 predicts that polymer film will be created. The small amount of powder that was generated in the plasma reactor shows that the transition from the powder and film region to the film region in Figure 2.75 is gradual.

The following characteritics have been demonstrated in experimental work with ethylene plasmas [214].

- At low pressures and low monomer flow rates, the polymer is deposited both as a powder and a film. Only at low pressures and high flow rates is a solid film deposited. The transitions from powder to film and film to oil regions are gradual and the demarcation lines in Figure 2.75 should be regarded as approximate values.

- At low pressure and low flow rate, the amount of powder formed is always less than half the total yield. The other part of the product is film.

- The chemical composition of the polymer indicates that the value of n in the

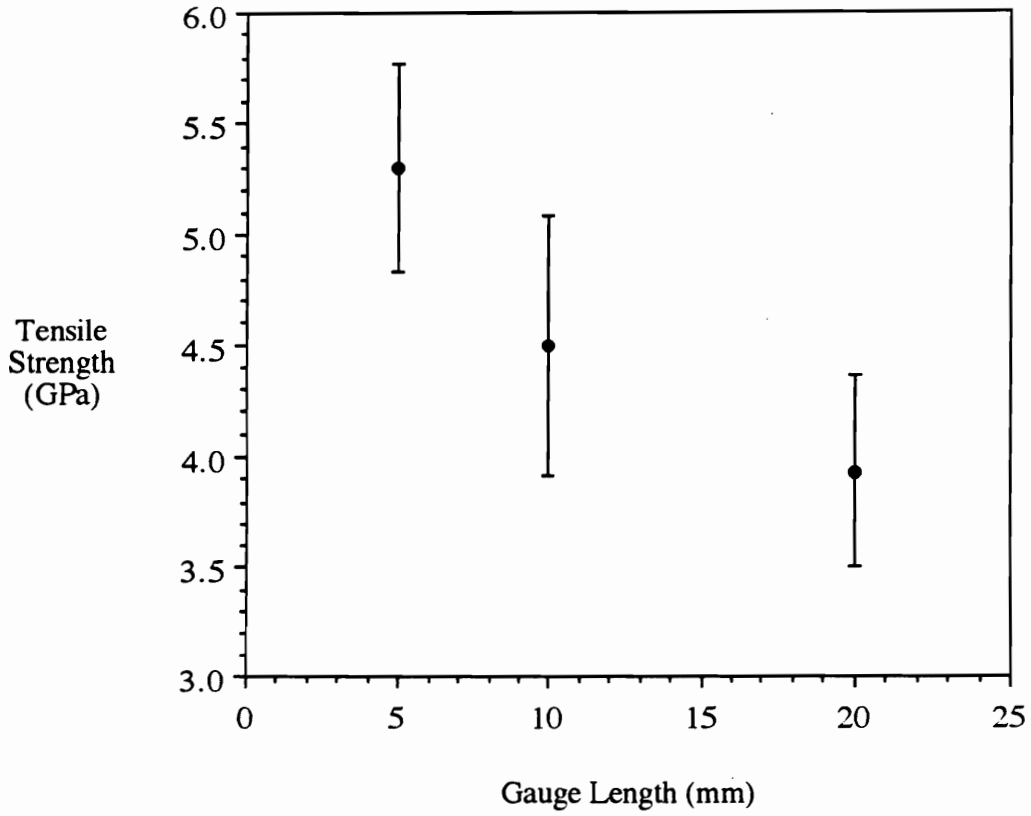

Figure 2.74. Tensile strength of "as received" AS-4 carbon fiber as a function of the fiber length.

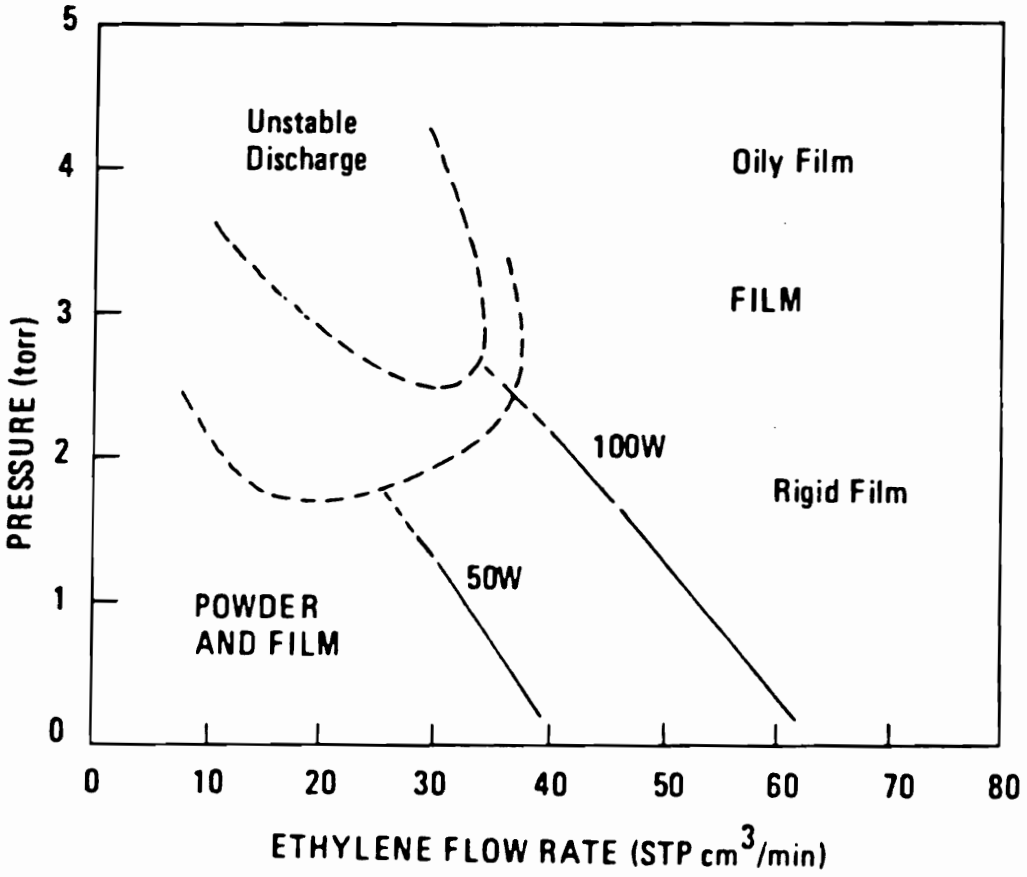

Figure 2.75. Ethylene pressure as a function of flow rate [214].

formula C_2H_n is between 2.6 and 3.0. The high value of n corresponds to polymers formed at low flow rates.

- For a given flow rate and pressure, the chemical compositions of the powder and the film show no significant difference.

The DSC scans of conventional poly(ethylene) and the plasma polymer generated in the ethylene plasma are shown in Figure 2.76. The poly(ethylene) melted around 110°C. The ethylene plasma polymer did not melt. In general, plasma polymers do not exhibit thermal transitions because they are highly crosslinked [265]. In the scan of the ethylene plasma polymer, there was a slight exotherm, which suggested that some additional cross-linking occurred in the plasma polymer upon heating. This may be the result of trapped free radicals in the plasma polymer. Trapped free radicals have been detected in plasma polymers using ESR [265]. The source of these radicals may be incorporation of gaseous free radicals formed in the discharge or bond rupture caused by impingement of energetic particles and radiation in the plasma.

The TGA scans obtained with the poly(ethylene) and the ethylene plasma polymer are shown in Figure 2.77. The ethylene plasma polymer was not as thermally stable in air as the conventional poly(ethylene). This is probably due to the fact that the ethylene plasma polymer sample was in the form of a very fine powder and, therefore, had a much greater surface area than the square sample of poly(ethylene) and because the ethylene plasma polymer contained reactive functional groups not present in polyethylene (i.e., hydroxyl, carbonyl, C=C) .

When the ethylene plasma polymer powder was analyzed by FT-IR, the spectra in Figure 2.78, was obtained. The band assignments are listed in Table 2.24. The structure of the ethylene plasma polymer was significantly different from that of poly(ethylene).

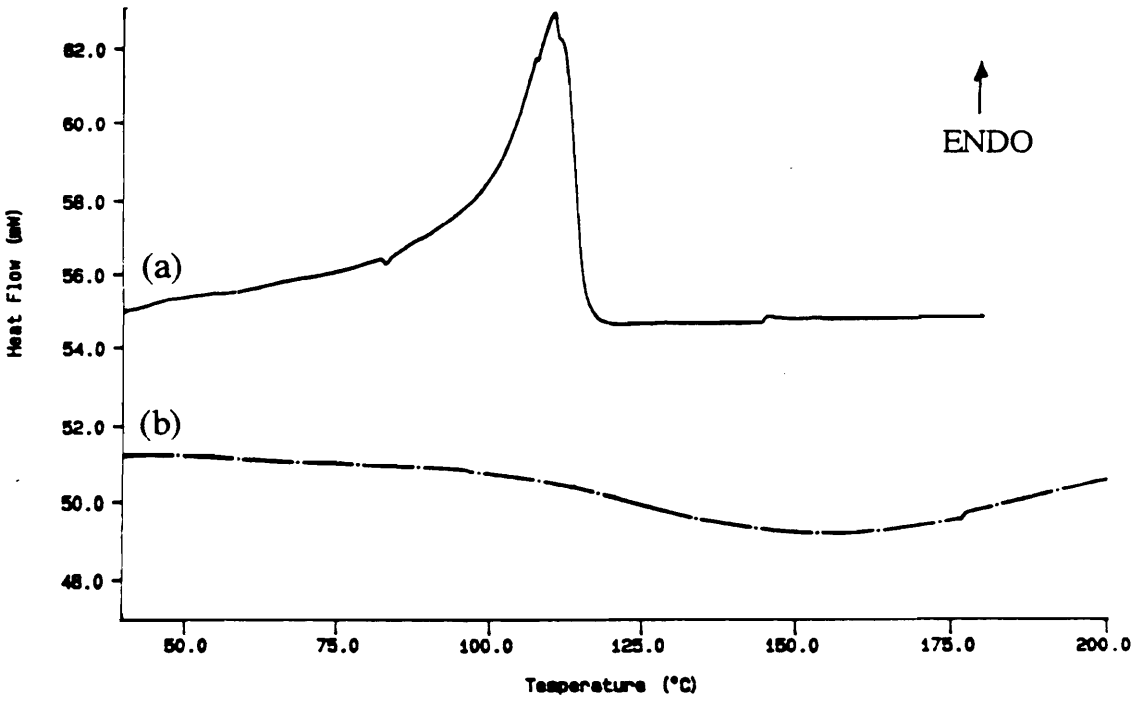

Figure 2.76. Differential scanning calorimetry scans with (a) conventional poly(ethylene) and (b) the polymer powder formed in the ethylene plasma.

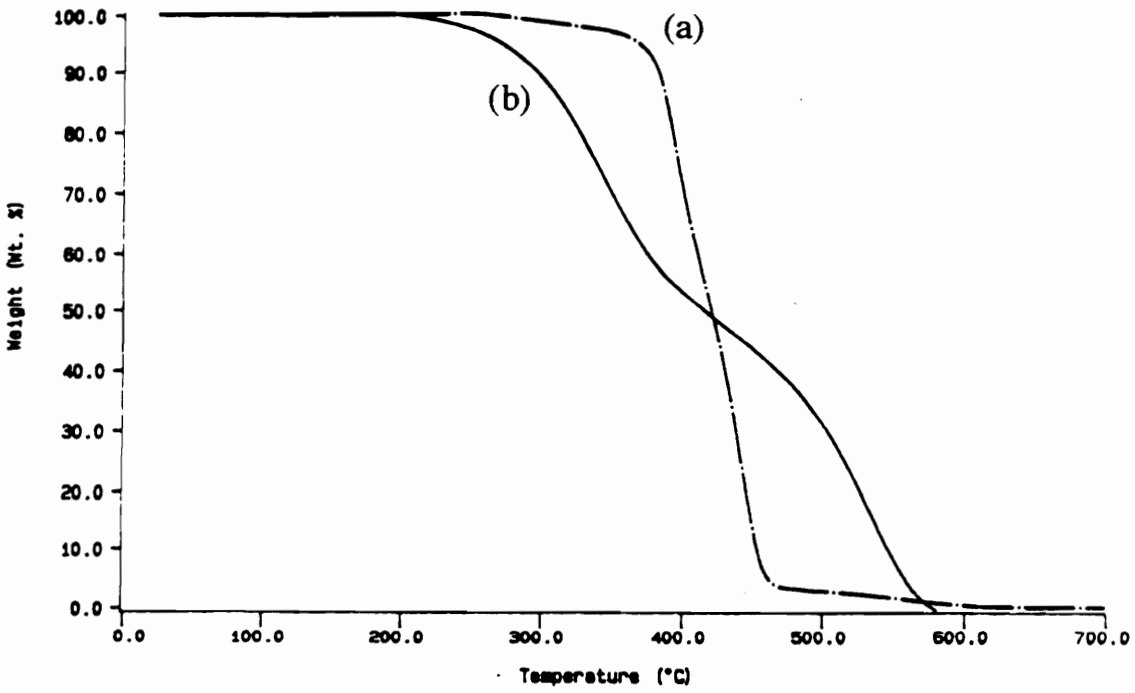

Figure 2.77. Dynamic thermogravimetric analysis scans of (a) conventional poly(ethylene) and (b) the polymer powder formed in the ethylene plasma.

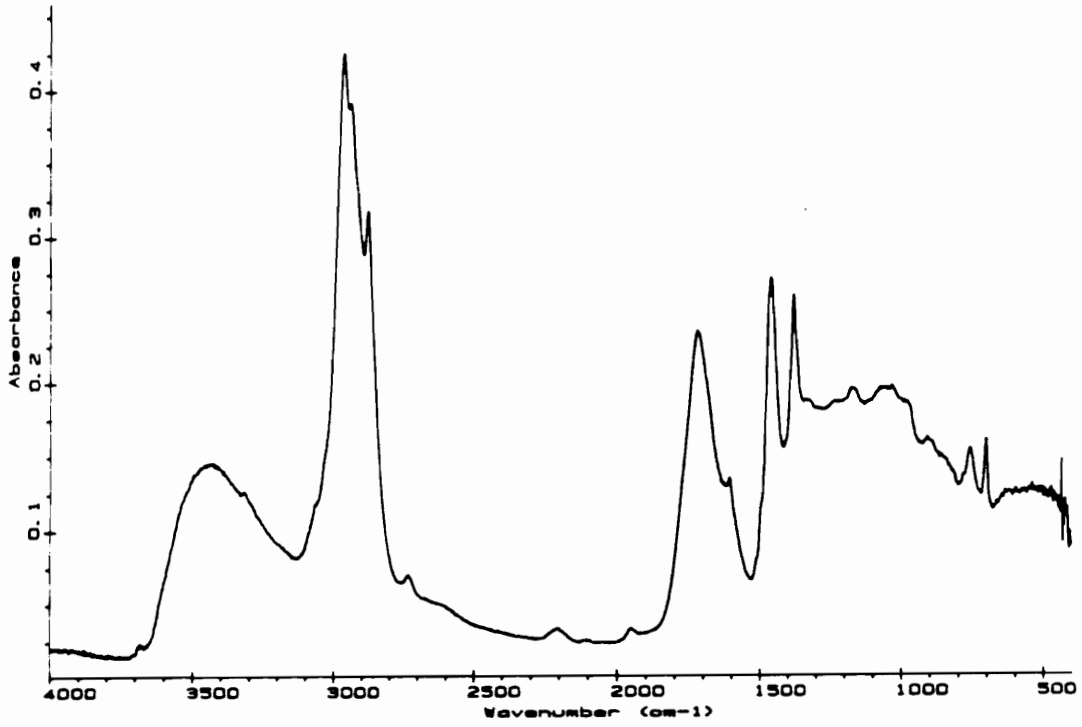

Figure 2.78. FT-IR spectrum of the polymer formed in an ethylene plasma.

Table 2.24. Assignment of IR absorption bands for polymer formed in an ethylene plasma.

Absorption frequency (cm^{-1})	Assignment
3445	O-H stretch
3060	C-H stretch in C=C-H
2959, 2935, 2875	C-H stretch
2214	C ≡ C stretch
1950	C=C stretch in C=C=C
1715	C=O stretch, C=C stretch (unconjugated)
1609	C=C stretch (conjugated)
1458	C-H bend in CH_2
1376	C-H bend in CH_3

The ethylene plasma polymer contained carbon to carbon double bonds and triple bonds as well as carbonyl and hydroxyl groups. In agreement with the FT-IR results, the XPS oxygen 1s photopeak of the ethylene plasma polymer (Figure 2.48(d)), suggested that O-C and O=C groups were present in the plasma polymer. The oxygen-containing functional groups were probably formed when free radicals in the plasma polymer were exposed to the atmosphere [265].

2.3.3 Characterization of AS-4 Carbon Fiber Tow Passed Through an Aqueous Suspension Prepregging Solution

The first step in preparing a thermoplastic matrix composite is to impregnate the carbon fiber tow with polymer. This may be accomplished using solvent coating, hot melt, dry powder, or suspension prepregging. As part of this research effort, Davis and coworkers prepared high performance thermoplastic composites using aqueous suspension prepregging [266]. An aqueous solution of polyamic acid and ammonium hydroxide was prepared and thermoplastic polymer powder was added to form a suspension. A carbon fiber tow was passed through this suspension and then the wet prepreg was dried. Finally, the dried prepreg was hot pressed to form a composite. LaRC-TPI thermoplastic polyimide and poly(etheretherketone) (PEEK) carbon fiber reinforced composites have been prepared using the ammonium salt of either LaRC-TPI polyamic acid or Bis P/BTDA polyamic acid to disperse the thermoplastic powders.

Interestingly, the composite properties were affected by the choice of polyamic acid used to disperse the thermoplastic powder [266]. It was proposed that the polyamic acid dispersant coated the carbon fibers during the aqueous suspension prepregging process, altered the fiber/matrix interphase properties, and improved the fiber/matrix adhesion. Indeed, Chuang, Chu, and Whang used the microbond adhesion test to show that polyamic acid fiber coatings improve the interfacial shear strength between carbon fibers and aromatic thermoplastic polymers [267]. They found that the interfacial adhesion

depended on the chemical affinity between the polyamic acid and the thermoplastic resin and on the physical properties of both the polyamic acid and the thermoplastic polymer.

To determine if the polyamic acid used to disperse the thermoplastic powder coated the carbon fibers during prepregging, carbon fibers were thoroughly wet with an aqueuous solution containing 3 wt.% LaRC-TPI polyamic acid and an excess of ammonium hydroxide (PAA/NH_4OH), dried at 110°C for 1 hour in a convection oven, and analyzed using x-ray photoelectron spectroscopy and scanning electron microscopy. Additional carbon fibers were wet with the aqueous PAA/NH_4OH solution and heated to convert the LaRC-TPI polyamic acid to the LaRC-TPI polyimide. The surface chemical compositions of these fibers were compared to that of LaRC-TPI polyamic acid and LaRC-TPI films prepared under vacuum from the aqueous PAA/NH_4OH solution.

2.3.3.1 Surface Chemistry

The x-ray photoelectron spectroscopy results for the AS-4 carbon fiber tow wet with the LaRC-polyamic acid solution, listed in Table 2.25, correlated relatively well to the XPS results for the film prepared from the polyamic acid solution and to the bulk theoretical values, showing that the AS-4 tow was coated with LaRC-TPI polyamic acid. When the polyamic acid fiber coating was imidized, the surface nitrogen content remained constant while the oxygen content decreased from 16 to 13%, consistent with the loss of water which occurs during the imidization reaction, depicted in Figure 2.20. As shown in Table 2.26, exposure of the AS-4 carbon fibers to water, ammonium hydroxide or the imidization conditions did not significantly alter the fiber surface chemistry.

Figure 2.79 shows the curve-fit carbon 1s, oxygen 1s, and nitrogen 1s photopeaks for the "as received" AS-4 carbon fibers, the fibers wet with the LaRC-TPI polyamic acid solution, and the LaRC-TPI film samples. The carbon 1s photopeak for the "as received"

Table 2.25. Surface composition of the "as received" AS-4 carbon fiber tow, the AS-4 carbon fiber tows wet with the aqueous LaRC-TPI polyamic acid solution, and the LaRC-TPI films (XPS, 45° take-off angle).

SAMPLE	CONCENTRATION (atomic %)		
	Carbon	**Oxygen**	**Nitrogen**
"as received" AS-4	87.8 ± 0.6	9.0 ± 0.2	3.3 ± 0.4
AS-4 tow wet with aqueous LaRC polyamic acid solution			
dried under ambient conditions	79.0 ± 0.3	16.0 ± 0.1	5.0 ± 0.2
dried at 110°C for 1 hour	78.7	16.3	5.0
imidized	82.1	12.9	5.0
film prepared from aqueous LaRC polyamic acid solution			
non-imidized	77.5	17.3	5.2
imidized	79.0	15.7	5.3
bulk theoretical values			
LaRC polyamic acid	75.0	20.0	5.0
LaRC-TPI	78.9	15.8	5.3

Table 2.26. Surface composition of the "as received" AS-4 carbon fiber tow and, the AS-4 carbon fiber tow exposed independently to water, ammonium hydroxide, and imidization conditions (XPS, 45° take-off angle).

SAMPLE	CONCENTRATION (atomic %)		
	Carbon	**Oxygen**	**Nitrogen**
"as received" AS-4	87.8 ± 0.6	9.0 ± 0.2	3.3 ± 0.4
AS-4 tow wet with aqueous NH_4OH solution			
dried under ambient conditions	87.5	10.2	2.3
stored 24 hours in dessicator	89.3	8.4	2.3
dried at 110°C for 1 hour	87.8	9.3	3.0
AS-4 tow wet with deionized H_2O			
dried under ambient conditions	85.2	11.8	3.0
dried at 110°C for 1 hour	86.9	10.5	2.6
"as received" AS-4 tow subjected to imidization conditions			
	88.8	8.2	3.0

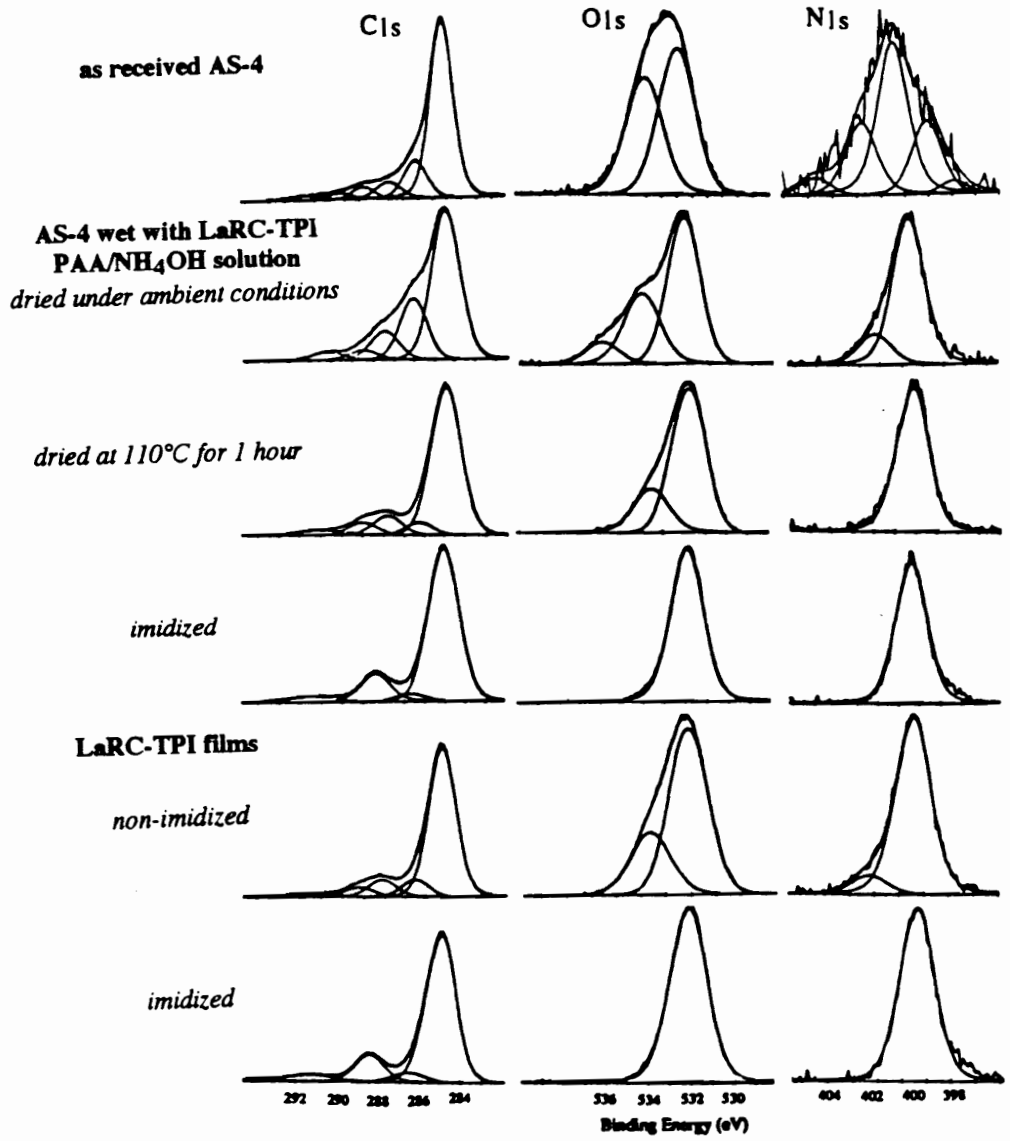

Figure 2.79. Curve-fit carbon 1s, oxygen 1s, and nitrogen 1s photopeaks of the "as received" AS-4 carbon fiber tow, the AS-4 carbon fiber tow wet with an aqueous solution of LaRC-TPI polyamic acid, and the LaRC-TPI films.

AS-4 carbon fiber tow was fit with photopeaks at 285.0, 286.5, 287.7, 289.1, 290.4, and 291.6 eV assigned to C-C, C-O and C-N, C=O, O-C=O, RO-C=O bonding, and π->π* shake-up, respectively [207, 248, 249]. The carbon 1s photopeak for the AS-4 fibers wet with the aqueous LaRC-polyamic acid solution and dried at 110°C for 1 hour were fit with curves at 285.0, 286.6, 287.7, 289.1, and 291.6 eV assigned to C-C, C-N, C=O, N-C=O and O-C=O bonding, and π -> π* shake-up [249, 268]. These curve-fitting results correspond much better to the chemical structure of LaRC-TPI polyamic acid and the carbon 1s region of the LaRC-TPI polyamic acid film than to the carbon 1s region of the "as received" AS-4 fiber. In addition, when the AS-4 fibers were wet with the polyamic acid solution and imidized, the carboxylic acid photopeak at 289.0 eV and the carbonyl photopeak at 287.7 eV merged to form a single imide carbonyl peak at 288.3 eV, confirming that the carbon fiber tow is coated with LaRC polyamic acid during aqueous powder prepregging.

The oxygen 1s photopeaks contained curves at 532.0, 533.7 and 535.7 eV attributed to O=C, O-C, and adsorbed water, respectively. The water peak at 535.7 eV was only present when the AS-4 carbon fiber tow was dried under ambient conditions. When the polyamic acid fiber coating and the polyamic acid film were imidized, there was only one peak resolved from the oxygen 1s and nitrogen 1s envelopes: an O=C peak at 532.0 eV and an imide nitrogen peak at 400.4 eV. When the "as received" AS-4 carbon fibers were exposed independently to water, ammonium hydroxide, or imidization conditions the binding energy and the shape of the carbon 1s and nitrogen 1s photopeaks were unchanged. The variation in the oxygen 1s lineshapes, shown in Figure 2.80, was attributed to adsorbed water.

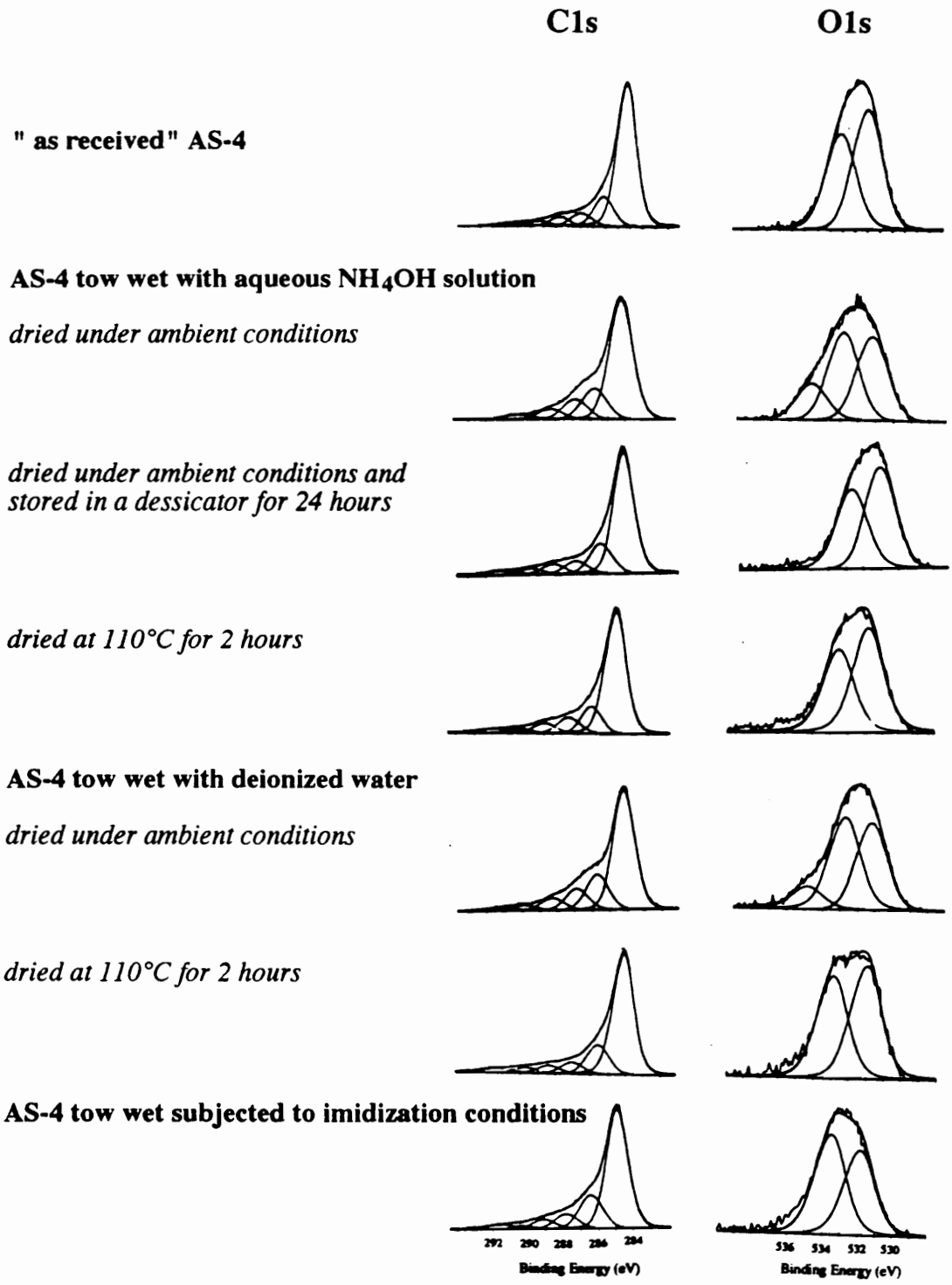

Figure 2.80. Curve-fit carbon 1s and oxygen 1s photopeaks of the "as received" AS-4 carbon fiber tow and the AS-4 carbon fiber tow exposed independently to water, ammonium hydroxide, and imidization conditions.

2.3.3.2 Fiber Topography and Coating Mechanism

When the AS-4 carbon fiber tow was wet with the polyamic acid solution and dried, the tow stiffened and the individual fibers were held tightly together. The scanning electron photomicrographs in Figure 2.81 show the LaRC-TPI polymer coating the fibers. Polymer was not deposited on individual fibers when they were wet with the polyamic acid solution. Therefore, since the polymer will only coat a bundle of fibers, capillary forces must hold the polyamic acid solution around the fibers and, the polymer is deposited on the fibers as the tow dries.

2.4. SUMMARY

The surface chemical composition, topography, tensile strength, and surface energy of "as received" AU-4 and AS-4 carbon fibers were evaluated. The commercial surface treatment which converted the AU-4 to the AS-4 fiber oxidized the carbon fiber surface. Air, oxygen, and ammonia plasma treatments were used to modify the carbon fiber surface. Following short plasma exposures (15 sec. to 1 min.) the carbon fiber surface atomic composition reached a steady state due to either saturation of the active sites on the fiber surface or equivalence of the rate of incorporation and the rate of removal of oxygen- and nitrogen-containing functional groups. Angle dependent XPS revealed that the air and ammonia plasmas only affected the outermost surface of the fiber. An ethylene plasma was used to deposit a layer of plasma polymer on the carbon fiber surface. The ethylene plasma polymer was crosslinked and contained some hydroxyl and carbonyl functional groups.

Fifteen second air and oxygen plasma treatments increased the surface oxygen concentration from 9 to 20 atomic%. A one minute ammonia plasma treatment increased the fiber surface nitrogen content from 3 to 5 atomic%. The curve-fit carbon 1s and nitrogen 1s photopeaks indicated that the air and oxygen plasmas increased the

(a)

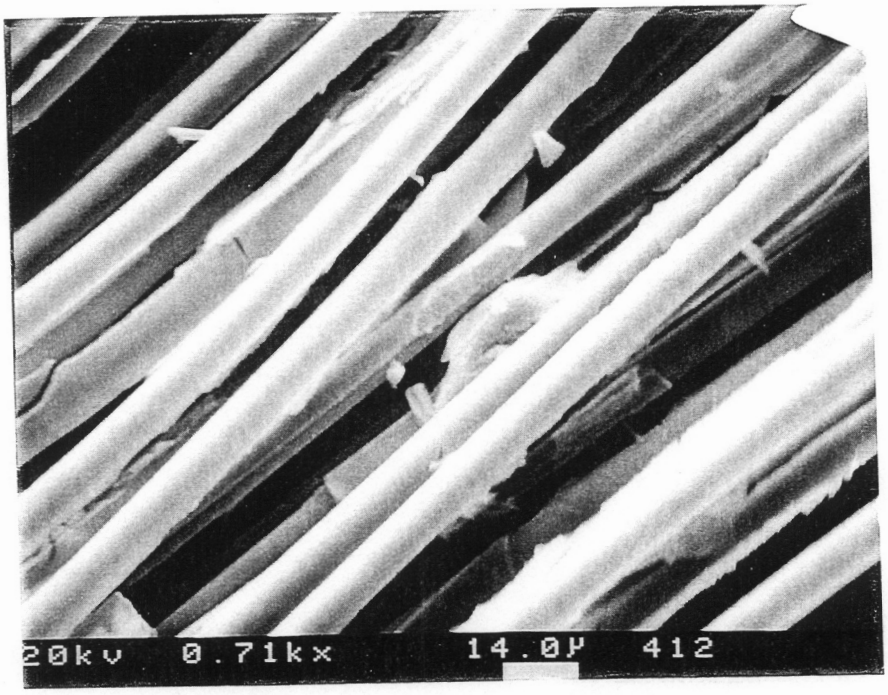

(b)

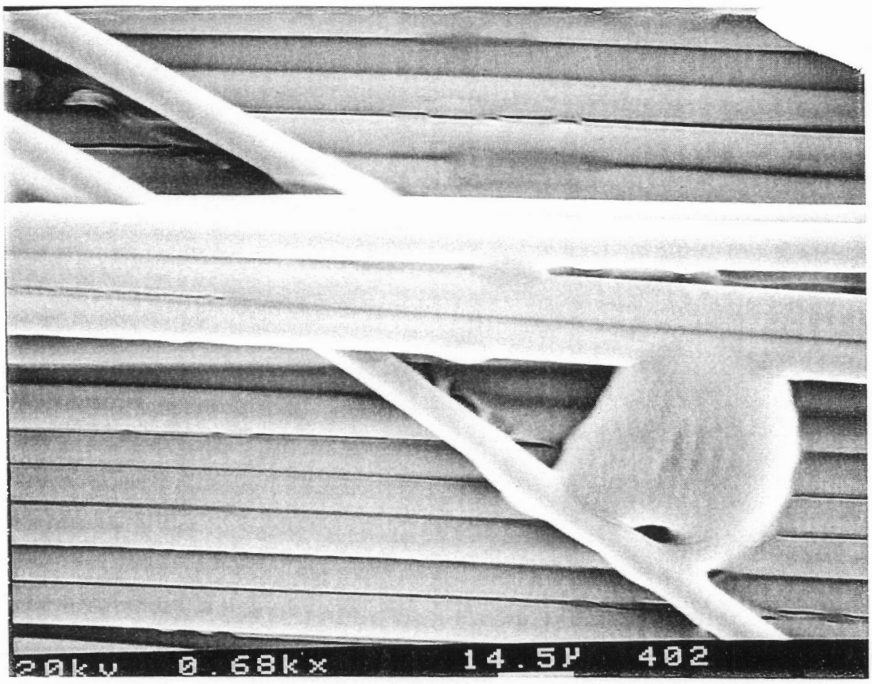

Figure 2.81. SEM photomicrographs of the AS-4 carbon fiber tow wet with the aqueous LaRC-TPI polyamic acid solution and (a) dried under ambient conditions (710X) and (b) imidized (680X).

concentration of oxygen-containing functional groups on the carbon fiber surface. The ammonia plasma increased the number of amine groups on the carbon fiber surface and decreased the concentration of oxygen-containing functional groups.

Both one-liquid and two-liquid wetting techniques were used to determine the total, dispersive, and polar surface energies of untreated, commercially surface treated, and plasma treated carbon fibers. With both wetting techniques, the polar component of the fiber surface energy increased as the concentration of the oxygen and nitrogen on the carbon fiber surface was increased. When the one-liquid technique was used, the dispersive surface energy was not affected by the fiber surface treatements. However, with the two-liquid technique, the dispersive component increased following ammonia plasma treatment.

The AS-4 carbon fiber tow was wet with an aqueous poly(amic acid) solution in which the matrix powder is dispersed during aqueous suspension prepregging of thermoplastic matrix composites. XPS and SEM analysis of the tow revealed that the fibers were coated with a layer of poly(amic acid). It was found that the mechanical properties of aqueous suspension prepregged thermoplastic composites are affected by the choice of poly(amic acid) dispersant. Apparently, the poly(amic acid) dispersant coats the fiber tow during prepregging and creates a distinct interphase between the fiber and matrix.

2.5 REFERENCES

1. L. H. Sharpe, *Proceedings of NATO-ASI on The Interfacial Interactions in Polymeric Composites*, June 15-26, 1992.

2. J. R. Huntsberger in Adhesion and Cohesion-Vol. 1, R. L. Patrick (ed.) Marcel Dekker, New York (1967).

3. D. H. Kaelble, Physical Chemistry of Adhesion, Wiley-Interscience, New York (1971) 450.

4. F. M. Fowkes in Treatise on Adhesion and Adhesives-Vol.1, R. L. Patrick (ed.), Marcel Dekker, New York (1967) 325.

5. M. Morra, E. Occhiello, and F. Garbassi, *Adv. in Colloid and Interface Science* **32** (1990) 79.

6. A. W. Adamson Physical Chemistry of Surfaces, 5th ed., Wiley-Interscience, New York (1990).

7. K. W. Allen, *J. Adhesion* **21** (1987) 261.

8. W. A. Zisman, J. J. Bikerman, I. Skeist, and R. F. Blomquist in Encyclopedia of Polymer Science and Engineering-Vol.1, 2nd ed., H. F. Mark, N. M. Bikales, C. G. Overberger, and G. Menges (eds.), Wiley-Interscience, New York (1985) 477.

9. D. J. Shaw, Introduction to Colloid and Surface Chemistry, 3rd. ed., Butterworths, London, (1980).

10. A. N. Gent and G. R. Hamed in Handbook of Adhesives, 3rd ed., I. Skeist (ed.), Van Nostrand Reinhold, New York (1990) 39.

11. L. H. Sharpe, *J. Adhesion* **4** (1972) 51.

12. E. M. Borroff and W. C. Wake, *Trans. Inst. Rubber Industry* **25** (1949) 199 and 210.

13. D. E. Packham in Aspects of Adhesion 7, D. J. Alner and K. W. Allen (eds.), Transcripta Books, London (1973) 51.

14. J. D. Venables in Adhesion 7, K. W. Allen (ed.), Applied Science, London (1983) 87.

15. J. D. Venables, *J. Materials Sci.* **19** (1984) 2431.

16. S. S. Voyutskii in Autohesion and Adhesion of High Polymers-Vol. 4, V. Vakula (ed.), Wiley-Interscience, New York (1963).

17. B. V. Deryaguin, *Research* **8** (1955) 70.

18. J.J. Bikerman, The Science of Adhesive Joints, 2nd ed., Academic Press, New York (1968).

19. L. H. Sharpe, *J. Adhesion* **6** (1974) 15.

20. W. D. Bascom in International Encyclopedia of Composites-Vol. 2, S. M. Lee (ed.), VCH Publishers, New York (1991) 411.

21. P. J. Herrera-Franco and L. T. Drzal, *Composites* **23**(1) (1992) 2.

22. L. T. Drzal in Controlled Interphases in Composite Materials, H. Ishida (ed.), Elsevier Science, New York (1990) 309.

23. M. Nardin and J. Schultz, *Proceedings of NATO-ASI on The Interfacial Interactions in Polymeric Composites*, June 15-26, 1992.

24. ASTM D. 2344-76.

25. N. Iosipescu, *J. of Materials* **2** (3) (1967) 537.

26. ASTM D 3518.

27. I. Verpoest, M. Desaeger, R. Keunings in Controlled Interphases in Composite Materials, H. Ishida (ed.) Elsevier Science, New York (1990) 653.

28. M. K. Tse, *SAMPE J.* (Sept./Oct. 1985) 11.

29. A. N. Netravali, D. Stone, S. Ruoff, and L. T. T. Topoleski, *Compos. Sci. Technol.* **34** (1989) 289.

30. J. J. Lesko, Masters Thesis, Virginia Polytechnic Institute and State University, Blacksburg, Virginia (1991).

31. U. Gaur and B. Miller, *Comp. Sci. Technol.* **34** (1989) 35.

32. L. T. Drzal, M. J. Rich, and P. F. Lloyd, *J. Adhesion* **16** (1982) 1.

33. J. M. Whitney and L. T. Drzal in Toughened Composites, N. Johnston (ed.), ASTM, Houston, TX (1985) 179.

34. A. S. Wimolkiatisak and J. P. Bell, *Polym. Comp.* **10** (3) (1989) 1373.

35. I. Narisawa and H. Oba, *J. Mater. Sci.* **1** (1984) 1777.

36. J. P. Favre and D. Jaques, *J. Mater. Sci.* **25** (1990) 1373.

37. V. Rao and L. T. Drzal, *Polym. Comp.* **12** (1) (1991) 48.

38. J. Schultz, L. Lavielle, and C. Martin, *J. Adhesion* **23** (1987) 45.

39. L. T. Drzal M. J. Rich, M. F. Koenig, and P. F. Lloyd, *J. Adhesion* **16** (1983) 133.

40. W. D. Bascom and R. M. Jensen, *J. Adhesion* **19** (1986) 219.

41. S. M. Lee and S. Holguin, *J. Adhesion* **31** (1990) 91.

42. A. N. Netravali, L. T. T. Topoleski, W. H. Sachse, and S. L. Phoenix, *Comp. Sci. Technol.* **35** (1989) 13.

43. A. T. DiBenedetto, *Comp. Sci. Technol.* **42** (1991) 103.

44. L. T. Drzal, M. C. Waterbury, and M. Madhukar, *37th Int. SAMPE Symp.* (1992) 770.

45. J. C. Figueroa, T. E. Carney, L. S. Schadler, and C. Laird, *Comp. Sci. Technol.* **42** (1991) 77.

46. X. S. Bian, L. Ambrosio, J. M. Kenny, L. Nicolais, E. Occhiello, M. Morra, F. Garbassi, and A. T. Dibenedetto, *J. Adhesion Sci. Technol.* **5** (5) (1991) 377.

47. G. Merle and M. Xie, *Comp. Sci. Technol.* **40** (1991) 19.

48. V. Rao and L. T. Drzal, *J. Adhesion* **37** (1992) 83.

49. H. F. Wu, G. Biresaw, and J. T. Laemmle, *Polymer Composites*, **12** (4) (1991) 281.

50. W. G. Pitt, J. E. Lakenan, A. B. Strong, *J. Thermoplastic Comp. Mat.*

51. T. A. DeVilbiss, Ph.D. Dissertation, Virginia Polytechnic Institute and State University, Blacksburg, Virginia (1987).

52. W. A. Frazer, F. H. Ancker, A. T. DiBenedetto, and B. Elbirli, *Polymer Composites* **4** (1983) 238.

53. T. Oshawa, A. Nakayama, M. Miwa, and A. Hasegawa, *J. Appl. Polym. Sci.* **22** (1978) 3203.

54. V. Rao, P. Herrera-Franco, A. D. Ozzello, and L. T. Drzal, *J. Adhesion* **34** (1991) 65.

55. D. H. Grande, J. F. Mandell, and H. C. C. Hong, *J. Mater. Sci.*, **12** (1988) 311.

56. M. K. Tse, *30th Nat. SAMPE Symp.* **30** (1985) 247.

57. J. F. Mandell, E. J. H. Chen, and F. J. McGarry, *Int. J. Adhesion and Adhesives* **1** (1) (1980) 40.

58. E. J. H. Chen and J. C. Young, *Comp. Sci. Technol.* **42** (1991) 189.

59. B. Miller, P. Muri, and L. Rebenfeld, *Compos. Sci. Technol.* **18** (1987) 17.

60. L. S. Penn and C. T. Chou, *J. Comp. Technol. & Res.* **12** (3) (1990) 164.

61. Y. L. Hsieh, M. Wu, and D. Andres, J. *Colloid Interf. Sci.* **144** (1) (1991) 127.

62. Y. L. Hsieh, S. Xu, and M. Hartzell, *J. Adhesion Sci. Technol.* **2** (12) (1991) 1023.

63. P. Commerçon and J. P. Wightman, *J. Adhesion* **38** (1992) 55.

64. L. S. Penn and B. Jutis, *J. Adhesion* **30** (1989) 67.

65. C. T. Chou and L. S. Penn, *J. Adhesion* **36** (1991) 125.

66. K. Küpper and P. Schwartz, *J. Adhesion Sci. Technol.* **5** (2) (1991) 165.

67. U. Gaur, G. Desio, and B. Miller, *Plastics Engineering* (Oct. 1989) 43.

68. B. Miller, U. Gaur, and D. E. Hirt, *Comp. Sci. Technol.* **42** (1991) 207.

69. U. Gaur and B. Miller in Controlled Interphases in Composite Materials, H. Ishida (ed.), Elsevier Science, New York (1990) 723.

70. S. L. Chuang and N. J. Chu, *J. Appl. Polym. Sci.* **41** (1990) 373.

71. V. Rao and L. T. Drzal, *J. Adhesion* **35** (1991) 245.

72. E. Mäder and K. H. Freitag, *Composites* **21** (5) (1990) 397.

73. J. P. Favre and J. Perrin, *J. Mater. Sci.* **7** (1972) 1113.

74. P. S. Chua and M. R. Piggott, *Comp. Sci. Technol.* **22** (1985) 107.

75. J. P. Favre and M. C. Merienne, *Int. J. Adhesion and Adhesives* (Oct. 1981) 311.

76. P. S. Chua and M. R. Piggott, *Comp. Sci. Technol.* **22** (1985) 185.

77. P. Marshall and J. Price, *Composites* **22** (1) (1991) 53.

78. D. N. Hild and P. Schwartz, *J. Adhesion Sci. Technol.* **6** (8) (1992) 897.

79. M. R. Piggott, *Int. SAMPE Symp.* **36** (1991) 1773.

80. M. R. Piggott and D. Adison, *J. Reinf. Plast. and Comp.* **6** (1987) 290.

81. M. R. Piggott and M. M. Reboredo, *34th Int. SAMPE Symp.* (1989) 1913.

82. L. S. Penn and C. T. Chou, *J. Comp. Tech. and Res.* **12** (3) (1990) 164.

83. M. J. Pikethly and J. B. Doble, *Composites* **21** (5) (1990) 389.

84. M. J. Pikethly and J. B. Doble in Interfacial Phenomena in Composite Materials, F. R. Jones (ed.) Butterworths, London (1989) 35.

85. R. V. Subraminian, J. J. Jakubowski, and F. D. Williams, *J. Adhesion* **9** (1978) 185.

86. D. B. Eagles, B. F. Blumentritt, and S. L. Cooper, *J. Appl. Polym. Sci.* **20** (1976) 435.

87. N. H. Ladizesky and I. M. Ward, *J. Mater. Sci.* **18** (1983) 533.

88. L. S. Penn, F. A. Bystry, and H. J. Marchionni, *Polymer Composites* **4** (1983) 26.

89. L. J. Broutman in Interfaces in Composites, ASTM STP 452, American Society for Testing and Materials (1969) 27.

90. L. J. Broutman, *Polym. Eng. Sci.* **6** (1966) 263.

91. Y. Qiu and P. Schwartz, *J. Adhesion Sci. Technol.* **5** (9) (1991) 741.

92. C. Galiotis, *Compos. Sci. Technol.* **42** (1991) 125.

93. A. I. Sviridenok, T. K. Sirotina, and E. V. Pisanova, *J. Adhesion Sci. Technol.* **5** (1991) 229.

94. T. R. King, D. F. Adams, D. A. Buttry, *Composites* **22** (5) (1991) 380.

95. W. Wenig and T. Schöller, *Colloid Polym. Sci.* **269** (1991) 1212.

96. A. G. Evans, F. W. Zok, and J. Davis, *Comp. Sci. Technol.* **42** (1991) 3.

97. E. Fitzer, K. H. Geigl, W. Hüttner, and R. Weiss, *Carbon* **18** (1980) 389.

98. B. Z. Jang, *Comp. Sci. Technol.* **44** (1992) 333.

99. S. M. Lee, *Comp. Sci. Technol.* **43** (1992) 317.

100. A. Khelawan and M. R. Piggott in Surface Engineering, S. A. Meguid (ed.), Elsevier Apllied Science, New York, 1990, 113.

101. S. Lehmann, C. Megerdigian, R. Papalia, *30th Nat. SAMPE Symp.* **30** (1985) 290.

102. C. Megerdigian, R. Robinson, and S. Lehmann, *32nd Int. SAMPE Symp.* **32** (1987) 1126.

103. H. W. Rhee and J. P. Bell, *Polymer Composites*, **12** (4) (1991) 213.

104. W. Weisweiler, *Proceedings of NATO-ASI on "The Interfacial Interactions in Polymeric Composites"* (June 15-26, 1992).

105. M. J. Pitkethly and J. B. Doble in Controlled Interphases in Composite Materials, H. Ishida (ed.), Elsevier Science, New York (1990) 809.

106. R. E. Allred and L. A. Harrah, *34th Int. SAMPE Symp.* **34** (1989) 2559.

107. G. Désarmot and J. P. Favre, *Comp. Sci. Tech.* **42** (1991) 151.

108. R. H. Norman, D. I. James, and G. M. Gale, *The Chemical Engineer (Trans. Inst. Chem. Engineering)* **182** (October 1964) 243.

109. F. J. Schmidt, I. J. Hess, C. H. Esola, and A. G. Buschow in *Materials and Processes for the 1970s, Proceedings of the 15th Nat. SAMPE Symp. and Exh.*, SAMPE, North Hollywood (1969) 117.

110. G. D. Andreevskaya and Yu. A. Gorbatkina, *Ind. Eng. Chem., Prod. Res. Devel.* **11** (1) (1972) 24.

111. R. V. deVekey and A. J. Majumdar, *Magazine of Concrete Research* **20**(65) (1968) 229.

112. A. Kelly and W. R. Tyson, *J. Mech. Phys. Solids* **13** (1965) 329.

113. L. S. Penn and S. M. Lee, *J. Composites Technol. Res.* **11**(1) (Spring 1989) 23.

114. L. S. Penn, G. C. Tesoro, H. X. Zhou, *Polymer Composites* **9** (3) (1988) 184.

115. U. Gaur and B. Miller, *Compos. Sci. Technol.* **34** (1989) 35.

116. L. B. Greszczuk in Interfaces in Composites, ASTM STP 452, American Society for Testing and Materials (1969) 42.

117. P. Lawrence, *J. Mater. Sci.* **7** (1972) 1.

118. A. Takaku and R. G. C. Arridge, *J. Phys. D: Appl. Phys.* **6** (1973) 2038.

119. R. J. Gray, *J. Mater. Sci.* **19** (1984) 861.

120. V. Laws, *Composites* **13** (1982) 145.

121. J. Banbaji, *Compos. Sci. Technol.* **32** (1988) 183.

122. J. Banbaji, *Compos. Sci. Technol.* **32** (1988) 195.

123. P. S. Chua and M. R. Piggott, *Compos. Sci. Technol.* **22** (1985) 33.

124. M. R. Piggott, A. Sanadi, P. S. Chua, and D. Adison in Composite Interfaces, H. Ishida and J. L. Koenig (eds.), North-Holland, New York (1986) 109.

125. M. R. Piggott, *Compos. Sci. Technol.* **30** (1987) 295.

126. M. R. Piggott and S. R. Dai, *Compos. Sci. Technol.* **31** (1988) 15.

127. K. R. Jiang and L. S. Penn, *Compos. Sci. Technol.* **45** (1992) 89.

128. R. A. Haaksma and M. J. Cehelnik, *Proc. Mat. Res. Society* **170**, Material Res. Soc., Pittsburgh (1990) 71.

129. H. F. Wu and C. M. Claypool, *J. Mater. Sci. Lett.* **10** (1991) 269.

130. H. F. Wu and C. M. Claypool, J. *Mater. Sci. Lett.* **10** (1991) 1072.

131. B. J. Carrol, *Langmuir* **2** (1986) 248.

132. H. D. Wagner, *J. Appl. Phys.* **67** (3) (1990) 1352.

133. J. P. Riggs in International Encyclopedia of Composites-Vol. 1, S. M. Lee (ed.), VCH Publishers, New York (1990) 197.

134. D. M. Riggs, R. J. Shuford, and R. W. Lewis in Handbook of Composites, G. Lubin (ed.), Van Nostrand Reinhold (1982) 196.

135. R. N. Lee in International Encylopedia of Composites-Vol.1, S. M. Lee (ed.), VCH Publishers, New York (1990) 241.

136. W. P. Hoffman, W. C. Hurley, P. M. Liu, and T. W. Owens, *J. Mater. Res.* **6** (8) (1991)1685.

137. W. N. Reynolds, Physical Properties of Graphite, Elsevier, New York (1968).

138. A. K. Gupta, D. K. Paliwal, and P. Bajaj, *J. Macromol. Sci.-Rev. Macromol. Chem. Phys.* **C31** (1991) 1.

139. P. J. Goodhew, A. J. Clarke, and J. E. Bailey, *Mat. Sci. & Eng.*, **17** (1975) 3.

140. L. H. Peebles, Jr., Encyclopedia of Polymer Science & Technology-Vol.1, Wiley-Interscience, New York (1976) 1.

141. G. Henrici-Olivé and S. Olivé, *Adv. in Polym. Sci.*, **51** (1983) 1.

142. W. Watt in Handbook of Composites-Vol. 1, W. Watt and B. V. Perov (eds.) Elsevier Science (1985) 327.

143. J. P. Riggs in Encyclopedia. of Polymer Science & Engineering- Vol. 2, 2nd ed., H. F. Mark, N. M. Bikales, C. G. Overberger, and G. Menges (eds.), Wiley-Interscience, New York (1985) 640.

144. D. J. Thorne in Handbook of Composites-Vol.1, W. Watt and B. V. Perov (eds.), Elsevier Science (1985) 475.

145. E. Fitzer, W. Frohs, and M. Heine,*Carbon* **24** (1986) 387.

146. E. Fitzer, *Carbon* **27** (1989) 621.

147. S. Damodaran, P. Desai, and A. S. Abhiraman, *J. Textile Inst. (U.K.)* , special edition on composites (1991).

148. P. Rajalingam and G. Radhakrishnan, *J. Macromol. Sci. - Rev. Macromol. Chem. Phys.* **C31** (1991) 301.

149. Z. Bashir, *Carbon* **29** (1991) 1081.

150. R. J. Diefendorf and E. Tokarsky, *Polym Eng. Sci.* **15** (3) (1975) 150.

151. R. J. Diefendorf, W. C. Stevens, and S. H. Chen, *Fiber Producer* (Dec. 1979) 16.

152. W. Gerhartz (ed.), Ullmann's Encyclopedia of Industrial Chemistry-Vol. A11, 5th ed., VCH Publishers, Weinheim, Germany (1988) 42.

153. L. H. Peebles, Jr., Carbon Fibers: Formation, Structure and Properties, to be published by CRC Press, Inc.

154. J. B. Donnet and R. C. Bansal, Carbon Fibers, 2nd ed., Marcel Dekker, New York (1990).

155. M. Guigon , A, Oberlin and G. Desarmot, *Fiber Science & Techn.* **20** (1984) 177.

156. S. C. Bennett, *J. Materials Sci.*, **18** (1983) 3337.

157. P. Kwizera, M. S. Dresselhaus, D. R. Uhlmann, J. S. Perkins, and C. R. Desper, *Carbon* **20** (1982) 387.

158. R. Perret & W. Ruland, *J. Appl. Crystallogr.* **3** (1970) 525.

159. W. Ruland, *Polymer* **9** (1969) 1368.

160. W. Ruland, *J. Appl. Phys.* **38** (1967) 3583.

161. S. C. Bennett and D. J. Johnson, *Carbon* **17** (1979) 25.

162. F. R. Barnet & M. K. Norr, *Composites*, **7** (1976) 93.

163. A. Proctor and P. M. A. Sherwood, *J. Electron Spectro. and Related Phenom.* **27** (1982) 39.

164. J. Delmonte, Technology of Carbon and Graphite Fiber Composites, Van Nostrand Reinhold, New York (1981).

165. P. Ehrburger and J. B. Donnet in Handbook of Composites-Vol. 1, W. Watt and B. V. Perov (eds.), Elsevier (1985) 577.

166. W. W. Wright, *Composite Polymers* **3** (1990) 231.

167. W. W. Wright, *Composite Polymers* **3** (1990) 360.

168. T. A. DeVilbiss and J. P. Wightman in Composite Interfaces, H. Ishida (ed.), Elsevier Science (1986) 307.

169. J. B. Donnet and G. Guilpain, *Carbon* **27** (1989) 749.

170. N. L. Weinberg and T. B. Reddy, *J. Appl. Electrochem.* **3** (1973) 73.

171. J. Harvey, C. Kozlowski, and P. M. A. Sherwood, *J. Materials Sci.* **22** (1987) 1585.

172. C. Kozlowski and P. M. A. Sherwood, *Carbon* **25** (1987) 751.

173. F. Nakao, Y. Takenaka, and H. Asai, *Composites* **23** (5) (1992) 36.

174. F. R. Barnet and M. K. Norr, *Carbon* **11** (1973) 281.

175. J. B. Donnet, S. Dong, G. Guilpain, and M. Brendle in Interfaces in Polymer, Ceramic, and Metal Matrix Composites, H. Ishida (ed.), Elsevier Science (1988)

176. G. J. Farrow and C. Jones, to be published in *J. Adhesion.*

177. C. Jones and E. Sammann, *Carbon* **28** (1990) 509.

178. L. Y. Yuan, S. S. Shyu, and J. Y. Lai, *Compos. Sci. Technol.* **45** (1992) 9.

179. J. Su, X. Tao, Y. Wei, Z. Zhang, and L. Liu in Interfaces in Polymer, Ceramic, and Metal Matrix Composites, H. Ishida (ed.), Elsevier Science (1988) 269.

180. L. Y. Yuan, C. S. Chen, S. S. Shyu, and J. Y. Lai, *Compos. Sci. Technol.* **45** (1992) 1.

181. S. Mujin, H. Baorong, W. Yisheng, T. Ying, H. Weiqiu, and D. Youxian, *Compos. Sci. Technol.* **34** (1989) 353.

182. M. Morra, E. Occhiello, and F. Garbassi, *Compos. Sci. Technol.* **42** (1991) 361.

183. J. B. Donnet, M. Brendle, T. L. Dhami, and O. P. Bahl, *Carbon* **24** (1986) 757.

184. J. B. Donnet, T. L. Dhami, S. Dong, and M. J. Brendle, *Phys. D: Appl. Phys.* **20** (1987) 269.

185. C. Jones, *Carbon* **27** (1989) 487.

186. C. Jones and E. Sammann, *Carbon* **28** (1990) 515.

187. H. H. Madden and R. E. Allred, *J. Vac. Sci. Technol.* **A4** (1986) 1705.

188. S. P. Wesson and R. E. Allred in Inverse Gas Chromatography, Characterization of Polymers and Other Materials, D. R. Lloyd, T. C. Ward, and H. P. Schreiber (eds.), ACS Symposium Series, No. 391, Amer. Chem. Soc., Washington, D.C. (1988) 203.

189. S. P. Wesson and R. E. Allred, *J. Adhesion Sci. Technol.* **4** (1990) 277.

190. W. Weisweiler, *Proc. of NATO-ASI on the Interfacial Interaction in Polymeric Composites*, June 15-26, 1992.

191. C. Jones, *Compos. Sci. Technol.* **42** (1991) 275.

192. M. Morra, E. Occhiello, and F. Garbassi, *Colloid Polym. Sci.* **270** (1992) 58.

193. Y. Da, D. Wang, M. Sun, C. Chen, and J. Yue, *Compos. Sci. Technol.* **30** (1987) 119.

194. W. D. Bascom and W. J. Chen, *J. Adhesion* **34** (1991) 99.

195. D. Youxian, W. Dianxun, S. Mujin, C. Chuanzheng, and Y. Jin, *Compos. Sci. Technol.* **30** (1987) 119.

196. R. V. Subramanian, *Pure Appl. Chem.* **52** (1980) 1929.

197. A. Crasto, S. H. Own, and R. V. Subramanian in Composite Interfaces, H. Ishida and J. L. Koenig (eds.), North-Holland, New York (1986) 133.

198. H. T. Chiu and J. S. Lin, *J. Materials Sci.* **27** (1992) 319.

199. M. Itoi, Y. Yamada, and R. B. Pipes, *Polymer Composites* **13** (1) (1992) 15.

200. H. W. Rhee and J. P. Bell, *Polymer Composites* **12** (4) (1991) 213.

201. H. F. Wu, G. Biresaw, and J. T. Laemmle, *Polymer Composites* **12** (4) (1991) 281.

202. G. Wachinger in Controlled Interphases in Composite Materials, H. Ishida (ed.), Elsevier Science, New York (1990) 457.

203. C. M. Chan in International Encyclopedia of Composites-Vol. 5, S. M. Lee (ed.), VCH Publishers, New York (1991) 372.

204. J. P. Wightman, T. A. DeVilbiss, and J. G. Dillard in International Encyclopedia of Composites-Vol. 1, S. M. Lee (ed.), VCH Publishers, New York (1991) 226.

205. J. D. H. Hughes, *Compos. Sci. Technol.* **41** (1991) 13.

206. E. Fitzer and H. P. Rensch in Controlled Interphases in Composite Materials, H. Ishida (ed.), Elsevier Science, New York (1990) 241.

207. E. Desimoni, G. I. Casella, A. Morone, and A. M. Salvi, *Surf. Interf. Analysis* **15** (1990) 627.

208. E. Occhiello, F. Garbassi, M. Morra, and L. Nicolais, *Compos. Sci. Technol.* **36** (1989) 133.

209. J. B. Donnet and G. Guilpain, *Carbon* **27** (1989) 749.

210. J. P. Randin in Encyclopedia of Electrochemistry of the Elements, A. J. Bard (ed.), Marcel Dekker, New York (1976) 1.

211. L. T. Drzal, *Carbon* **15** (1977) 129.

212. C. Sellitti, J. L. Koenig, H. Ishida, *Carbon* **28** (1) (1990) 221.

213. E. M. Liston, *J. Adhesion* **30** (1989) 199.

214. H. V. Boenig, Plasma Science and Technology, Cornell Univ. Press, Ithaca, New York (1982).

215. A. T. Bell in Techniques and Applications of Plasma Chemistry, J. R. Hollahan and A. T. Bell (eds.), Wiley-Interscience, New York (1974) 1.

216. F. Garbassi and E. Occhiello in International Encyclopedia of Composites-Vol. 5, S. M. Lee (ed.), VCH Publishers, New York (1991) 390.

217. M. Hudis in Techniques and Application of Plasma Chemistry, J. R. Hollahan and A. T. Bell (eds.), Wiley-Interscience, New York (1974) 113.

218. H. Yasuda, Plasma Polymerization, Academic Press, Orlando, FL (1985).

219. D. T. Clark and A. Dilks, *J. Polym. Sci., Polym. Chem. Ed.* **15** (1977) 2321.

220. A. Inspecktor, J. E. Koresh, S. S. Barton, and M. J. B. Evans, *Carbon* **24** (1986) 325.

221. I. Loh, R. E. Cohen, and R. F. Baddour, *J. Materials Sci.* **22** (1987) 2937.

222. P. Commerçon, PhD. Dissertation, Virginia Polytechnic Institute and State University, Blacksburg, Virginia (1992).

223. Y. Z. Wei, Z. Q. Zhang, Y. Li, Z. H. Guo, B. L. Zheng in Controlled Interphases in Composite Materials, H. Ishida (ed.), Elsevier Science, New York (1990) 167.

224. P. Pattabiraman, N. M. Rodriguez, B. Z. Jang, and R. T. K. Baker, *Carbon* **28** (6) (1990) 867.

225. W. P. Hoffman, *Carbon* **30** (1992) 315.

226. A. Benatar and T. Gutowski, *Polym. Compos.* **7** (1986) 84.

227. A. T. Bell, *J. Macromol. Sci.-Chem.* **A10** (1976) 369.

228. Hercules technical data sheets.

229. J. R. Hollahan in Techniques and Applications of Plasma Chemistry, J. R. Hollahan and A. T. Bell (eds.), Wiley-Interscience, New York (1974) 229.

230. A. W. Czanderna, Methods of Surface Analysis, Elsevier Science, New York (1985).

231. A. Kumar and S. Hartland, *J. Colloid Interf. Sci.* **136** (2) (1990) 455.

232. J. Schultz, C. Cazeneuve, M. E. R. Shanahan, and J. B. Donnet, *J. Adhesion* **12** (1981) 221.

233. G. E. Hammer and L. T. Drzal, *Applic. of Surf. Sci.* **4** (1980) 340.

234. D. H. Kaelble, P. J. Dynes, and E. H. Cirlin, *J. Adhesion* **6** (1974) 23.

235. M. Weinberg in Toughened Composites, N. Johnston (ed.), ASTM STP 937, Houston, TX (1985) 166.

236. D. R. Lovell, Carbon and High Performance Fibers Directory, 5th ed., Chapman & Hall,

237. D. K. Owens and R. C. Wendt, *J. Appl. Polym. Sci.* **13** (1969) 1741.

238. P. J. Dynès and D. H. Kaelble, *J. Adhesion* **6** (1974) 195.

239. D. H. Kaelble and P. J. Dynes, *J. Adhesion* **6** (1974) 239.

240. D. H. Kaelble and K. C. Uy, *J. Adhesion* **2** (1970) 50.

241. F. M. Fowkes, *J. Adhesion Sci. Tehnol.* **1** (1987) 7.

242. M. E. R. Shanahan, C. Cazeneuve, A. Carré, and J. Schultz, *J. Chim. Phys.* **79** (1982) 241.

243. C. P. Beetz, Jr., *Fiber Science & Technology*, **16** (1982) 45.

244. K. J. Hook, R. K. Agrawal, and L. T. Drzal, *J. Adhesion* **32** (1990) 157.

245. L. Lavielle and J. Schultz, *Langmuir* **7** (1991) 978.

246. A. J. Vukov and D. G. Gray in Inverse Gas Chromatography, ACS Symposium Series 391, D. R. Lloyd, T. C. Ward, and H. P. Schreiber (eds.), ACS, Washington, D.C. (1989) 168.

247. S. P. Wilkinson, PhD dissertation, Virginia Polytechnic Institute & State University, Blacksburg, Virginia (1991).

248. E. Desimoni, G. I. Casella, T. R. I. Calaldi, A. M. Salvi, T. Rotunno, E. DiCroce, *Surf. Interf. Analysis* **18** (1992) 623.

249. G. Beamson and D. Briggs, High Resolution XPS of Organic Polymers, John Wiley & Sons, New York (1992).

250. A. Proctor and P. M. A. Sherwood, *J. Electron Spectrosc. Related Phenom.* **27** (1982) 39.

251. C. Kozlowski and P. M. A. Sherwood, *J. Chem. Soc., Faraday Trans.* **80** (1984) 2099.

252. C. Kozlowski and P. M. A. Sherwood, *J. Chem. Soc., Faraday Trans.* **81** (1987) 2745.

253. Y. Xie and P. M. A. Sherwood, *Chem. Mater.* **1** (1989) 427.

254. Y. Nakayama, F. Soeda, and A. Ishitani, *Carbon* **28** (1990) 21.

255. M. E. R. Shanahan and J. M. diMeglio, *Polymer Preprints, Am. Chem. Soc. Div. Polym. Chem.* **34** (1993) 286.

256. C. A. Arnold, D. Chen, Y. P. Chen, J. D. Graybeal, R. H. Bott, T. Yoon, B. E. McGrath, and J. E. McGrath, *Polymer Preprints, Am. Chem. Soc. Div. Polym. Mater. Sci. Eng.* **59** (1988) 934.

257. C. A. Arnold, D. H. Chen, Y. P. Chen, R. O. Waldbauer, M. E. Rogers, and J. E. McGrath, *High Perf. Polym.* **2** (2) (1990) 83.

258. N. J. Chou, C. H. Tang, J. Paraszczak, and E. Babich, *Appl. Phys. Lett.* **46** (1) (1985) 31.

259. C. D. Smith, H. Grubbs, H. F. Webster, A. Gungör, J. P. Wightman, and J. E. McGrath, *High Perf. Polym.* **3** (4) (1991) 211.

260. P. Marshall and J. Price, *Composites* **22** (5) (1991) 388.

261. J. B. Donnet and R. Y. Qin, *Carbon* **30** (5) (1992) 787.

262. W. P. Hoffman, W. C. Hurley, T. W. Owens, and H. T. Phan, *J. Materials Sci.* **26** (1991) 4545.

263. M. R. Havens, K. G. Mayhan, and W. J. James, *J. Appl. Polym. Sci.* **22** (1978) 2799.

264. W. N. Reynolds and J. V. Sharp, *Carbon* **12** (1974) 103.

265. M. Millard in Techniques and Applications of Plasma Chemistry, J. R. Hollahan and A. T. Bell (eds.), Wiley-Interscience, New York (1974) 177.

266. R. M. Davis, A. Texier, T. H. Yu, K. Lyon, A. Gungor, J. E. McGrath, and J. S. Riffle, *ACS Polymer Preprints* **33** (1) (1990) 416.

267. S. L. Chuang, N. J. Chu, and W. T. Whang, *J. Appl. Polym. Sci.* **41** (1990) 373.

268. J. W. Chin and J. P. Wightman, *J. Adhesion* **36** (1991) 25.

CHAPTER 3
EFFECT OF FIBER SURFACE TREATMENT ON CARBON FIBER/BISMALEIMIDE ADHESION

3.1 LITERATURE REVIEW

3.1.1 Bismaleimide Synthesis and Properties

Bismaleimides are a leading class of thermosetting polyimides. Thermosetting polyimides are low molecular weight, at least difunctional monomers or prepolymers, or mixtures thereof, which carry imide moities in their backbone structure and are terminated by reactive groups which undergo homo- and/or copolymerization by thermal or catalytic means [1]. Bismaleimides were developed to fill the demand for composite matrix resins with good processability and good thermal properties. Figure 3.1 illustrates how the bismaleimide use temperatures at short and long service times compare with the use temperatures of epoxies and polyimides [2].

Bismaleimides exhibit a balance of thermal and mechanical properties which make them popular for use in advanced composites, structural adhesives and in electronic applications [1, 3]. Bismaleimide resins are of interest because they process in a manner similar to epoxies, exhibit improved temperature resistance and hot-wet performance, and cure without the evolution of by-products [3]. However, brittleness and micro-crack formation in cured products are some of the problems attributed to the high crosslink density of bismaleimides [4]. Another problem is the relatively high melting temperature and narrow processing window of bismaleimide resins.

Recently, it was also discovered that, unlike epoxies, bismaleimide resin composites are subject to galvanic degradation. However, very specific conditions must exist for a bismaleimide composite to galvanically degrade. The bismaleimide composite must be

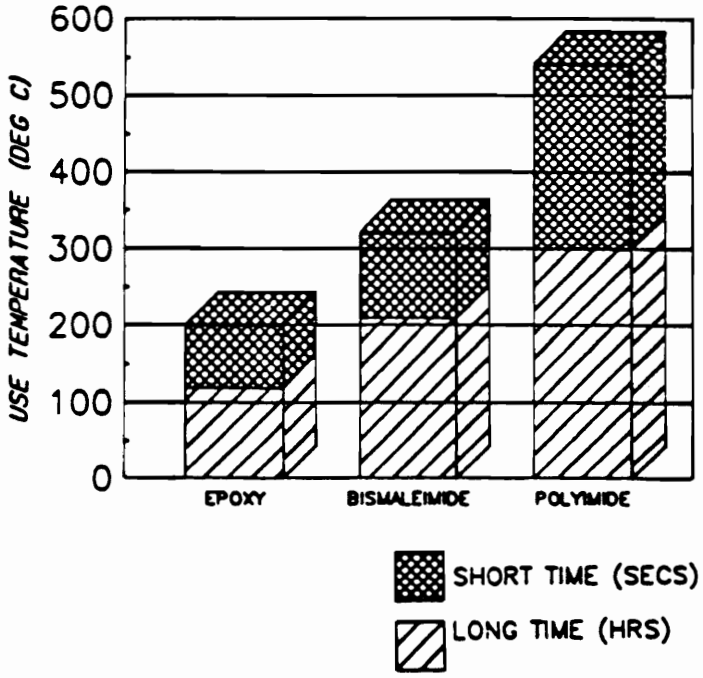

Figure 3.1. Use temperatures of resin matrix composites [2].

electrically conductive and be in physical contact with an actively corroding metal in the presence of both an electrolyte and oxygen [5].

Stenzenberger stated that future application of bismaleimides as composite matrix resins and as adhesives requires improvements in their temperature capability, toughness and stability in hot-wet environments [3]. Research must be concentrated in the synthesis of new bismaleimide building blocks, new bismaleimide co-monomer chemistry for linear extension of the polymer chain, synthesis of new co-monomers for bismaleimides, study of the fiber surface chemistry for improved fiber/resin adhesion, and bismaleimide-reactive elastomer copolymerization for improved adhesive systems [3].

Bismaleimides are synthesized by reacting a diamine with maleic anhydride [3, 6]. Aromatic diamines are used to produce high temperature performance bismaleimides. A wide variety of bismaleimides with tailored properties have been synthesized by changing the structure and molecular weight of the precursor diamine. The driving force behind the development of new bismaleimides is the need for high temperature imide polymers with convenient processability and good thermal properties. Unfortunately, as thermal properties are increased, the ease of processability of the resin is often reduced [7].

Table 3.1 shows the chemical structure, melting temperature, the maximum in the cure exotherm, and the heat of cure for some bismaleimides [1]. In general, bismaleimides based on aromatic diamines are crystalline materials with high melting points and narrow processing windows between the melting temperature and the onset of the exothermic cure reactions [3]. Once the bismaleimide resin melts, it immediately begins to cure, making processing difficult. Commercially available bismaleimide resins are low molecular weight and are based on inexpensive aromatic diamines. The most widely used commercial bismaleimide is 4,4'-bismaleimidodiphenylmethane. The precursor diamine, methylene dianiline, is readily available at low cost [1]. In order to

Table 3.1. Properties of bismaleimides [1].

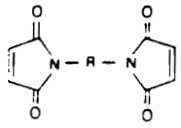

—R—	DSC Data[1] Mp (°C)	T_{MAX}[2] (°C)	$\Delta H_{pol.}$[3] (J/g)
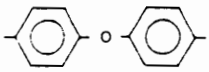	173–176	286	135
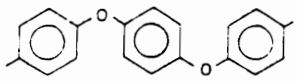	239	252	187
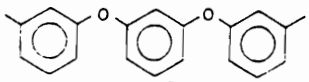	163	254	221
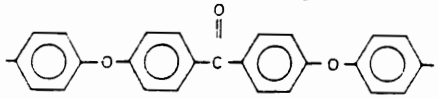	239	250	160–180
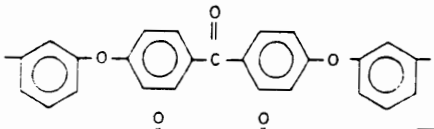	85–91	304	222
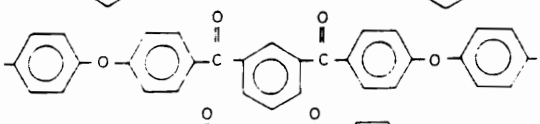	226	285	113
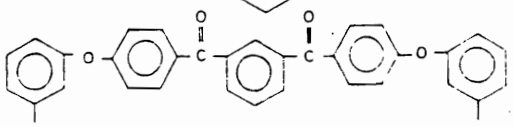	60–65	314	224

1 DSC = Differential Scanning Calorimetry, heating rate 10 C min
2 T_{MAX} = cure exotherm peak maximum
3 $\Delta H_{pol.}$ = heat of polymerisation
[A] Data generated by Technochemie GmbH — Verfahrenstechnik

Table 3.1. Properties of bismaleimides (cont.) [1].

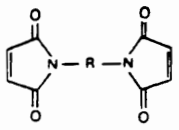

—R—	Mp (°C)	DSC DATA[1] T_{MAX}[2] (°C)	DSC DATA[1] ΔH_{pol}[3] (J/g)
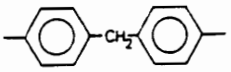	155–157	235	198
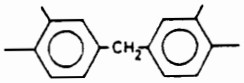	195–196	NA	NA
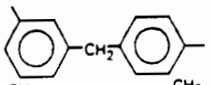	164–165	NA	NA
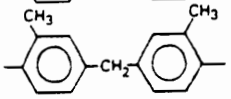	210–212	NA	NA
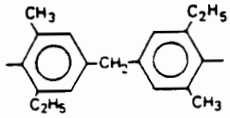	150–154	298	187
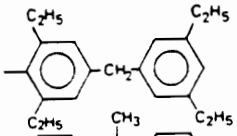	149–151	328	206
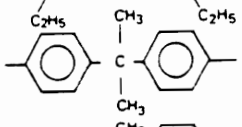	235	290	216
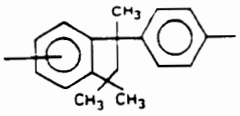	90–100	203	89

1 DSC = Differential Scanning Calorimetry, heating rate 10°C/min
2 T_{MAX} = cure exotherm peak maximum
3 ΔH_{pol} = heat of polymerisation
A Data generated by Technochemie GmbH-Verfahrenstechnik
NA Data not published

fulfill the processing requirements, bismaleimides are often formulated for use as highly concentrated solutions or hot melts.

One means to toughen a bismaleimide, reduce the melting point, and improve the processability is to extend the length of the polymer chain between crosslinks and decrease the crosslink density [8]. Bismaleimides are often toughened by copolymerizing the bismaleimide with a low melting monomer via a linear chain extension. This decreases the crosslink density in the cured material [9]. Diallylphenyl and allylphenol are used extensively as reactive diluents in commercial bismaleimide resin systems. Allylphenyl and allylphenol, which are liquid at room temperature, decrease the viscosity of the bismaleimide resin and copolymerize with the bismaleimide to increase the molecular weight between crosslinks [1, 10]. Bismaleimides have also been copolymerized with dienes, dithiols, diamines, triazines, and epoxies [1]. Thermoplastic polymers of varying molecular weight, with both reactive and nonreactive end groups, have also been used to toughen bismaleimides [11-18].

3.1.2 Bis(3-maleimido phenoxy) triphenylphosphine oxide

Bis(3-maleimido phenoxy) triphenylphosphine oxide (BMPPO) was synthesized by Wood and McGrath by reacting bis(3-amino phenoxy) triphenylphosphine oxide (BAPPO) and maleic anhydride in acetone using acetic anhydride and sodium acetate as catalysts. The reaction scheme is shown in Figure 3.2 [19]. The BAPPO precursor material was synthesized by reacting bis(4-fluoro benzoyl) benzene with m-aminophenol in DMAC and toluene (80% DMAC:20% toluene v/v) using K_2CO_3 as a catalyst [20].

The differential scanning calorimetry scan, in Figure 3.3, showed that the BMPPO bismaleimide melts at 92°C and cures at temperatures exceeding 180°C. Therefore, unlike the methylene dianiline-based bismaleimides which begin to cure almost immediately upon melting, the BMPPO bismaleimide has a practical processing window.

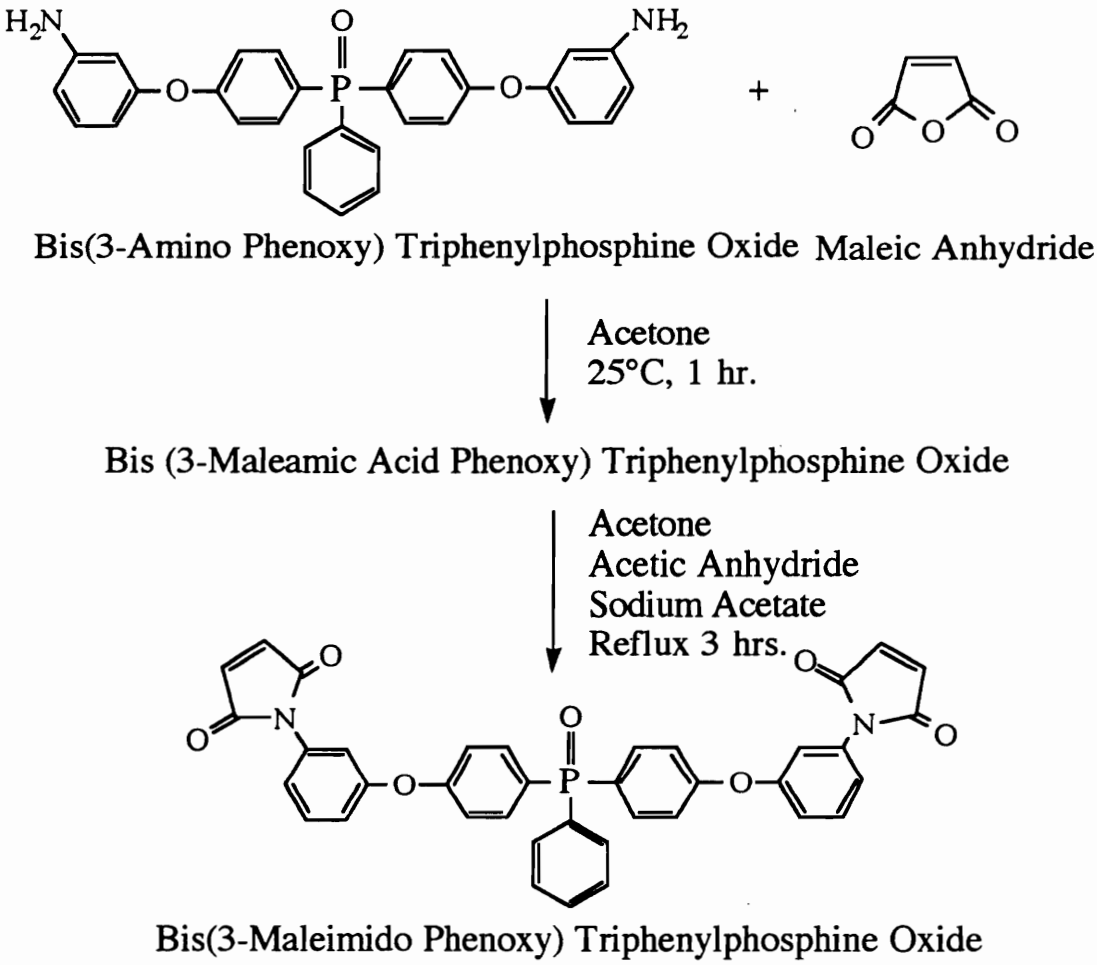

Figure 3.2. Synthesis of bis(3-maleimido phenoxy) triphenylphosphine oxide [19].

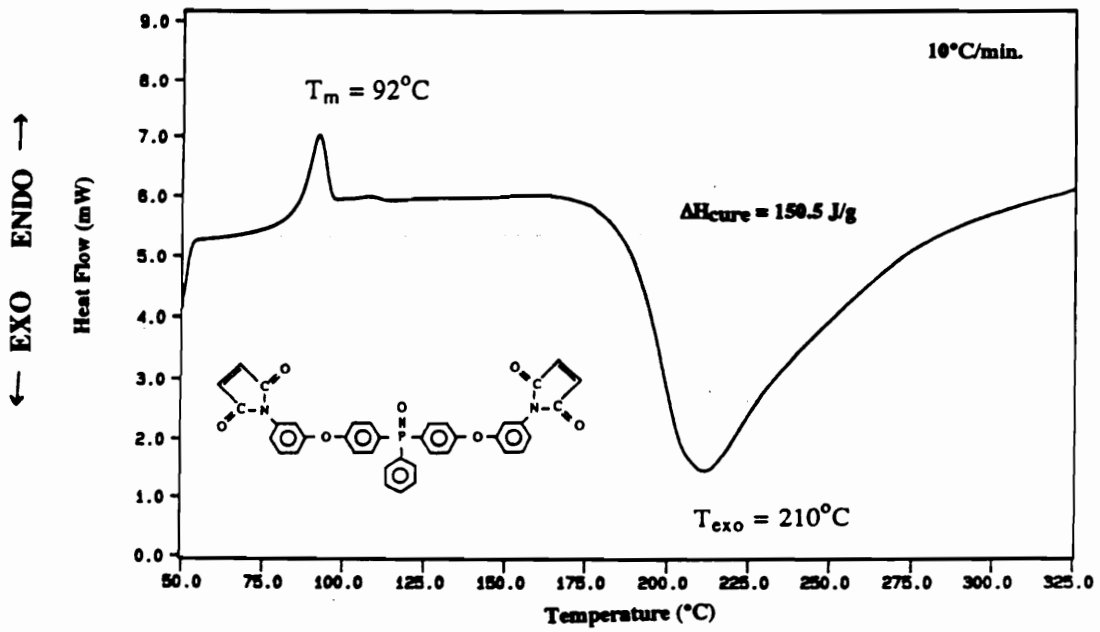

Figure 3.3. Differential scanning calorimetry scan of the BMPPO bismaleimide [19].

The fully cured BMPPO bismaleimide has a glass transition temperature around 360°C, as demonstrated by the large scale decrease in modulus seen in the thermomechanical and dynamic mechanical analysis scans in Figure 3.4. The thermogravimetric analysis results in Figure 3.5 showed that the fully cured BMPPO bismaleimide is stable in air at 300°C for at least 12 hours. A significant amount of char remained at 800°C during the thermogravimetric analysis.

The formation of char was previously correlated with the flame resistance of many polymers [21]. Smith et al. reported that when phosphine oxide is incorporated into the backbone of poly(arylene ether)s a substantial amount of char remained when the polymer was heated to 800°C [22]. These phosphine-oxide containing polymers showed excellent self-extinguishing characteristics and resistance to oxygen plasma relative to other engineering thermoplastics. A phosphorus-containing bismaleimide with outstanding non-flammability characteristics was synthesized by Varma and coworkers from bis(3-aminophenyl) methyl phosphine oxide [23]. In addition to imparting flame retardancy and resistance to atomic oxygen attack, the presence of phosphorus in a polymer also improves adhesion of the polymer to metals [24].

3.1.3 Cure Reaction

Bismaleimides may be crosslinked thermally or chemically [1, 3]. Figure 3.6 shows the thermal and chemical crosslinking pathways for bismaleimide polymerization through the electron deficient double bonds. The reactivity of the maleimide double bond is a consequence of the electron-withdrawing nature of the two adjacent carbonyl groups [3]. Figure 3.7 demonstrates the reactivity of the maleimide double bond. When heated above their melting points to 149-399°C, bismaleimides undergo a radical-type homopolymerization and form highly crosslinked polymers. The chemical crosslinking pathway is a nucleophilic Michael addition. Nucleophilic (electron-donating) species

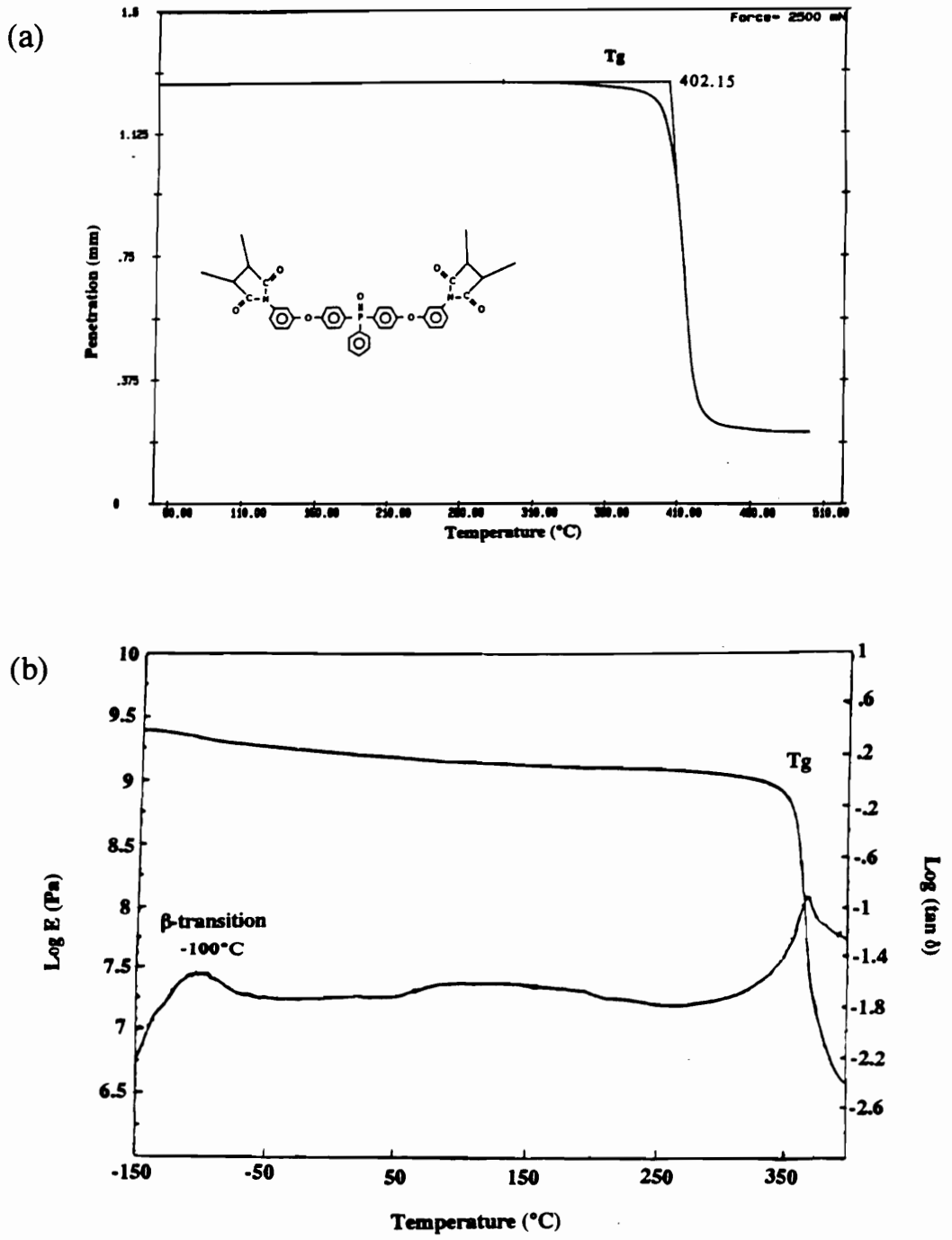

Figure 3.4. (a) Thermomechanical analysis and (b) dynamic mechanical analysis of the fully cured BMPPO bismaleimide [19].

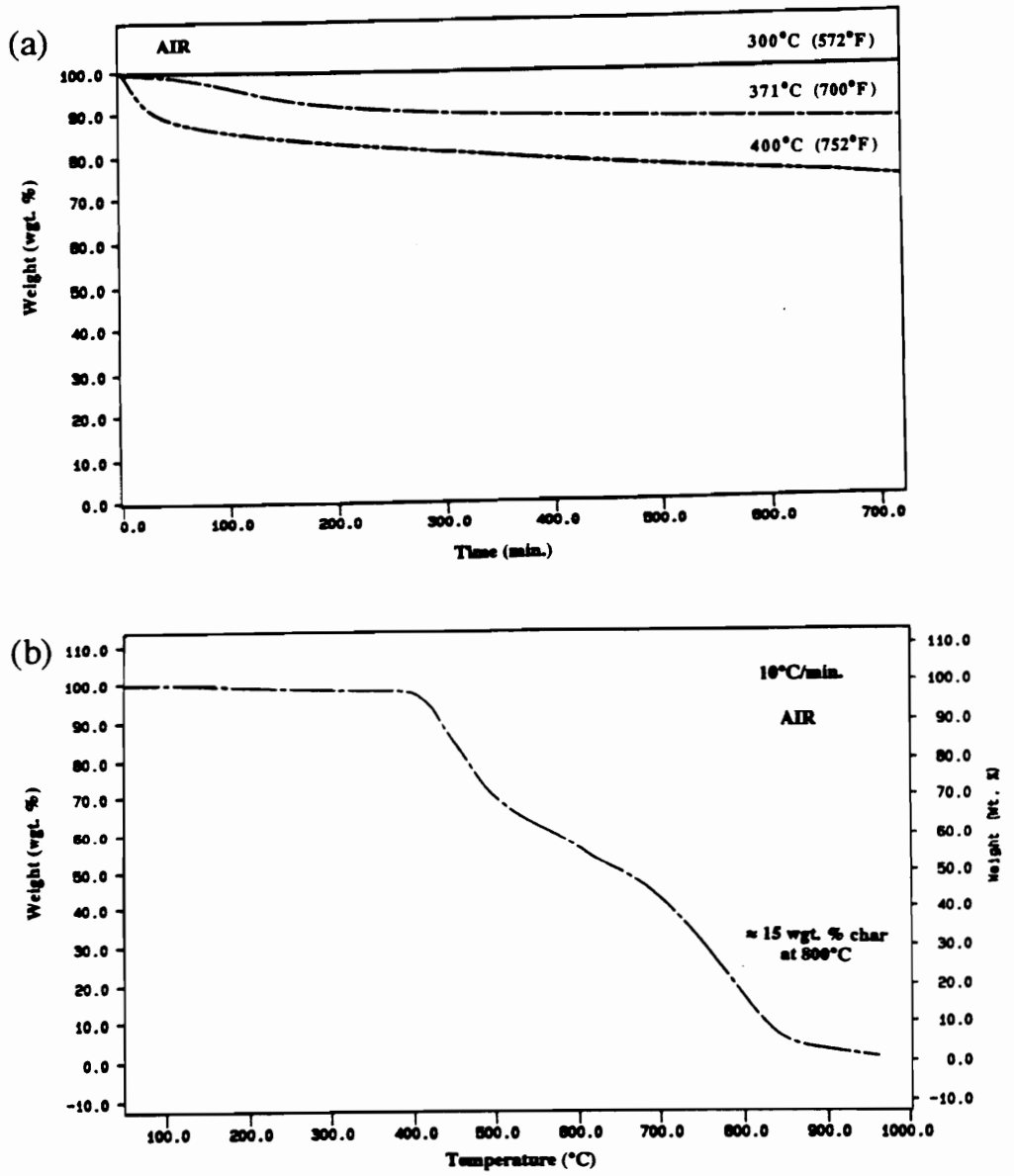

Figure 3.5. (a) Isothermal and (b) dynamic thermogravimetric analysis in air of the fully cured BMPPO bismaleimide [19].

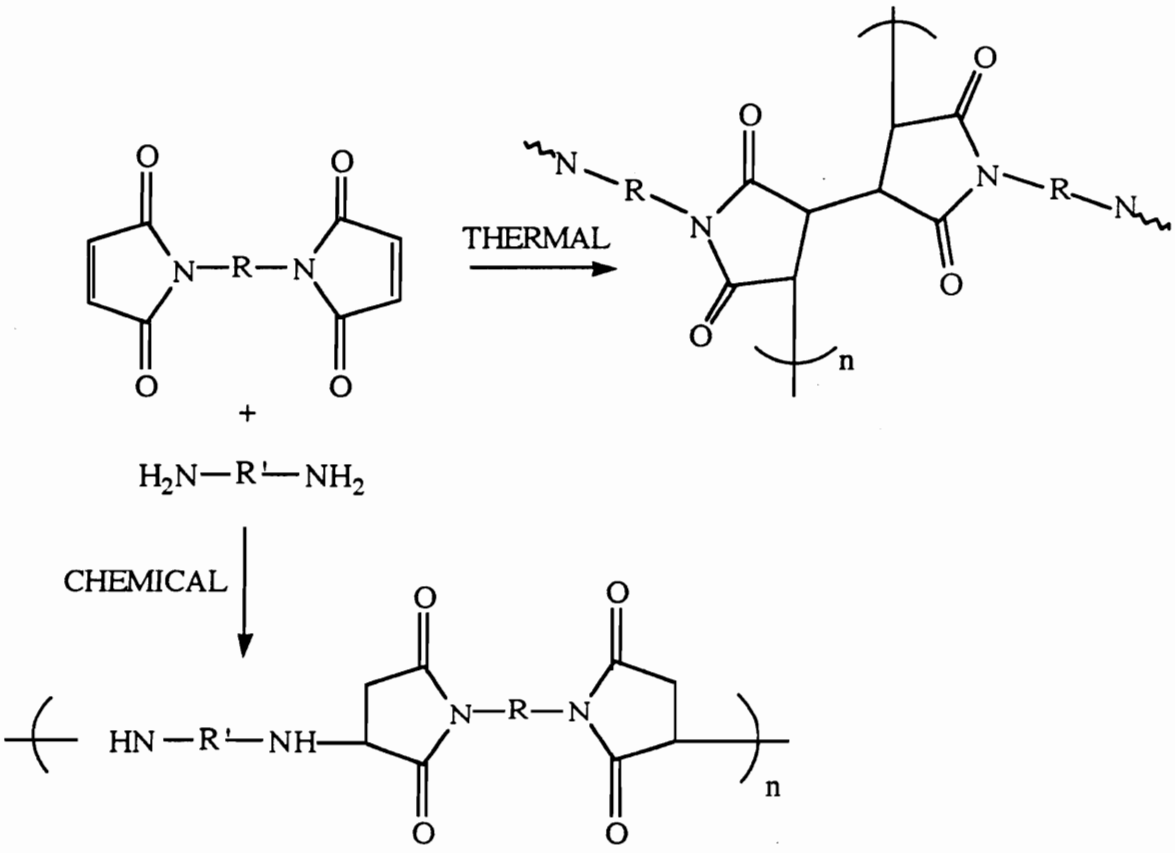

Figure 3.6. Bismaleimide cure chemistry.

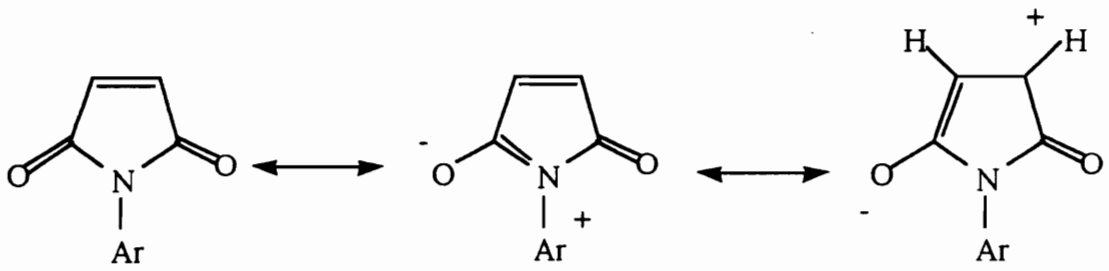

Figure 3.7. Reactivity of maleimide double bond [3].

such as primary and secondary amines and phenols undergo a Michael addition reaction with maleimides. Nucleophilic attack of the imide ring is also possible.

When the methylene dianiline-based bismaleimide is copolymerized with a o,o'-diallyl bisphenol A, as in the Matrimid 5292 resin used in this work, several reactions occur during cure. These reactions include an addition reaction between the allyl groups attached to the aromatic ring and the double bond of the maleimide, a Diels-Alder reaction, homopolymerization of the maleimide double bonds, homopolymerization of the allyl double bond, high temperature dehydration of the hydroxyl, a Michael addition of the hydroxyl to the maleimide double bond, and an attack on the methylene group in the bismaleimide by double bonds of the allyl or maleimide groups [25-28].

3.1.4 Effect of Fiber Surface Treatment on Carbon Fiber Adhesion of Thermosetting Resins

The effect of carbon fiber surface treatments on the adhesion of epoxy resins has been widely reported in the literature [29-43]. Waltersson showed that in carbon fiber/epoxy composites, both the epoxy and the amine groups of the matrix can interact with hydroxyl and carboxyl groups on the carbon fiber surface to form chemical bonds [42, 43]. Bian et al. treated PAN-based carbon fibers with argon, oxygen, CF_4/O_2, and N_2/H_2 plasmas and measured the interfacial shear strength between the fibers and an epoxy matrix (Epon 828/MDA) using the single fiber fragmentation test. The interfacial shear strength increased with the concentration of oxygen and nitrogen on the fiber surface, as shown in Figure 3.8 [36]. It was concluded that the epoxy adhesion improved as the number of hydroxyl and amine groups on the carbon fiber surface was increased.

Drzal and coworkers also used the single fiber fragmentation test to measure the interfacial shear strength between an epoxy resin (DER 331/m-PDA) and surface treated PAN-based IM6 carbon fibers [39]. As shown in Figure 3.9, a direct linear relationship was found between the interfacial shear strength and both the surface oxygen content and

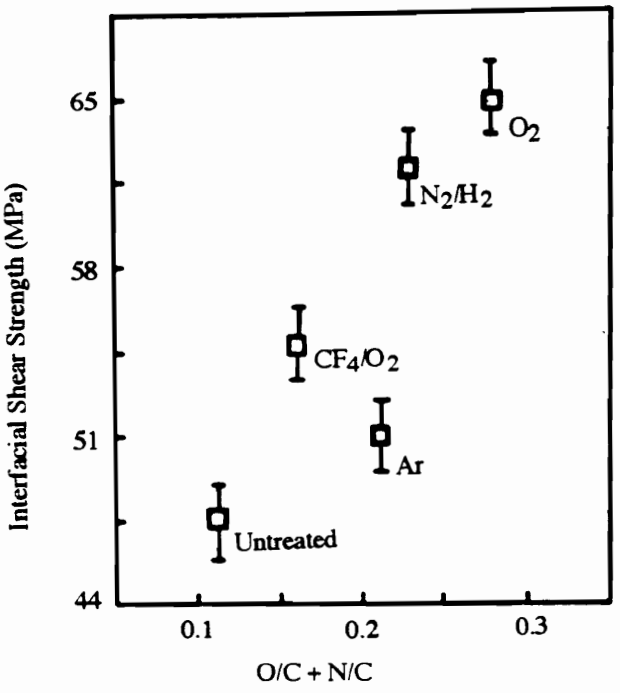

Figure 3.8. Interfacial shear strength as a function of the XPS O/C + N/C ratio of untreated and plasma treated carbon fibers [36].

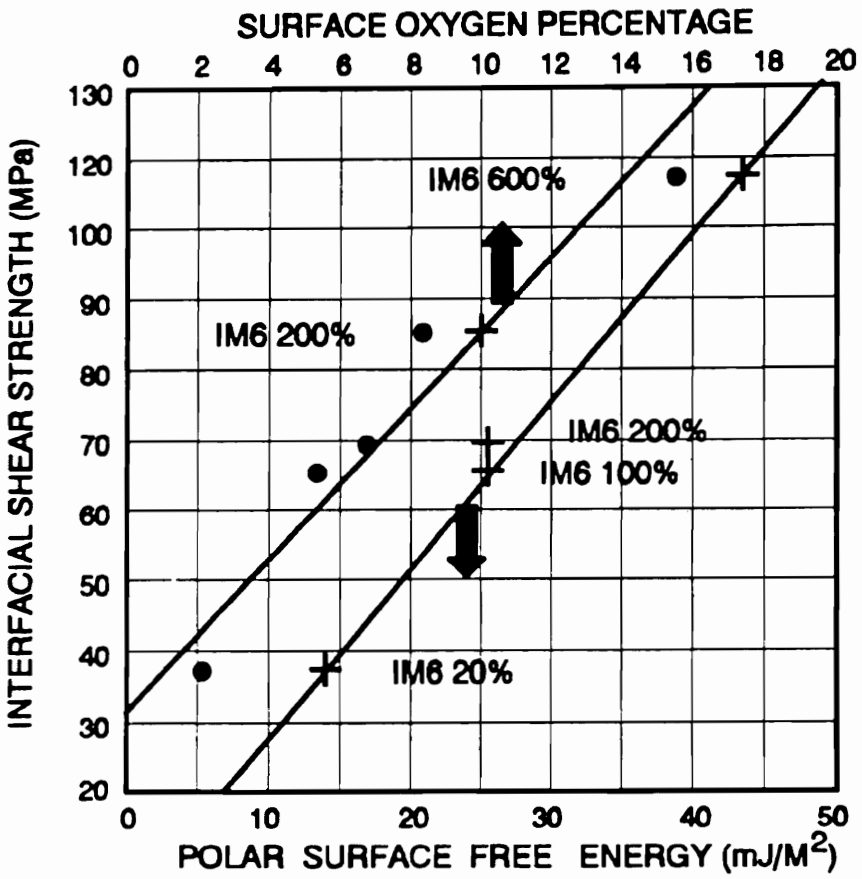

Figure 3.9. Epoxy/carbon fiber interfacial shear strength as a function of the fiber surface oxygen content and polar surface energy [39].

the polar component of the fiber surface energy. In earlier work, Drzal and coworkers reported a similar relationship with PAN-based type A and HM carbon fibers [40]. As seen in Figure 3.10, the surface treatment which converted the AU fiber to an AS fiber doubled the surface oxygen content and caused the interfacial shear strength to rise to a value over three times that of the AU. When the oxygen and nitrogen functional groups were removed from the AS-4 carbon fiber surface by heating the fibers to 600°C under vacuum or to 750°C with hydrogen, the interfacial shear strength was less than that of the AS fiber but much higher than that of the AU fiber. It was concluded that oxidative surface treatments increase carbon fiber/epoxy adhesion by removing a weak, defect -laden outer surface layer from the fiber and increasing the concentration of oxygen-containing functional groups on the fiber surface.

Herrara-Franco and Drzal measured the adhesion of an epoxy resin (Epon 828/m-PDA) to untreated AU-4 and surface treated AS-4 carbon fibers using the single-fiber fragmentation, microbond, micro-indentation, $(\pm 45)_{3s}$ tension, Iosipescu shear, and short-beam shear tests [41]. The results of each test, listed in Table 2.1, showed that the adhesion of epoxy was greater to the surface treated AS-4 fiber than to the untreated AU-4 carbon fiber .

The adhesion of bismaleimide resins to carbon fibers has been studied by measuring the mechanical properties of "real" bismaleimide composites. Jang prepared composites using the Matrimid 5292 bismaleimide resin and either "as received" or plasma treated AU-4 carbon fibers [44]. Argon, air, and ammonia plasma treatments improved the transverse strength of the carbon fiber-reinforced bismaleimide composites. Wilkinson added 15% poly(ethersulfone) to the Matrimid 5292 bismaleimide resin and prepared AU-4 and AS-4 carbon fiber-reinforced composites [45]. The micro- and meso-indentation tests showed that the bismaleimide adhered better to the surface treated AS-4 carbon fiber than to the untreated AU-4 carbon fiber.

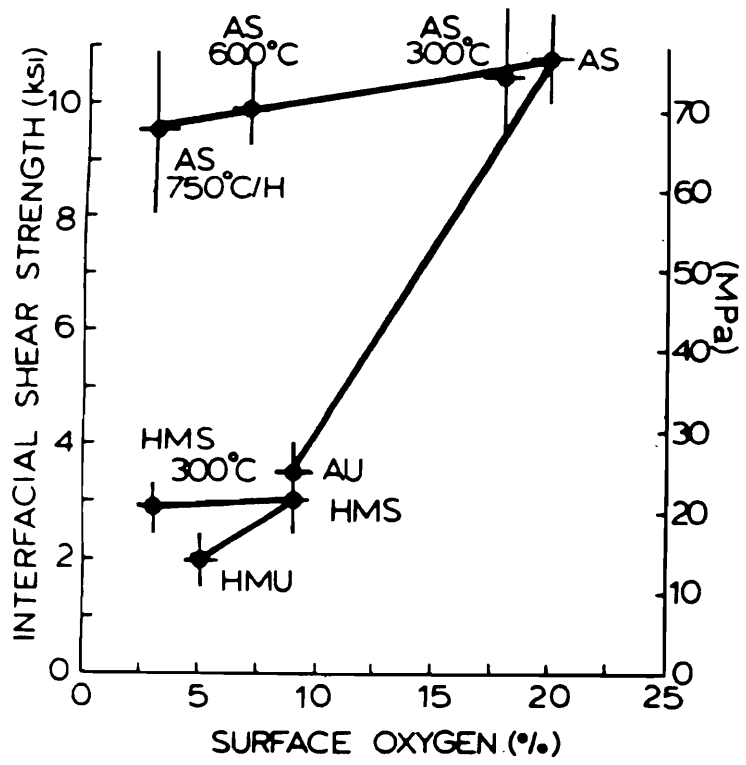

Figure 3.10. Interfacial shear strength plotted as a function of surface oxygen concentration determined by XPS for type A and HM carbon fibers [40].

Allred and Harrah measured the transverse tensile and transverse flexure strength of carbon fiber-reinforced bismaleimide composites [46]. The bismaleimide adhesion improved when the carbon fibers were exposed to an "acidic" plasma and, the failure mode was shifted from interfacial for the untreated fibers to cohesive within the bismaleimide for the plasma treated fibers. Lee and Holguin developed a modified single fiber fragmentation test for use with a highly cross-linked brittle bismaleimide matrix, however, the effect of fiber surface treatment on the carbon fiber/bismaleimide adhesion was not investigated [47].

3.2 OBJECTIVE

The goal of this work was to evaluate the effect of fiber surface treatments on bismaleimide/carbon fiber adhesion using the microbond single fiber pull-out test. The adhesion of a novel phosphorus-containing bismaleimide and a commercially available methylene dianiline-based bismaleimide was studied using untreated, commercially surface treated, and "in house" plasma treated carbon fibers.

3.3 EXPERIMENTAL

3.3.1 Materials

The PAN-based high strength, low modulus carbon fibers used in this study and their properties are summarized in Table 2.5. The "S" designation indicates that the fiber underwent a proprietary surface treatment as part of production. The "U" designation indicates that the fiber was not surface treated. The fibers were used as received. The AS-4 fibers were treated with either an air or ammonia plasma as described in Chapter 2.

The bis(3-maleimido phenoxy) triphenylphosphine oxide (BMPPO) was synthesized by McGrath and coworkers and characterized using ^{1}H-NMR and ^{13}C-NMR solution measurements, Fourier transform infrared spectroscopy, and bismaleic acid

titration to ensure that the intended structure was obtained [19]. The Matrimid® 5292 A/B thermosetting bismaleimide resin system was supplied by Ciba-Geigy.

The chemical structures of the two components of the Matrimid A/B bismaleimide resin system are shown in Figure 3.11. Part A is 4,4'-bismaleimidodiphenyl methane, the common bismaleimide based on methylene dianiline. Part B is o,o'-diallyl bisphenol A (DABA), a reactive diluent which is liquid at room temperature. The DABA serves as a solvent for the bismaleimide under hot-melt conditions and improves the processing window. Improvement in the processing window is required since, this methylene dianiline-based bismaleimide normally reacts and gels just a few degrees above its 140°C melting point. The ratio of DABA to bismaleimide was held constant at 1.0 mole bismaleimide to 0.85 moles of DABA (57:43 parts by weight).

3.3.2 Polymer Characterization

3.3.2.1 Differential Scanning Calorimetry (DSC)

A DuPont TA Instruments DSC 912 calorimeter was used to obtain the crystalline endothermic melting temperature (T_m) and the exothermic heat of cure (ΔH_{cure}) of the BMPPO bismaleimide. Dynamic thermograms were obtained at 10°C per minute in a nitrogen atmosphere using crimped aluminum pans. To determine appropriate cure conditions for the BMPPO bismaleimide, the degree of cure was calculated for BMPPO samples cured at temperatures ranging from 200°C to 300°C for various times. Samples of the BMPPO powder were degassed at 130°C for $1\frac{1}{2}$ hours under vacuum, cured isothermally in a convection oven for various times, cooled to room temperature, and then scanned in the DSC. The area under the exothermic DSC peak was recorded as the residual heat of cure ($\Delta H_{t,residual}$) remaining after the cure time (t). The degree of cure (α_t) was calculated using equation (3.1) [48].

4,4'-bismaleimidodiphenyl methane

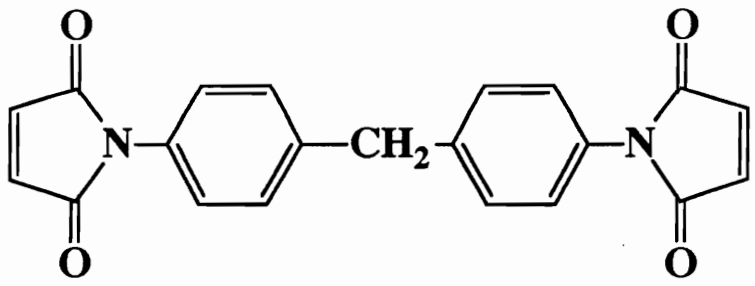

- yellow crystalline powder
- 140°C melting point
- maleimide double bond content 85% of theoretical

o,o'-diallyl bisphenol A (DABA)

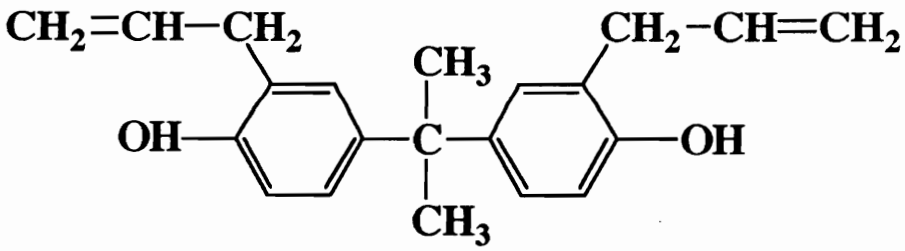

- amber liquid
- viscosity at 25°C: 12 - 20 Pa s

Figure 3.11. Matrimid® 5292 A/B thermosetting resin system.

$$\alpha_t = \frac{\Delta H_{cure} - \Delta H_{t,residual}}{\Delta H_{cure}} \times 100\% \quad (3.1)$$

3.3.2.2 Dynamic Mechanical Analysis (DMA)

Bismaleimide bars (1 x 3 x 15 mm) were prepared in silicon rubber molds. The BMPPO was degassed at 130°C in a vacuum oven and then cured in a convection oven. The cured BMPPO bars were mounted in a Perkin-Elmer DMA-7 using a single cantilever clamp. The dynamic mechanical behavior (log storage modulus ε' and log $\tan\delta$) was plotted as a function of temperature with a heating rate of 10°C per minute and a frequency of 1 Hz.

3.3.2.3 Thermogravimetric Analysis (TGA)

Thermogravimetric analysis was performed using a Perkin-Elmer Thermogravimetric Analyzer TGA-7. Dynamic thermograms were obtained at a heating rate of 10°C per minute in air.

3.3.2.4 Thermomechanical Analysis (TMA)

Thermomechanical analysis was performed on a Perkin-Elmer Thermomechanical Analyzer TMA-7. Thermograms were run at 5°C per minute in the expansion mode from 30°C to 200°C. The thermal expansion coefficient of the BMPPO and Matrimid 5292 bismaleimides was determined in the temperature range of 90°C to 140°C, where expansion was linear. The bismaleimide samples were 1.5 to 2.0 millimeters thick.

3.3.2.5 Mechanical Properties

The room temperature tensile stress-strain behavior of the BMPPO and Matrimid 5292 bismaleimides was evaluated by straining dogbone-shaped tensile coupons using an Instron model 1123. The gauge length was 12.7 mm (0.50 inches). The samples were 2.54 mm (0.10 inches) wide and from 1.24 to 1.40 mm (0.049 to 0.055 inches) thick. The

crosshead speed was 1.27 mm (0.05 inch) per minute. Five dogbond samples of each bismaleimide were tested and the results were averaged.

The Matrimid 5292 dogbond coupons were prepared as follows. The diallyl of bisphenol A compound (DABA) was weighed into a clean round bottom flask. A PTFE-coated magnetic stir bar was placed in the flask and a vacuum adaptor was fitted to the flask. The flask was placed in a 130°C silicon oil bath. A vacuum was slowly applied to the stirring mixture to degas the resin and remove volatiles such as residual solvent and entrapped air. The temperature was increased to 140°C and the bismaleimide resin was added using a powder funnel. Again, vacuum was applied to the reaction flask, and the resin was stirred for approximately 20 minutes. A dark reddish brown homogeneous hot-melt solution was obtained. The hot melt resin was poured into preheated silicon dogbond coupon molds. The mold was covered with a PTFE film, a preheated weight was placed on top, and the samples were cured in a convection oven for 1 hour at 200°C and 2 hours at 250°C.

The BMPPO bismaleimide dogbone coupons were prepared by overfilling silicon rubber molds with BMPPO powder and degassing the resin at 130°C for 4 hours in a vacuum oven. The BMPPO bars were then cured in a convection oven at 225°C for 3.5 hours and 300°C for 3 hours.

3.3.3 Microbond Sample Preparation

To form a microbond specimen, one end of a 4 cm long carbon fiber was affixed to a hole-punched aluminum tab using 3M Scotch™ glass cloth electrical tape. The metal tab was attached with a screw to one side of an aluminum frame. The central 2.5 cm of the fiber was suspended horizontally over open space and the free end of the carbon fiber was then affixed to the far end of the aluminum frame using another small square of electrical tape.

To prepare the Matrimid 5292 microbeads, the diallyl of bisphenol A compound (DABA) was weighed into a clean round bottom flask. A PTFE-coated magnetic stir bar was placed in the flask and the flask was lowered into a 130°C silicon oil bath. The temperature of the oil bath was increased to 140°C and the bismaleimide resin was added using a powder funnel. The resin was stirred for approximately 20 minutes. A dark reddish brown homogeneous hot-melt solution was obtained. The BMPPO bismaleimide powder was simply heated to melt on a hot plate in an aluminum pan.

Very long, thin strands of the bismaleimide resin were pulled out of the flask using a small diameter copper wire. This bismaleimide strand was laid perpendicular to the carbon fiber and a soldering iron was used to melt the strand of bismaleimide down around the fiber forming an axisymmetric drop of bismaleimide on the fiber. The soldering iron was not brought into direct contact with the bismaleimide, but simply used to heat the air directly around the bismaleimide. The maximum temperature recorded by a thermocouple just in front of, but not touching, the soldering iron tip was 140°C. Thirteen microbond test specimens were prepared simultaneously on the metal frame.

The Matrimid bismaleimide resin was heated on the carbon fibers at 130°C for 2 hours in a vacuum oven and then cured in a convection oven at 200°C for 1 hour and 250°C for 2 hours. The BMPPO bismaleimide was heated on the carbon fibers at 130°C for 1.5 hours in a vacuum oven and then cured in a convection oven at 225°C for 3.5 hours and at 300°C for 3 hours. Following the bismaleimide cure cycle, the carbon fibers were bonded to the aluminum tabs using Devcon Corporation TruBond® 2-Ton® epoxy and the epoxy was cured overnight at room temperature.

The length of the fiber embedded in each cured bismaleimides drop was measured using a Nikon-UM2 Measurescope. Void-free bismaleimide drops with embedded lengths ranging from 40 to 200 μm were successfully cured around single carbon fibers.

Figure 3.12 is a scanning electron photomicrograph of a BMPPO bismaleimide drop cured on a single AS-4 carbon fiber.

3.3.4 Microbond Adhesion Testing

The microbond single fiber pull-out test was used to measure the force required to debond the cured bismaleimide drops from the carbon fibers. Figure 3.13 is a schematic illustration of the microbond test set-up. The fiber was suspended by a metal hook from a Mettler PM 300 balance. The samples were tested in shear using a custom-made microvise. The shearing plates were closed to a distance just greater than the fiber diameter with the aid of a video camera and monitor. The microvise was fixed on a motorized stage that moved downward at a rate of 5 μm/second. The data was transmitted from the balance to a personal computer at a rate of 6 data points/second.

3.3.5 Scanning Electron Microscopy (SEM)

An ISI-SX-40 scanning electron microscope was used to obtain photomicrographs of the bismaleimide drops cured around the carbon fibers. The samples were secured on SEM mounts using double-sided adhesive tape and metallic silver paint. The specimens were coated with gold for two minutes using an Edwards Sputter-Coater S150B.

3.4 RESULTS AND DISCUSSION

3.4.1 Cure Study

The DSC scan, in Figure 3.3, reveals that the uncured BMPPO bismaleimide melts around 92°C (T_m) and begins to cure at 180°C. The maximum in the cure exotherm peak was at 210°C and the heat of cure (ΔH_{cure}) was 155 J/g. Figure 3.14 is a plot of the degree of cure (α_t) versus cure time (t) for BMPPO samples cured at temperatures ranging from 200°C to 300°C for 30 minures to 12 hours. Based on these results, and on

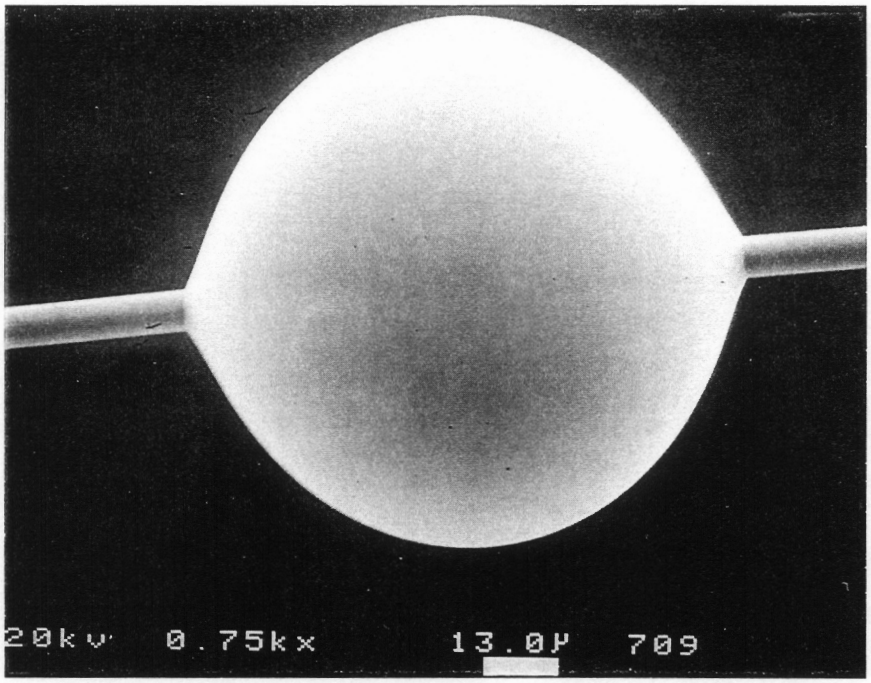

Figure 3.12. SEM photomicrograph of a BMPPO bismaleimide drop cured around an AS-4 carbon fiber (750X).

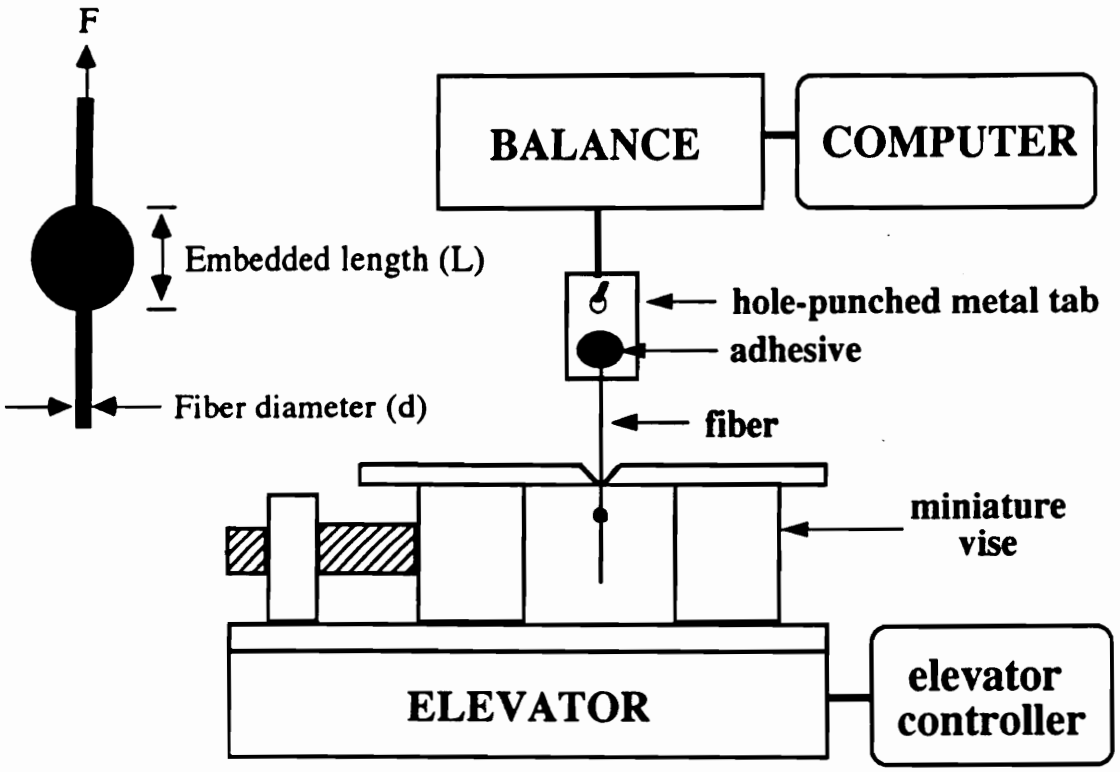

Figure 3.13. Schematic illustration of the microbond single fiber pull-out test.

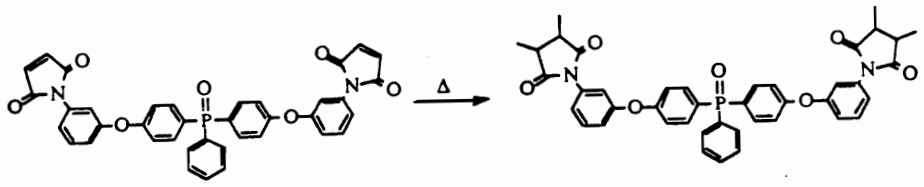

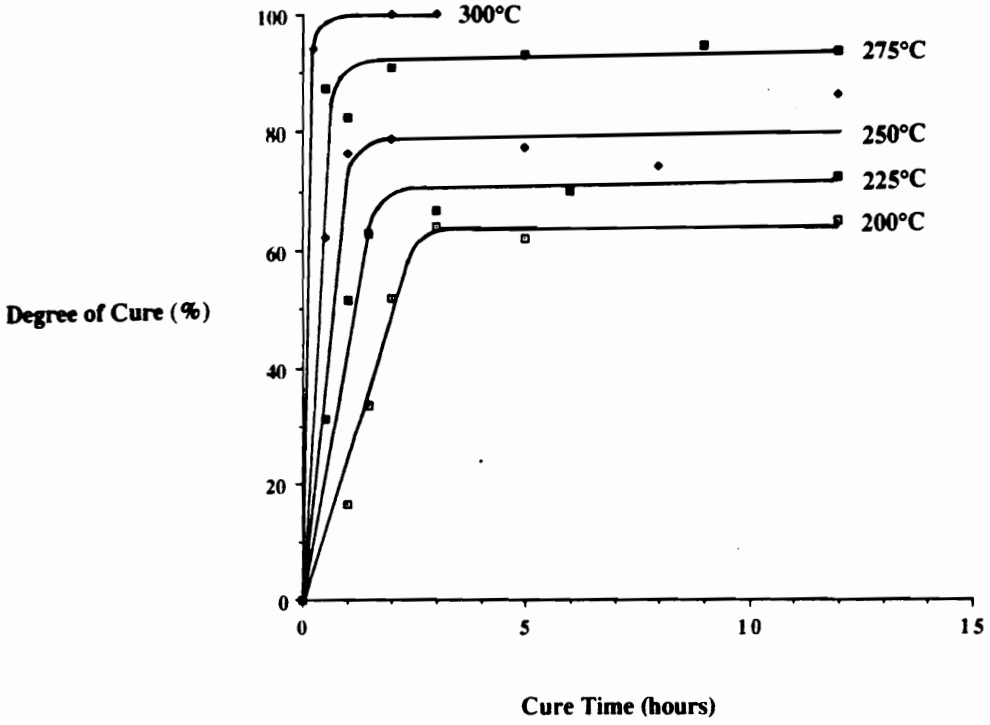

Figure 3.14. Degree of cure as a function of isothermal cure time for the BMPPO bismaleimide.

the loss of the vitrification peak observed using DMA, the BMPPO bismaleimide was cured at 225°C for 3.5 hours and 300°C for 3 hours.

3.4.2 Microbond Results

The microbond test results may be affected by the loading conditions and the mechanical and chemical properties of the fiber, matrix, and interphase. Figure 3.15 is a schematic illustration which demonstrates a number of the variables involved in the microbond test.

3.4.2.1 Debonding mechanism

Examples of the load versus displacement plots obtained during microbond experiments with the BMPPO and Matrimid 5292 bismaleimides are shown in Figures 3.16 and 3.17, respectively. The load rose linearly from zero as the fiber was strained and dropped when the bismaleimide drop debonded. A second linear rise was then observed up to a second peak force. A plateau where the force was randomly displaced about a mean followed the second peak force force. The maximum load measured was recorded as the debond load.

The features in the load versus displacement curves obtained in the fiber pull-out test were explained by Marshall and Price [49]. As the load increases from zero, the fiber is strained. Due to the Poisson's ratio of the fiber, the fiber elongates and the fiber diameter decreases between the points of load application. When the drop debonds, the strain energy in the fiber relaxes, causing a sudden decrease in the fiber length and a sudden increase in the fiber diameter. When the fiber diameter returns to its original value, the fiber resumes contact with the internal surface of the matrix. Chemical bonding no longer exists between the fiber and the matrix and, the fiber is now physically locked in the bead.

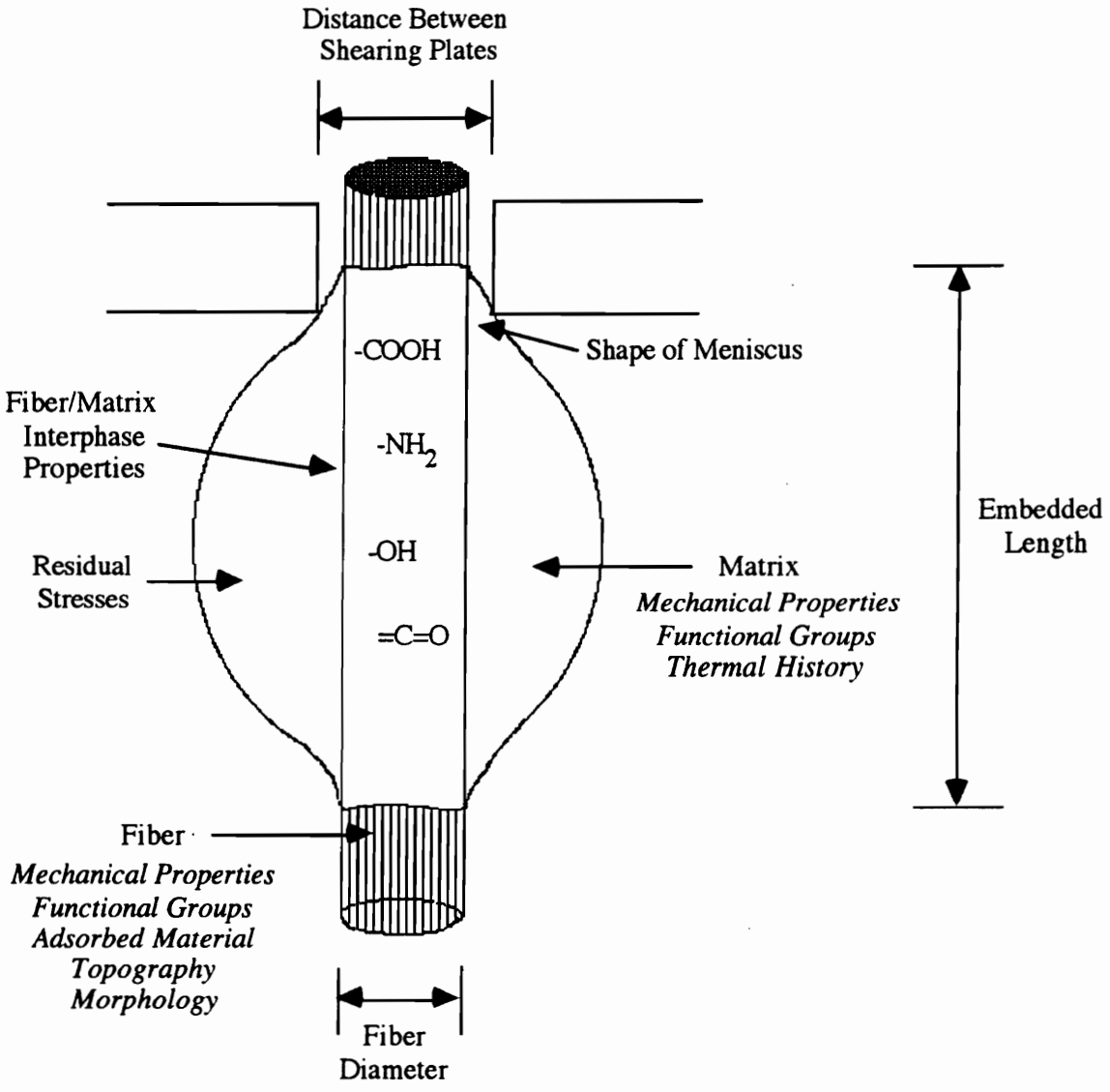

Figure 3.15. Characteristics of the microbond single fiber pull-out test.

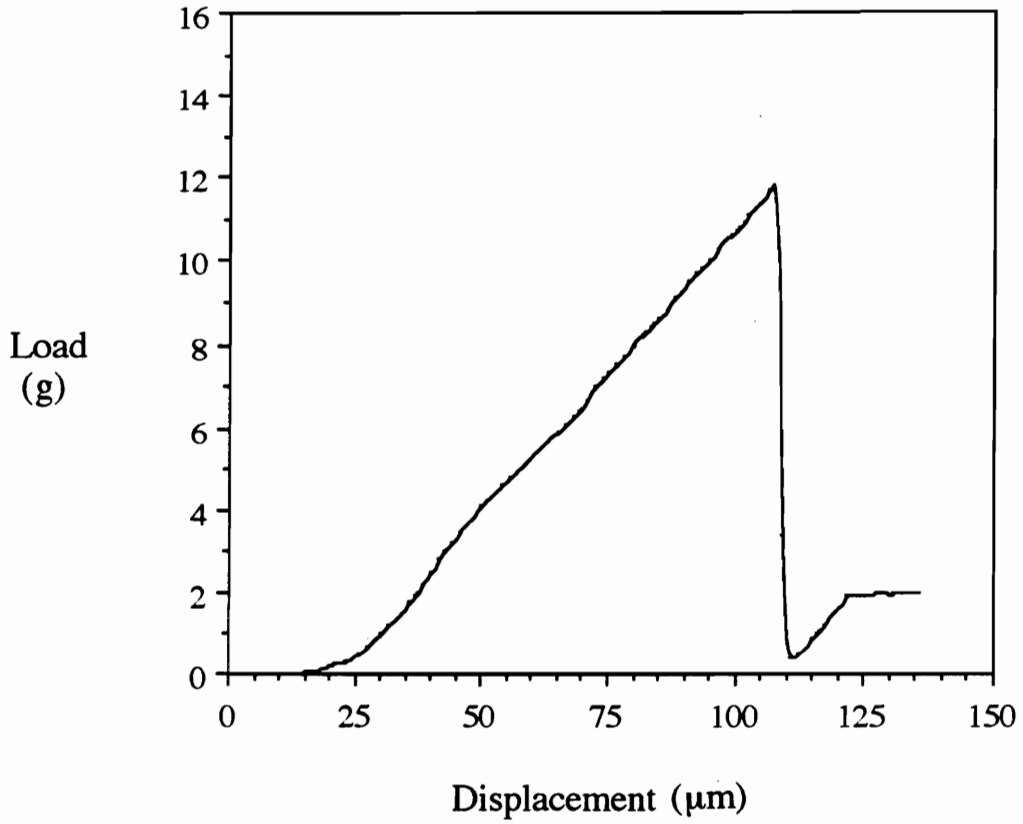

Figure 3.16. Load versus displacement plot obtained when a Matrimid 5292 bismaleimide drop was debonded from an AU-4 carbon fiber.

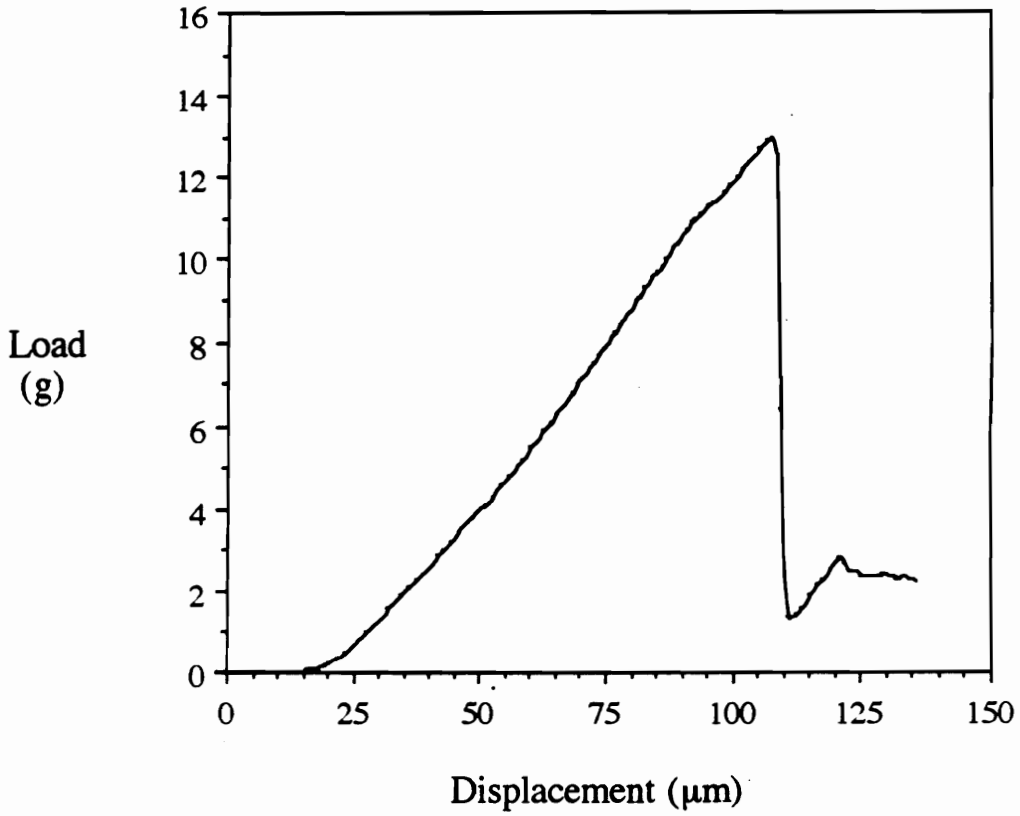

Figure 3.17. Load versus displacement plot for obtained when a BMPPO bismaleimide drop was debonded from an AU-4 carbon fiber.

The second increase in load is required to overcome the "static" frictional force due to the lateral compressive forces which physically lock the fiber within the drop. This lateral force is the result of the radial compressive stresses set up by residual stresses in the cured drop and increases with the fiber embedded length. Once the "static" frictional force is overcome, the bead is pushed down the fiber and the slight variations in force are associated with features on the fiber surface or on the inner surface of the resin drop. The "plateau" may be considered a dynamic frictional force. Its magnitude is also affected by the embedded length, showing that the radial compressive stresses on the debonded fiber increase with the area of the contacting surfaces.

The second peak force in the load versus displacement plots was taken as a measure of the "static" frictional force. The "static" frictional force for the BMPPO and the Matrimid 5292 bismaleimide drops is plotted versus the fiber embedded length in Figure 3.18. With both bismaleimides, the "static" frictional force increased with the embedded length. However, the "static" frictional force was greater in the BMPPO bismaleimide drops than in the Matrimid 5292 bismaleimde drops.

Even though the "static" frictional force is smaller than the actual lateral compressive force in the drop, due to the decrease in the fiber diameter as load is applied, the "static" frictional force provides a relative comparison of the compressive stresses in the bismaleimide drops. When linear regression was used to fit the "static" frictional forces of the BMPPO drops with a line with a y-axis intercept of zero (see Figure 3.18), the fit was not as good as with the Matrimid 5292 data. Due to the drop geometry, the relationship between the "static" frictional force and the fiber embedded length may be more complex than a simple linear relationship.

Residual stresses develop when the bismaleimide drops are cured around the carbon fibers and cooled to room temperature. Whenever a thermoset matrix is used in a composite, a volumetric contraction of the matrix occurs during cure without a

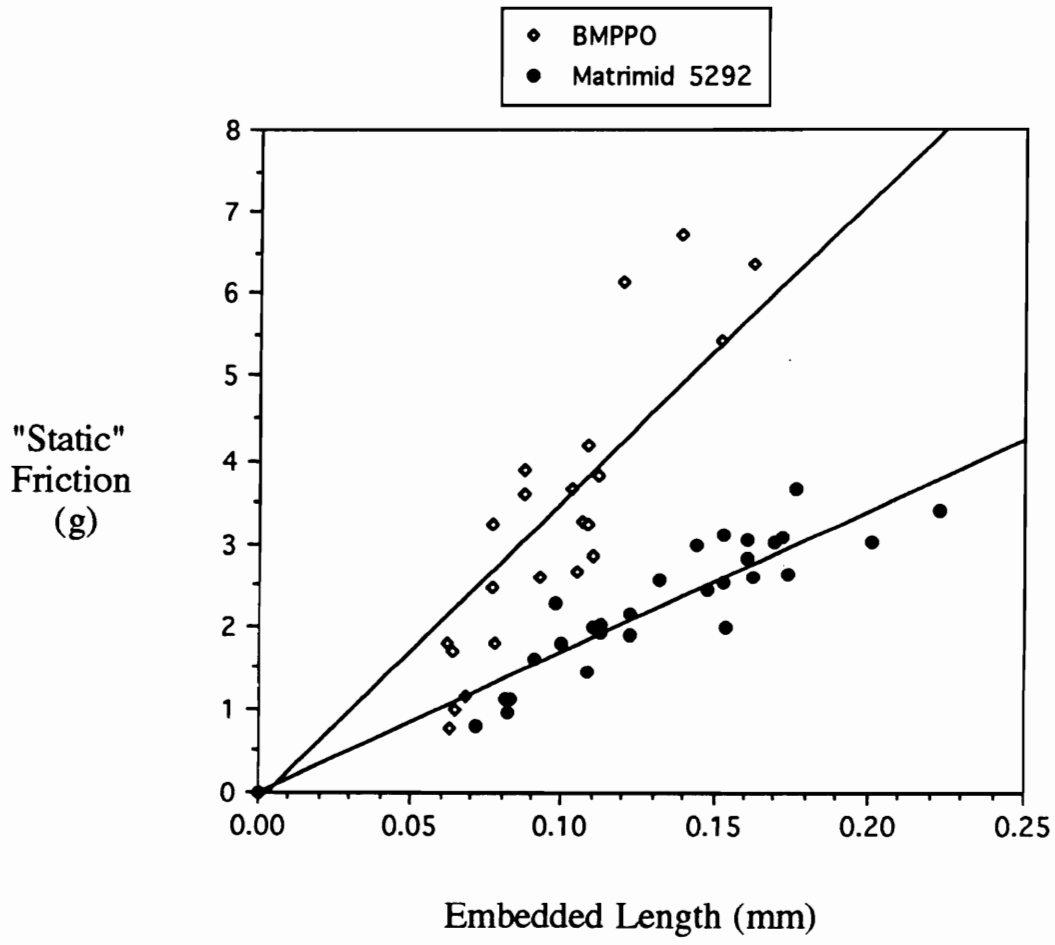

Figure 3.18. "Static" frictional force of the BMPPO and Matrimid 5292 bismaleimide drops as a function of the fiber embedded length.

corresponding contraction of the fiber. In the cure reaction, no matter what the temperature, the matrix molecules move closer to one another when covalent bonds are formed [50]. Residual stresses also develop due to temperature change whenever the thermal expansion coefficients of the fiber and the matrix are not equal [50]. As the composite is cooled to ambient temperature, the fiber and the matrix contract unequally. As illustrated in Figure 3.19, when the thermal expansion coefficient of the matrix is greater than that of the fiber, the matrix contraction will place the fiber under compression as the temperature drops.

The magnitude of the thermally induced compression (P) in the fiber's radial direction may be estimated using equation 3.2,

$$P = \frac{(\alpha_m - \alpha_f)\Delta T}{\frac{(1+\nu_m)}{E_m} + \frac{(1-\nu_f)}{E_f}} \tag{3.2}$$

where α is the coefficient of linear thermal expansion, ν is Poisson's ratio, E is the modulus of elasticity, ΔT is the temperature drop, and the subscripts f and m denote the fiber and matrix, respectively [50]. With anisotropic fibers, such as carbon fibers, there are longitudinal and transverse values for the Poisson's ratio, modulus, and thermal expansion coefficient of the fiber. Therefore, determination of the thermally induced residual stresses in a carbon fiber-reinforced composite is more complex. In addition, to arrive at an exact value of the residual stress in a microbond test specimen, the geometry of the resin drop and the shrinkage due to the formation of covalent bonds in the resin during cure must also be considered.

The coefficient of thermal expansion, Young's modulus, and the Poisson's ratio of the BMPPO and the Matrimid 5292 bismaleimides, as well as the temperature difference between cure and ambient conditions are listed in Table 3.2. Thermal and elastic

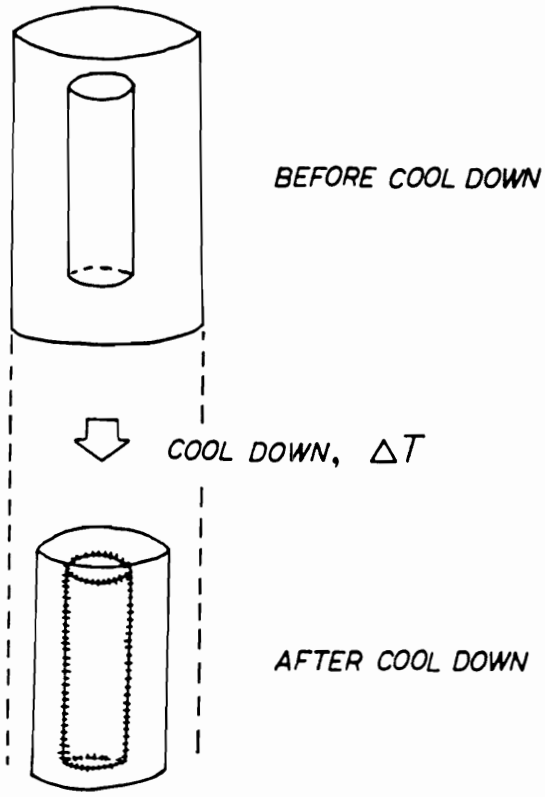

Figure 3.19. Formation of residual stresses. (a) The fiber and the surrounding matrix fit each other without stress at the elevated cure temperature. (b) When the temperature drops, the matrix contracts more than the fiber and squeezes the fiber to induce stress, as depicted by the hatch marks [50].

Table 3.2. Elastic and thermal properties of the Matrimid® 5292 and BMPPO bismaleimides.

Property	Matrimid 5292 Bismaleimide	BMPPO Bismaleimide
Young's modulus, E (GPa)	4.1 ± 0.4	3.8 ± 0.3
thermal expansion coefficient, α (ppm/°C)	37 ± 6	39 ± 4
*Poisson's ratio, ν	0.27	0.27
ΔT (°C)	225	275

*estimated

properties of the AU-4 and AS-4 carbon fibers are given in Table 3.3 [51]. By substituting the appropriate values in Tables 3.2 and 3.3 into equation 3.2, the magnitude of the thermally induced residual stresses exerted radial to the fiber surface in the Matrimid
5292 bismaleimide was estimated as 15 MPa and as 17 MPa in the BMPPO bismaleimide. Therefore, both the "static" frictional force measured experimentally and the magnitude of the thermally induced residual stress estimated using equation 3.2 were greater with the BMPPO bismaleimide than with the Matrimid 5292 bismaleimide.

The maximum load measured in the microbond tests with the Matrimid 5292 and BMPPO bismaleimides is plotted versus the fiber embedded length in Figures 3.20 and 3.21. With both bismaleimides, there was significant scatter in the data and the bismaleimide debond load was independent of the embedded area. In many cases, the carbon fibers failed during the microbond test before sufficient load was applied to debond the bismaleimide drops. The striped region on each graph marks the average fiber failure load plus and minus one standard deviation determined for a one centimeter long fiber in the tensile tests described in section 2.2.7.

When the debonded bismaleimide drops were examined using the scanning electron microscope, a "crown" of polymer was seen on the fiber where the bismaleimide drop was originally located. Scanning electron photomicrographs of the debonded Matrimid 5292 and BMPPO bismaleimide drops are shown in Figures 3.22 to 3.25. The debonding process initiated when the meniscus at the top of the bismaleimide drop failed. Herrara-Franco and Drzal used finite element and photoelastic stress analysis to show that in the microbond test, the maximum stress is generated in the mensicus region [41]. The existence of the polymer crown shows that the bismaleimide was well bonded to the fiber surface. If "good" adhesion did not exist between the polymer drop and the fiber, the

Table 3.3. Elastic and thermal properties of the Hercules AU-4 and AS-4 carbon fibers [51].

Property	Hercules Type A Carbon Fiber
Longitudinal modulus, E_l (GPa)	235
Transverse modulus, E_t (GPa)	14
Longitudinal thermal expansion coefficient, α_l (ppm/°C)	-0.36
Transverse thermal expansion coefficient, α_t (ppm/°C)	18
Major Poisson's ratio	0.20
In-plane Poisson's ratio	0.25
Longitudinal tensile strength, σ_l (GPa)	3.59
Transverse tensile strength, σ_t (GPa)	0.35

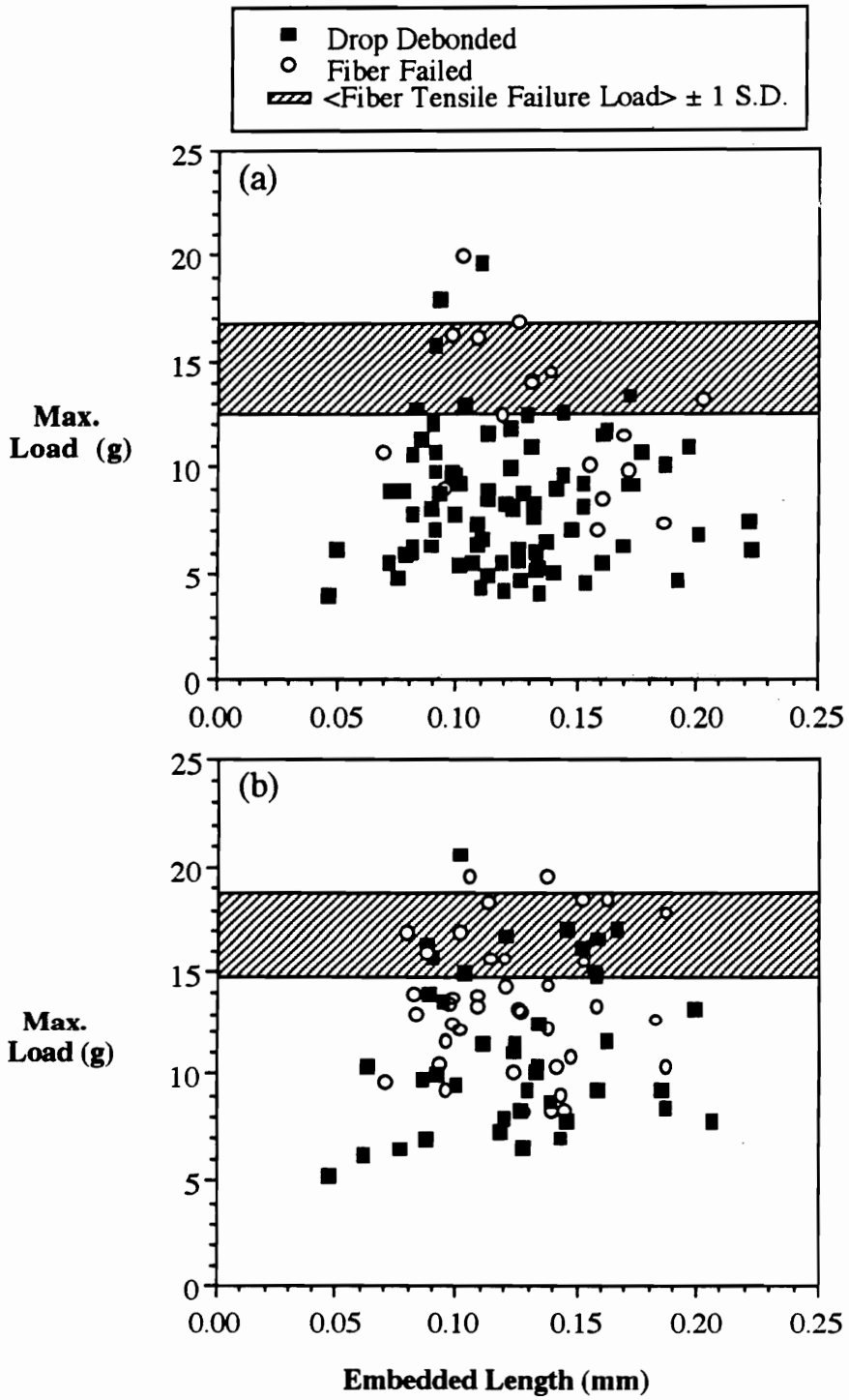

Figure 3.20. Maximum force measured in the microbond experiment as a function of the fiber embedded length with the Matrimid 5292 bismaleimide and "as received" (a) AU-4 and (b) AS-4 carbon fibers.

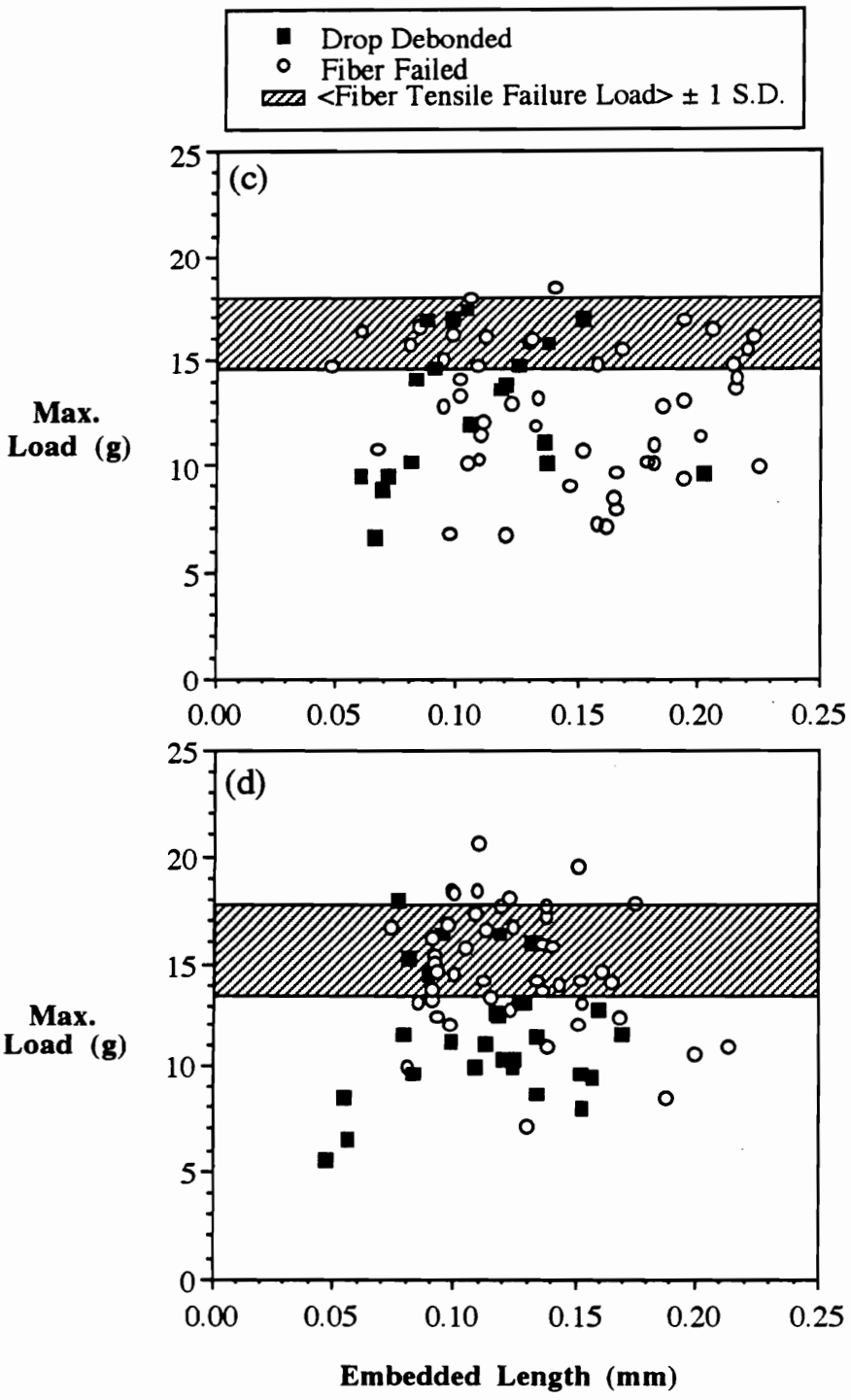

Figure 3.20 (cont.). Maximum force measured in the microbond experiment as a function of the fiber embedded length with the Matrimid 5292 bismaleimide and (c) 1 min. ammonia plasma and (d) 15 sec. air plasma treated AS-4 carbon fibers.

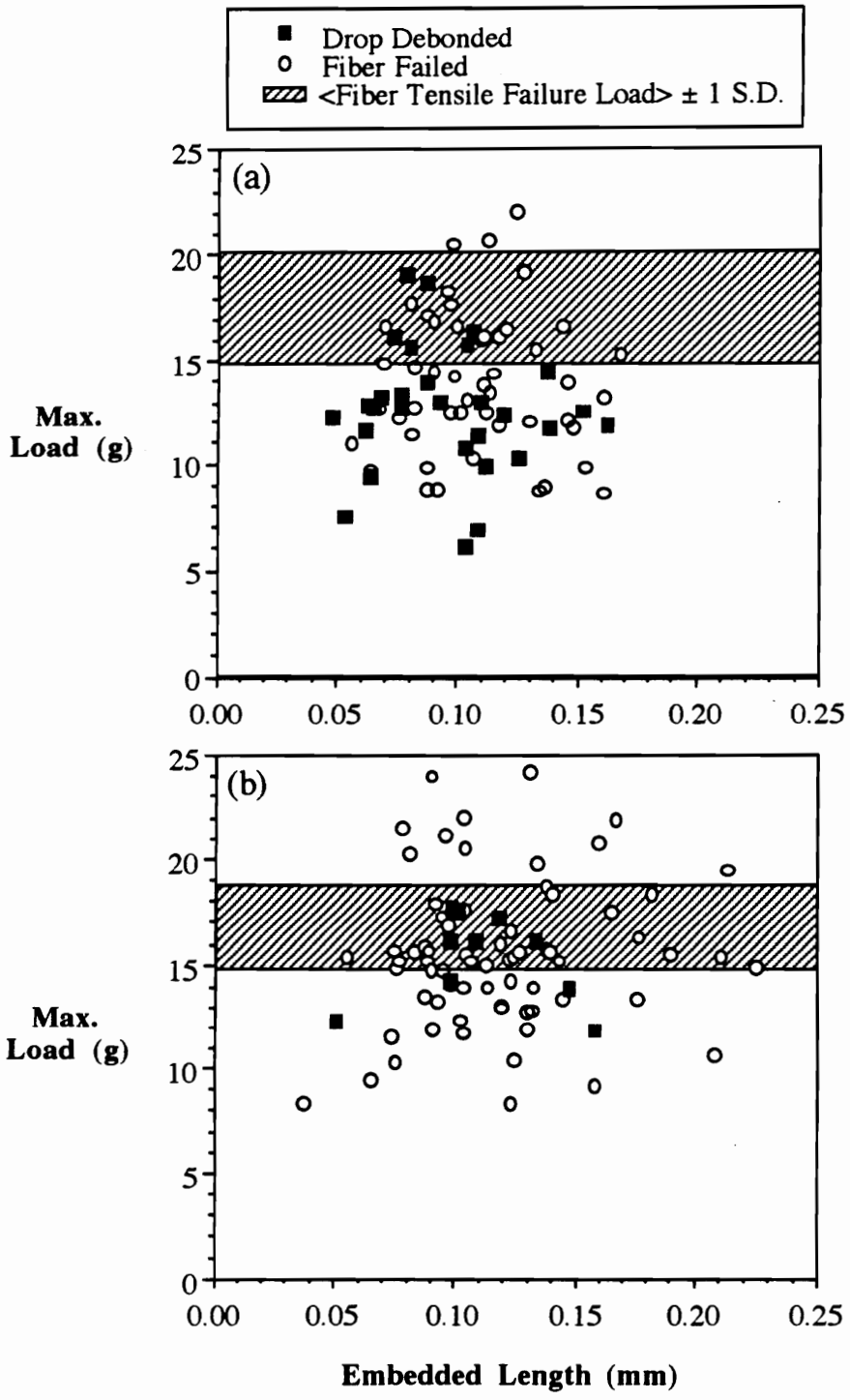

Figure 3.21. Maximum force measured in the microbond experiment as a function of the fiber embedded length with the BMPPO bismaleimide and "as received" (a) AU-4 and (b) AS-4 carbon fibers.

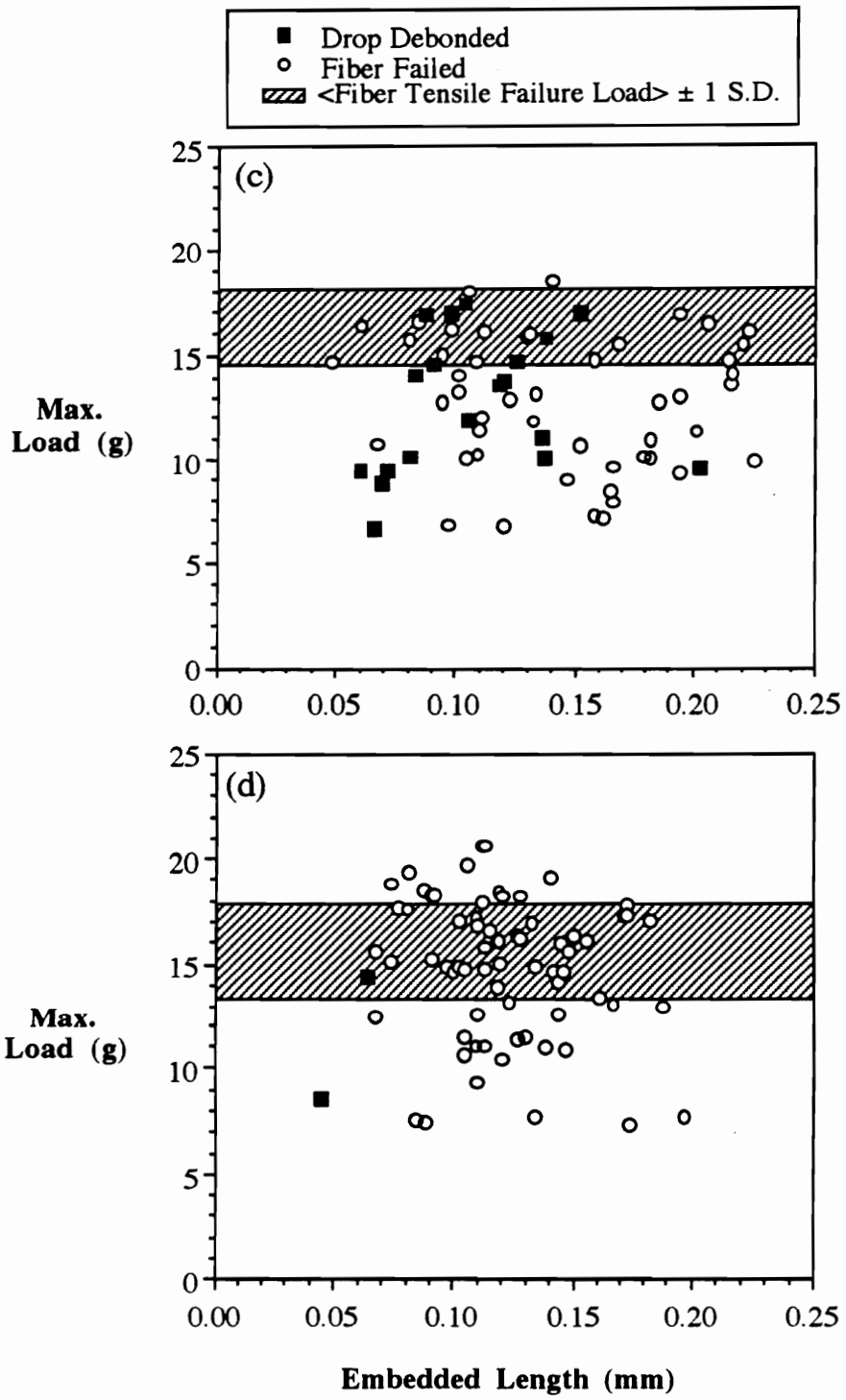

Figure 3.21 (cont.). Maximum force measured in the microbond experiment as a function of the fiber embedded length with the BMPPO bismaleimide and (c) 1 min. ammonia plasma and (d) 15 sec. air plasma treated AS-4 carbon fibers.

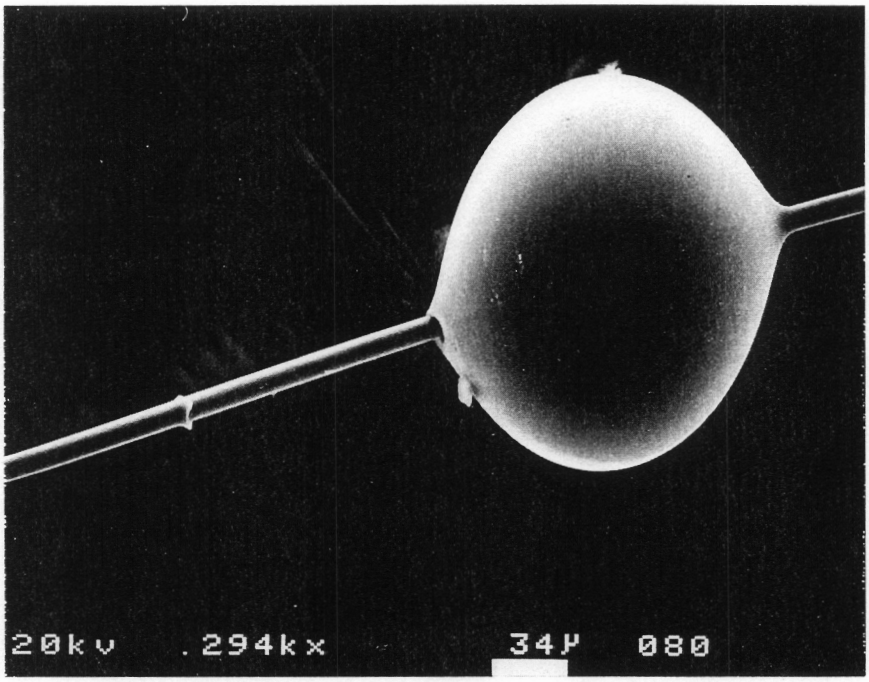

Figure 3.22. SEM photomicrograph of a Matrimid 5292 bismaleimide drop debonded from a 15 sec. air plasma treated AS-4 carbon fiber (294X).

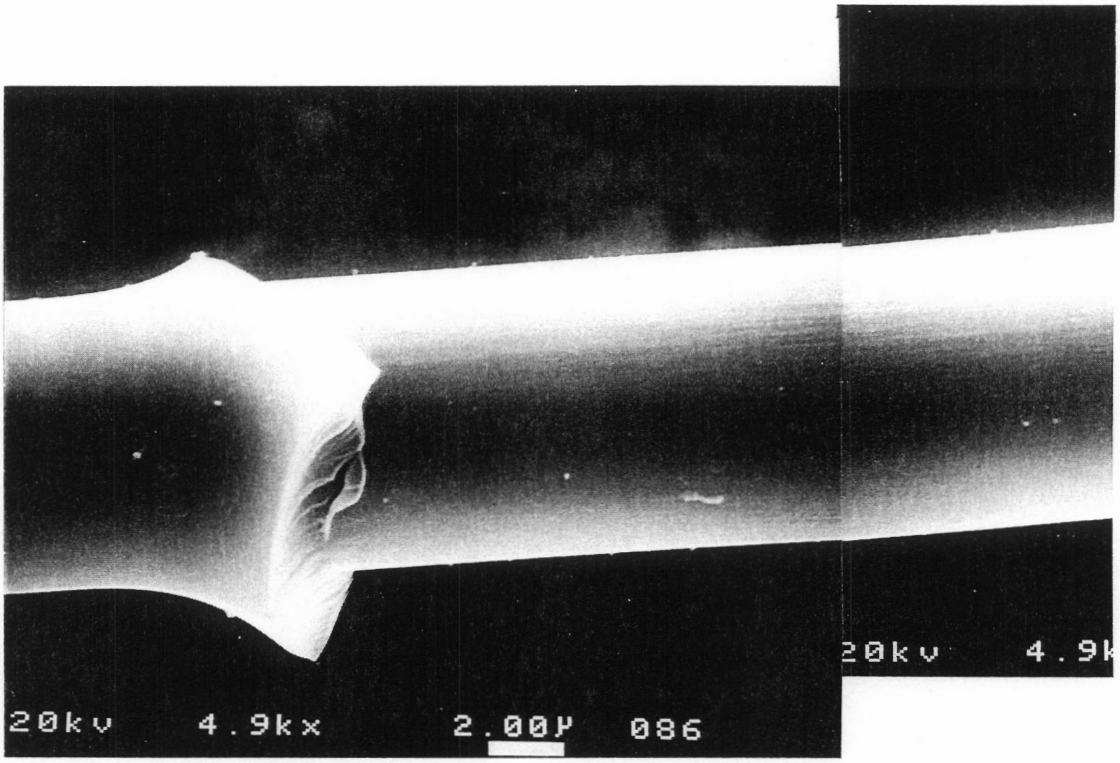

Figure 3.23. SEM photomicrographs of the Matrimid 5292/carbon fiber fracture site (4,900X).

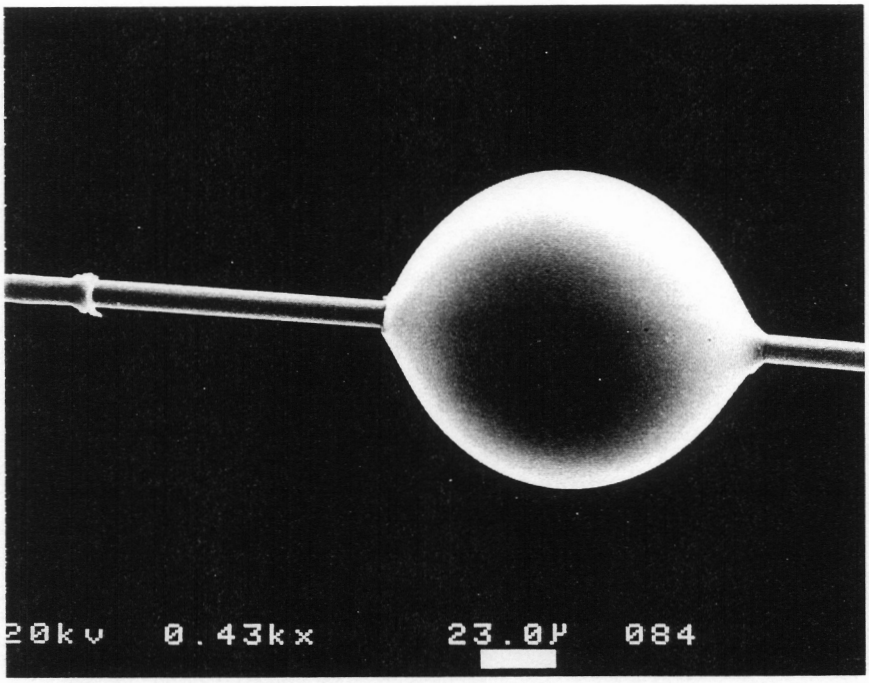

Figure 3.24. SEM photomicrograph of a BMPPO bismaleimide drop debonded from an "as received" AS-4 carbon fiber (430X).

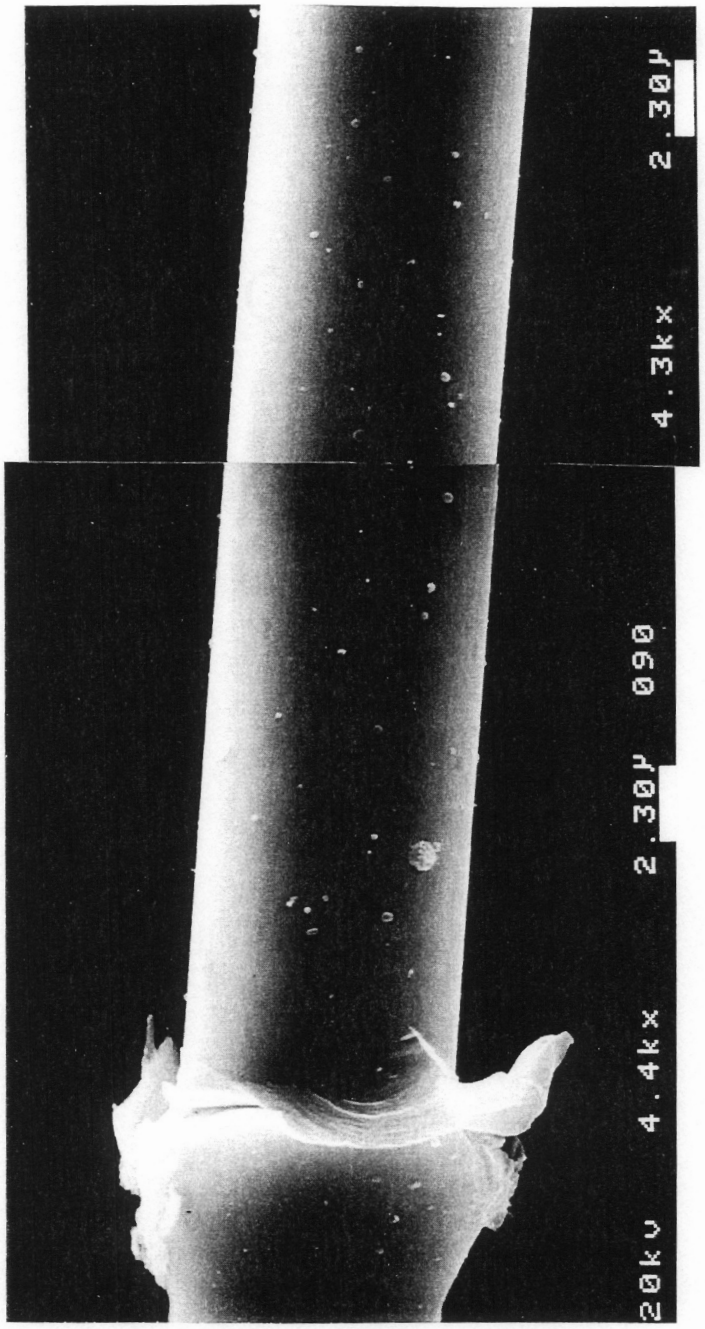

Figure 3.25. SEM photomicrographs of the BMPPO/AS-4 carbon fiber fracture site (4,400X).

entire bead would have simply slid down the fiber when load was applied and the meniscus would not have failed.

In the microbond pull-out experiment, the interfacial shear strength (τ) is obtained by dividing the debond load by the bonded area as in equation 3.3,

$$\tau = \frac{F_d}{\pi \; d \; L} \tag{3.3}$$

where, F_d is the force required to debond the drop, d is the fiber diameter, and L is the embedded length. The interfacial shear strength could not be calculated for the bismaleimide microbond results because the debond load was independent of the embedded length. This suggests that the fiber/bismaleimide interface failed catastrophically rather than with a yielding mechanism. The matrix failed in the meniscus due to the high stress concentration imposed in this region by the shearing plates. The crack extended toward the fiber, forming the polymer "crown", and propagated straight through the fiber/matrix interface.

With a few of the bismaleimide microbond samples, a load versus displacement curve like that in Figure 3.26 was obtained. In this case, it appears that a crack intiated, but did not propagate down the entire embedded length. An additional increase in load was required to completely debond the bismaleimide drop from the fiber.

In contrast to the bismaleimides, when the carbon fiber adhesion of a pyridine-containing thermoplastic polymer (Chapter 4) and a cyanate ester thermosetting resin (Appendix) was evaluated using the microbond test, the debond load was dependent on the fiber embedded length. There was also much less scatter in the data and very few fibers broke during microbond testing. The carbon fiber interface of the poly(pyridine-bis A) and the cyanate ester matrices appear to fail with a yielding mechanism, instead of

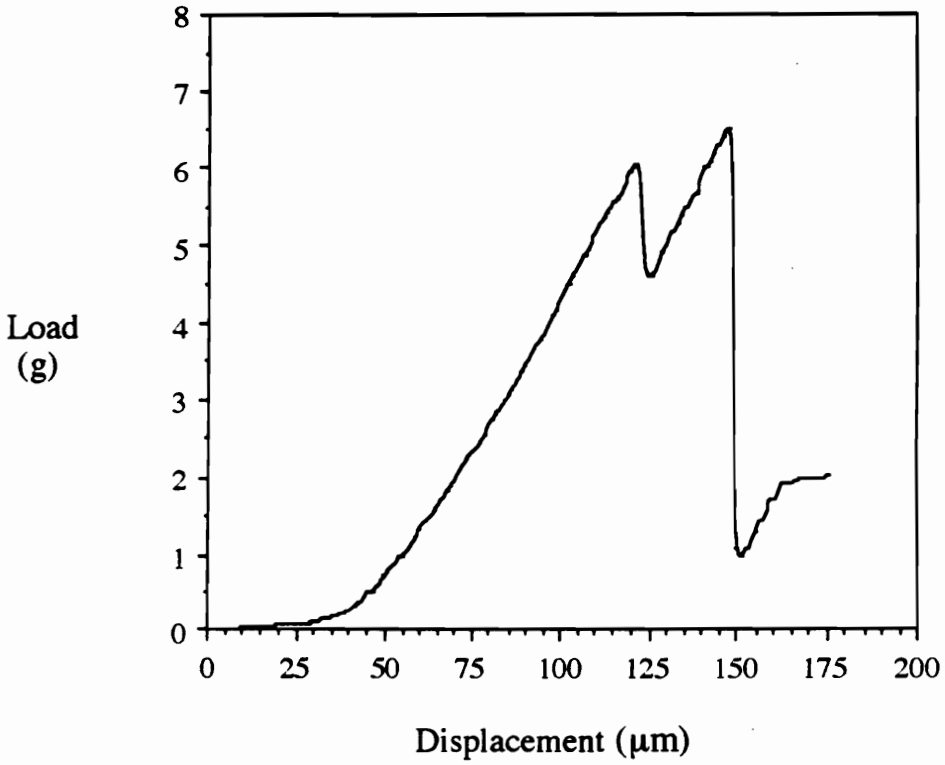

Figure 3.26. Load versus displacement plot obtained in a few cases when a bismaleimide drop was debonded from a carbon fiber using the microbond test.

the catastrophic failure observed with the bismaleimides. The different failure mechanisms are probably the result of the mechanical properties of the polymers.

The debond load of the bismaleimide drops was independent of the embedded length because the bismaleimides have a higher modulus and a lower strain to failure than the poly(pyridine-bis A) and the cyanate esters. In terms of the pull-out test model developed by Penn and Jiang, discussed in section 2.1.4.2.1, the debond load is dependent on the embedded length at low embedded lengths and becomes independent of embedded length at large embedded lengths. As shown in Figure 2.8(b), with a low modulus matrix, the critical embedded length above which the debond load is independent of embedded length is lower than that for a high modulus matrix.

3.4.2.2 Fiber failure mechanism

With the exception of the Matrimid 5292/AU-4 microbond samples, a significant portion of the fibers failed during the bismaleimide microbond tests. An example of the load versus displacement curves obtained during microbond testing when the fiber failed is shown in Figure 3.27. While the curve shown in Figure 3.27 is representative of the majority of fiber failure plots, in a few cases, the load versus displacement plot appeared like that in Figure 3.28. In this case, the bond started to fail, but the crack did not propagate down the entire embedded length. When an additional load was applied to the drop, the fiber failed. Figure 3.29 is a bar chart which shows the percentage of the bismaleimide drops which were successfully debonded without fiber failure during microbond testing with AU-4, AS-4, 1 min. ammonia plasma, and 15 sec. air plasma treated AS-4 carbon fibers.

When the fibers failed during microbond testing, the samples fell and were collected on a piece of adhesive tape positioned below the shearing plates. In many cases the failed

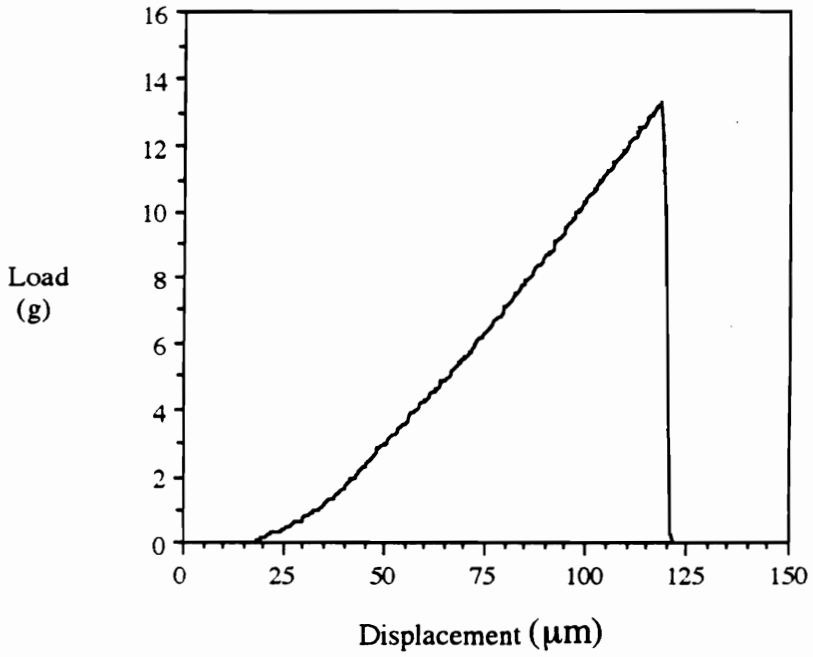

Figure 3.27. Load versus displacement curve obtained when the fiber failed during the microbond test.

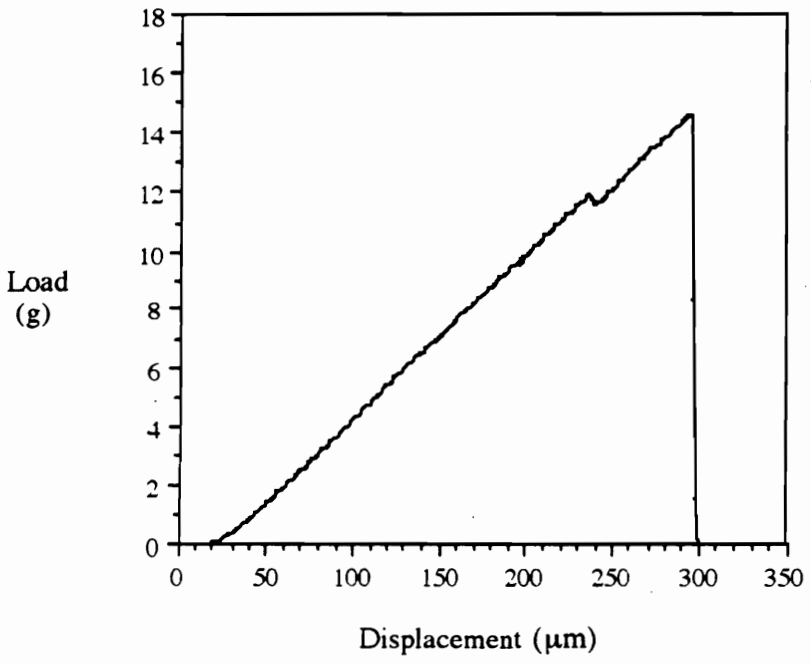

Figure 3.28. Load versus displacement curve obtained when the fiber failed during the microbond test.

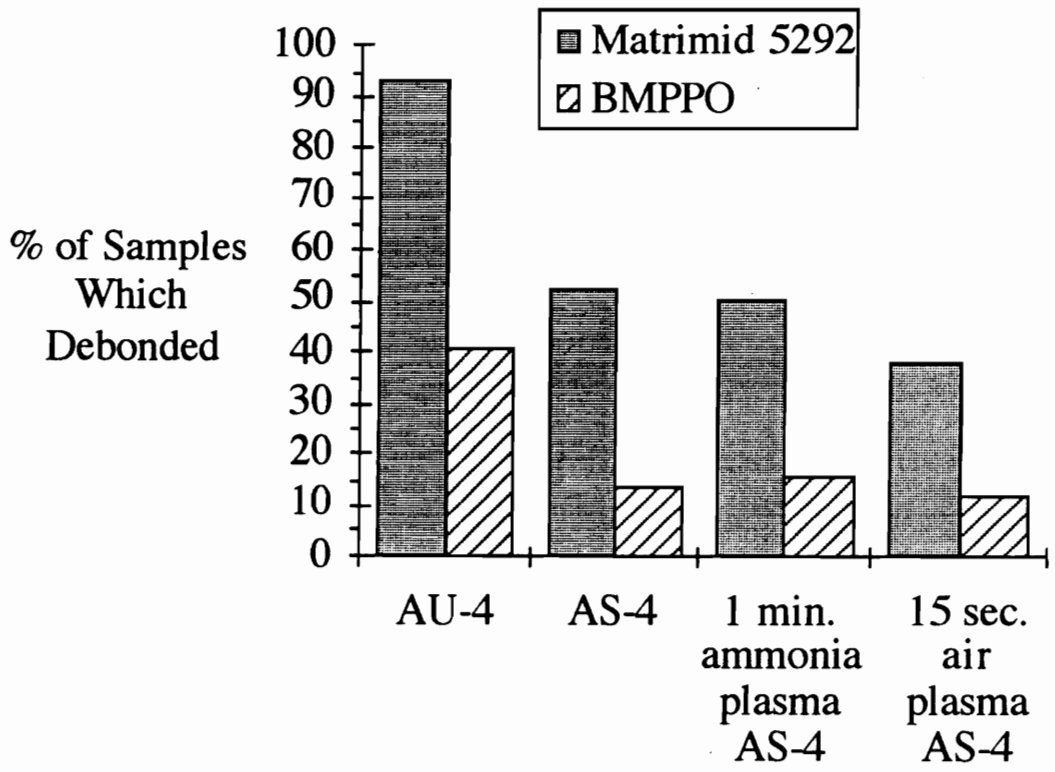

Figure 3.29. Percentage of bismaleimide drops which debonded during microbond testing with untreated AU-4, commercially surface treated AS-4, and plasma treated AS-4 carbon fibers.

samples appeared as shown in the scanning electron photomicrographs in Figure 3.30. The polymer meniscus failed, a crack propagated for some length down the fiber/matrix interface, and then, at some point, the fiber failed within the drop. There is a hole in the top of the drop where the upper portion of the broken fiber pulled out of the bismaleimide. The lower portion of the failed fiber extends from the bottom of the drop.

Herrara-Franco and Drzal used finite element analysis and photoelastic stress analysis to show that in the microbond experiment there is a radial and a shear component to the applied load [41]. The radial load is tensile where the fiber enters the drop, but becomes compressive closer to the center of the drop. The transverse compressive strength of a carbon fiber is significantly less than the longitudinal tensile strength.

As noted in the load versus embedded length plots in Figures 3.21 and 3.22, many of the fibers failed during microbond testing at a significantly lower load than the average tensile strength of one centimeter long fibers measured independently (see Chapter 2). This may be due to the radial compressive forces exerted on the fiber during loading in the microbond test as well as the fact that, when the microbond specimens were prepared, the bismaleimide drop was not always located one centimeter from the metal tab. The distance between the top of the bismaleimide drop and the metal tab ranged from 0.5 to 2 centimeters. As shown in Figure 2.74 the tensile strength of the carbon fibers decreased as the gauge length of the fiber was increased.

3.4.2.3 Effect of carbon fiber surface treatment

Figure 3.31 shows the average load required to debond the bismaleimide drops from AU-4 and AS-4 carbon fibers. With both bismaleimides, a greater load was required to fail the interface with the surface treated AS-4 fiber than with the untreated AU-4 carbon.

(a)

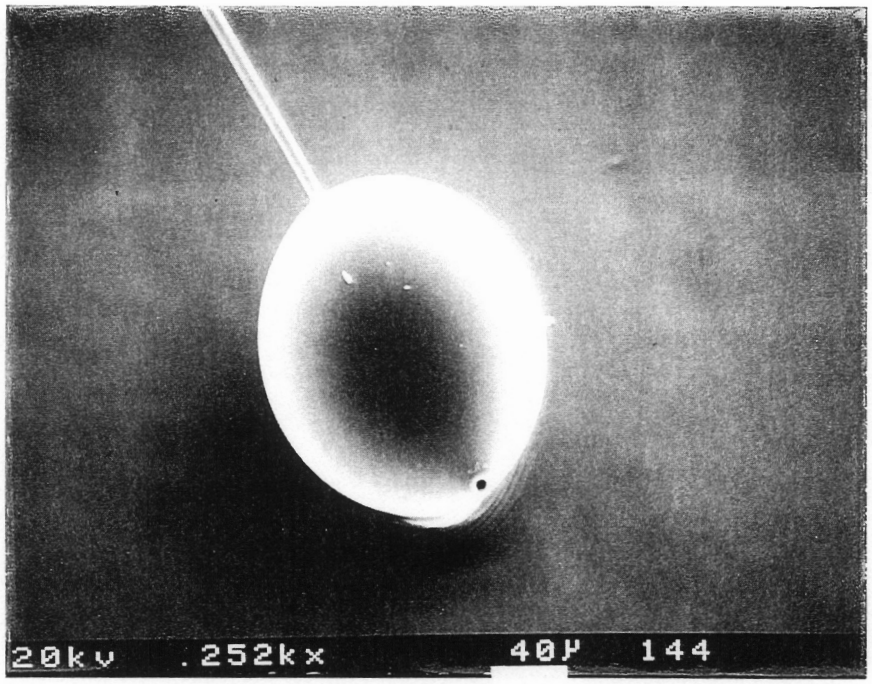

(b)

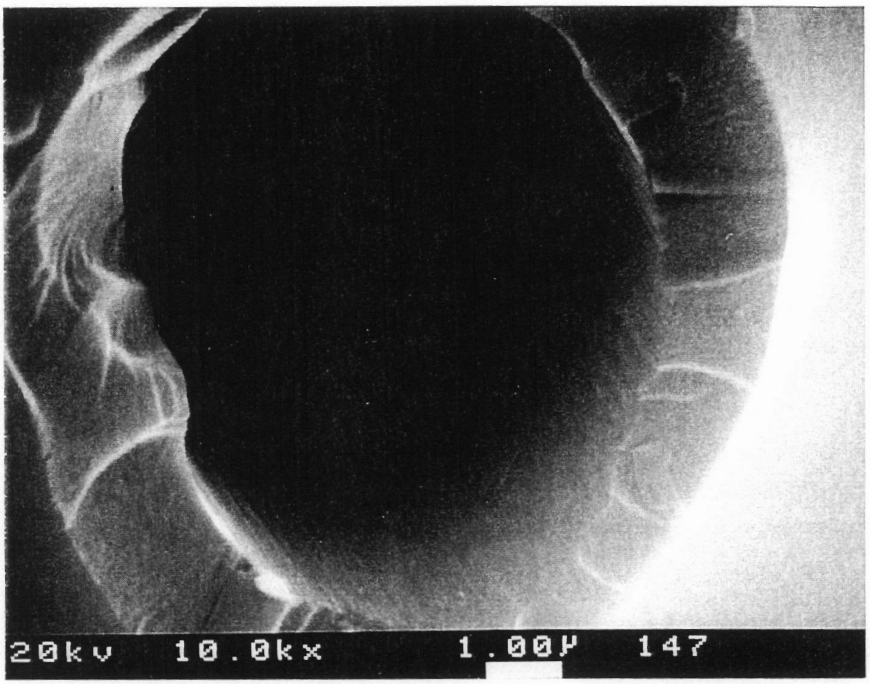

Figure 3.30. SEM photomicrographs of a bismaleimide microbond test specimen in which the fiber failed during microbond testing at (a) 252X and (b) 10,000X.

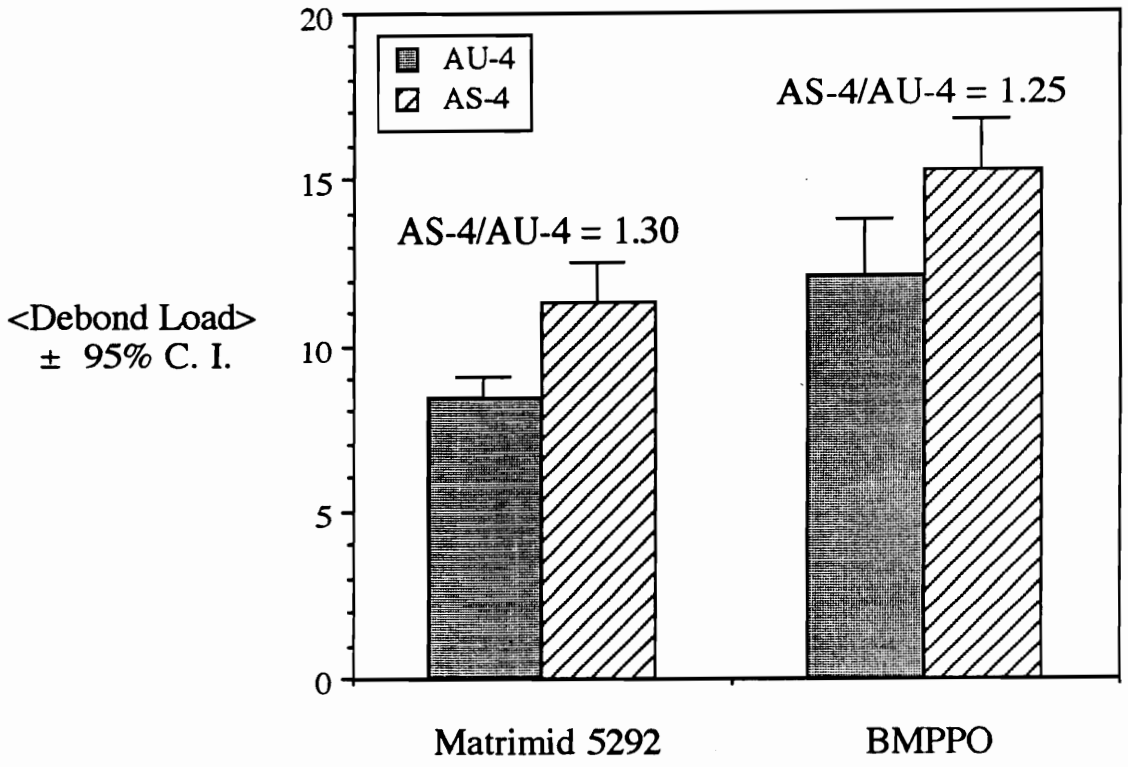

Figure 3.31. Average debond load of the Matrimid 5292 and BMPPO bismaleimides with "as received" AU-4 and AS-4 carbon fibers.

When the debond load measured with the AS-4 carbon fiber was ratioed to that of the AU-4 carbon fiber, the ratio was 1.30 for the Matrimid 5292 bismaleimide and 1.25 for the BMPPO bismaleimide. These values correspond well to the AS-4/AU-4 ratios obtained by Wilkinson using Matrimid 5292 composites [45]. When the Matrimid 5292 bismaleimide composites were tested using the micro-indentation and meso-indentation tests, the AS-4/AU-4 ratio was 1.20 and 1.26, respectively.

As shown in Figure 3.32, the number of bismaleimide drops successfully debonded without fiber failure decreased as the concentration of oxygen and nitrogen on the fiber surface was increased. Only the bismaleimide data for embedded lengths less than 100 μm was used to calculate the percentage of drops successfully debonded due to the increased probability of fiber failure as the embedded length increased. The number of bismaleimide drops successfully debonded decreased as the interfacial strength increased to a point where the fiber strength was exceeded during microbond testing. As in this work, when Penn and Jutis used the microbond test to measure the epoxy adhesion of untreated and surface treated aramid fibers, the average debond load and the percent occurrence of fiber failure were used as a measure of the fiber/matrix adhesion [52].

Enhanced bismaleimide adhesion to the surface treated carbon fibers may be attributed to,

- an increase in the surface energy and wettability of the fiber surface
- removal of a weakly bound fiber surface layer
- promotion of mechanical interlocking between the fiber and the matrix as the fiber was roughened, and
- an increase in the number of active sites on the fiber surface for specific chemical interactions with the polymer matrix.

XPS and wetting analyses showed that the proprietary commercial surface treatment used to convert the AU-4 to the AS-4 carbon fiber increased both the fiber surface energy and

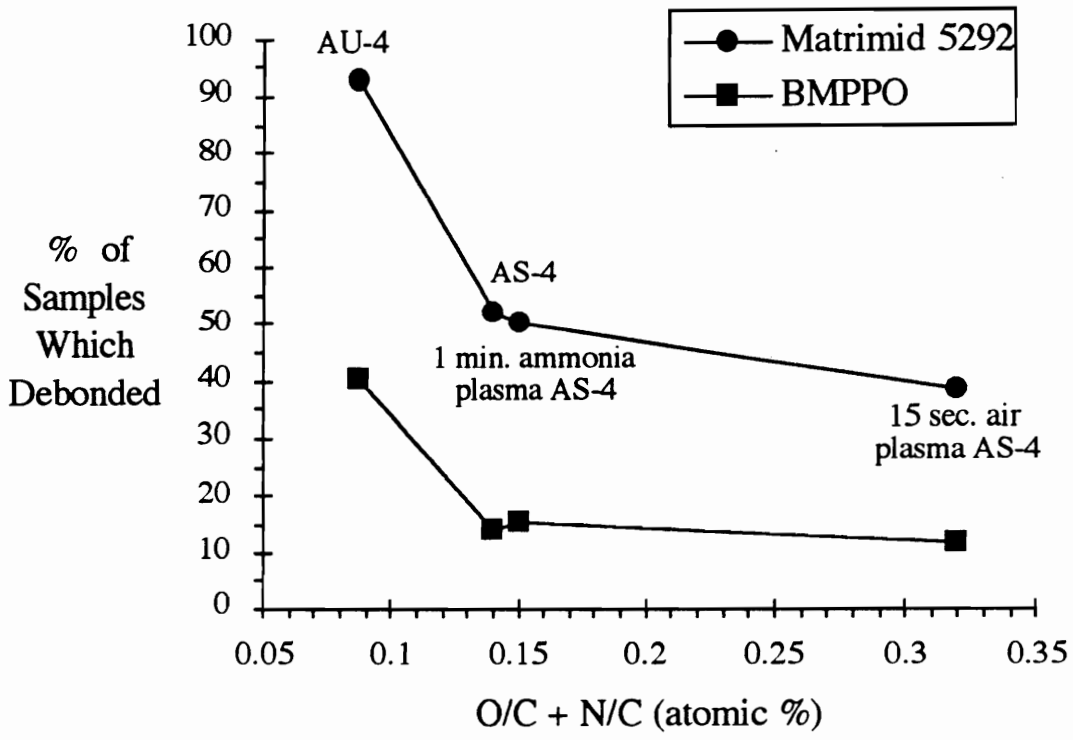

Figure 3.32. Percentage of bismaleimide drops with an embedded length less than 100 μm successfully debonded without fiber failure plotted versus the carbon fiber XPS (O+N)/C ratio.

the concentration of oxygen and nitrogen on the fiber surface. No change in the surface topography was evident by SEM at a magnification of 50,000X. This suggests that the AS-4/bismaleimide adhesion was greater than the AU-4/bismaleimide adhesion due to an increase in the fiber wettability and the creation of active sites on the fiber surface capable of interacting chemically with the bismaleimide resins. In addition, as reported by Drzal and coworkers the proprietary surface treatment may remove a weakly bound surface layer from the AU-4 carbon fiber surface [40].

The ammonia plasma cleaned the fiber surface, increased the fiber surface nitrogen content, and decreased the fiber surface oxygen content. At a 50,000X magnification, the ammonia plasma did not alter the fiber topography. Therefore, since the ammonia plasma fiber treatment did not significantly improve the bismaleimide adhesion, it appears that it is the concentration of oxygen and nitrogen on the fiber surface, not just the surface nitrogen content, which improves the fiber/bismaleimide adhesion. It was postulated by Jang that the amine groups created on the carbon fiber surface improve bismaleimide adhesion by undergoing nucleophilic Michael additions with the maleimide double bond [44]. The importance of the fiber surface nitrogen content was not demonstrated in this work. However, since most of the AS-4 and plasma treated fibers failed during the microbond test, the adhesion results are skewed to lower values than would have been attained if 100% of the microbond samples debonded.

The air plasma treatment roughened the fiber surface and increased the concentration of oxygen and nitrogen on the fiber surface. Therefore, superior bismaleimide adhesion to the air plasma treated carbon fibers may be due to both mechanical interlocking effects and adsorption interactions.

In general, the adhesion of both the Matrimid 5292 bismaleimide and the BMPPO bismaleimide increased following a commercial surface treatment and "in house" plasma treatments. The BMPPO bismaleimide adhered better than the Matrimid 5292

bismaleimide to all four carbon fibers. It is believed that this is due, at least in part, to the higher residual stress and greater radial compressive force in the BMPPO drops. While the residual stress in the bismaleimide drops do physically "clamp" the drop on the fiber, the effect of fiber surface treatment on bismaleimide adhesion demonstrates that fiber surface properties also play an important role in fiber/bismaleimide adhesion.

3.4.2.4 Explanations for data scatter

The scatter in the microbond data may be attributed to testing parameters such as the position of the drop in the loading fixture, droplet gripping, shape of the meniscus on the polymer drop, and faulty measurement of the fiber diameter and embedded length. In addition, variations in the chemical, physical or morphological nature of the fiber along its length may affect the carbon fiber/polymer adhesion [41].

When the bismaleimide drops were examined following microbond testing, it was evident that the shape of the meniscus played a role in the data scatter. For example, in Figure 3.33(a), the meniscus was not axisymmetric. When the meniscus is not axisymmetric, the shearing plates do not come into contact with both sides of the bismaleimide drop simultaneously and the drop is loaded in a skewed, off-axis direction. In Figure 3.33(b), the bismaleimide meniscus extended well down the length of the fiber. Interfacial failure initiated above the shearing plates, creating a much greater embedded length than measured prior testing using an optical microscope.

3.5 SUMMARY

The carbon fiber adhesion of both a novel phosphorus-containing bismaleimide and a commercially available bismaleimide improved when the fibers were surface treated prior to bonding. Both bismaleimides adhered better to the commercially surface treated AS-4 carbon fiber and the "in house" air and ammonia plasma treated carbon fibers than to the untreated AU-4 carbon fiber. Possible explanations for improved bismaleimide

(a)

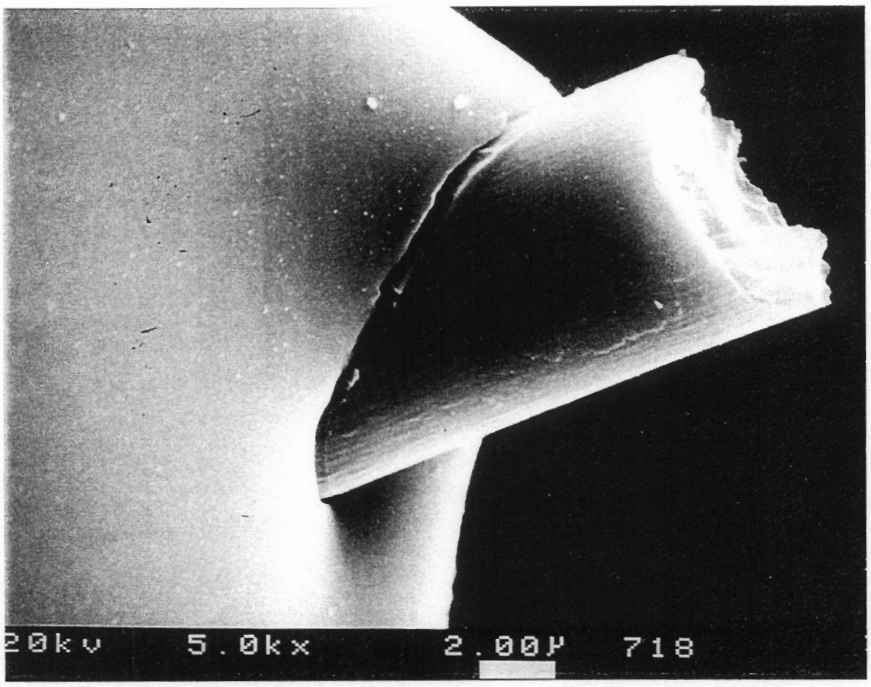

(b)

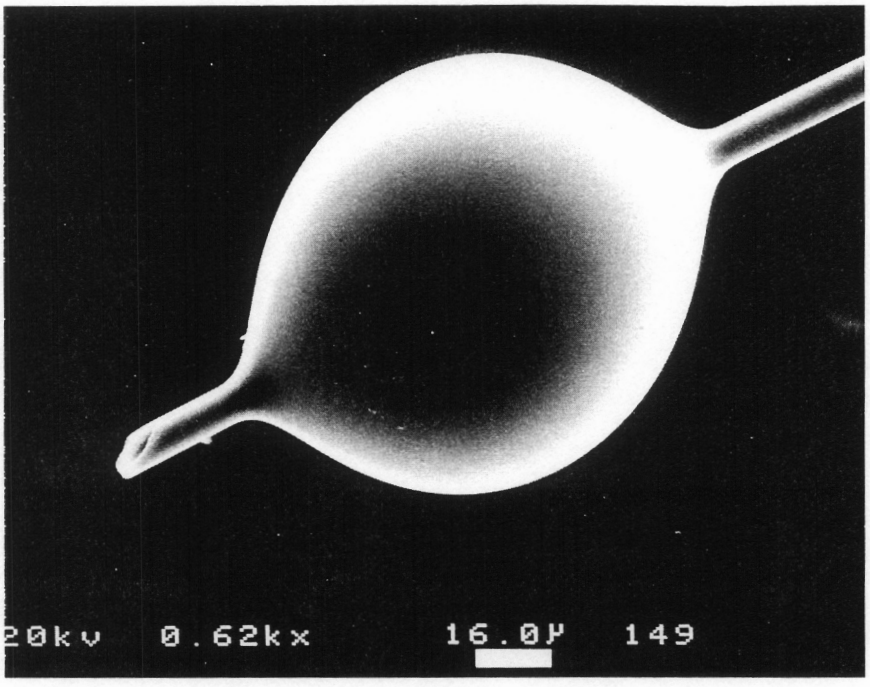

Figure 3.33. SEM photomicrographs at magnifications of (a) 5,000X and (b) 620X demonstrating the effect of the bismaleimide/carbon fiber meniscus on the scatter in the microbond data.

adhesion to the AS-4 carbon fiber include an increase in the fiber surface energy and wettability, removal of a weakly bound fiber surface layer, and an increase in the number of active sites on the fiber surface for specific chemical interactions with the polymer matrix.

The enhanced bismaleimide adhesion to the air plasma treated fiber may have been due to promotion of mechanical interlocking and to increased adsorption interactions between the fiber and the polymer. The ammonia plasma increased the number of amine groups and decreased the concentration of oxygen-containing functional groups on the fiber surface but, did not significantly affect the fiber/bismaleimide adhesion. This suggests that bismaleimide/carbon fiber adhesion depends more on the total concentration of polar functional groups on the fiber surface than on the number of amine groups available to react with the maleimide double bond.

Only a small number of bismaleimide/carbon fiber adhesion studies are reported in the literature. These studies have evaluated bismaleimide/carbon fiber adhesion by testing the mechanical properties of 'real' composite samples. In this work, due to the limited quantity of the novel BMPPO bismaleimide available, the bismaleimide/carbon fiber adhesion was studied using model single fiber composites. The single fiber fragmentation test could not be used due to the brittle nature and low strain-to-failure of the bismaleimides. Therefore, a single fiber pull-out test was used.

A technique was developed to cure axisymmetric bismaleimide drops around single carbon fibers for microbond testing. However, use of the microbond test to evaluate bismaleimide/carbon fiber adhesion was limited by the fiber strength. Even though the length of the fiber embedded in the bismaleimide drops ranged from only 40 to 200 μm, a large portion of the fibers failed during the microbond test. The percentage of fibers which failed during microbond testing, a measure of the bismaleimide/carbon fiber adhesion, was affected by the carbon fiber surface properties.

3.6 REFERENCES

1. H. Stenzenberger in Polyimides, D. Wilson, H. D. Stenzenberger, and P. M. Hergenrother (eds.), Chapman & Hall, New York (1990) 79.

2. D. Wilson in Polyimides, D. Wilson, H. D. Stenzenberger, and P. M. Hergenrother (eds.), Chapman & Hall, New York (1990) 189.

3. Stenzenberger, H., in Structural Adhesives: Developments in Resins and Primers, A. J. Kinloch (ed.), Elsevier Applied Science Publishers, New York, (1986) 77.

4. T. Takekoshi, *Adv. in Polymer Science* **94** (1990) 1.

5. L. M. Bates, *Plastics World* (Aug. 1991) 82.

6. H. D. Stenzenberger, M. Herzog, W. Romer, R. Scheiblich, and N. J. Reeves, *British Polym. J.* **15** (1983) 2.

7. P. M. Hergenrother, *Agnew. Chem. Int. Ed. Engl.* **29** (1990) 1262.

8. Varma, I. K., and S. Sharma, *Indian J. Technol.*, **25** (1987) 136.

9. H. D. Stenzenberger, P. Konig, M. Herzog, and W. Romer, *32nd Int. SAMPE Symposium*, **32** (1987) 44.

10. J. J. King, M. Chaudhari, and S. Zahir, *29th Nat. SAMPE Symp.* **29** (1984) 392.

11. G. D. Lyle, J. S. Senger, D. H. Chen, S. Kilic, S. D. Wu, D. K. Mohanty, and J. E. McGrath, *Polymer* **30** (1989) 978.

12. T. Pascal, R. Mercier, and B. Sillion, *Polymer* **30** (1989) 739.

13. T. Pascal, R. Mercier, and B. Sillion, *Polymer* **31** (1990) 78.

14. S. P. Wilkinson, PhD. Dissertation, Virginia Polytechnic Institute and State University, Blacksburg, VA (1991).

15. H. D. Stenzenberger, W. Romer, P. M. Hergenrother, and B. J. Jensen, *Int. SAMPE Symp.* **34** (1989) 2054.

16. H. D. Stenzenberger, W. Romer, P. M. Hergenrother, B. J. Jensen, and W. Breitigam, *35th Int. SAMPE Symp.* **35** (1990) 2175.

17. M. T. Blair, P. A. Steiner, and E. N. Willis, *33rd Int. SAMPE Symp.* **33** (1988) 524.

18. C. R. Lin, W. L. Liu, and J. T. Hu, *34th Int. SAMPE Symp.* **34** (1989) 1803.

19. Wood, P. A., G. D. Lyle, A. Gungor, C. D. Smith, and J. E. McGrath, *36th Int. SAMPE Symposium*, **36** (1991) 1355.

20. J. E. McGrath and P. A. Wood, III, U.S. Patent filed for Akzo America, Inc., August 15, 1990.

21. D. A. Kourtides and J. A. Parker, *Polym. Eng. Sci.* **18** (11) (1978) 855.

22. C. D. Smith, H. Grubbs, H. F. Webster, A. Gungor, J. P. Wightman, and J. E. McGrath, *High Perf. Polym.* **3** (4) (1991) 211.

23. I. K. Varma, G. Fohlen, and J. A. Parker, US Patent 4276344 1981.

24. J. E. Mark, H. R. Allcock, and R. West, Inorganic Polymers, Prentice Hall, Edgewood Cliffs, New Jersey (1992) 237.

25. J. M. Cartwright, S. P. Wilkinson, J. Hellgeth, T. C. Ward, and D. E. Kranbeuhl, *Proc. ACS Div. Polym. Materials: Sci. and Eng.* **67** (1992) 51.

26. R. J. Morgan, R. Jurek, and D. E. Larive, *Proc. ACS Div. Polym. Materials: Sci. and Eng.* **63** (1990) 681.

27. M. S. Chaltha and R. A. Dickie, *J. Appl. Polym. Sci.* **40** (1990) 411.

28. J. Mijovic and B. Schafran, *SAMPE J.* **26** (3) (1990) 411.

29. P. Pattabiraman, N. M. Rodriguez, B. Z. Jang, and R. T. K. Baker, *Carbon* **28** (6) (1990) 867.

30. E. Fitzer and R. Weiss, *Carbon* **25** (1987) 455.

31. E. Fitzer, K. H. Geigl, W. Huttner, and R. Weiss, *Carbon* **18** (1980) 389.

32. C. Megerdigian, R. Robinson, and S. Lehmann, *32nd Int. SAMPE Symp.* **32** (1987) 1126.

33. D. H. Kaelble, P. J. Dynes, and E. H. Cirlin, *J. Adhesion* **6** (1974) 23.

34. G. J. Farrow and C. Jones, to be published in *J. Adhesion.*

35. J. Schultz, L. Lavielle, and C. Martin, *J. Adhesion* **23** (1987) 45.

36. X. S. Bian, L. Ambrosio, J. M. Kenny, L. Nicolais, E. Occhiello, M. Morra, F. Garbassi, and A. T. DiBenedetto, *J. Adhesion Sci. Technol.* **5** (5) (1991) 377.

37. M. J. Pitkethly and J. B. Doble in Controlled Interphases in Composite Materials, H. Ishida (ed.), Elsevier, New York (1990) 809.

38. A. Garton and W. T. K. Stevenson, *J. Polym. Sci.: Part A: Polym. Chem.* **26** (1988) 541.

39. L. T. Drzal, M. C. Waterbury, and M. Madhukar, *37th Int. SAMPE Symp.* **37** (1992) 770.

40. L. T. Drzal, M. J. Rich, and P. F. Lloyd, *J. Adhesion* **16** (1982) 1.

41. P. J. Herrara-Franco and L. T. Drzal, *Composites* **23** (1) (1992) 2.

42. K. Waltersson, *Compos. Sci. Technol.* **22** (1985) 223.

43. K. Waltersson, *Compos. Sci. Technol.* **23** (1985) 303.

44. B. Z. Jang, *Compos. Sci. Technol.* **44** (1992) 333.

45. S. P. Wilkinson, PhD. Dissertation, Virginia Polytechnic Institute and State University, Blacksburg, Virginia 24061 (1991).

46. R. E. Allred and L. A. Harrah, *34th Int. SAMPE Symp.* **34** (1989) 2559.

47. S. M. Lee and S. Holguin, *J. Adhesion* **31** (1990) 91.

48. R. B. Prime in Thermal Characterization of Polymeric Materials, E. A. Turi (ed.), Academic Press, New York (1981) 435.

49. P. Marshall and J. Price, *Composites* **22** (1) (1991) 53.

50. L. S. Penn and C. T. Chou in International Encylopedia of Composites-Vol. 5, S. M. Lee (ed.), VCH Publishers, New York (1991) 308.

51. D. F. Adams, *J. Reinf. Plastics and Composites* **6** (1987) 66.

52. L. S. Penn and B. Jutis, *J. Adhesion* **30** (1989) 67.

CHAPTER 4
EFFECT OF FIBER SURFACE TREATMENTS ON ADHESION OF A NOVEL PYRIDINE CONTAINING THERMOPLASTIC

4.1 LITERATURE REVIEW

4.1.1 Thermoplastic Composite Preparation

Several techniques have been developed to combine thermoplastic polymers with carbon fibers and prepare continuous-fiber-reinforced thermoplastic "prepregs" for the fabrication of composites. These include solvent coating, hot melt, dry powder, and suspension prepregging. High performance thermoplastic polymers are only soluble in expensive and hazardous solvents and have high thermal transitions. Therefore, solution and melt prepregging is impractical.

Aqueous suspension prepregging is a relatively new technique which could circumvent many of the environmental and processing problems of solution and hot melt prepregging [1-6]. In suspension prepregging, a carbon fiber tow is passed through a suspension of polymer particles. A soluble polymer is added to the suspension to disperse the polymer matrix particles for good processing [7, 8]. The preparation of thermoplastic matrix composites using aqueous suspension prepregging is illustrated schematically in Figure 4.1 [9].

Davis and coworkers have prepared LaRC-TPI and PEEK composites using aqueous suspension prepregging [6]. The ammonium salt of either LaRC-TPI polyamic acid or Bis P/BTDA polyamic acid was used to disperse the thermoplastic powders in water. Scanning electron photomicrographs revealed that when transverse tensile strength experiments were performed on the PEEK composites, the fracture surface of the composite fabricated using LaRC-TPI polyamic acid was characterized by brittle failure at the fiber-matrix interface whereas the fracture surfaces of the laminates prepared with

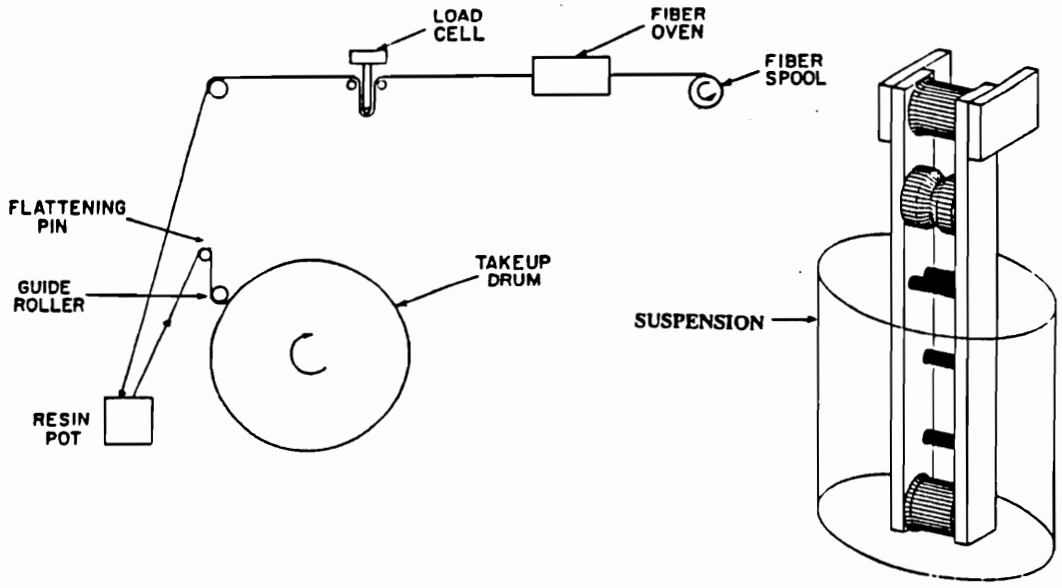

Figure 4.1. Schematic illustration of the preparation of continuous fiber reinforced thermoplastic matrix composites using suspension prepregging [9].

the Bis-P/BTDA polyamic acid showed ductile failure at the interface and there were virtually no bare carbon fibers. Therefore, it was concluded that the soluble polymer used to disperse the matrix polymer particles in the prepregging suspension also modifies the fiber/matrix interphase and binds the matrix to the fibers.

4.1.2 Thermoplastic/Fiber Adhesion Studies

The carbon fiber adhesion of thermoplastic polymers has not been studied as extensively as thermoset/carbon fiber adhesion since the majority of the commercially prepared composites have thermoset matrices. In the research devoted to thermoplastic/carbon fiber adhesion, it has been reported that some carbon fibers which show good adhesion to epoxy resins do not adhere well to thermoplastics. Although this is not well understood, it is true that, unlike thermosets, many thermoplastic polymers do not contain functional groups capable of forming covalent bonds with the groups on the fiber surface. In general, for a specific thermoplastic polymer, the carbon fiber adhesion will depend on the polymer chemistry and on the conditions under which the adhesion test specimens were prepared, for example, the thermal conditions, use of solvent, and cooling rate.

Bolvari and Ward studied the acid-base characteristics of carbon fibers and thermoplastic polymers and concluded that acid-base interactions only accounted for part of the fiber/matrix interfacial strength measured using a modified single fiber fragmentation test [10]. Bascom and coworkers found that different levels of fiber surface treatment and various organic sizings had no effect on the adhesion of polycarbonate to AS-4 carbon fibers [11]. However, Bascom and Chen reported that treating AS-1 and AS-4 carbon fibers in an oxygen plasma, significantly improved the adhesion of carbon fibers to polycarbonate and polysulfone [12]. Gaur and coworkers

showed that an acid plasma treatment produced a significant increase in carbon fiber bond strength with polyphenylene sulfide [13].

Commerçon and Wightman found that the adhesion of polyethersulfone to IM-7 carbon fibers improved when the fibers were exposed to an ammonia plasma and when the microbond samples were annealed above the glass transition temperature of the polymer [14]. Chuang and coworkers used the microbond test to obtain the interfacial shear strengths, in Table 4.1, with Hysol-Grafil type X/HS carbon fibers and several thermoplastics [15]. In general, the carbon fiber adhesion of the thermoplastics was poor and annealing was necessary to promote interfacial bonding.

4.2 OBJECTIVE

The goal of this work was to determine if the carbon fiber adhesion of poly(pyridine-bis A) was affected by the concentration of oxygen-containing functional groups on the fiber surface. Pyridine-containing thermoplastics are being developed at Virginia Tech for use as dispersant/binders in the aqueous suspension prepregging of thermoplastic matrix composites. The interfacial shear strength between poly(pyridine-bis A) and "as received" and plasma treated carbon fibers was measured using the microbond test.

4.3 EXPERIMENTAL

4.3.1 Materials

The PAN-based high strength, low modulus carbon fibers used in this study and their properties are listed in Table 2.5. The "S" designation indicates that the AS-4 fiber underwent a proprietary surface treatment as part of production. The "U" designation indicates that the AU-4 fiber was not surface treated. The fibers were used as received. The AS-4 fibers were treated in an air plasma as described in Chapter 2. The chemical

Table 4.1. Interfacial shear strengths obtained with the microbond test using the Hysol-Grafil X/HS carbon fiber and thermoplastic matrix resins [15].

Matrix Resin	Interfacial Shear Strength (MPa)	
	Without Annealing	With Annealing
polyethersulfone (PES)	27.6	31.8
polyetherimide (PEI)	13.8	35.2
polyetheretherketone (PEEK)	2.5	37.2
polyphenylene sulfide (PPS)	7.0	27.0

structure of the poly(pyridine-bis A), synthesized by Riffle and coworkers at Virginia Tech , is shown in Figure 4.2.

4.3.2 Polymer Characterization

4.3.2.1 Differential Scanning Calorimetry (DSC)

DSC was used to determine the glass transition temperature of the poly(pyridine-bis A) and to evaluate the thermal history of quenched and slow cooled samples. DSC was conducted on a Perkin Elmer DSC7 under a nitrogen atmosphere. The thermal history of the quenched and slow cooled poly(pyridine-bis A) samples was evaluated by heating the polymer samples through the polymer glass transition (T_g) at a heating rate of 10°C/minute. The T_g was obtained during a second heating cycle, after rapid cooling from above the T_g. The transition temperature was taken as the exotherm midpoint.

4.3.2.2 Thermogravimetric Analysis (TGA)

Dynamic TGA was performed on a Perkin Elmer TGA7 to determine the thermal stability of the poly(pyridine-bis A). Samples were heated at a rate of 10°C per minute in an air atmosphere. Weight loss of the sample was measured as a function of temperature. The thermal stability of the polymer was reported as a 5% weight loss.

4.3.2.3 Intrinsic Viscosity

An instrinsic viscosity was determined for the poly(pyridine-bisA). A Cannon-Ubbelohde dilution viscometer was used to collect data. The polymer was run in chloroform at 25°C. The viscosity was determined at four different polymer concentrations and the results were linearly extrapolated to the zero concentration.

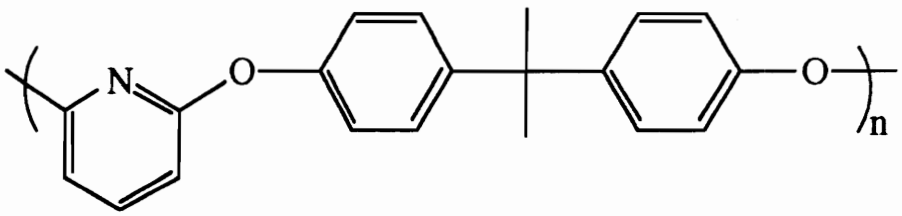

T_g = 108°C

5% weight loss @ 430°C

Intrinsic viscosity = 0.13 dl/g

Figure 4.2. Chemical structure and some properties of poly(pyridine-bis A).

4.3.3 Preparation of Microbond Samples

To form a microbond specimen, one end of a 4 cm long carbon fiber was affixed to a hole-punched aluminum tab using 3M Scotch™ glass cloth electrical tape. The metal tab was attached with a screw to one side of an aluminum frame. The central 2.5 cm of the fiber was suspended horizontally over open space and the free end of the carbon fiber was then affixed to the far end of the aluminum frame using another small square of electrical tape.

A small amount of poly(pyridine-bis A) powder was placed on the carbon fiber using a thin wire as an applicator. A soldering iron was used to heat the surrounding environment and melt the polymer on the fiber. The maximum temperature measured with a thermocouple just in front of, but not touching, the soldering iron tip was 140°C. The polymer formed an axisymmetric drop around the fiber when heated in a 200°C oven for 20 minutes. The length of fiber embedded in each polymer bead was measured using a Nikon UM-2 Measurescope. Some samples were annealed at 140°C for 2 hours in a convection oven and either slow cooled or quenched to room temperature. During the slow cooling procedure, the oven temperature decreased with time as shown in Figure 4.3.

4.3.4 Microbond Adhesion Testing

The microbond single fiber pull-out test was used to measure the force required to debond the cured bismaleimide drops from the carbon fibers. A schematic illustration of the microbond test set-up was shown in Figure 3.13. The fiber was suspended by a metal hook from a Mettler PM 300 balance. The samples were tested in shear using a custom-made microvise. The shearing plates were closed to a distance just greater than the fiber diameter with the aid of a video camera and monitor. The microvise was fixed on a

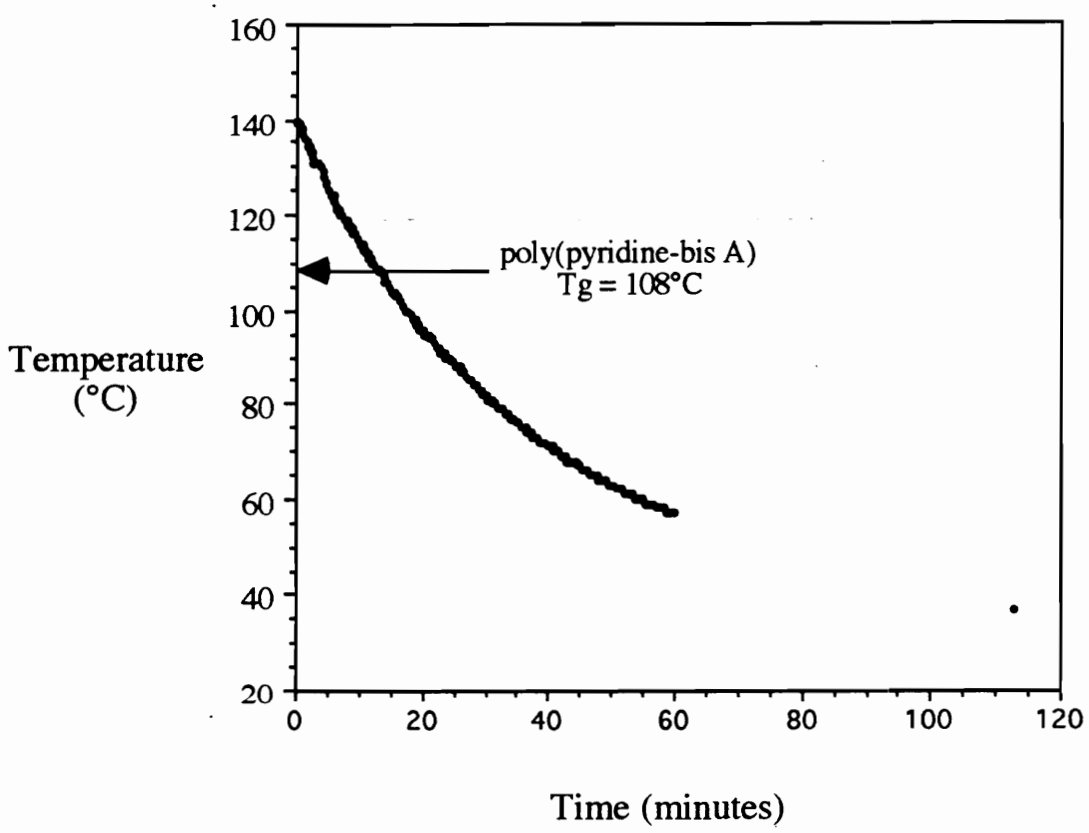

Figure 4.3. Oven temperature versus time when the poly(pyridine-bis A) microbond test samples were slow cooled from 140°C.

motorized stage that moved downward at a rate of 5 μm per second. The data was transmitted from the balance to the personal computer at a rate of 6 data points per second.

4.3.5 Scanning Electron Microscopy (SEM)

An ISI-SX-40 SEM was used to obtain photomicrographs of the bismaleimide beads cured around the carbon fibers. The samples were secured on an SEM mount using double-sided adhesive tape and metallic silver paint. The specimens were coated with gold using an Edwards Sputter-Coater S150B.

4.4 RESULTS AND DISCUSSION

4.4.1 Microbond Results

Examples of the load versus displacement curves obtained during microbond pull-out tests with poly(pyridine-bis A) are shown in Figure 4.4. In Figure 4.4(a), the polymer drop debonded and in Figure 4.4(b) the load required to debond the polymer drop exceeded the fiber tensile strength and the fiber failed. When the drop debonded during the microbond test, the load rose as the fiber and the matrix were strained, and then dropped when the fiber/matrix interface failed. At this point, the fiber was physically locked in the polymer drop. The load increased a second time until the polymer drop began to move down the fiber. As the fiber was pushed down the fiber, the load leveled off and varied about a mean value. When the fiber failed during the microbond test, the load rose, and then dropped to zero. The debond load and the fiber failure load were reported as the maximum load measured in the microbond test.

During pull-out experiments with poly(pyridine-bis A), the polymer drops were deformed by the shearing plates as shown in Figure 4.5, The deformation was limited to two indentations on opposite sides of the drop. A small "crown" of polymer was left on

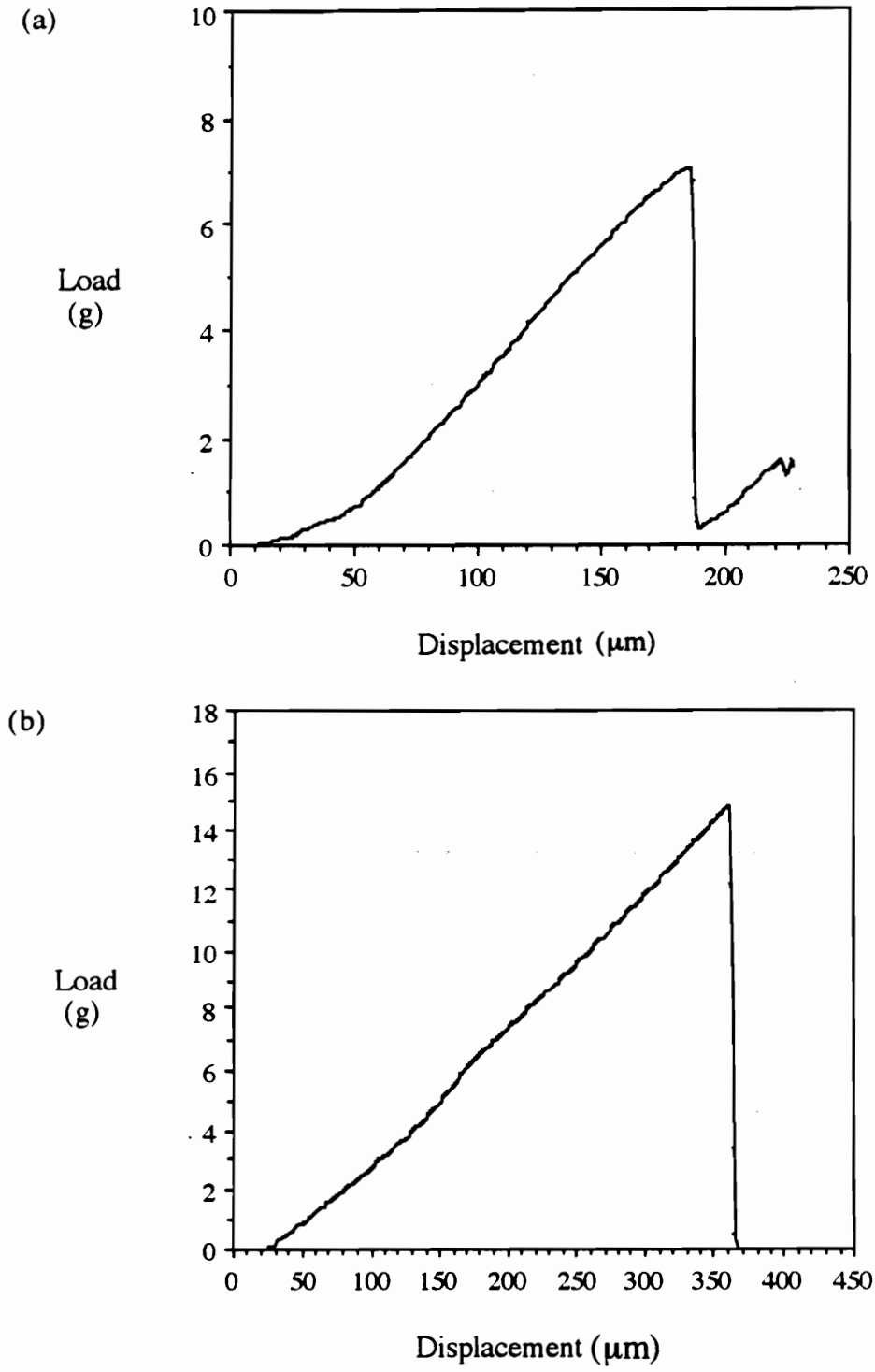

Figure 4.4. Load versus displacement plots obtained during microbond tests with poly(pyridine-bis A) when (a) the drop debonded and (b) the fiber failed.

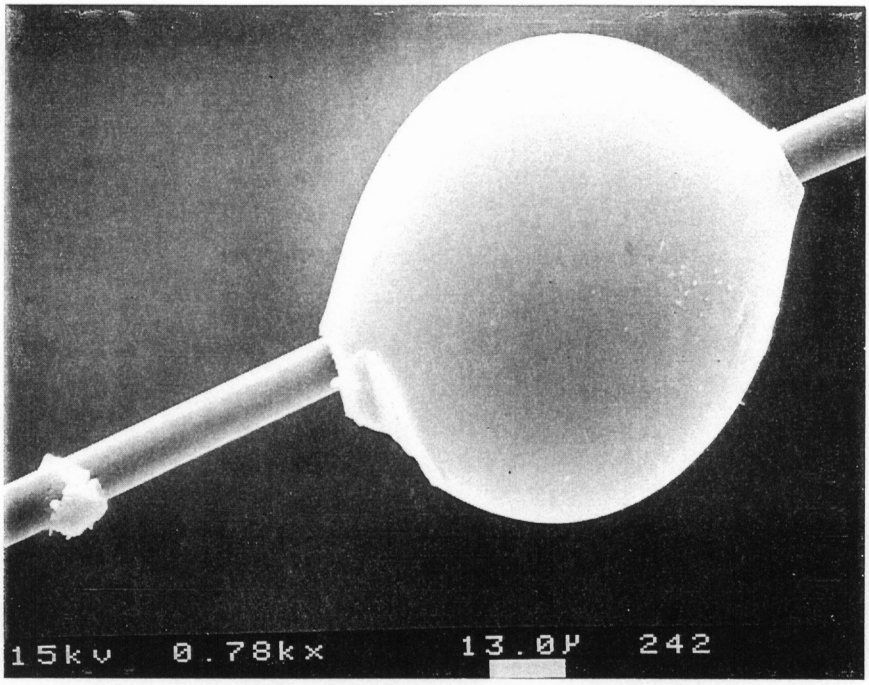

Figure 4.5. SEM photomicrograph of a poly(pyridine-bis A) drop debonded from an AS-4 carbon fiber (780X).

the fiber where the droplet was originally located. The matrix failed in the meniscus at the top of the drop due to the high stress concentration imposed in this region by the shearing plates. The crack extended toward the fiber, forming the "crown", and propagated through the fiber/matrix interface. This "crown" is evidence that the polymer was well bonded to the fiber. If "good" adhesion did not exist between the polymer drop and the fiber, the entire bead would have simply slid down the fiber when load was applied and the meniscus would not have failed.

The poly(pyridine-bis A) debond load is plotted as a function of the embedded length for AU-4, AS-4, and 15 sec. air plasma treated AS-4 carbon fibers in Figure 4.6. The load to failure was proportional to the bonded area. This suggests that the polymer/fiber interface failed with a yielding type of mechanism, rather than with catastrophic failure, as seen with the bismaleimides (Chapter 3).

The interfacial shear strength (τ) was calculated using equation 4.1,

$$\tau = \frac{F_d}{\pi\ d\ L} \tag{4.1}$$

where F_d is the debond load, d is the fiber diameter, and L is the fiber embedded length. An interfacial shear strength was determined for each data point and an average interfacial shear strength was averaged. The interfacial shear strength was also determined using another technique commonly reported in the literature. A linear curve with a zero intercept was fit to a plot of F_d vs. L. The slope of this line ($\Delta F_d/\Delta L$) was then used in equation 4.1 to obtain a value for τ. Jiang and Penn stated that while using a slope to calculate τ is an extremely bad practice in terms of fracture mechanics, it is of some utility when comparing samples whose elastic constants and specimen dimensions are the same [16].

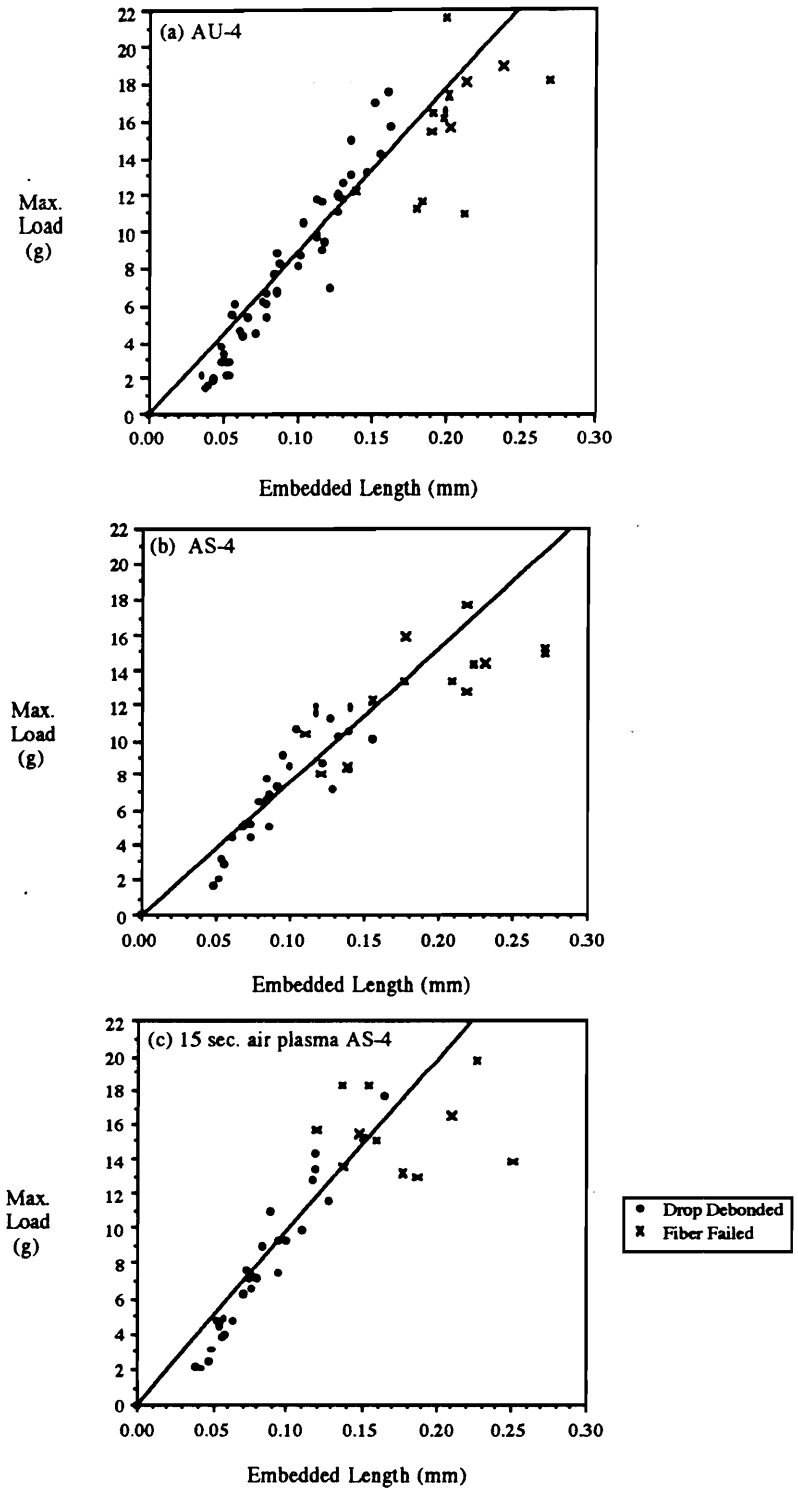

Figure 4.6. Maximum load measured in microbond test plotted versus the embedded length of (a) AU-4, (b) AS-4, and (c) 15 sec. air plasma treated AS-4 carbon fibers when the poly(pyridine-bis A) drops were quenched from 200°C.

4.4.2 Effect of Fiber Surface Treatments on Poly(pyridine-bis A) Adhesion

The average (± 95% confidence interval) poly(pyridine-bis A) interfacial shear strengths are shown in Figure 4.7 for the AU-4, AS-4, and air plasma treated AS-4 carbon fibers . The results in Figure 4.7 were obtained by calculating an interfacial shear strength for each data point and averaging the values. The interfacial shear strengths determined using the slopes of the linear lines fit to the data in Figures 4.6 are given in Figure 4.8. The oxidative carbon fiber surface treatments did not significantly affect the poly(pyridine-bis A) adhesion. Due to steric hindrance, the pyridine functional group in the polymer may not be able to come into close enough contact with the carboxylic acid and hydroxyl groups on the fiber surface for chemical interactions to take place.

In addition, scanning electron microscopy provided evidence that some cohesive failure within the polymer occurred in the poly(pyridine-bis A) microbond tests. As seen in Figure 4.9, pieces of polymer were left on the fiber surface where the poly(pyridine-bis A) drops were originally located. This demonstrates, along with the presence of the polymer "crown," that the polymer did adhere well to the carbon fiber surfaces. The cohesive polymer failure may be due, at least in part, to the low poly(pyridine-bis A) molecular weight. Intrinsic viscosity measurements (IV= 0.13 dl/g) as well as the fact that a solvent cast poly(pyridine-bis A) film could not be creased without the film breaking into many small pieces indicated that the poly(pyridine-bis A) was of low molecular weight.

4.4.3 Effect of Thermal History on Poly(pyridine-bis A) Adhesion

The load versus embedded length plots obtained when the poly(pyridine-bis A) samples were annealed and either slow cooled or quenched to room temperature are shown in Figures 4.10 and 4.11, respectively. As shown in Figure 4.7, when the poly(pyridine-bis A) microbond samples were annealed at 140°C (30°C > T_g) and either

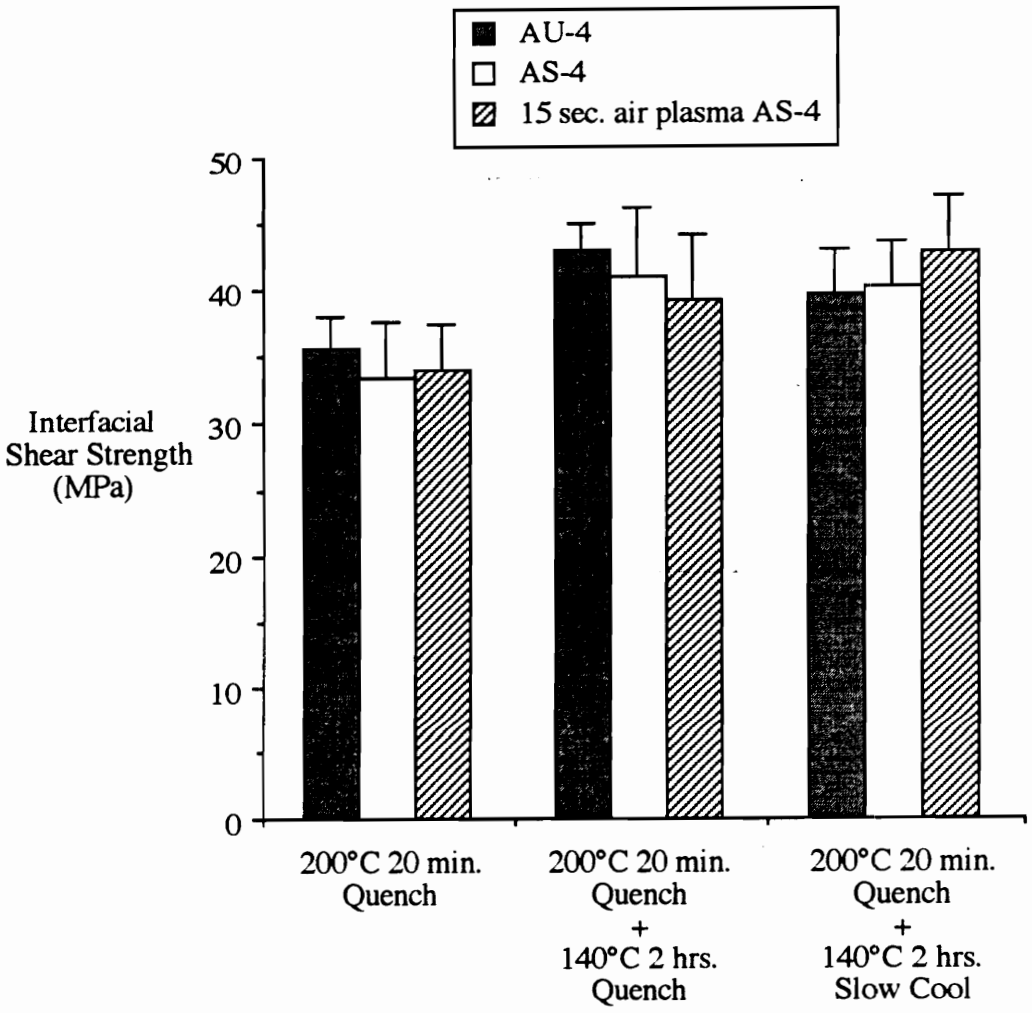

Figure 4.7. Average poly(pyridine-bis A) interfacial shear strengths obtained using the microbond test with three different fibers and three different thermal cycles.

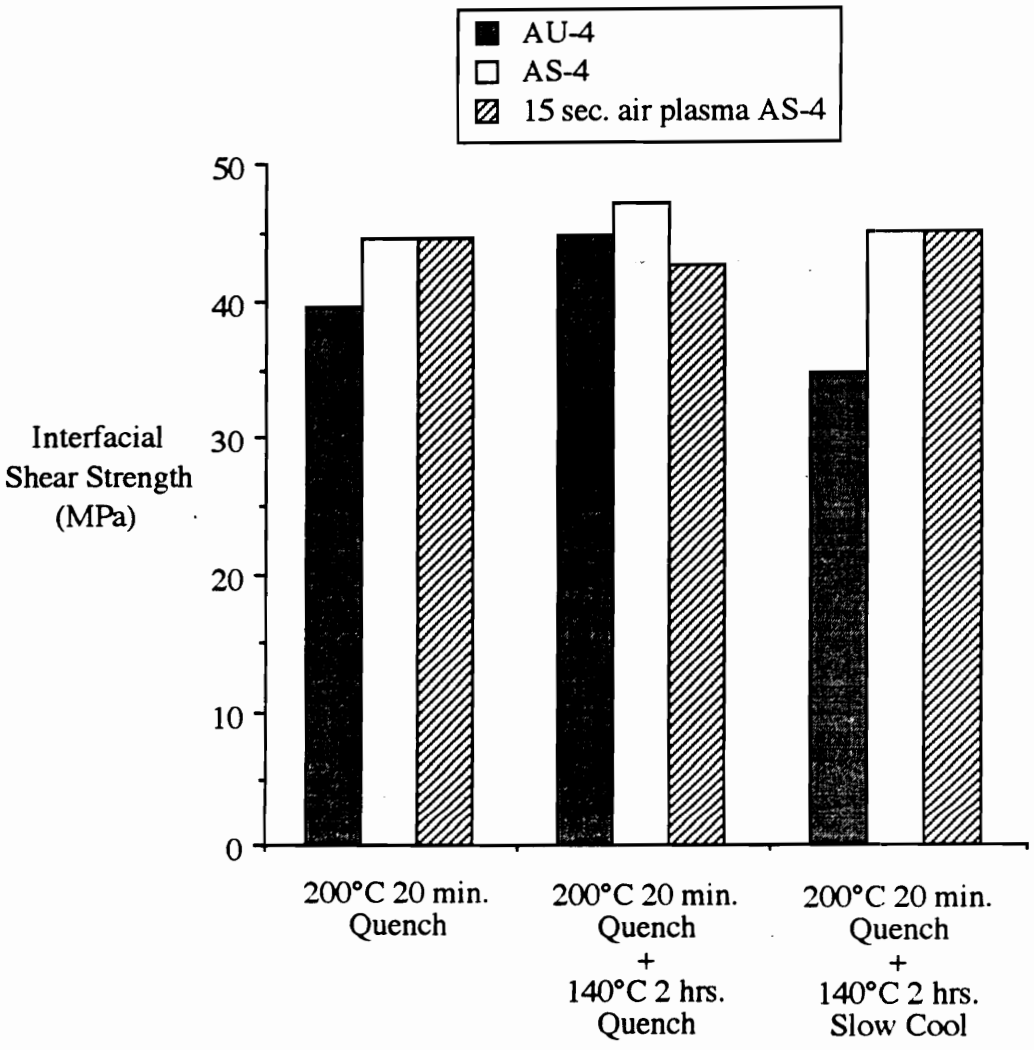

Figure 4.8. Poly(pyridine-bis A) interfacial shear strengths calculated from the slope of a linear curve fit to the microbond data for three different fibers and three different thermal cycles.

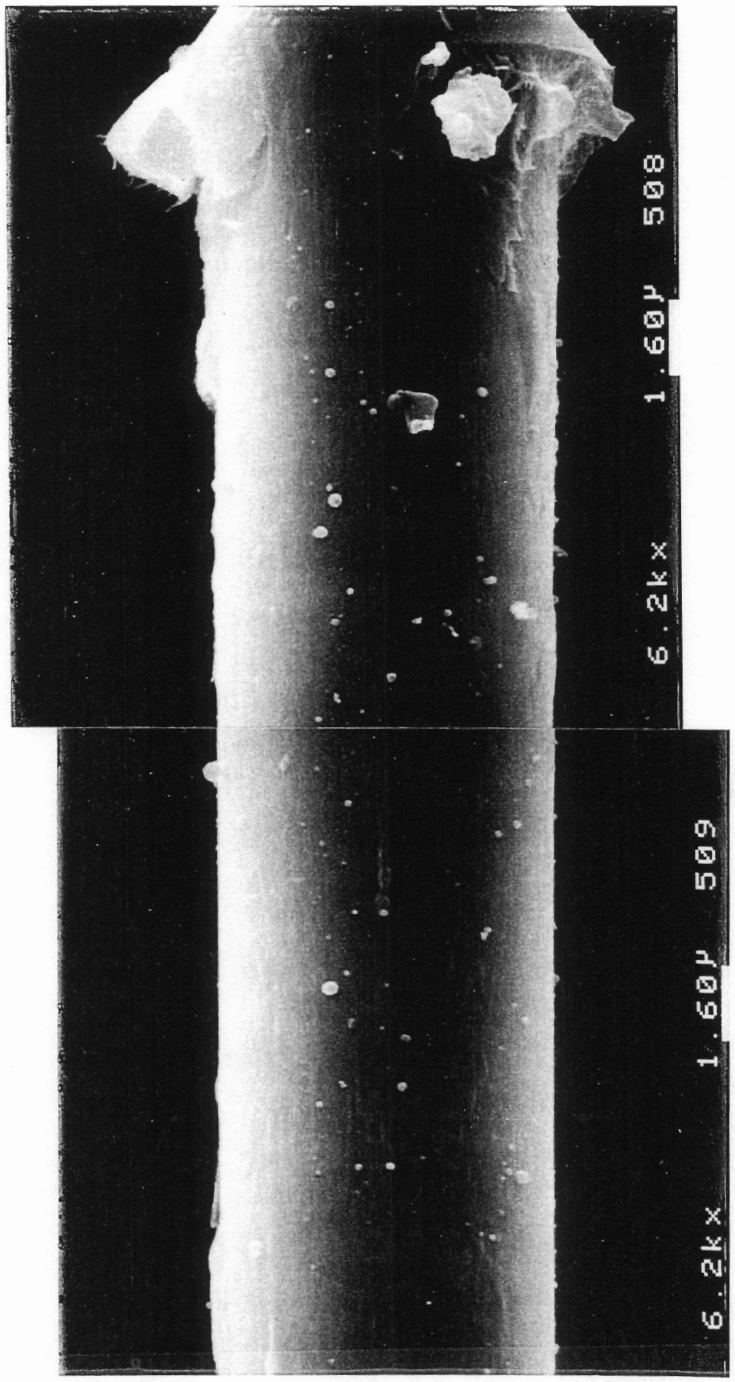

Figure 4.9. SEM photomicrographs of the poly(pyridine-bis A)/carbon fiber failure site demonstrating cohesive failure within the polymer (6,200X).

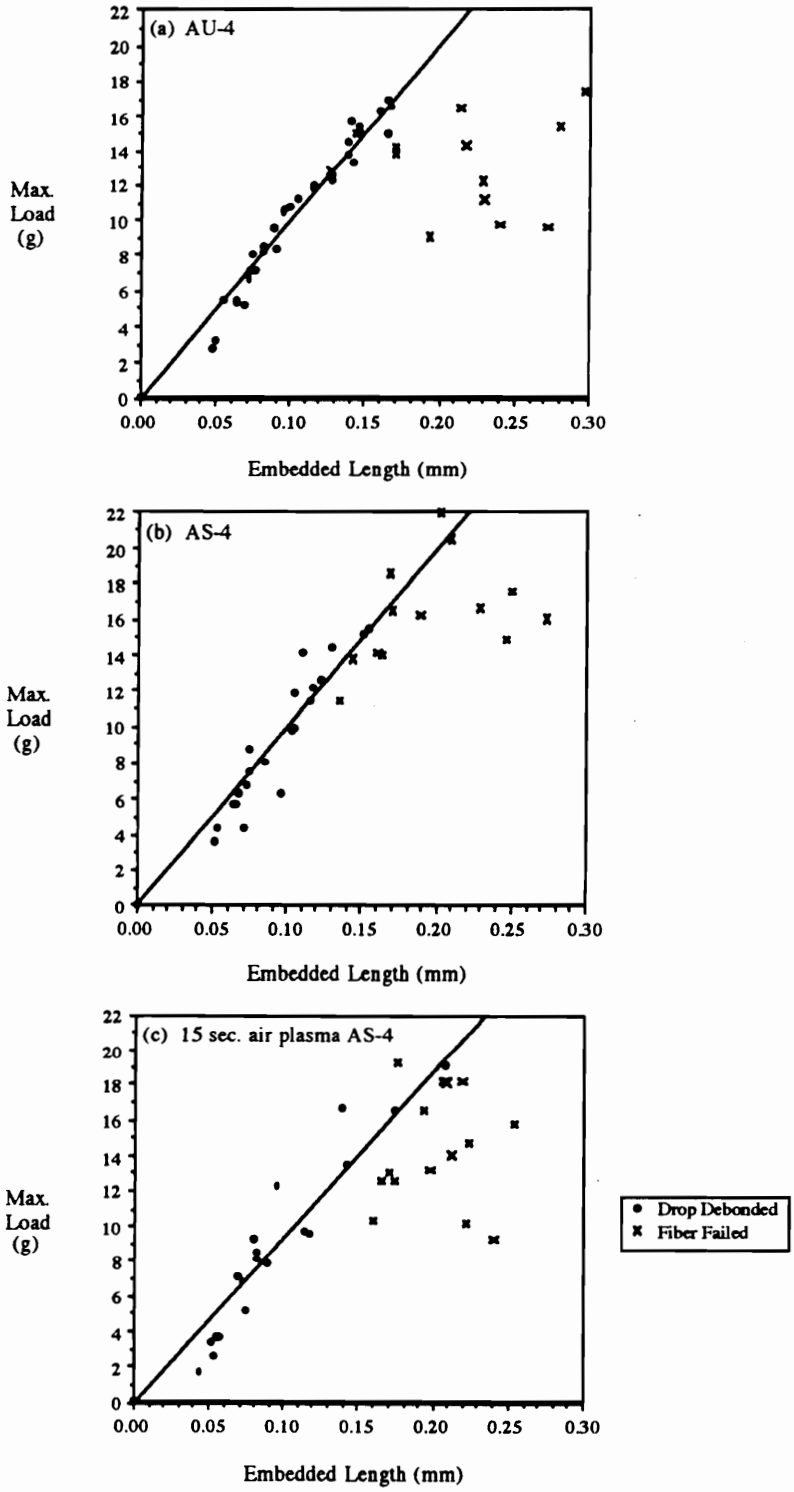

Figure 4.10. Maximum load measured in the microbond test plotted versus embedded length of (a) AU-4, (b) AS-4, and (c) 15 sec. air plasma treated AS-4 carbon fibers when the poly(pyridine-bis A) drops were annealed and slow cooled.

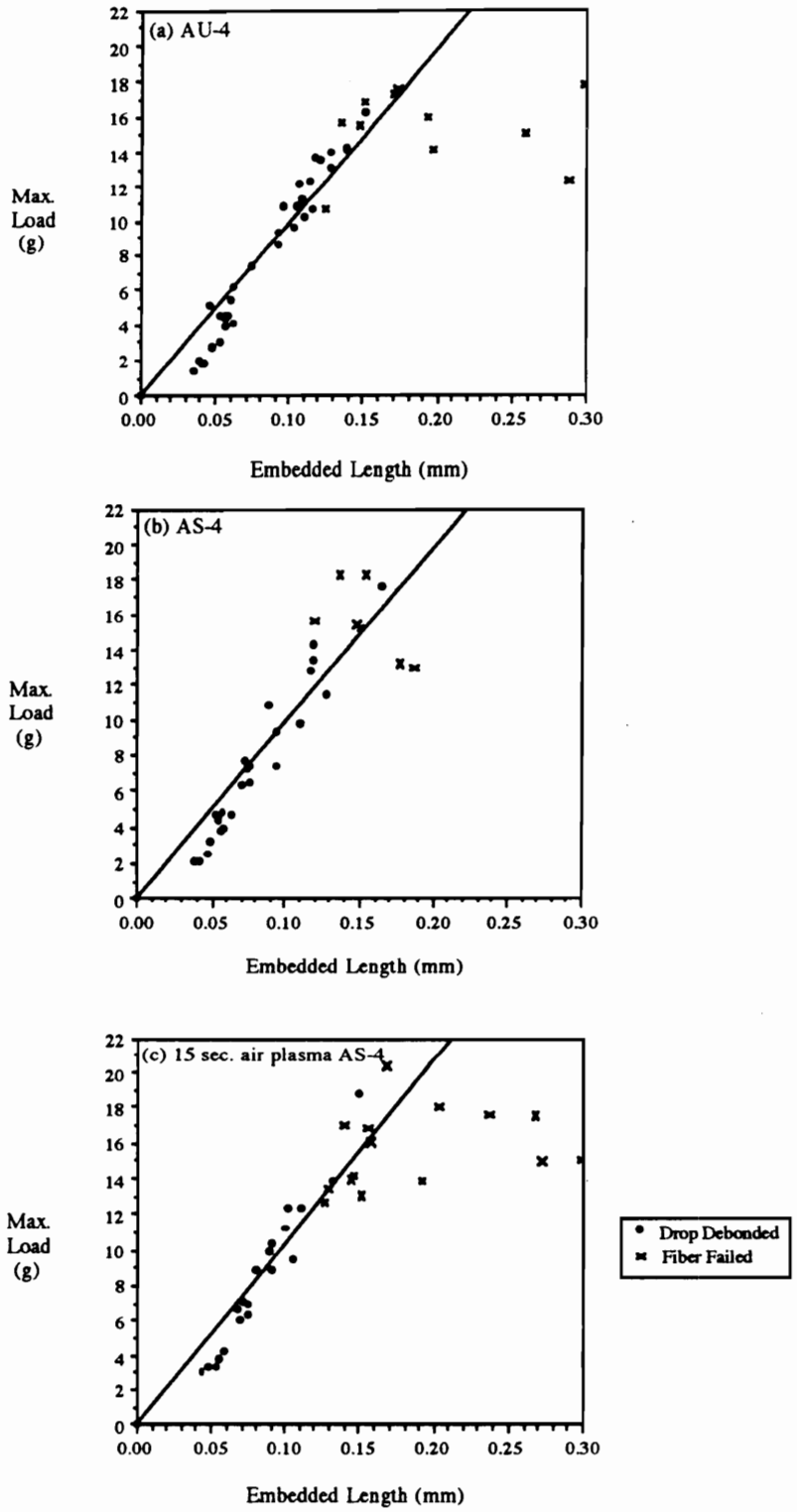

Figure 4.11. Maximum load measured in microbond test plotted versus embedded length of (a) AU-4, (b) AS-4, and (c) 15 sec. air plasma treated AS-4 carbon fibers when the poly(pyridine-bis A) drops were annealed and quenched.

slow cooled or quenched to room temperature, there was a slight increase in the average interfacial shear strength. Commerçon and Wightman [14] and Chuang and coworkers [15] both showed an improvement in fiber/thermoplastic adhesion when the microbond samples were annealed above the T_g of the polymer. This may be due to improved wetting and interfacial adsorption interactions or, it may be due to a decrease in the polymer free volume. As the polymer free volume decreases, the polymer shrinks around the fiber and exerts a greater radial compressive or "clamping" force on the fiber.

When the interfacial shear strength was determined using the slopes of the linear curves fit to the microbond data, in Figure 4.8, there was no effect of annealing on the fiber/matrix adhesion. This may be attributed to the poor fit of the data at low embedded lengths. If the linear curve was not given a zero intercept, the slopes of the lines would have been higher. The lack of correlation between the interfacial shear strengths calculated using these two different techniques demonstrates the complexity of interpreting microbond data and the difficulty in comparing interfacial shear strength values reported in the literature.

The DSC traces observed with the poly(pyridine-bis A) samples subjected to the three different thermal cycles used in the microbond experiments are shown in Figure 4.12. Small humps or aging peaks were visible on the trace of the annealed and slow cooled sample. This suggests that slow cooling (see Figure 4.3) induced physical aging of the polymer. Therefore, the annealed and slow cooled microdrops should have a smaller free volume and therefore exert a greater compressive radial force on the fiber than those quenched from 200°C. However, there was no significant difference in interfacial shear strength between the slow cooled and quenched samples. Therefore, the compressive radial force exerted by the poly(pyridine-bis A) drops on the fiber did not affect the fiber/matrix interfacial shear strength measured by the microbond test.

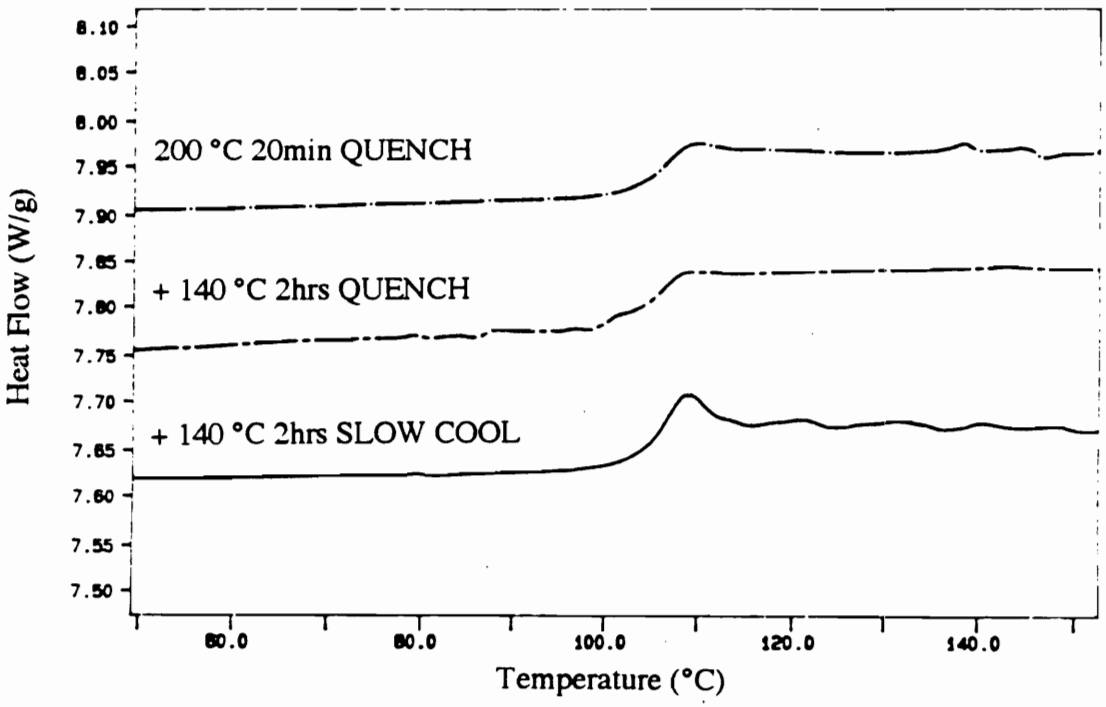

Figure 4.12. DSC traces of quenched and annealed poly(pyridine-bis A) samples.

4.5 SUMMARY

The adhesion of poly(pyridine-bis A) to untreated AU-4, commercially surface treated AS-4, and 15 sec. air plasma treated AS-4 carbon fibers was measured using the microbond single fiber pull-out test. XPS revealed that the surfaces of the AU-4, AS-4, and 15 sec. air plasma treated AS-4 carbon fibers contained 6, 9, and 20 atomic% oxygen, respectively. The adhesion of poly(pyridine-bis A) was not affected by the concentration of oxygen on the carbon fiber surfaces. Due to steric hindrance, the pyridine functional group in the polymer may not be able to come into close enough contact with the carboxylic acid and hydroxyl groups on the fiber surface for chemical interactions to take place. In addition, scanning electron microscopy provided evidence that some cohesive failure occurred within the polymer when the poly(pyridine-bis A) drops were debonded. When failure occurs within the polymer drop, the cohesive strength of the polymer is measured instead of the true strength of the fiber/polymer interface.

The interfacial shear strength of the annealed poly(pyridine-bis A)/AS-4 carbon fiber interface was 39.3 MPa. This corresponds well with the carbon fiber interfacial shear strengths of polyetherimide (35.2 MPa) and polyetheretherketone (37.2 MPa) in Table 4.1. However, the interfacial shear strength obtained with the AS-4 carbon fiber and poly(pyridine-bis A) was significantly less than that given for epoxy (50.3 MPa) in Table 2.1.

4.6 REFERENCES

1. A. E. Brink, S., Gutzeit, T. Lin, H. Marand, K. Lyon, J. E. McGrath, and J. S. Riffle, *ACS Polymer Preprints* **33** (1) (1992) 402.

2. T. W. Towell, D. E. Hirt, and N. J. Johnston, *22nd Int. SAMPE Tech. Conf.* **22** (1990) 1156.

3. D. E. Hirt, J. M. Marchello, and R. M. Baucom, *22nd Int. SAMPE Tech. Conf.* **22** (1990) 360.

4. S. R. Iyer and L. T. Drzal, *J. Thermoplastic Comp. Materials* **3** (1990) 325.

5. S. Clemans and T. Harness, *SAMPE Quarterly* **20** (4) (1989) 38.

6. R. M. Davis, A. Texier, T. H. Yu, K. Lyon, A. Gungor, J. E. McGrath and J. S. Riffle, *ACS Polymer Preprints* **33** (1) (1992) 416.

7. T. W. Towell, D. E. Hirt, and N. J. Johnston, SAMPE J.

8. A. Texier and R. M. Davis, *Proc. of the Society of Plastics Engineers ANTEC '91* **37** (1991) 2018.

9. A. Texier, Masters Thesis, Virginia Polytechnic Institute and State University, Blacksburg, Virginia (1991).

10. A. E. Bolvari and T. C. Ward in Inverse Gas Chromatography - Characterization of Polymers and Other Materials, D. R. Lloyd, T. C. Ward, and H. P. Schreiber (eds.), ACS Symposium Series No. 391, ACS, Washington, D.C. (1988) 217.

11. W. D. Bascom, K. J. Yon, R. M. Jensen, and L. Cordner, *J. Adhesion* **34** (1991) 79.

12. W. D. Bascom and W. J. Chen, *J. Adhesion* **34** (1991) 99.

13. U. Gaur, G. Desio, and B. Miller, *Plastics Engineering* (October 1991) 43.

14. P. Commerçon and J. P. Wightman, *J. Adhesion* **38** (1992) 55.

15. S. L. Chuang, N. J. Chu, and W. T. Whang, *J. Appl. Polym. Sci.* **41** (1990) 373.

16. K. R. Jiang and L. S. Penn, *Compos. Sci. Technol.* **45** (1992) 89.

CHAPTER 5
OVERALL SUMMARY

As stated in Chapter 1, the objective of this work was to study the adhesion of high performance polymers to "as received" and plasma treated carbon fibers. The goal was to support several of the interdisciplinary research efforts of the NSF Science and Technology Center for High Performance Polymeric Adhesives and Composites by determining the chemical and mechanical properties of the carbon fiber and the polymer which effect the fiber/polymer adhesion in a given composite system. The microbond single fiber pull-out test was used to study the carbon fiber adhesion of a phosphorus-containing bismaleimide, a cyanate ester resin, and a pyridine-containing thermoplastic.

The surface chemical composition, topography, tensile strength, and surface energy of untreated AU-4 and AS-4 carbon fibers were evaluated. The commercial surface treatment which converted the AU-4 to the AS-4 fiber oxidized the carbon fiber surface. Air, oxygen, and ammonia plasma treatments were used to modify the carbon fiber surface. Following short plasma exposures (15 sec. to 1 min.) the carbon fiber surface atomic composition reached a steady state due either to saturation of the active sites on the fiber surface or equivalence of the rate of incorporation of oxygen- and nitrogen-containing functional groups with the rate of removal of these groups. Angular dependent XPS revealed that the inorganic plasmas only effected the outermost surface of the fiber. An ethylene plasma was used to deposit a layer of plasma polymer on the carbon fiber surface. The ethylene plasma polymer was crosslinked and containe some hydroxyl and carbonyl groups.

Fifteen second air and oxygen plasma treatments increased the surface oxygen concentration from 9 to 20 atomic%. A one minute ammonia plasma treatment increased the fiber surface nitrogen content from 3 to 5 atomic%. The curve-fit carbon 1s

photopeaks indicated that the air and oxygen plasmas increased the concentration of oxygen-containing functional groups on the carbon fiber surface. The ammonia plasma increased the number of aromatic amine groups on the carbon fiber surface and decreased the concentration of oxygen-containing functional groups.

Both one-liquid and two-liquid wetting techniques were used to determine the total, dispersive, and polar surface energies of untreated, commercially surface treated, and plasma treated carbon fibers. With both wetting techniques, the polar component to the fiber surface energy increased as the concentration of the oxygen and nitrogen on the carbon fiber surface was increased. When the one-liquid technique was used, the dispersive surface energy was not affected by the fiber surface treatements. However, with the two-liquid technique, the dispersive component increased following ammonia plasma treatment.

The AS-4 carbon fiber tow was wet with the aqueous poly(amic acid) solution in which the matrix powder is dispersed during aqueous suspension prepregging of thermoplastic matrix composites. XPS and SEM analysis of the tow revealed that the fibers were coated with a layer of poly(amic acid). It was found that the mechanical properties of aqueous suspension prepregged thermoplastic composites are affected by the choice of poly(amic acid) dispersant. Apparently, the poly(amic acid) dispersant coats the fiber tow during prepregging and creates a distinct interphase between the fiber and matrix.

The carbon fiber adhesion of both a novel phosphorus-containing bismaleimide and a commercially available bismaleimide improved when the fibers were surface treated prior to bonding. Both bismaleimides adhered better to the commercially surface treated AS-4 carbon fiber and the "in house" air and ammonia plasma treated carbon fibers than to the untreated AU-4 carbon fiber. Possible explanations for improved bismaleimide adhesion to the AS-4 carbon fiber include an increase in the fiber surface energy and

wettability, removal of a weakly bound fiber surface layer, and an increase in the number of active sites on the fiber surface for specific chemical interactions with the polymer matrix.

The enhanced bismaleimide adhesion to the air plasma treated fiber may have been due to promotion of mechanical interlocking and to increased adsorption interactions between the fiber and the polymer. The ammonia plasma increased the number of amine groups and decreased the concentration of oxygen-containing functional groups on the fiber surface, but did not significantly affect the fiber/bismaleimide adhesion. This suggests that bismaleimide/carbon fiber adhesion depends more on the total concentration of polar functional groups on the fiber surface than on the number of amine groups available to react with the maleimide double bond.

Only a small number of bismaleimide/carbon fiber adhesion studies are reported in the literature. These studies have evaluated bismaleimide/carbon fiber adhesion by testing the mechanical properties of 'real' composite samples. In this work, due to the limited quantity of the novel bismaleimide available, the bismaleimide/carbon fiber adhesion was studied using model single fiber composites. The single fiber fragmentation test could not be used due to the brittle nature and low strain-to-failure of bismaleimides. Therefore, a single fiber pull-out test was used.

A technique was developed to cure axisymmetric bismaleimide drops around single carbon fibers for microbond testing. However, use of the microbond test to evaluate bismaleimide/carbon fiber adhesion was limited by the fiber strength. Even though the length of the fiber embedded in the bismaleimide drops ranged from only 50 to 200 μm, a large portion of the fibers failed during the microbond test. The percentage of fibers which failed during microbond testing, a measure of the bismaleimide/carbon fiber adhesion, was affected by the carbon fiber surface properties.

The adhesion of poly(pyridine-bis A) to untreated AU-4, commercially surface treated AS-4, and 15 sec. air plasma treated AS-4 carbon fibers was measured using the microbond single fiber pull-out test. XPS revealed that the surfaces of the AU-4, AS-4, and 15 sec. air plasma treated AS-4 carbon fibers contained 6, 9, and 20 atomic% oxygen, respectively. The adhesion of poly(pyridine-bis A) was not affected by the concentration of oxygen on the carbon fiber surfaces. Due to steric hindrance, the pyridine functional group in the polymer may not be able to come into close enough contact with the carboxylic acid and hydroxyl groups on the fiber surface for chemical interactions to take place. In addition, scanning electron microscopy provided evidence that some cohesive failure occurred within the polymer when the poly(pyridine-bis A) drops were debonded. When failure occurs within the polymer drop, the cohesive strength of the polymer is measured instead of the true strength of the fiber/polymer interface.

The interfacial shear strength of the annealed poly(pyridine-bis A)/AS-4 carbon fiber interface was 39.3 MPa. This value corresponds well with the carbon fiber interfacial shear strengths of polyetherimide (35.2 MPa) and polyetheretherketone (37.2 MPa) reported in the literature (see Table 4.1). However, the interfacial shear strength obtained with the AS-4 carbon fiber and poly(pyridine-bis A) was significantly less than that given for epoxy (50.3 MPa) given in the literature (see Table 2.1).

APPENDIX
Microbond experiments with cyanate esters

The "as received" AS-4 carbon fibers were affixed to a metal rack as described in Section 3.3.3. Arocy B-10 [2,2'-bis(4-cyanatophenyl) propane], provided by Ciba-Geigy, Inc. was the commercial cyanate ester thermosetting system studied. The resin was used neat and was blended with 20 wt.% of a hydroxy-terminated poly(arylene ether) prepared from phenolphthalein and dichlorodiphenyl sulfone. The cyanate ester monomer was heated in a glass flask immersed in a 90°C silicone oil bath to provide a homogeneous melt and then degassed under vaccum. The catalyst (250 ppm aluminum acetylacetonate / 2pph nonyl phenol) was added with stirring and the system was further degassed.

The cyanate ester resins were applied to the carbon fibers using a thin wire applicator. A soldering iron was used to heat the surrounding environment and melt the cyanate ester resin on the fiber. The maximum temperature measured with a thermocouple just in front of, but not touching, the soldering iron tip was 140°C. The resin was then cured by heating to 104°C for 3 hours, 200°C for 1 hour, and 250°C for 2 hours in a convection oven. The adhesion between the cyanate ester and the AS-4 carbon fibers was measured using the microbond test as described in Section 3.3.4.

The debond load was plotted versus the drop embedded length in Figure A.1 and linear regression was used to fit a line with a zero y-axis intercept to the data. The slope ($\Delta F_d/\Delta L$) of this line was used in equation 4.1 to calculate the fiber/matrix interfacial shear strength. The interfacial shear strengths between the "as received" AS-4 carbon fiber and the neat cyanate ester and thermoplastic-modified cyanate ester were 64.4 and 75.9 MPa, respectively. However, since only a limited number of data points were generated, more investigation is neccessary before any conclusions can be drawn.

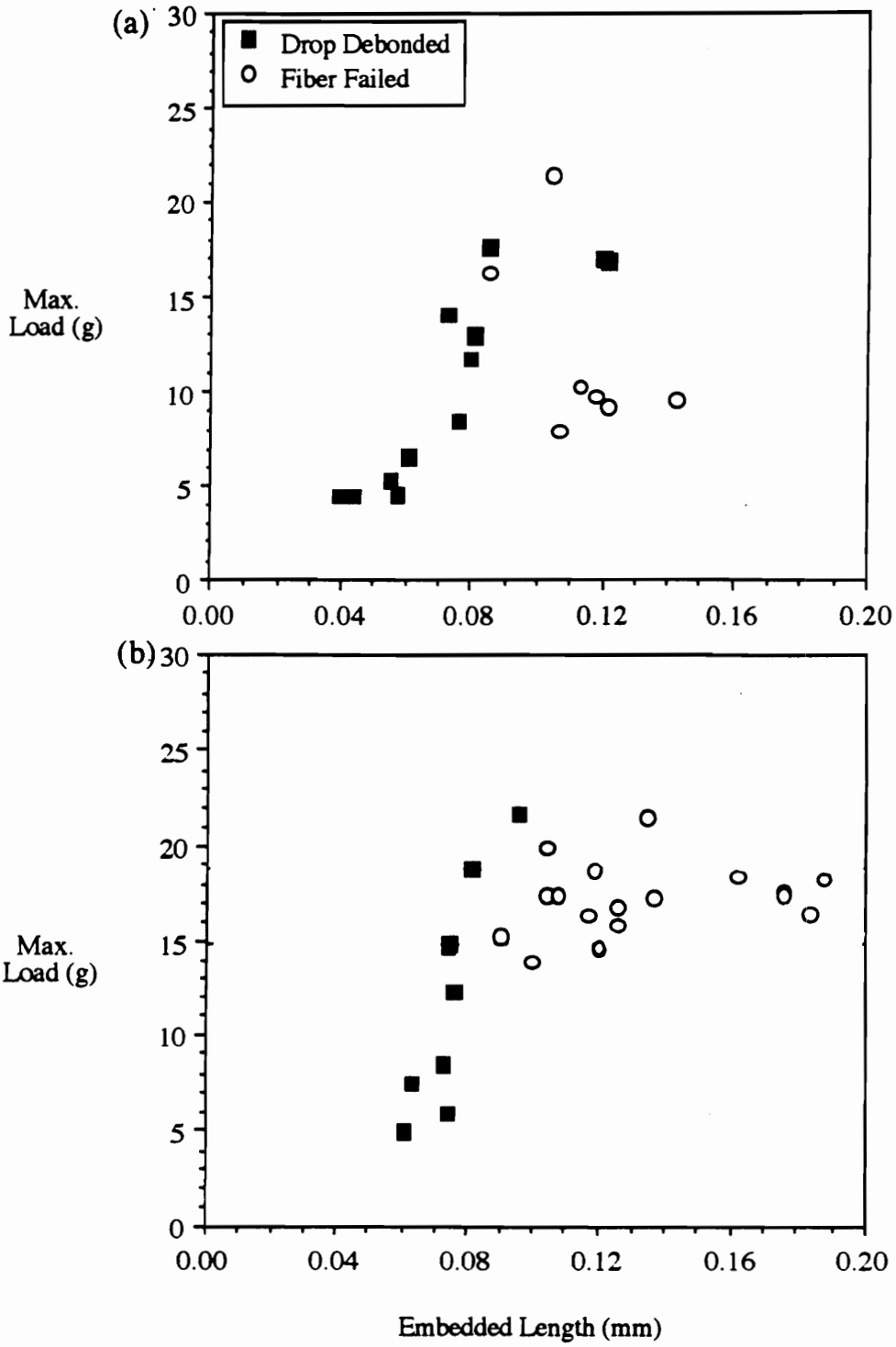

Figure A.1. Maximum force measured in the microbond experiment as a function of the "as received" AS-4 carbon fiber embedded length with the (a) neat cyanate ester and the (b) thermoplastic-modified cyanate ester resin.

VITA

Cheryl L. Heisey was born in Winchester, Virginia on May 23, 1967, the daughter of Menno and Carolyn Heisey. She graduated from James Wood High School in Winchester, Virginia in June 1985. In May 1989, she obtained a Bachelor of Science degree in Biochemistry from Virginia Polytechnic Institute and State University in Blacksburg, Virginia. As an undergraduate, she evaluated commercial explosive vapor detectors under the direction of George Reiner and Dr. H. M. McNair and presented her findings at Sandia National Laboratory.

During the summer of 1989 she was employed by the General Electric Corporate Research and Development Center in Schenectady, New York where she studied paint adhesion in the laboratory of Dr. D. G. LeGrand. In August of 1989, she married Martin E. Rogers and began graduate studies in chemistry at Virginia Polytechnic Institute and State University. She joined the research group of Dr. J. P. Wightman in January 1990 and began studying carbon fiber/polymer adhesion.

The author has participated in the Center for Adhesive and Sealant Science, the Center for Composite Materials Science, and the National Science Foundation Science and Technology Center for High Performance Polymeric Adhesives and Composites. She is a member of the Adhesion Society, the American Chemical Society, and Sigma Xi. She was awarded a Fellowship from the Adhesive and Sealant Council, Inc. in 1991. Cheryl accepted a position as an Advanced Chemist in the Packaging Research Laboratory at Eastman Chemical Company in Kingsport, Tennessee.

Cheryl L. Heisey